

# Aerodynamics

## 16. Aerodynamics

Vehicle aerodynamics has its roots in aviation, and the same is true for the related experimental techniques. The wind tunnel is the key carry-over element. Wind tunnels have been adapted stepwise to meet the specific needs of vehicle aerodynamic studies. Three areas of development must be mentioned: With vehicles a much greater blockage can be tolerated; to simulate the relative motion between vehicle and road or track different belt systems and mechanisms to reproduce wheel rotation have turned out to be useful; for tests in various climates a variety of specialized smaller wind tunnels have been developed. Measurement techniques are very much the same as in aeronautics at low Mach number and increasingly particle image velocimetry (PIV) is being applied to study the complex flow fields around vehicles. Nevertheless, flow visualization and photogrammetry still remains an indispensable tool for a quick evaluation of different geometries, also for dynamic flow conditions.

<b>16.1 Ground Vehicle Aerodynamics</b>	1043
16.1.1 Vehicles in Their Natural Environment	1043
16.1.2 Simulation of the Drive on Road and Track	1044
16.1.3 Wind Tunnels for Ground Vehicles	1044

### 16.1 Ground Vehicle Aerodynamics

#### 16.1.1 Vehicles in Their Natural Environment

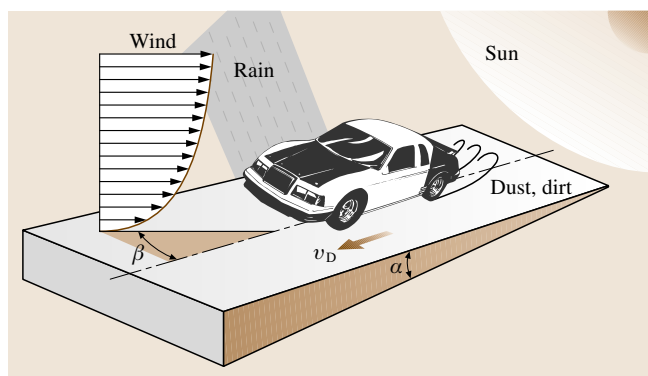
The environment to which a ground vehicle is exposed during cruise is sketched in Fig. 16.1. The flow around it and its thermal loading depend on various conditions:

- vehicle speed
- grade of road or track
- strength and gustiness of wind
- rain or snow

16.1.4 Wind-Tunnel Design	1047
16.1.5 Equipment for Automotive Wind Tunnels	1054
16.1.6 Limits of Simulation	1058
16.1.7 Typical Vehicle Wind Tunnels	1063
16.1.8 Tests with Moving Models and Full-Scale Vehicles	1068
16.1.9 Measurement Technique	1070
16.1.10 Support by Computational Fluid Dynamics	1080
<b>16.2 Short-Duration Testing of High Enthalpy, High Pressure, Hypersonic Flows</b>	1081
16.2.1 Working Principle of Shock Tubes/Tunnels and Shock Expansion Tubes/Tunnels	1082
16.2.2 Measurement Techniques	1095
16.2.3 Typical Applications of Shock Tunnel and Shock Expansion Tunnel Facilities	1111
<b>16.3 Bluff Body Aerodynamics</b>	1125
16.3.1 Flow Physics, Facilities, and Approach	1125
16.3.2 How Bluff is a Bluff Body?	1128
16.3.3 Base Pressure, Drag, Lift, and Strouhal Number	1133
16.3.4 Overview of Vortex Shedding Regimes	1135
16.3.5 Concluding Remarks	1145
<b>References</b>	1146

- road dirt
- sun load

As can be seen in Fig. 16.1 the flow field past a vehicle on a road or track is made up of two components: the airflow equivalent to a vehicle's forward motion, and the other originating from the natural wind, which forms a turbulent boundary layer above the rough soil. The size of the turbulent eddies is on the same order of magnitude as the vehicle's length. As a consequence, the resulting oncoming flow is far from uniform. On the



**Fig. 16.1** A vehicle in its real environment

contrary, as sketched in Fig. 16.2, its velocity profile is skewed. Due to the gustiness of the wind, the magnitude and direction of the velocity vary randomly with locus and time. Additionally, this turbulence can be increased by a superimposed unsteady flow field resulting from the vehicle's motion through the wakes of other vehicles, and from obstacles in the surroundings such as trees, bridges, and houses.

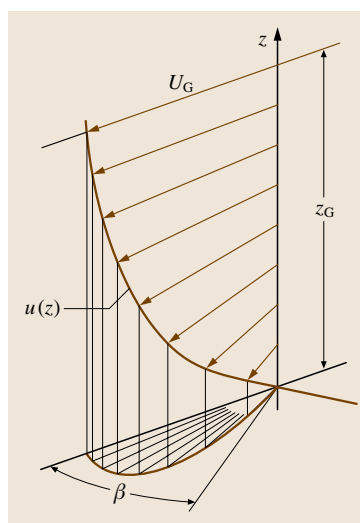
In addition, the temperature field above a road is not necessarily homogeneous. Intense sunlight will heat the surface of the road more than the surrounding air, generating a temperature boundary layer above the road.

Altogether, both fields around the vehicle, air flow and temperature, are very inhomogeneous and nonstationary.

### 16.1.2 Simulation of the Drive on Road and Track

Most of the development work necessary for high-quality aerodynamics and thermal properties of a vehicle is carried out in wind tunnels. According to the requirements of the different category of tests – aerodynamic, aero-acoustic, thermal – various types of test facilities have been developed in which air is blown past a vehicle. They all together are called wind tunnels, and are all in the focus of what follows.

Specific experiments must be carried out with moving models, and of course with real vehicles. These are described in Sect. 16.1.8. Typical examples are: investigating the pressure pulse when trains meet, when they pass through a station, or when they enter a tunnel. Another example is the response of a car to a sudden crosswind gust, and to the wakes of passing vehicles. Such tests are performed with scale models catapulted crosswise through a wind tunnel, or with self-propelled small-



**Fig. 16.2** The skewed wind profile of the boundary layer over the ground

scale trains on track, with scale models and full-scale vehicles towed in water tanks, and with real vehicles in crosswind sections – and, of course, under real environmental conditions on the road and track. In the latter two cases the vehicle has to deal with other vehicles.

In any case, on a test bed the drive on a road or track is only *simulated*, never *reproduced* exactly. As is typical, this simulation is associated with deviations from reality, and it is not easy to quantify all the errors resulting therefrom.

Measurement techniques applied in vehicle aerodynamics will be treated in Sect. 16.1.9; they are very similar to those used in aircraft aerodynamics.

### 16.1.3 Wind Tunnels for Ground Vehicles

#### Configuration Considerations

The manner in which the real flow on a road or track is represented in a wind tunnel is a more or less severe simplification. As depicted in Fig. 16.3, the relative motion is reversed: the vehicle is at rest and is subjected to moving air. However, with ground vehicles this would be an incomplete simulation, because the relative motion between the vehicle and ground, and the rotation of the wheels should not be overlooked. How this requirement is fulfilled will be outlined in Sect. 16.1.5.

Different from reality, in a wind tunnel the oncoming flow is made as uniform as possible, and the turbulence level is very low. This *ideal* flow is a carryover from aircraft aerodynamics, where it is valid for flight at high altitude. As a means of making results from different wind tunnels comparable,

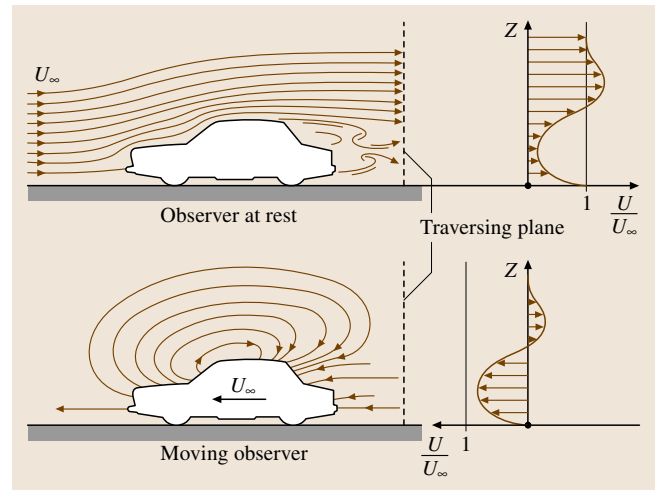
this may have its justification. However, extra expense for realizing extremely low turbulence is not reasonable for vehicle aerodynamics. On the contrary, the turbulence level should be high. And in fact, quite recently, one automotive wind tunnel was equipped with a device for artificially increasing turbulence. A description will follow in the section on turbulence (Sect. 16.1.5).

The climate inside a passenger compartment depends not only on the temperature of the air inside but also on direct radiation from the sun and diffuse radiation from the environment. The radiation from sunlight – intensity, spectrum, direction – can be simulated with sufficient accuracy; diffuse radiation is normally neglected. Furthermore, the comfort of passengers depends on the humidity of the surrounding air. Accordingly, this property of air also has to be reproduced. Humidity, in turn, interacts with components of the air conditioning system. Therefore, dewing and icing must be considered when the evaporator and its housing are tested.

In bad weather a vehicle is exposed to water from various directions: natural rain, and dirty water whirled up by the vehicle's own or other vehicles' wheels. Simulating rain in a wind tunnel is comparatively easy. A definite volume flow of water is sprayed into the undisturbed airstream ahead of the vehicle. Experiments on soiling – real or simulated – should be carried out in wind tunnels only with extremely small quantities of *dirt*, since it is difficult to protect installed probes and pressure taps from dirt, and cleaning costs are very high for a large wind tunnel.

During thermal tests the vehicle's engine must be loaded according to the road load. A chassis dynamometer must be installed, suited for front-, rear- and all-wheel drive. During the (full-scale) model phase of vehicle development the heat fluxes in the engine – water, oil, etc. – must be simulated by external boilers.

Not only flow and temperature fields but also the acoustic environment must be simulated. For cars, buses and wagons interior wind noise is an important criterion for comfort. For trains external wind noise is also important. Generally, wind tunnels are very noisy. The tunnel sound field, which is largely determined by its fan, masks the sound field produced by the flow around a vehicle. Specifically designed aero-acoustic wind tunnels have overcome this problem. They make it possible to discriminate wind noise from tunnel noise *objectively*, and allow for *subjective* assessment of the wind noise spectrum.



**Fig. 16.3** Relative motion between the vehicle, wind, and ground on the road and in a wind tunnel

### Evolutionary Development of Vehicular Wind Tunnels

In principle, vehicle wind tunnels resemble so-called *normal* wind tunnels that are common in aeronautics, and were in fact derived from them. However, with regard to their fluid-dynamic properties the test objects in both cases differ significantly from each other. Generally aircrafts are well-streamlined bodies, and the flow around them is mainly attached. They produce *lift*, which causes the airstream of a wind tunnel to bend. On the other hand, ground vehicles are *bluff* bodies, and the flow past them is characterized by separation. They experience high *drag*, and tend to *block* the jet of a wind tunnel. Vehicles with wings that produce high downwards force – like Formula 1 cars – also bend the airstream. This the more as vehicles are preferably tested at full scale in wind tunnels whose test sections, according to the *classical* layout rules, are by far too small. In addition, vehicle wind tunnels must also be suited for aero-acoustic investigations, and equipped for thermal tests.

Early ground-vehicle aerodynamics made use of wind tunnels that had been designed for aircraft. The scale of the vehicle models was as small as 1 : 10; later larger scales were preferred: in Europe 1 : 4 and 1 : 5, in USA 3 : 8 (1 : 3.75). Originally, the ground was simulated by the mirror image of the model. Later, when it was recognized that this was neither physically correct (vortices forming at the underside and at the rear oscillated from the model to the image and vice versa) nor practical (two models and a wind tunnel of twice

the original size were needed), a rigid ground board was applied.

When automobile designers turned to full-scale models, as shapes in small scale are difficult to assess aesthetically, vehicle aerodynamics had to follow. W. Kamm in 1938 built the first full-scale automotive wind tunnel in the world, which is still operational. This wind tunnel (and several others built thereafter) was designed according to the rules for wind tunnels for aircrafts: accordingly, the blockage ratio, the key parameter that determines the overall dimensions of the tunnel, had to be about 5%.

Later, wind-tunnel development progressed down two routes:

1. while vehicle aerodynamicists were originally interested in forces and moments – mainly drag, and those components of the resulting air force controlling directional stability – other items later attracted attention, namely thermal problems such as engine cooling and air conditioning inside the passenger compartment, wind noise, and soiling. The corresponding tests led to particular test beds, so-called thermal wind tunnels, which were further specialized to hot and cold tunnels.
2. for pure aerodynamic testing at full scale, smaller wind tunnels were built with blockage ratios of up to 20%. Low-noise, so-called aero-acoustic, wind tunnels were developed, ground simulation was improved, and rotation of the wheels was implemented.

Despite the lack of enthusiasm of the designers to perform their modeling in a small scale, wind-tunnel tests with small-scale models are still carried out today, preferably in the early development phase of a new vehi-

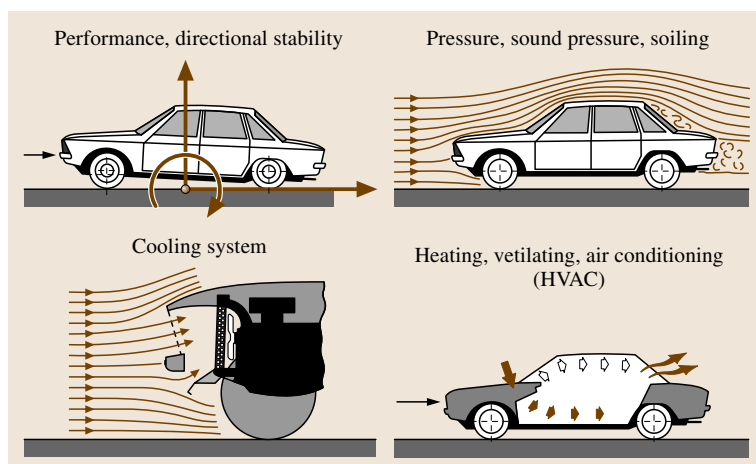
cle, and in research. The scale 1 : 2.5, the classical scale applied by mechanical engineers, was rediscovered for wind-tunnel models. Provided that the wind speed of a tunnel is high enough this scale allows testing at high enough Reynolds numbers – and with heavy-duty vehicles even for full-scale Reynolds numbers – without coming into conflict with Mach-number effects.

### Selecting the Model Scale and Appropriate Wind Tunnel

Most of the work performed during the modeling phase is done in a wind tunnel. Water tunnels only serve as a supplement for special purposes, and are very well suited for flow visualization.

The question of which model scale to be selected – either in a wind or water tunnel – has to be considered with care, and in cooperation with design staff. The advantages of a small scale – low cost for both model and wind tunnel, and easy handling – must be weighed against the risk of errors due to insufficient fidelity of the model and too low a Reynolds number.

Detailed optimization and fine-tuning of cars must be made at full scale, and as soon as drivable prototypes are on hand, it has to be decided whether individual tests should be carried out on the road or in a wind tunnel. Tests on the road and track offer the advantage of realistic conditions. However, their drawbacks should not be ignored: test conditions are rarely repeatable, confidentiality is difficult to secure, and making measurements is more difficult. The advantages of the wind tunnel are obvious: faster and more-precise measurement techniques, and the possibility of unraveling different effects, such as noise from the drive train, tires, and wind around the body. However, as cannot be emphasized often enough,



**Fig. 16.4** The four main objectives of vehicle aerodynamics



the limitations of the wind tunnel should not be overlooked: deficiencies in simulation, high cost, and limited availability.

With respect to its objectives, vehicle aerodynamics can be classified into four categories, as illustrated in Fig. 16.4. The two sketches in the upper row represent the management of the outer flow, while those in the lower row symbolize thermal management and the related inner flow. Both the outer and inner flows are closely linked to each other. Their individual simulation requirements can be fulfilled in two kinds of facilities.

1. All physical parameters that have an influence according to Fig. 16.4 are simulated in one and the same facility. This leads to a large climatic aero-acoustic wind tunnel.
2. Only those parameters are reproduced that are significant during the specific test, all others being reproduced with less expense; this requires several specialized test beds:
  - full-scale aero-acoustic wind tunnel
  - hot and cold tunnels
  - chassis dynamometer with fan
  - small-scale wind tunnel.

Both routes – *all in one* and *several specialized tunnels* – have been followed. However, experience has shown the latter to be superior: investment and operational cost are lower, and instead of one test bed three to four are available – a number which is needed anyhow.

In any case, the more that physical parameters are neglected during the simulation, the greater the effort

necessary to assure that the results achieved on a test bed will be confirmed on the road. Comparative measurements among the various test facilities and with the road must be carried out to uncover and quantify the deficiencies of any specific kind of simulation.

### 16.1.4 Wind-Tunnel Design

#### Configuration Considerations

As sketched in Fig. 16.5, there are two ways to lay out the air path in a wind tunnel:

1. closed return; known under the brand *Göttingen*, the first of which was designed by Ludwig Prandtl;
2. open, no return; designed by Gustave Eiffel and in his honor called an *Eiffel* tunnel.

In order to remain independent of environmental conditions, tunnels of the latter type are generally erected in a closed building, either in an existing one or one specifically designed to host the wind tunnel. In the latter case a flow pattern called *open return* is produced.

The pros and cons of both types of wind tunnels are discussed in detail in [16.1]. In vehicle aerodynamics the *Göttingen* type is clearly preferred. All hot and cold tunnels, and with only a few exceptions, also the full-scale aero and aero-acoustic vehicle wind tunnels, work with a closed air circuit. Examples of both will be presented in Sect. 16.1.7.

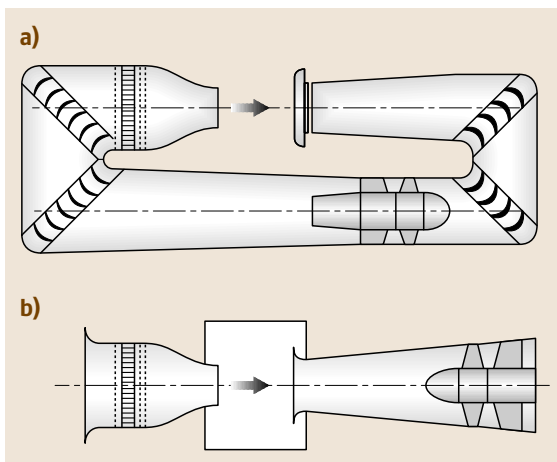
#### Properties of the Essential Components

When planning a test, the *user* of a wind tunnel is looking for answers to the following five questions:

1. What kind of wind tunnel do I need?
2. How do the expected results correlate with those from road tests? What are the specific deficits of the simulation, and can they be tolerated or adjusted?
3. How many wind tunnel hours are needed?
4. At what time is the specific wind tunnel needed available?
5. What are the costs of the test campaign?

Answering the first question appears to be trivial: it must be derived from the purpose of the test. What kind of information is needed: aerodynamic, aero-acoustic, thermal properties? The answer to the second question depends on the characteristics of the following components of the tunnel:

1. Test section (size, open or closed flow, kind of ground simulation)
2. Nozzle (including the settling chamber)



**Fig. 16.5a,b** The two types of air circuit of wind tunnels: (a) closed return, *Göttingen* type, (b) open, no return, *Eiffel* type

3. Collector (for tunnels with an open test section)
4. Chamber surrounding an open test section (known as the *plenum*)
5. Heat exchanger, sun load, rain and snow (in climatic tunnels).

In the following, these key components will first be discussed with no regard to the purpose for which the wind tunnel is specialized. Subsequently, in a separate section, examples of existing vehicle wind tunnels will be given. All other technical details, such as the design of the diffusers, turning vanes in the bends, the fan, fan drive and control, will be touched on only insofar as they are different from wind tunnels for aeronautical purposes [16.2].

The nature of the remaining three questions above is predominantly economic. The items to look at are:

1. How many data points can be acquired per unit time?
2. What are the costs per data point acquired?

A high hourly price can be more than compensated by fast test techniques, data acquisition, and evaluation.

**Test Section.** The test section is the point where the test engineer meets the wind tunnel. Together with its adjacent components, namely the nozzle, collector, and plenum, it is depicted in Fig. 16.6. The properties of the test section are decisive for the conception of his experiment and the assessment of the results. Subsequently, they will be discussed with special attention to bluff bodies such as automobiles and trains.

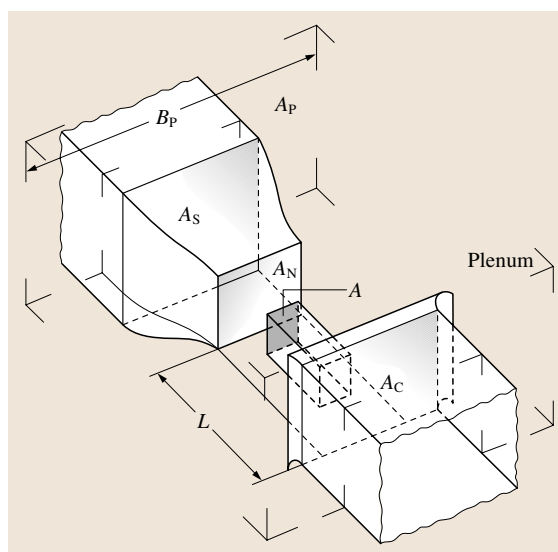
Two properties of the test section are characteristic: the magnitude of the airstream's cross section,  $A_N$ , which is measured at the nozzle exit, and the nature of its circumferential boundaries.

The nozzle cross section has to be seen in relation to the dimensions of the test object which, in vehicle aerodynamics, are characterized by its frontal area  $A$ , as defined in Fig. 16.7. The quotient of frontal area  $A$  and nozzle cross section  $A_N$  is called the blockage ratio  $\varphi = A/A_N$ , which, of course, strictly speaking is not a property of the wind tunnel. However, this relation emphasizes that it is not the size of the tunnel per se that is essential but its relation to the size of the model.

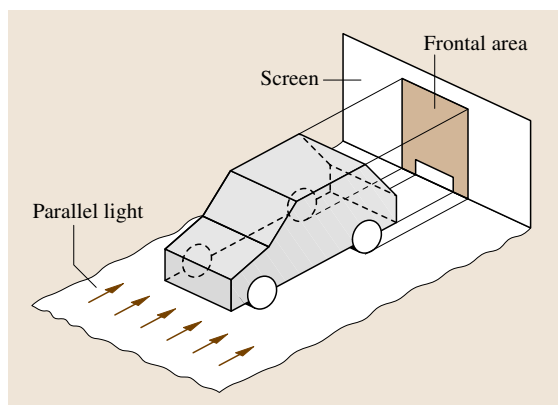
In order to provide kinematic similarity of the flow in a wind tunnel to that on road, the blockage ratio  $\varphi$  – which is zero on the road or track – should be as small as possible. However, cost considerations – construction and operation – demand a blockage ratio as large as *feasible*. However, what *feasible* means in this context is still a matter of discussion.

When the first full-scale automotive wind tunnels were built, the value of the blockage ratio  $\varphi$  was carried over from aeronautical wind tunnels, where  $\varphi = 0.05$  was a target value. With a frontal area of  $A = 2 \text{ m}^2$  typical for cars, this would have led to a nozzle cross section of  $A_N = 40 \text{ m}^2$ . Indeed, full-scale wind tunnels were built with nozzle cross sections of 30–40  $\text{m}^2$  and above, the largest by General Motors in USA, with  $A_N = 52.6 \text{ m}^2$ .

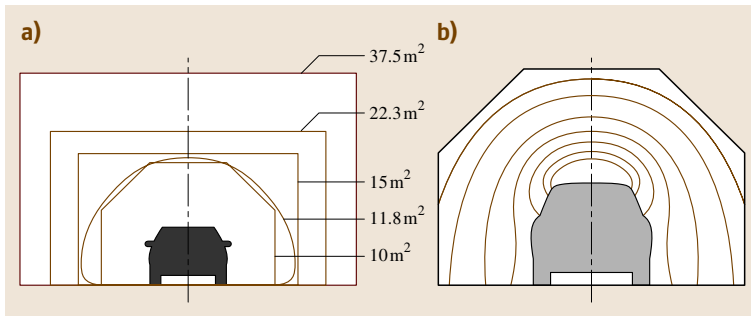
Later, comparative measurements and investigations on test section dimensions resulted in the finding that a larger blockage ratio could be well tolerated;  $\varphi = 0.1$  seems to be a reasonable limit for cars. Several wind tunnels have been designed according to this number,



**Fig. 16.6** The main geometric parameters of the test section of a wind tunnel



**Fig. 16.7** Definition of the frontal area of a vehicle



**Fig. 16.8a,b** Size and shape of the cross section of the airstream (after Janssen); (a) various sizes, (b) shape matched to the isobars around a car

having a cross section of  $A_N \approx 20 \text{ m}^2$ . Yet, even  $\varphi \approx 0.2$  is used; the smallest full-scale wind tunnel has only  $A_N = 10 \text{ m}^2$ .

However, this consideration has to be seen in light of the fact that most car companies have vans and *sports utility vehicles* (SUVs) in their line-up, which have frontal areas of up to  $3 \text{ m}^2$ .

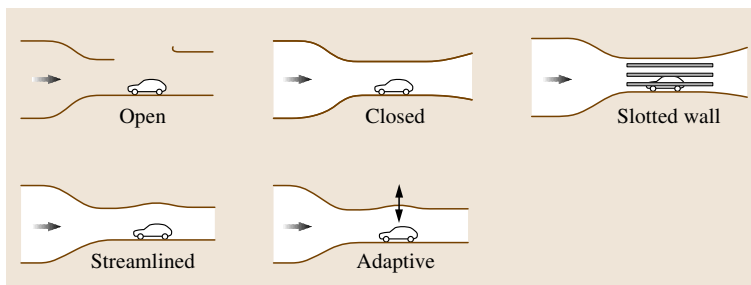
Not only the *magnitude* of the nozzle cross section  $A_N$  but also its circumferential *contour* has an effect on the flow field past the test object. Some typical cross sections of automotive wind tunnels are compiled in Fig. 16.8. Most frequently the shape of an open-jet cross section is rectangular. The ratio of the height  $H$  to the width  $B$  is about  $H/B \approx 0.6$ . Sometimes the corners are rounded off or chamfered. Very small full-scale wind tunnels that are exclusively used for cars have non-rectangular cross sections. A. Morelli [16.3], when designing the  $11 \text{ m}^2$  wind tunnel at Pininfarina, selected a semicircle with its lower edges rounded off. His intuition was to create a cross section that was similar to the shape of the frontal area of a car. By cutting off the corners of a rectangle, L. J. Janssen, designer of the first aero-acoustic wind tunnel on behalf of BMW ( $A_N = 10 \text{ m}^2$ ), intended to approximate the shape of the isobars around a car.

The other characteristic property of a test section is the nature of the circumferential boundary of the airstream. Three types of test section can be distin-

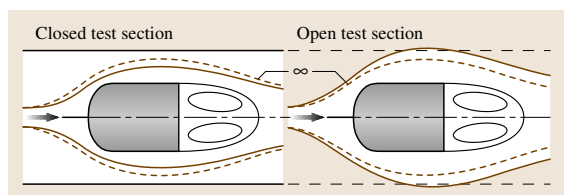
guished: open, closed, and slotted walls. The closed test section has been further developed to specific configurations such as streamlined and adaptive walls. All five types of jet boundaries are sketched in Fig. 16.9. The ground floor, which is typical for a vehicle wind tunnel, is *not* a component of the test section, although physically bound to it. Be it stationary or moveable, it is part of the test set-up representing either the road or rails.

Kinematically, the flow around a test object in a jet of finite dimensions is not exactly the same as in free air. The nature of the difference depends on the boundaries of the jet, as can be seen from the streamlines sketched in Fig. 16.10. In an open-jet test section the air flowing around a vehicle has room to make way. In comparison to free air the streamlines are further apart from each other and so the speed of the air at any given point in the vicinity of a vehicle is somewhat lower than in an airstream of infinite dimensions.

In contrast, in a closed test section the streamlines are constrained by the walls, and so the local speed in the vicinity of a vehicle is raised. In both cases, open and closed test sections, the effect of the jet's boundaries become more pronounced the nearer they are to the model, i.e., the larger the blockage ratio  $\varphi$ . The motivation for the various types of test-section boundaries shown in Fig. 16.9 is to minimize the effect of the limited tunnel size, thereby permitting a blockage ratio as large as possible.



**Fig. 16.9** Various test section boundaries



**Fig. 16.10** Effect of the airstream boundary on the flow past a (bluff) body in comparison to free flow; *left*: closed test section, streamlines are quenched, *right*: open test section, streamlines are expanding

Both kinds of jet boundaries, open and closed, have their merits and drawbacks with respect to the physical properties of the wind tunnel, and the peculiarities of daily work; they will be discussed below. The corrections that compensate for the physical differences compared to the flow in free air are outlined in Sect. 16.1.6.

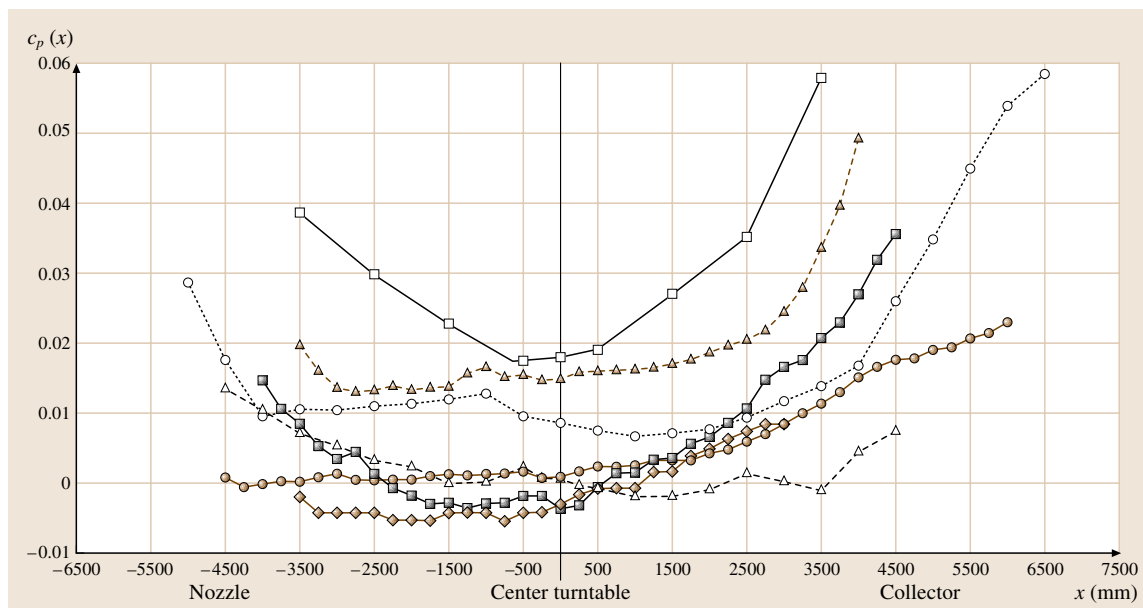
Frequently, the flow in an empty *open* test section is said to be comparable to that in an ideal *free jet*. The constant ambient pressure is impressed on its flow field, and, as a logical result, the static pressure along its axis is constant. Such a property would be highly advantageous for experiments with bluff bodies because, when measuring the drag of long bodies with large vertical surfaces at the front and the rear, even a small axial pressure gradient in the test section may lead to a significant error.

However, in most wind tunnels with an open test section the static pressure is anything but constant, as shown by the comparison of several wind tunnels in Fig. 16.11 from [16.4]. Generally, the pressure gradient along the tunnel axis is negative downstream of a nozzle exit. Near the center of the test section the pressure gradient goes through zero, and further downstream it becomes positive, being steepest immediately in front of the collector.

The second considerable advantage previously attributed to an open test section is a lower absolute value of correction. However, this argument no longer holds. For a long time, the only correction considered was *blockage correction*, and this in fact is small for an open jet. However, blockage (precisely, solid blockage) is only one of a series of interference effects that have to be considered, and so should not be looked at in isolation.

Finally, the third – and real – advantage of an open test section is its good accessibility, which facilitates model installation and the placement of probes, permits out-of-flow acoustic measurements, and allows easy photography of the flow.

The greatest drawback of an open test section is its limited usable length. The jet coming out of the nozzle mixes with the quiescent air in the surrounding plenum. The width of the jet's core (in which the set wind speed  $U_\infty$  can be found) decreases rapidly. Furthermore, turbulent mixing processes at the jet's boundary are more



**Fig. 16.11** Static pressure coefficient  $c_p(x)$  along the axis of several automotive wind tunnels with an open test section (after [16.4])

intense than in a turbulent boundary layer adjacent to a wall, and this mixing causes higher losses than the friction on a plane wall. Therefore the power requirement of an open test section is higher than for a closed one. Other disadvantages of the open jet are its susceptibility to low-frequency oscillations (surge) and its unconstrained sound radiation, which may be regarded as a nuisance by wind-tunnel personnel. Finally, for climatic wind tunnels the plenum must be included within the air-conditioned area; hence large wall panels have to be insulated.

A specific problem arises when racing cars are tested in an open test section. Their rear wings produce a high down-force (negative lift). The related upwash can be so strong that it bends the airflow behind a car upwards and over the collector mouth. Air behind the car is then drawn in from the sides and this may significantly alter the flow pattern at the rear end of the car.

The negative properties of an open test section are corresponding positive properties of the closed. An advantage of a *closed* test section is its large usable length. The negative pressure gradient due to pressure loss at the walls can be compensated for by slightly increasing the tunnel cross section in the flow direction. However, this compensation is only correct for one specific configuration, namely for an empty test section; with a model installed this is only an approximation. A further advantage of a closed test section is the stability of its flow, i.e., the problem of pumping does not exist.

A disadvantage of a closed test section is its sensitivity to blockage; its correction is approximately twice that of a free jet (and is of opposite sign). Furthermore, at a high yaw angle  $\beta$ , the lateral deflection of the airstream may be so strong that the related adverse pressure gradients on the adjacent sidewalls of the test section may lead to boundary-layer separation there.

The *slotted-wall* test section is an attempt to combine the advantages of the open and closed test sections, and at the same time eliminate the drawbacks of both. The slots in the walls give ambient-pressure access to the flow inside the test section; thus the pressure along the axis is (almost) constant. The solid part of the walls prevents the jet from mixing with the ambient air; the core of the jet therefore remains usable for a greater length.

One means of avoiding the large corrections necessary for blockage in a closed test section is to *streamline* its walls. This idea is based on the fact that the flow pattern at a certain distance, even from a bluff body like a vehicle (and its wake), in the so-called far field, is only weakly dependent on the individual details of the model's shape. The far field is mainly determined

by the overall parameters of the test object: its length, height, and width (and thus some kind of fineness ratio that can be derived from them). If the tunnel walls are shaped according to the free-air flow pattern of an average mid-sized vehicle, the flow around smaller and larger vehicles will only be slightly distorted, in any case far less than by parallel walls.

The disadvantage of a test section with streamlined but fixed walls is that its contour does not fit vehicles whose main dimensions differ significantly from the one used to define the contours of its walls. This, for example, will be the case if a box-type light truck is put into a test section that has been configured for passenger cars. A possibility for overcoming this problem is offered by *adaptive* walls, albeit at the price of great expense.

**Nozzle.** The function of the nozzle is fourfold, it:

1. accelerates the flow
2. makes the velocity distribution over the cross section of the flow more uniform
3. reduces the intensity of the turbulence in the airstream
4. serves to measure the wind speed in the test section

The requirements (specifications) for the flow properties for vehicle wind tunnels have not yet been formulated on a rational basis. However, the following data are typical for existing tunnels:

1. local deviations from average wind speed  $\Delta u/U_\infty = (u - U_\infty)/U_\infty \leq \pm 0.5\%$ ;
2. angularity in pitch and yaw  $\alpha, \beta \leq \pm 0.2^\circ$ ;
3. turbulence level  $Tu = \sqrt{u'^2}/U_\infty \leq 0.5\%$ .

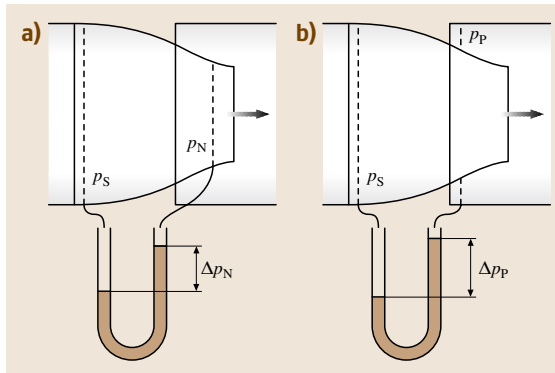
These quantities are determined by two geometric properties of a nozzle: the contraction ratio and contour of the walls. The contraction ratio  $\kappa$  is defined as the relation of the nozzle's entrance cross section to its outlet:  $\kappa = A_S/A_N$ , where  $A_S$  is the cross section of the nozzle's entrance, and  $A_N$  that at its exit.

According to experience the effect of the contraction ratio  $\kappa$  on the flow quality is:

$$\frac{\Delta u}{U_\infty} \sim \frac{1}{\kappa}, Tu_x \sim \frac{1}{\kappa}.$$

However, the contraction ratio  $\kappa$  determines not only the quality of the flow but also the size and thus the cost of a wind tunnel, and so it should not be larger than necessary.

From experience it is known that a turbulence level of 0.5% is achieved with a contraction ratio of  $\kappa = 4$ , a value which had already been proposed by L. Prandtl.



**Fig. 16.12a,b** Measuring the wind speed  $U$  in an open jet wind tunnel; (a) nozzle method, (b) plenum method

This value can be taken as reasonable for automotive wind tunnels with a Göttingen circuit. For Eiffel tunnels, where the flow upstream of the nozzle is not disturbed by a fan, diffuser, turning vanes etc., an even smaller contraction ratio is sufficient:  $\kappa = 2-3$ . How turbulence can be increased for special investigations will be discussed in Sect. 16.1.5.

The shape of a nozzle – length and contour – should be selected so as to provide a rectangular velocity profile at its exit. Even more importantly, the angle between the jet and the geometrical axis of the test section should be small, because the flow around bluff bodies close to the ground is very sensitive to differences in the angle of attack (or pitch). Therefore a tolerance of  $\alpha \leq \pm 0.5^\circ$ , as recommended in [16.5], is rather generous;  $\alpha \leq \pm 0.2^\circ$  seems to be more reasonable. The sensitivity of vehicles to small deviations in yaw near  $\beta = 0$  is less pronounced.

The *wind speed* in a test section is determined in the *classical* manner by measuring the difference  $\Delta p$  of static pressure between the entrance of the nozzle (i. e., in the settling chamber) and its exit. The dynamic head  $q_\infty$  within the jet leaving the nozzle is

$$q_\infty = \frac{\rho}{2} U_\infty^2 = k \Delta p, \quad (16.1)$$

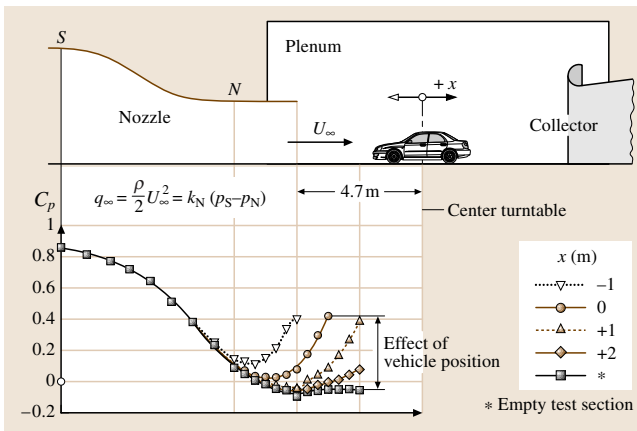
where  $k$  is a nozzle factor to be determined by measuring (and averaging over the jet's cross section, excluding the mixing zone at its boundaries) the dynamic head in an empty test section. Generally, the numerical value of the nozzle factor  $k$  is greater than one, because the wind speed in the settling chamber is not exactly zero, and hence the local static pressure there is (slightly) lower than the total pressure.

In a wind tunnel with an *open* test section there exist two possibilities for the position of the *downstream* pressure tap, and therefore there are two possibilities to measure the wind speed. The first, the so-called *nozzle method*, is the same as for a closed test section. The location of the downstream pressure tap is close to the exit of the nozzle. The related pressure signal is:  $\Delta p_N = p_{SC} - p_N$ ; see the left-hand side of Fig. 16.12. Alternatively, in the *plenum method*, the downstream pressure tap is located in the plenum surrounding the open jet; see the right-hand side of same figure. If the plenum is well vented, as is normally the case, this pressure  $p_P$  is equal to the atmospheric pressure. The pressure difference is designated  $\Delta p_P = p_{SC} - p_P$ .

For a long time there has been an intense dispute among wind-tunnel operators about which method should be preferred. However, comparative measurements [16.6] have clearly proven the superiority of the plenum method. The major reason for the inferiority of the nozzle method is the influence of the model on the pressure tap at the nozzle exit. For bluff bodies this effect is strong, and as shown in Fig. 16.13 is dependent on the model position (the distance between the nozzle exit and the front of the model).

In small wind tunnels, such as thermo tunnels, where the blockage ratio is extremely high ( $\varphi \approx 0.3-0.4$ ), the wind speed is measured in a different way; details will be described in Sect. 16.1.6 together with wind-tunnel corrections.

Wind speed must be controllable at all levels, even at low speed. For instance, driving slowly uphill on a long steep grade represents one of the serious criteria for dimensioning the radiator and cooling fan (the other being maximum speed). The wind from the vehicle's forward motion as well as the radiator's fan contribute



**Fig. 16.13** The effect of model position on the pressure distribution inside the wind-tunnel nozzle [16.1]



to the cooling effect; therefore, accurate control of the (low) wind speed is important.

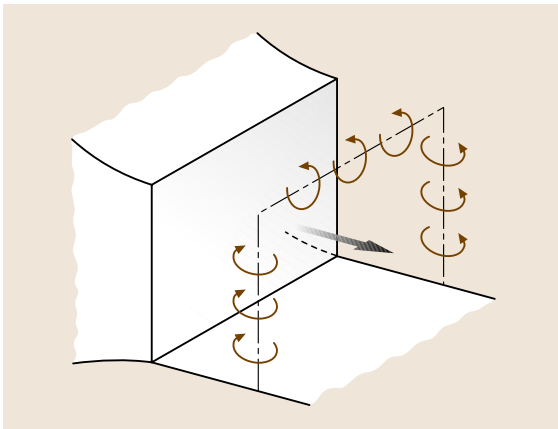
Technically, two solutions are available for adjusting wind speed: variable pitch of the fan's blades at constant fan speed, and continuously variable fan speed with fixed fan blades. Today, the latter is used more widely. Variable pitch permits a very quick change of wind speed. However, this advantage is offset by a high noise level at *all* wind speeds, including idle. For test engineers and craftsmen who have to work on a model in a tunnel between two runs while the fan is idling, this is rather unpleasant.

**Collector.** The collector's function is to gather the air transported by the free jet of an open test section and to guide it into the first diffuser. However, this task is accompanied by the following two phenomena:

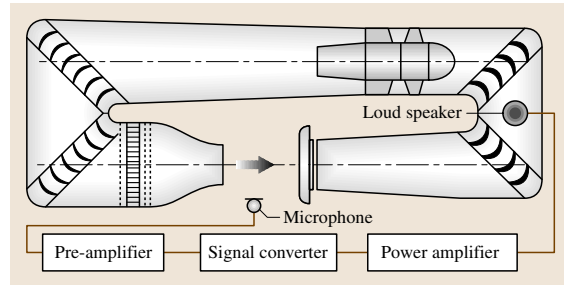
- the static pressure along the axis of the test section is increasing in front of the collector, as shown in Fig. 16.11;
- the flow in the test section may pulsate at low frequency.

This has four major consequences:

1. drag is measured too low,
2. pressures and forces may be altered (the Katzmeier effect),
3. the pulsation will modulate the flow noise around the test vehicle,
4. the pulsation may grow to an extent at which the structure of the wind-tunnel building is endangered.



**Fig. 16.14** Formation of ring vortices in the shear layer which builds up at the border of the free jet



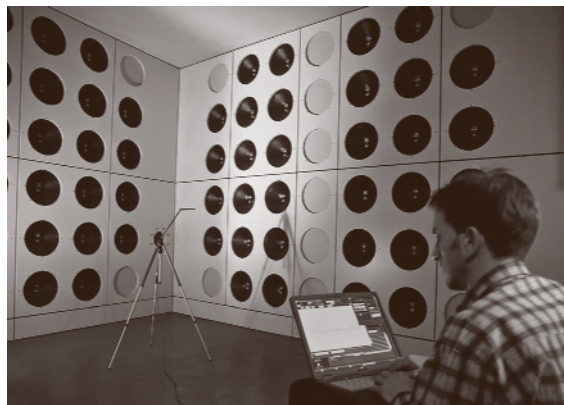
**Fig. 16.15** Closed-loop control to attenuate low-frequency oscillations (booming) (after [16.7])

Despite significant effort, satisfactory measures against the pressure increase in front of the collector has not yet been found. Perhaps *active* devices, for example suction at the inlet, will lead to a solution.

The physics of the pumping in an open-jet wind tunnel – called *wind-tunnel buffeting* – has not yet been completely deciphered. There are two potential resonance effects:

- Vortices are shed from the nozzle mouth, as sketched in Fig. 16.14, and move downstream where they impinge on the collector mouth. The pressure pulse caused there travels back to the nozzle and triggers the formation of the next vortex.
- A standing wave is generated within the wind-tunnel duct.

In any case Seifert wings that break up these vortices, widely used in aeronautical wind tunnels, are not suitable for aero-acoustic wind tunnels because of the



**Fig. 16.16** Array of loud speakers in an open chamber in the wall of the wind-tunnel tube behind the first corner (photo Audi AG)

high-frequency noise they generate. Therefore, vehicle wind tunnels are equipped with Seifert wings that can be removed during acoustic measurements.

An alternative is described in [16.8]: an active resonance control. Its use in a wind tunnel can be seen in the schematic in Fig. 16.15. It consists of an *out-of-flow* microphone that picks up the pressure fluctuations in the plenum, an array of loudspeakers mounted in a chamber behind the first turning vane open to the tunnel wall, see Fig. 16.16, and a time delay for phase adjustment between the microphone input and loudspeaker output. Low-frequency pulsations are attenuated by 20 dB without introducing any additional noise into the tunnel.

A drawback of the first implementation of this system was that it had to be adjusted to each new test configuration, because the frequency and amplitude of the excited resonance not only depend on the flow speed but also on the model. For this reason an improved, self-adjusting system has been developed [16.7].

**Plenum.** The plenum surrounding the free jet of an open test section, as sketched in Fig. 16.6, must be wide enough to avoid interference of the jet with the walls of the plenum. According to [16.9] drag is underpredicted if the volume of the plenum is less than a specific minimum value. Its main dimensions should not fall below the values compiled in Table 16.1.

Here  $A$  is the frontal area of the test object,  $b_F$  is its width, and  $B_P$  is the width of the plenum. The height and width of a plenum have to be large enough to keep the crane and traversing gear out of the flow. The room on both sides of the jet must be wide enough to keep test equipment such as an acoustic mirror or microphone array out of flow.

**Anechoic Measures.** Generally, if no specific precautions have been taken, normal wind tunnels are so loud that they are not suited for aero-acoustic investigations. In particular subjective assessment of noise level and character inside a car, such as speech recognition, is not possible. The noise level of anechoic wind tunnels is 20–40 dB(A) lower than in normal wind tunnels.

The guiding principles for an aero-acoustic wind tunnel are to avoid the generation of all noise, and to attenuate any remaining generated noise. Three essential measures have to be taken to build a low-noise wind tunnel:

- installation of a low-noise fan (low noise has higher priority than high efficiency); this requires three measures:

**Table 16.1** Dimensions of the plenum related to the frontal area and width of the vehicle investigated

Cross section of plenum, related to vehicle frontal area $A_P/A$	> 45
Width of plenum, related to the width of the vehicle $B_P/b_F$	> 8

- low rpm to keep the tip speed and corresponding tonal noise low;
- a large number of blades to shift the first blade-passing frequency and thus the corresponding harmonics to high frequencies, where noise is easier to attenuate;
- limit broadband noise due to the boundary layer on the blades to the same level as tonal noise.
- fan noise has to be trapped in front of and behind the fan; the best suited elements for this task are turning vanes, designed as a *scene silencer*;
- the walls of the plenum have to be covered with broadband noise absorbers.

Technical details are given in Sect. 16.1.7.

**Control of Air Temperature.** In wind tunnels not dedicated to thermal tests the air temperature must be controlled only insofar as plasticine models do not lose their consistency. The air temperature should be kept below 30 °C. Control of the air temperature should not be performed by an in-stream cooler because of its additional power requirement – and thus additional noise. Air exchange or cooling of the air in a bypass are proper approaches.

This is not the case in thermal wind tunnels where air temperature is the key parameter. Uniformity across a test section should be  $\pm 1$  K. Because of the cross-flow nature of the tunnel’s heat exchanger this specification is not easy to meet. The heat exchanger must be operated under *saturated* conditions, i. e., the volume flux of coolant has to be very high. Furthermore, not only steady-state operation has to be considered when the heat exchanger is laid out. Tunnel time is rare and expensive; therefore the performance of the cooler should permit the desired temperature to be reached quickly. To keep the pressure loss of the air flow through the cooler low the cooler must be placed in a location where the cross section of the tunnel duct is large. The end of the large diffuser following the fan appears to be more suitable than inside the settling chamber. Disturbances in the air flow caused by the cooler (wakes from its tubes and struts) then have a longer flow path to level out.

### 16.1.5 Equipment for Automotive Wind Tunnels

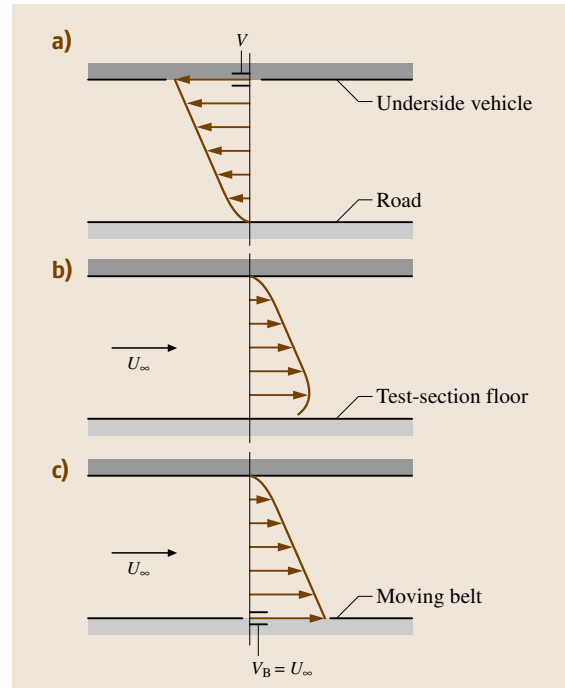
Depending on the test spectrum for which the facility is designed it must be possible to reproduce or at least simulate a variety of physical processes or effects. These are compiled in Table 16.2 and discussed in the following text, along with their production methods.

#### Ground Floor

When the motion of a vehicle on the road or track is reversed in a wind tunnel, as indicated in Fig. 16.3, the flow between the vehicle's underside and the ground requires special attention. On the road, as drawn in Fig. 16.17a, a channel flow develops under the vehicle, with a no-slip condition at both walls. The upper wall, the underside of the vehicle, is moving, and the lower wall, the road or track, is at rest. When the flow reversal is correctly reproduced, the floor of the test section has to move, as sketched in Fig. 16.17c and, at the same time, the wheels of the vehicle must rotate.

Because of the high effort necessary to fulfill this condition – details will be discussed below – in many vehicle wind tunnels the relative motion between the vehicle and ground is not reproduced, and consequently the resulting velocity profile underneath the vehicle (Fig. 16.17b) differs from reality. However, measurements carried out with standard passenger cars have shown that the differences between wind tunnel and road are confined to a very thin layer immediately above the ground [16.10]. For this reason, for many tests one can refrain from reproducing the relative motion between the vehicle and the ground.

However, technically it is feasible to reproduce the relative motion, and the same holds for the rotation of



**Fig. 16.17a–c** Flow underneath a car; (a) on the road, (b) in a wind tunnel with a rigid (non-moving) floor, (c) in a wind tunnel with a moving floor

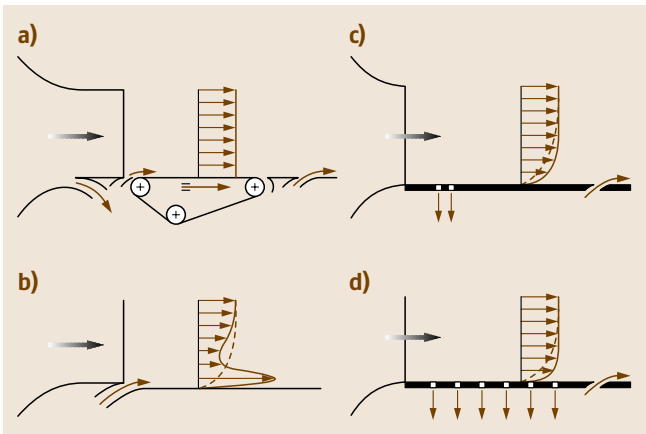
the wheels. The proper means for doing this is a moving belt that spans the entire width of the test section on which the wheels are rolling [16.11]. However, for the time being, belts able to carry the full weight of a vehicle are not available. Therefore this technique is used in special applications only, for instance for monoposto race cars. There the wheels are mechanically separated from the vehicle and held by slender struts (with an internal balance) from outside. Suspension of the (heavy) vehicle's body is performed by a sting from above, or sometimes from the rear; because of interference effects between the sting and vehicle both are debatable solutions.

To avoid this effort simpler simulation techniques are used; commonly applied methods are compiled in Fig. 16.18:

- a simple ground board, sometimes called a *rigid* ground floor;
- cut-off of the oncoming boundary layer by a *scoop* (left part Fig. 16.18a);
- boundary-layer removal by *basic* or *distributed* suction (Fig. 16.18c,d);

**Table 16.2** Physical processes or effects and measures to reproduce or simulate them in a wind tunnel

Physical effect	Measure to perform it
Relative motion to the road	Blowing, suction, moving ground
Turbulence and boundary layer	Mesh, swiveling flaps
Tractive force	Chassis dynamometer
Sun radiation	Bulbs with spectrum of sun
Heat flux	External boilers for air, oil, and water
Humidity	External steam generator
Rain	Water spray system
Dirt	Water (plain or colored)
Geometry	Traversing gear



**Fig. 16.18a–d** The major possibilities to simulate the relative motion underneath a car; (a) moving belt with scoop, (b) basic suction either through a sheet of porous material or through slot; (c) tangential blowing, (d) distributed suction

- filling of the velocity deficit by tangential blowing (Fig. 16.18b);
- narrow belt as above, supplemented by short belts in front of the frontwheels (*T-belt* [16.12]).

Single measures may be combined, as can be seen in Fig. 16.18a, where a scoop and tangential blowing support the moving floor to further reduce the thickness of the oncoming boundary layer. All the aforementioned techniques can be combined with wheel rotation. The pros and cons of these techniques are discussed in [16.13].

Despite many investigations, to date no fully satisfactory solution for the simulation of the road or track has been found. Furthermore, it has turned out to be impossible to establish a general rule for

correcting or compensating for the various negative effects.

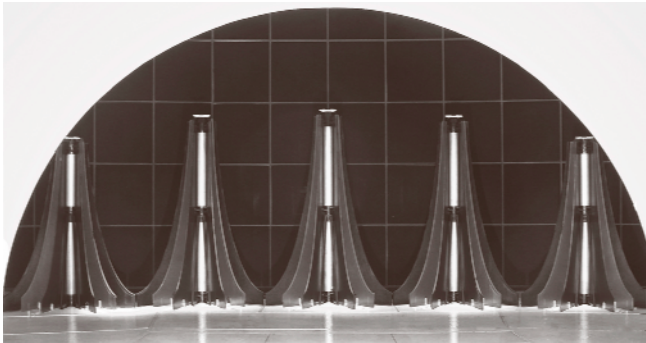
**Chassis Dynamometer**

During thermal tests the power of the engine must be braked by a chassis dynamometer. To avoid overheating of the tires during long tests, the diameter of the rollers should be not smaller than 2 m. In order to cope with front- and rear-wheel-drive vehicles the rollers must be movable along the axis of the wind tunnel. Two dynamometers are needed for four-wheel-drive vehicles. For thermal brake tests the tractive power at high speed must be close to the braking power. However, because abraded brake material soils the wind tunnel and may be toxic, braking tests are rarely carried out in a wind tunnel anymore.

**Turbulence**

Traditionally, as mentioned already in Sect. 16.1.4, vehicle wind tunnels are designed to have an airstream with low *turbulence*. However, vehicles generally operate in an environment with high turbulence, which has two origins: the natural wind, and from the wakes of other vehicles and of trees, buildings, and other obstacles along the roadside. This turbulence has at least two effects that bother for the passengers: it modulates the spectrum of wind noise, and it shakes the car.

To be able to generate reproducible turbulence with respect to spectrum, scale, and its distribution above



**Fig. 16.19** Swiveling flaps to generate a highly turbulent boundary layer; design A. Cogotti; multiple exposures (photo Pininfarina)



**Fig. 16.20** Sunlight simulation with a matrix of lamps assembled in a panel that can be tilted; climatic chamber Modine GmbH (photo Media Fotograf)



the ground, the wind tunnel of Pininfarina was equipped with flaps as shown in Fig. 16.19. They are used in a fixed position when the wake of a preceding vehicle is simulated, or in a swiveling motion to generate specific turbulence effects; for further details see [16.14, 15].

### Sun Load

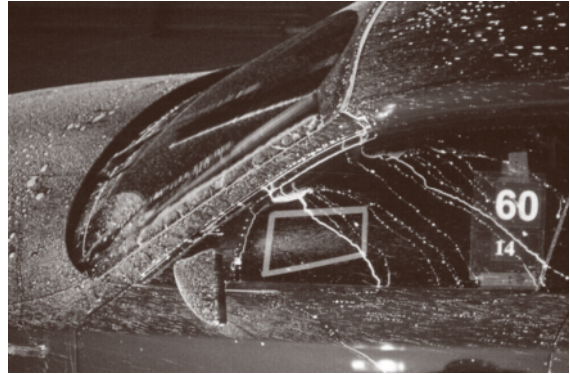
To simulate sun load the intensity of radiation must be  $1000 \text{ W/m}^2$ , the solar value. A homogeneity of  $\pm 10\%$  is said to be sufficient. Light sources with a spectrum close to the sun's are commercially available. Two technical solutions are in use. In the older one (Fig. 16.20) the lamps are arranged in a matrix and assembled in a large overhead panel that can be turned to the side to expose a test object to radiation from an oblique angle. The newer version, see Fig. 16.21, make use of single lamps assembled in two frames that can be moved and swiveled. The lamps are equipped with flaps with which the radiation can be quickly switched on and off to simulate, for example, entering or leaving a tunnel.

### Rain, Snow, and Dirt

*Rain* is simulated by water that is sprayed into the oncoming air through nozzles that are mounted on a tube crossing the test section horizontally. To make the wa-



**Fig. 16.21** Sunlight simulation with distributed movable spot lights; climatic wind tunnel Behr GmbH (photo Behr GmbH)

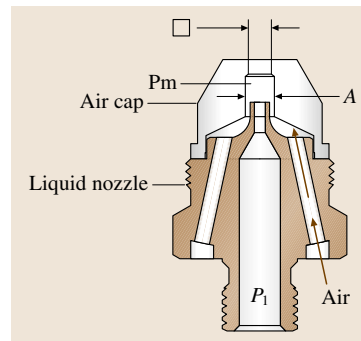


**Fig. 16.22** Water streaks on a vehicle's body made visible with sprayed water doped with an ultraviolet (UV)-sensitive pigment, and UV light (photo BMW AG)

ter streaks and drop deposition on the vehicle visible a fluorescent liquid is added to the water. With ultraviolet illumination flow patterns such as those shown in Fig. 16.22 become visible.

In practice *snow* could be produced using commercially available snow guns. However, they need a long distance to freeze the spray. Therefore in wind tunnels an array of snow nozzles is used, which is positioned in front of the vehicle, similar to the rain nozzles. A mixture of cold water and high-pressure air (5–10 bar) is ejected through a nozzle (Fig. 16.23) into the ambient air. Depending on the water content, pressure, and temperature the quality of the snow can be varied between *wet* (adhesive, particle size  $45 \mu\text{m}$ , density  $450 \text{ kg/m}^3$ ) and *dry* (particle size  $20 \mu\text{m}$ , density  $200 \text{ kg/m}^3$ ).

Considering the sensibility of the test equipment and the high cost of cleaning the simulation of *dirt* has to be performed with care. Generally dirt is simulated by water, either blended with a fluorescent liquid or with whiting. Realistic dirt tests have to be performed on a specially prepared test track.



**Fig. 16.23** Cross section through a spray nozzle of a snow-gun (drawing after RTA Rail Tec Arsenal Fahrzeugversuchsanlage GmbH)

### Traversing Gear

Every aero-acoustic wind tunnel should be equipped with a traversing gear covering the entire test section. This device should be committed together with the construction of the wind tunnel because it is urgently needed during the calibration tests. In thermo tunnels, where such a device is generally not needed, these calibration tests are performed with a temporary set up.

## 16.1.6 Limits of Simulation

### General Remarks

The effectiveness of all aerodynamic measurements on a vehicle have to be proved on the road or track. In a wind tunnel a real cruise can only be simulated, never reproduced exactly. The limitations of simulation fall into two categories:

- violation of the law of similarity
- deficits of the wind-tunnel technique.

In the next two sections both will be only briefly discussed; for more details see [16.1].

### Experiments with Small-Scale Models

When considering whether a wind-tunnel test should be carried out at full or small scale the following questions have to be answered:

- How can we assure that the results from small-scale tests will agree with those at full scale?
- What wind tunnels are available?
- What is the time advantage compared to a full-scale test?
- What is the cost advantage of small-scale testing?

The first is the key question. If no satisfactory agreement with full-scale testing can be expected, the remaining questions are meaningless. Another question is: what, in this context, is *satisfactory*? Is it sufficient to assess shape *modifications* with regard to drag (or other forces and moments)? Or will the data be used to *compare* two or more design variants?

Coincidence of results from small- and full-scale testing is achieved if exact similarity is present with respect to the:

- geometry of the model. However, regardless of the skill of the model maker, not every detail can be reproduced in small scale. Therefore an *exact* similarity is not possible.

- kinematics of the flow. This will be achieved, when the Reynolds number is the same in both cases, i.e., at full (1) and small (2) scale:

$$\text{Re}_1 = \text{Re}_2, \\ \frac{U_1 \cdot l_1}{\nu_1} = \frac{U_2 \cdot l_2}{\nu_2},$$

where  $U$  is the velocity of the undisturbed oncoming flow, and  $l$  is a typical geometrical dimension, generally the length of the vehicle or, as discussed below, a specific radius  $r$ .

Since generally small- and full-scale tests are carried out in air the above formula results in the following rule: to attain kinematic similarity the wind speed in small-scale tests has to be increased by the same factor as the dimensions of the model are scaled down.

For two reasons this rule is not easy to observe exactly:

- the maximum wind speed in the model wind tunnel may not be high enough;
- if the oncoming speed exceeds a critical value, Mach-number effects become noticeable.

The latter is critical in vehicle aerodynamics because bluff bodies such as vehicles are sensitive to compressibility effects. While generally  $\text{Ma} = 0.3$  is said to be the limit up to which flow can be treated as incompressible, for vehicles this value is  $\text{Ma} = 0.2$ . For further details see [16.16].

Generally, when testing road vehicles, the maximum Reynolds number in small-scale tests is two to five times smaller than at the full scale. In order to assess the effect of the Reynolds number, so-called Reynolds series are run, as demonstrated in Fig. 16.24. There, the drag coefficient  $c_D$  is plotted versus Reynolds number  $\text{Re}$ . Two different vehicles were investigated: in the upper part of the diagram a constant  $c_D$  was achieved at  $\text{Re} = 5 \times 10^6$ , which compares pretty well with full-scale data. The vehicle in the lower part of the diagram was completely different;  $c_D = \text{constant}$  was not achieved at all, neither at small nor full scale. The latter example may serve as a warning: the effect of the Reynolds number on the drag coefficient can be significant and is hard to predict.

There is one exception to this: the radius of the leading edges of a rectangular block, like a bus, or the cabin of a truck. For such a configuration a so-called *optimum radius* exists; the definition of *optimum* is explained with the aid of Fig. 16.25: if the leading edges of a block are rounded off in increments  $\Delta r$ , starting with sharp edges ( $r = 0$ ),  $c_D$  will decrease, at first almost linearly with a steep gradient, and then more moderately with bigger



radii, finally reaching a constant value. The *optimum radius* is the smallest radius  $r_{\text{opt}}$ , where  $c_D = \text{const}$ . As seen in the figure, its value depends on the Reynolds number: the higher the Reynolds number, the smaller the optimum radius [16.1]. From many experiments such as that displayed in Fig. 16.25a a general relation has been derived:

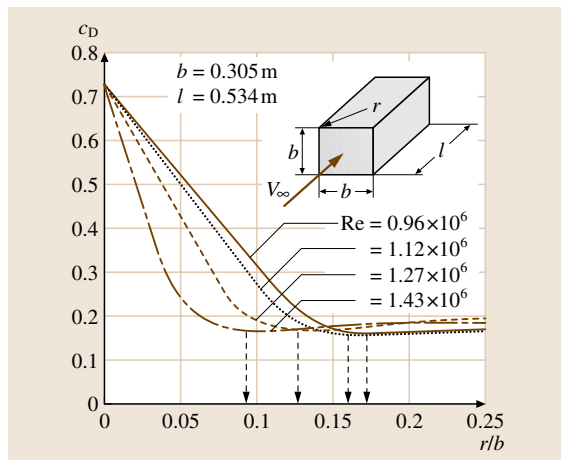
$$\text{Re}_{(r/b)\text{opt}} = \frac{U_\infty \cdot r_{\text{opt}}}{\nu} = 1.3 \times 10^5.$$

This number is close to the critical Reynolds-number of a circular cylinder, where the Reynolds-number is formed with the diameter.

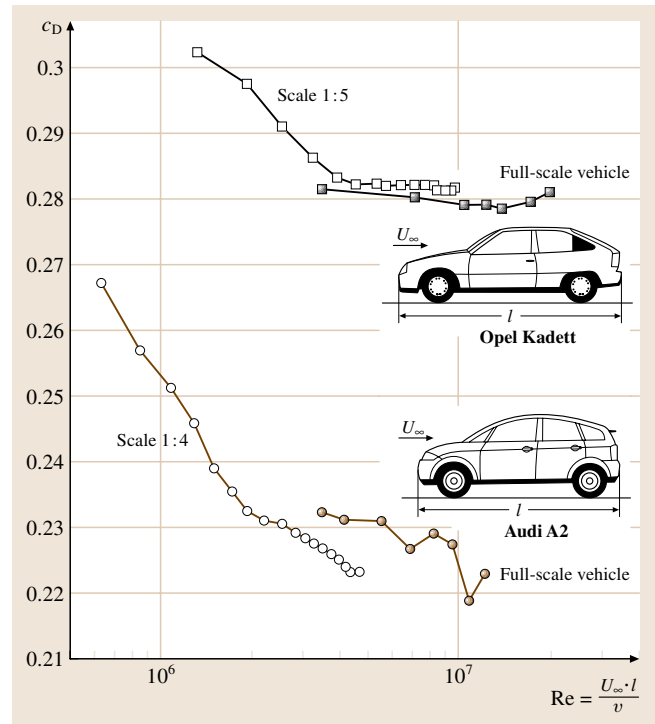
The sensitivity to Reynolds number of other details typically found in the geometry of vehicle bodies, such as tapering of the rear (*boat tailing*), and rounding of the C-pillars, have not yet been investigated in depth.

The attitude of vehicle aerodynamicists to working with small-scale models has undergone several changes. In early vehicle aerodynamics they had no choice because the only wind tunnels available were those from aeronautics. Initially they were pretty small; a scale of 1 : 10 was used for cars, and even smaller for trains. Later, when large wind tunnels became available, full-scale investigations were preferred – if tests were made at all, because vehicle development was interrupted for some years.

After 1945, this sequence repeated itself. Aerodynamic development started with models at a scale of 1 : 5 and 1 : 4. Only the large wind tunnel of Forschungsinsti-



**Fig. 16.25** Effect of Reynolds number on the value of the optimum front radius of a prismatic block with rectangular cross section (data from [16.16])



**Fig. 16.24** Drag coefficient  $c_D$  versus Reynolds number  $\text{Re}$  for two different passenger cars, comparison between small- full-scale vehicles. Top: Opel Kadett, bottom: Audi A2 (data from Adam Opel GmbH and Audi AG)

tut für Kraftfahrwesen und Fahrzeugmotoren Stuttgart (FKFS, now belonging to Daimler Chrysler) allowed for full-scale models and cars, and was used mainly for final tests. When the vehicle manufacturers began to erect their own wind tunnels they built them for full-scale vehicles, and small-scale testing was pushed into the background again, more so as designers prefer full-scale models to assess their appearance. If they are fully equipped (e.g., with a *real* underbody), design models can be (and often are) used for wind-tunnel tests.

Some vehicle manufacturers made use of small-scale models in the early phase of development. However, these were displaced again, this time by numerical models. In some cases a scale of 1 : 2.5 was preferred. Models this large can be tested at the full-scale Reynolds number (in a full-scale wind tunnel) without conflicting with the Mach-number.

A full-scale Reynolds number can also be achieved with small models in a high-pressure (100 bar) or cryogenic wind tunnel (100 K) [16.16].

### Wind-Tunnel Corrections

When driven on the road or track a vehicle moves through a space that is unlimited in all directions (free air), with the ground below (the road or track) being the only limiting surface. The dimensions of a wind tunnel's airstream, however, are finite. Its cross section and its usable length are limited, and the static pressure along its axis is not constant. The proximity of the airstream's boundaries to the test object modifies the flow around it compared to that in an unlimited space. The angularity of the flow, the distribution of velocity and pressure around a vehicle, and at least in principle, the shear stresses on its surface, are all modified and so, consequently, are the forces and moments acting on the vehicle. The smaller a wind tunnel relative to a vehicle, the larger these discrepancies are.

There are two possibilities to cope with the systematic errors resulting from these effects:

- corrections (some prefer the term *adjustments*), which are performed a posteriori, i.e., *after* the measurement. This is standard practice in large wind tunnels;
- correcting the setting of the wind speed *during* the test. This is practised in small (mainly thermal) wind tunnels.

The basic premise of wind-tunnel corrections is that the shape of the flow is assumed to remain unchanged by the finite size of the airstream's dimensions. In other words, the shape of the streamlines, the shape of the pressure distribution, and the locations and kinds of separation are all the same as in free air. The only effect of the finite dimensions is that the velocity of the oncoming flow is altered. By modeling the various perturbations resulting from the finite dimensions of the airstream this speed change is computed.

The development of these so-called *classical* corrections was performed in three steps. In the first, the perturbations of the flow field caused by the boundaries were identified and analyzed. In the second step, each perturbation was modeled and computed. Finally, the effects were superimposed, which means that it was assumed that the perturbations do not interact with each other (a linear approach).

Originally, this kind of corrections was carried over from aeronautics, where they had been developed for configurations with attached flow, i.e., slender bodies such as wings, nacelles and fuselages. Furthermore, they were limited to small blockage ratios, i.e., small models in comparatively large wind tunnels [16.2].

However, for vehicles both conditions are not fulfilled because:

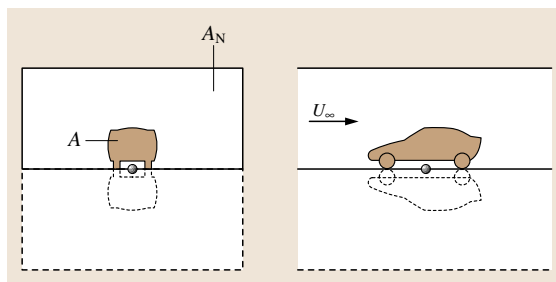
- generally vehicles are bluff bodies, and their flow is characterized by separation and reattachment;
- commonly, blockage is high; i.e., large models are investigated in comparatively small wind tunnels.

Therefore it is questionable whether it is justified to apply these classical corrections for vehicles. However, because they have been developed so far that single perturbation effects can be discriminated [16.4], they are still applied – if applied at all.

The axial pressure gradient,  $dp/dx$ , within the airstream is taken into account differently; it is assumed that the axial pressure gradient with a model in the test section is the same as that in the empty tunnel. Its effect is horizontal buoyancy and will be computed as such, and the drag force will be corrected by adding the force resulting therefrom.

Already in Fig. 16.10 it was indicated that the effect of a test section's boundary on the flow pattern around a vehicle is opposite for open and closed test sections. In the former the streamlines around a car are wider apart from each other than in free air, while in the latter they are squeezed together. If this deformation of streamlines due to the boundaries of the jet were the only effect, the corrections for both kinds of test section could be treated simultaneously. However, a number of other perturbations exist, and these depend on the type of test section. Therefore it is appropriate to treat the corrections for each type separately.

The overall configuration of a car in a wind tunnel is asymmetric with respect to the tunnel floor. This floor (the ground plane) simulates the road and therefore should be interpreted as part of the test set up, not of the tunnel. When the model and ground plane are reflected about the ground plane, as shown in Fig. 16.26, the resultant configuration can be viewed as a test chamber



**Fig. 16.26** Duplex test section, generated by reflecting the real test section in the floor

with double the cross section with a centrally mounted test object made up of the model itself and its mirror image, including the road or track. The advantage of this so-called *duplex test section with duplex test object* is easier formulation of the numerical models by which the perturbation effects are quantified, even more so if the model is replaced by a body of revolution and the cross section of the wind tunnel is assumed to be circular.

*Closed test section:* in a closed test section three kinds of perturbation are present:

- solid blockage
- wake blockage
- horizontal buoyancy.

The first two have the same effect as if the speed of the measured undisturbed oncoming flow,  $U_m$ , is superimposed by an additional speed  $u$ . When the nondimensional coefficients, such as the drag coefficient  $c_D$ , are computed, the corrected speed, namely  $U_{\text{corr}}$ , has to be used:

$$c_D = \frac{D}{\frac{\rho}{2} U_{\text{corr}}^2 A},$$

$$U_{\text{corr}} = U_m + u = U_m + \varepsilon U_m = U_m(1 + \varepsilon),$$

$$q_{\text{corr}} = q_m(1 + \varepsilon)^2,$$

where  $\varepsilon$  is the so-called blockage coefficient, which is made up from the solid,  $\varepsilon_{\text{SB}}$ , and wake blockage,  $\varepsilon_{\text{WB}}$ :

$$\varepsilon = \varepsilon_{\text{SB}} + \varepsilon_{\text{WB}}.$$

Horizontal buoyancy adds a value  $\Delta c_{D \text{ HB}}$  to the drag coefficient  $c_D$ . How it is affected by the (near) wake of the body is still a matter of discussion.

Finally, the corrected drag coefficient  $c_{D \text{ corr}}$  is computed as follows:

$$c_{D \text{ corr}} = \frac{c_{D m} + \Delta c_D}{q_{\text{corr}}/q_m} = \frac{c_{D m} + \Delta c_{D \text{ HB}}}{(1 + \varepsilon)^2},$$

where the index m is the label for the measured values.

So far this calculation is strictly formal. To evaluate this equation, the blockage coefficient  $\varepsilon$  must be determined from the essential geometric parameters of the test section and the model, such as the blockage ratio  $\varphi$  and the length of the model. To date this has preferably been done using analytical models of the test section and model. Because only the far field is affected, the model is replaced by a body of revolution with the same thickness ratio.

*Open test section:* for a long time, vehicle aerodynamicists held the opinion that a wind tunnel with a free jet does not need corrections at all. And indeed, for larger wind tunnels the *classical* corrections are so small that they can be neglected. Furthermore, it was common understanding that the axial pressure gradient in the airstream of the empty test section is zero. This is because, according to textbooks, a free jet has the same pressure as the plenum into which it is ejected. However, comparative measurements disclosed that this is not true, and Fig. 16.11 is a striking result.

Following [16.4], compared to the closed test section several additional perturbations have to be taken into consideration. These are (Fig. 16.27)

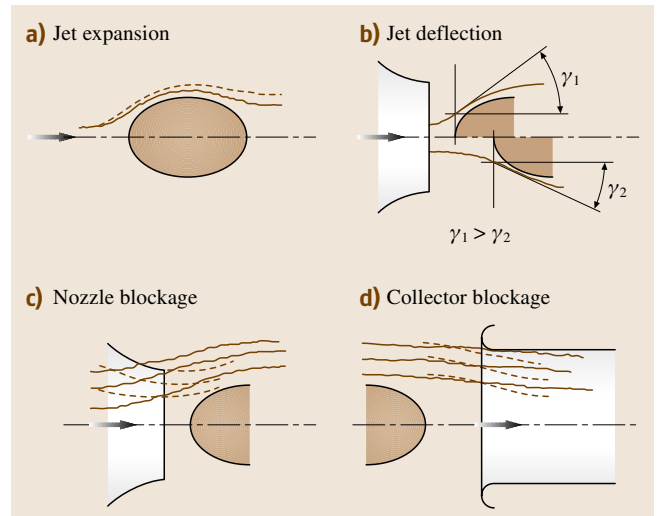
1. jet expansion  $\varepsilon_{\text{JE}}$
2. jet deflection  $\varepsilon_{\text{JD}}$
3. nozzle blockage  $\varepsilon_{\text{N}}$
4. collector blockage  $\varepsilon_{\text{C}}$ .

As before, the correction for the dynamic pressure of the undisturbed oncoming flow is the result of an addition:

$$\frac{q_{\text{corr}}}{q_m} = (1 + \varepsilon_{\text{JE}} + \varepsilon_{\text{JD}} + \varepsilon_{\text{N}} + \varepsilon_{\text{C}})^2.$$

The physical effects 1 to 4 are explained and modeled in [16.4].

The pressure gradient  $dp/dx$  (horizontal buoyancy) is treated as for the closed test section. However, its value, and consequently its perturbation effect, is much



**Fig. 16.27** Four major flow disturbances of the flow past a model in an open test section (after [16.4])

higher, and in some wind tunnels it may override all others.

The state of the art in computational fluid dynamics (CFD) makes it possible to surmount the restrictions of the *classical* corrections: low blockage, slender bodies, and questionable assumptions regarding the effect of the near wake. Making use of the panel method, the test object and test section, including the nozzle and the diffuser, can be modeled as shown in Fig. 16.28.

This method of correction is based on the assumption that the differences between the flow fields in free air,  $\varphi = 0$ , and with finite blockage,  $\varphi \neq 0$ , is the same in a real flow as in an inviscid flow. The wake can be modeled according to one of the methods described in [16.16]. As long as only *global* corrections are required, as described above, the model of the test object including its wake can be described using a rather coarse panel structure. Computation time will be extremely short; online and real-time computation of the corrections is possible. Beyond this, correction of the flow in specific locations can be carried out, for instance for the flow angle at the rear wing of a racing car, which is affected by the final dimensions of the airstream.

Such models have been developed for the closed test section [16.17], but not yet for the open. There the nozzle and the collector have to be included in the model, and the edge of the free jet must be modeled by imaging the model plus its near wake.

Correction of the yawing angle is generally not performed in vehicle aerodynamics. If necessary, the method can be taken from aeronautics, especially from slender wings. The yaw angle  $\beta$  of a vehicle corresponds to the angle of attack  $\alpha$  of a wing.

*Thermal tests:* when tests are performed in a thermal wind tunnel, a posteriori correction is not possible. The effective wind speed must already *during the test* be the same as the circumferential speed of the rollers of the dynamometer. This is ensured by an *implicit correction*. Several suggestions have been made for how this can be carried out [16.1, 18, 19]:

- The effective wind speed is that which follows from the pressure at the stagnation point of the test object, which is the Pitot pressure  $p_0$  of the oncoming flow

$$U_{\infty \text{ eff}} = \sqrt{\frac{2(p_0 - p_{\infty})}{\rho}}.$$

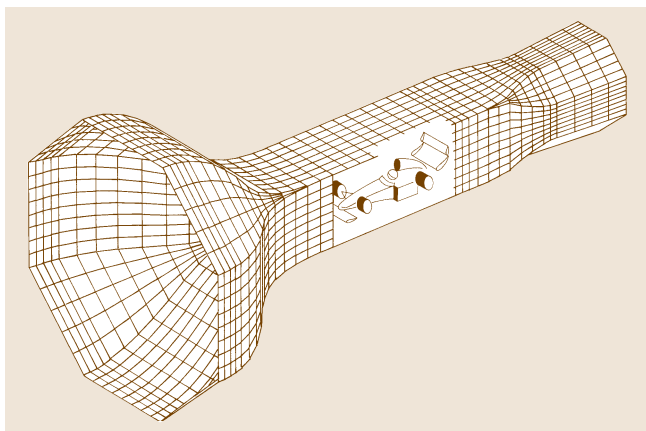
Of course, the Pitot pressure is the same across the oncoming flow. However, the advice to measure it at the stagnation point of the test object is a clear and reproducible one, more so as it must be ensured that the Pitot tube is approached at a zero yaw angle.

- The vertical velocity profile in front of the test car is measured on the road (or in a large wind tunnel). Comparison with the same profile measured in the thermal wind tunnel and a linear regression results in a nozzle factor  $k$ :

$$k = \frac{\overline{U}_{\infty \text{ set}}}{U_{\infty}}.$$

This method is preferred for experiments with cooling systems. From the measured velocity profile this segment is taken for the computation of  $k$  in front of the radiator inlet.

- As an alternative the cooling flow duct itself can be used as a flow meter and be calibrated on the road.
- When radiators of buses are tested, their air intake is on one side of the vehicle at the rear. The wind speed is set equal to the road speed (and thus the circumferential speed of the dynamometer) at the sides of the vehicle.
- Comparative pressure distributions are measured in the longitudinal center section of the hood and in the scuttle on the road and in the thermal tunnel, and a blockage factor  $k$  is determined via linear regression. Generally the result is different from that determined with the velocity profile in front of the vehicle. This kind of adjustment is applied when climatic tests are performed.



**Fig. 16.28** Panel model for computing wind tunnel corrections: nozzle, test section plus model, first diffuser

- When climatic tests are performed with (long) train coaches the wind speed on the sides of the coaches has to be set as for the radiator test with buses.

### 16.1.7 Typical Vehicle Wind Tunnels

#### Classification of Wind Tunnels for Vehicle Aerodynamics

In the motor industry and research organizations a large variety of wind tunnels are in operation. Although their objects, namely cars and light-duty trucks, are very similar, the variety of the design of wind tunnels is surprising. In order to provide a survey they will be classified into four categories:

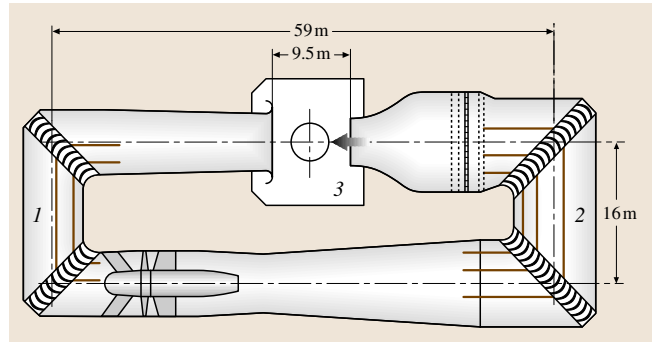
- large full scale
- small full scale
- thermal
- small scale.

Each will be characterized by one example. Additionally, some smart design details will be emphasized. For further details see [16.1], where the major full-scale wind tunnels worldwide are compiled, and some are described. In Europe, vehicle aerodynamicists prefer an open test section, and this type is gradually gaining preference in the US. All but one of the wind tunnels discussed have an open test section.

#### Large Full-Scale Aerodynamic and Aero-Acoustic Wind Tunnels

A typical large full-scale vehicle wind tunnels is that of the Institut für Verbrennungsmotoren und Kraftfahrwesen (IVK), at the University of Stuttgart. It was erected in 1988, when the wind tunnel built by Kamm in 1939 had to be given to Daimler-Benz AG. The air circuit (*Göttingen* type) together with its main dimensions are compiled in Fig. 16.29. The cross section of the jet is  $22.5 \text{ m}^2$ .

Originally, this wind tunnel was built as a purely aerodynamic facility, and as such it came into service in 1988; the maximum wind speed was  $270 \text{ km/h}$  ( $\approx 168 \text{ mph}$ ). However, provision was made for later improvements to expand the testing possibilities of the tunnel to include wind-noise investigations [16.20]. This upgrade was performed in 1993 with a novel silencing concept. The air path (Fig. 16.29) shows how the fan noise is *locked in*. Both cross legs, (1) and (2), together with their turning vanes act as U-bend silencers. The plenum (3) is covered with noise-absorbing elements laid out for two frequency ranges. In the low range,  $80\text{--}200 \text{ Hz}$ , the fan noise is damped by the novel membrane absorber sketched in Fig. 16.30a. The middle and



**Fig. 16.29** Aero-acoustic wind tunnel at IVK (after [16.20]). Cross section  $A_N = 22.5 \text{ m}^2$ , maximum wind speed  $V_{\max} = 257 \text{ km/h}$ , SPL at  $140 \text{ km/h} = 69 \text{ dB(A)}$ , five-belt system, rotating wheels

high frequencies are damped by porous polyester foam (Fig. 16.30b). The A-weighted self-noise level (SPL) measured *out of flow* and plotted versus tunnel speed (Fig. 16.31) is a proof of the effectiveness of this concept. The IVK aero-acoustic wind tunnel is now one of the quietest full-scale wind tunnels ever built (Fig. 16.31). The maximum wind speed of the tunnel was only reduced by  $7 \text{ km/h}$  by the damping measures.

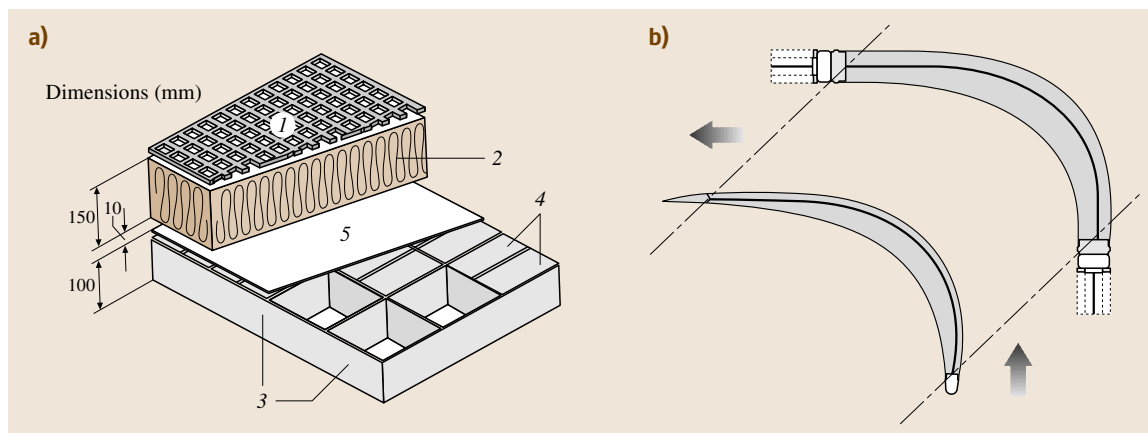
Another outstanding property of the IVK wind tunnel is its ground simulation, called the *five-belt system*. It is made up of a *narrow belt* (narrow compared to a belt that spans the entire width of the test section) moving between the wheel tracks and four *mini belts*, one under each wheel. Together with a system of tangential blowing and basic suction the boundary layer underneath the vehicle can be almost completely removed, and the wheels can be rotated, both up to the full wind-tunnel speed. J. Potthoff, the designer of this system and a similar one for the small-scale wind tunnel of IVK, has presented a description [16.21] and thoughts for future development.

#### Small Full-Scale Aero-Acoustic Wind Tunnels

The first small full scale wind tunnel ( $A_N = 11.75 \text{ m}^2$ ) built for vehicle aerodynamics was designed on behalf of the Italian designer Pininfarina by Morelli (1971) [16.3], followed by the aeroacoustic wind tunnel ( $A_N = 10 \text{ m}^2$ ) designed on behalf of BMW by L.J. Janssen (1988), both with an air path according to Eiffel.

In 1999 the small full-scale aero acoustic wind tunnel at Audi AG became operational [16.22]. Its air path is reproduced in Fig. 16.32 ( $A_N = 11 \text{ m}^2$ ). Based on the correction method developed by Mercker and Wiedemann [16.4] the dimensions of the test section were fixed as to minimize corrections. The turning vanes in

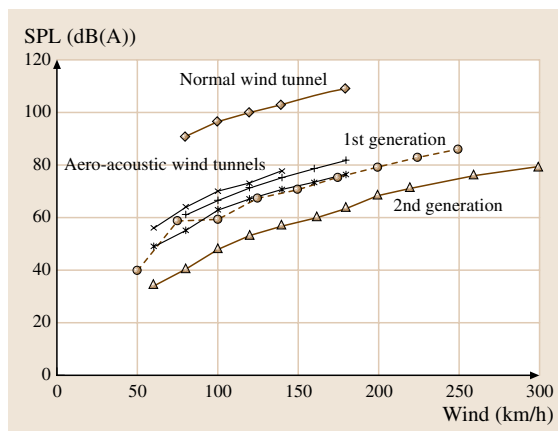




**Fig. 16.30a,b** Wind noise attenuation in the aero-acoustic wind tunnel at FKFS; **(a)** broadband absorber, **(b)** corner vanes covered with closed damping foam [16.20]

the 2nd and 3rd corner are designed as scene silencers to lock in the noise of the fan. The fan itself was designed to low noise generation [16.23]. As can be recognized from Fig. 16.31, this wind tunnel is the most silent at all.

Over the years the above mentioned wind tunnel of Pininfarina was converted into an aeroacoustic one, and upgraded. Due to design limitations it had not been possible to lock in the fan noise. Therefore a special fan was designed according to rules mentioned in Sect. 16.1.4. Noise level is now not as low as in newer aero acoustic tunnels; however, it is low enough to perform aero acoustic investigations of all kind. To increase top wind speed from 150 km/h to 260 km/h the semi-circle arch in the open return path was *filled* with 13 axial blowers (Fig. 16.33).



**Fig. 16.31** Measured out-of-flow SPL of several open jet wind tunnels (source Audi AG)

### Thermal Wind Tunnels

For each new vehicle two thermo systems have to be developed and tested:

- engine cooling, radiator and several heat exchangers
- heating, ventilation, and air conditioning (HVAC).

For the former a hot climate is needed, for the latter hot and cold, including further climate parameters such as humidity, sunlight, rain, and snow. Accordingly, two types of wind tunnels have been built:

- purely hot tunnels
- hot and cold tunnels.

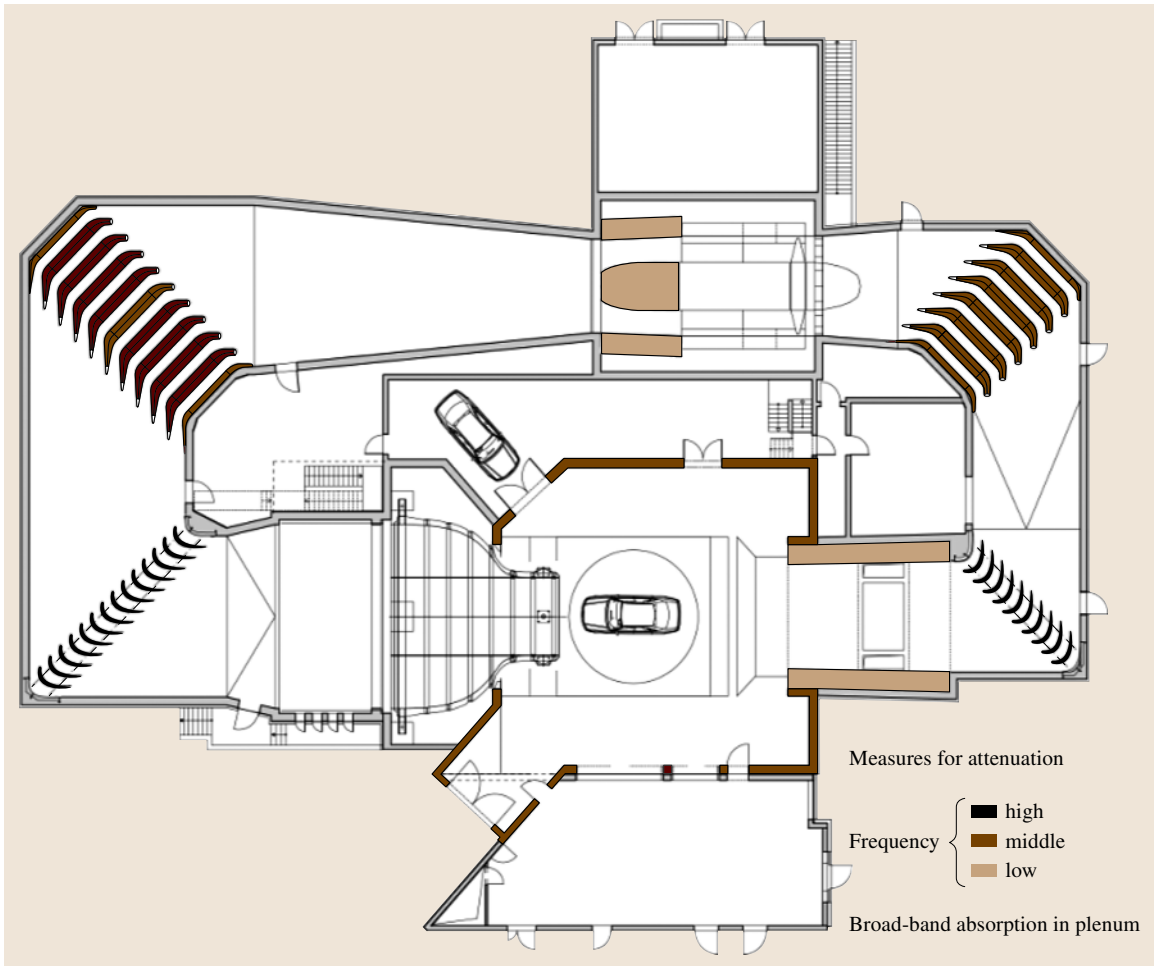
With regard to their size (cross section  $A_N$ ), three kinds of wind tunnels can be distinguished:

- 10–12 m<sup>2</sup> for full-size trucks and buses;
- 6 m<sup>2</sup> for cars;
- ≤ 4 m<sup>2</sup> for radiator tests with cars.

Generally the air path for all these tunnels is a closed return (*Göttingen*) type, as shown in Fig. 16.34, and the test section is open. Comparative tests confirmed the aforementioned finding that ground simulation can be simple: a rigid floor is sufficient.

Representative of the first category are the two Fiat thermo tunnels [16.24]. They are part of a wind-tunnel center including a 31 m<sup>2</sup> normal wind tunnel. One of the two 12 m<sup>2</sup> tunnels is laid out for high temperatures and sunlight simulation (hot tunnel), the other for cold environment (cold tunnel). Equipped with dynamometers, this pair of wind tunnels is well suited for all kinds of thermal tests.





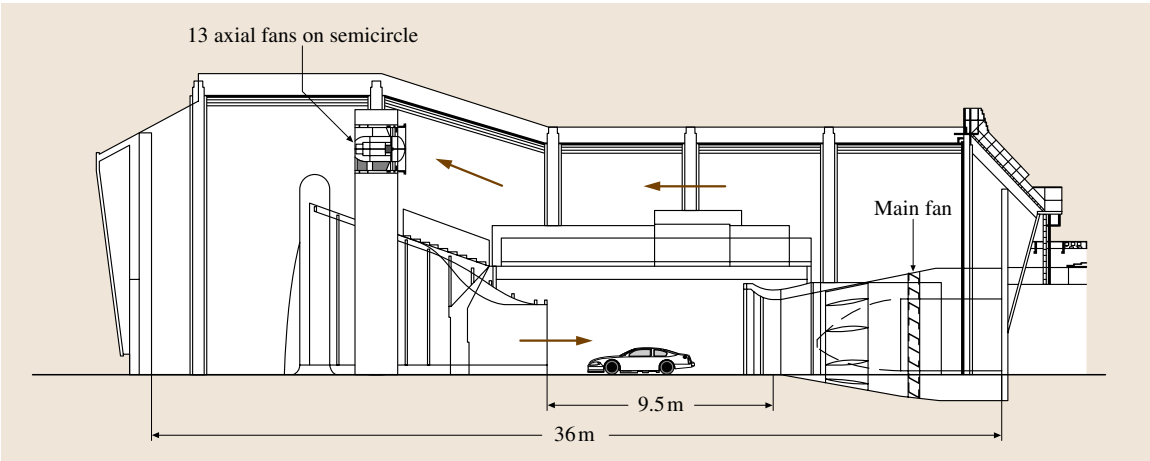
**Fig. 16.32** Aero-acoustic wind tunnel of Audi AG; design Wiedemann [16.22]; cross section  $A_N = 11 \text{ m}^2$ , maximum wind speed  $V_{\max} = 300 \text{ km/h}$ , OSPL at  $140 \text{ km/h} = 57 \text{ dB(A)}$ , moving floor, rotating wheels.

For thermal tests with cars a cross section of  $12 \text{ m}^2$  is more than sufficient. From the investigations mentioned in [16.25, 26] and from experience  $A_N = 6 \text{ m}^2$  has proven to be sufficient. However, in order also to be able to test full-size trucks and buses, several of these thermal tunnels are equipped with nozzles that allow for different cross sections:  $6 \text{ m}^2$  for cars and  $10\text{--}12 \text{ m}^2$  for large vehicles. The loss of top speed with the greater nozzle area can be accepted because of the speed limit of these larger vehicles. Two types of nozzles have been developed for this purpose:

- nozzles with a flexible upper wall (Fig. 16.35)
- tandem nozzles (Fig. 16.36).

A particular vehicle type comes with a variety of cooling systems (engine, oil, intercooler, condenser, exhaust gas, etc.). To develop these different systems requires a large effort. However, many of the related tests can be performed at ambient temperature. This work is performed in wind tunnels or with blowers with a nozzle cross section of ca.  $2 \text{ m}^2$ . Only fine-tuning is done in a hot tunnel.

For tests with *rolling stock* for railways and street cars a large wind tunnel is needed. Coaches are about  $30 \text{ m}$  long. The only way to simulate the flow on all four sides of the coach is in a *closed* test section. In its design a compromise has to be made between reproducing the axially constant flow velocity and a zero axial pressure



**Fig. 16.33** Wind tunnel of Pininfarina, design *Morelli* [16.3]; upgrade *Cogotti* [16.27]; cross section  $A_N = 11.75 \text{ m}^2$ , maximum wind speed  $V_{\max} = 260 \text{ km/h}$ , OSPL at  $140 \text{ km/h} = 77 \text{ dB(A)}$ , moving floor, rotating wheels

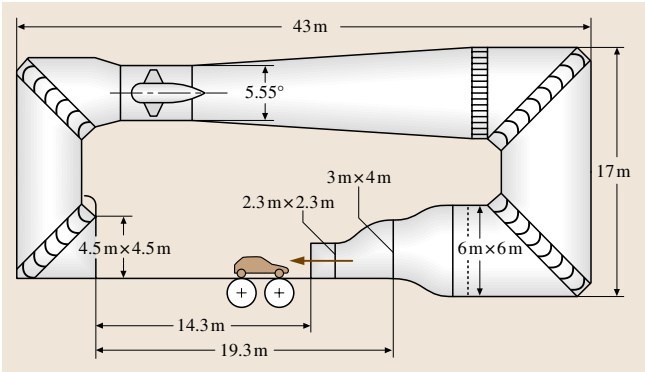
gradient. The air-conditioning units' air inlet and the outlet of the used air must be at the same pressure as on the track, where it is atmospheric.

Two such wind tunnels exist at Rail Tec Arsenal (RTA), Vienna. A view into a test section is reproduced with Fig. 16.37. The cross section of both test sections is  $A_N = 16 \text{ m}^2$ . The length of the large tunnel is 100 m, enough to host a train of three coaches and a complete street-car train. The length of the smaller tunnel (30 m) is sufficient for articulated buses (maximum length 18.75 m) and full-size trucks. One side wall of the test section is equipped with lamps at an angle of  $30^\circ$  (standard for railway testing). Intensity can be varied from  $250$  to  $1000 \text{ W/m}^2$ . Both tunnels are equipped with dynamometers (for data

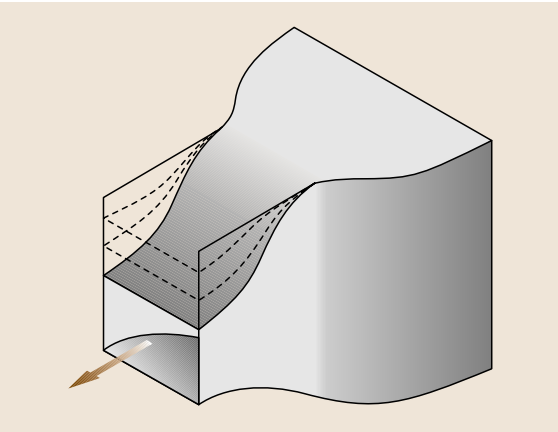
see the figure caption). The maximum wind speed is  $300 \text{ km/h}$  for the large and  $120 \text{ km/h}$  for the smaller tunnel.

**Small-Scale Wind Tunnels for Automobiles**

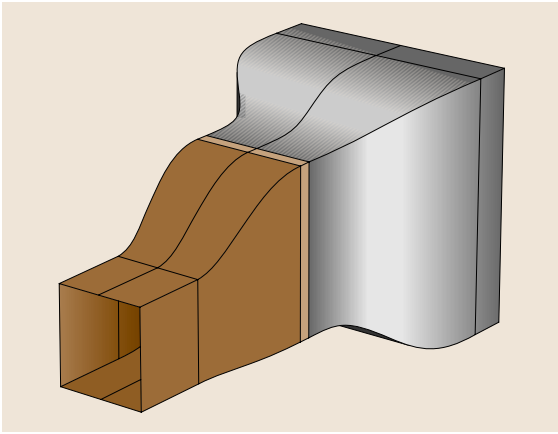
There are many wind tunnels that are well suited for testing small-scale vehicle models. Several are in academia, where they are used for this purpose only occasionally. Others, which were specifically designed for vehicle aerodynamics, are in research institutes. Some existing small-scale wind tunnels have served as pilot



**Fig. 16.34** Typical climatic wind tunnel (data from Modine GmbH) cross section  $A_N = 5.3/12 \text{ m}^2$ , maximum wind speed  $V_{\max} = 250$  or  $130 \text{ km/h}$ , four-roller dynamometer



**Fig. 16.35** Adjustable wind tunnel nozzle of the climatic wind tunnel of Behr GmbH; cross section  $A_N = 2.0/8.0/10.0 \text{ m}^2$ , maximum wind speed  $V_{\max} = 139/100/80 \text{ km/h}$  four roller dynamometer, temperature  $-30 < T < +50^\circ \text{C}$ ; sunlight  $1000 \text{ W/m}^2$



**Fig. 16.36** Tandem nozzle of the climatic wind tunnel (graphic after Modine GmbH)

tunnels during the design of a full-scale tunnel. Because of geometrical similarity, simulation deficits such as blockage are the same as in the full-scale tunnel. Differences occur only in the boundary layer of the ground floor. With such model tunnels it is reliable taking over results developed at small scale to the full scale.

Reduced-scale wind tunnels *can* be built at very low cost; the quarter-scale tunnel at the Motor Industry Research Association (MIRA), shown in Fig. 16.38, is a striking example [16.28,29]. Also the operating costs of such facilities are low, and flexibility is high. Both arguments are reasons why small-scale testing is coming into fashion again.

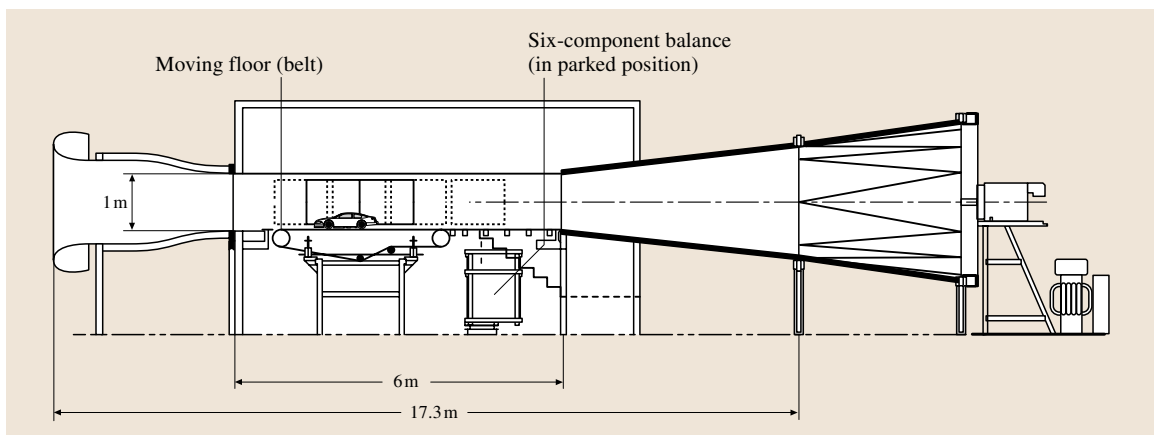


**Fig. 16.37** Test section of one of the two large climatic wind tunnels of RTA Rail Tec Arsenal, Wien (photo RTA); cross section  $A_N = 16 \text{ m}^2$ , length 100/30 m, maximum wind speed  $V_{\max} 300/120 \text{ km/h}$ , dynamometer 850/250 km/h temperature  $-50 < T < +60^\circ \text{C}$ ; sunlight  $1000 \text{ W/m}^2$

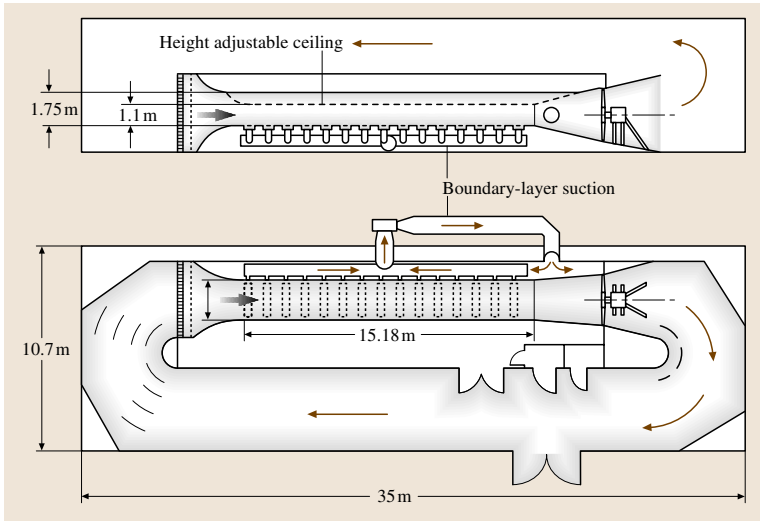
### Small-Scale Wind Tunnels for Trains

Generally, aerodynamic investigations with trains are carried out in normal wind tunnels, which are otherwise used in aviation. A scale of 1 : 10 is common. Because the test sections of these tunnels are relatively short, only short trains can be investigated, the head (locomotive) and two to three coaches. Tests at higher Reynolds numbers are carried out in a cryogenic tunnel.

A wind tunnel specially laid out for testing trains is shown in Fig. 16.39. It is the *soufflerie à veine longue* at Saint-Cyr-L'École, France [16.30]. The model scale is 1 : 20, and for special tests (pressure measurements) 1 : 10. The height of the ceiling of the closed test section



**Fig. 16.38** Small scale wind tunnel of MIRA, Nuneaton, UK (graphic MIRA); cross section  $A_N = 2.12 \text{ m}^2$ , maximum wind speed  $V_{\max} 90 \text{ mph}$ , moving floor



**Fig. 16.39** *La soufflerie à veine longue* in Saint-Cyr-L'École, France [16.30]

can be reduced from 1.75 m to 1.1 m to increase the wind speed from 40 m/s to 60 m/s. The axial pressure loss is compensated by the angle of the roof. Ground simulation was improved by boundary-layer suction. Later the first 6 m were equipped with a moving belt with rails and sleepers.

Tests with pantographs are performed with their originals in full scale, mainly in aero-acoustic wind tunnels from the automobile industry.

**16.1.8 Tests with Moving Models and Full-Scale Vehicles**

**Small-Scale Models**

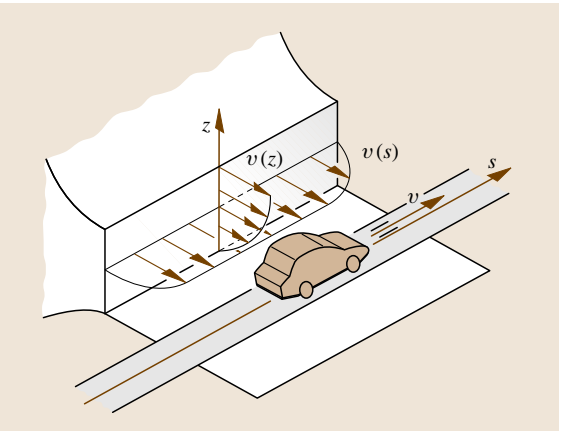
*Model track:* as discussed, the boundary layer developing on a wind-tunnel floor impairs the simulation of the flow underneath a vehicle, more so with decreasing ground clearance. Other tests, for example the meeting of two trains or a train entering a tunnel, cannot be simulated under dynamic conditions in a wind tunnel at all. Model tracks for small-scale train models are suitable for such tests [16.31].

*Catapult:* unsteady effects can also be studied by shooting the model – train or car – crosswise through the jet of a wind tunnel [16.32] (Fig. 16.40). In order to keep the sections of the track needed to accelerate and break the model short, the balance inside the model must be able to bear a high acceleration. In any case, the test signal will be superposed by large amounts of noise from the spring–mass system formed by the model and balance, and must be filtered.

*Towing tank:* another possibility to avoid an impairing ground-floor boundary layer or to study transient effects is offered by a towing tank, in which a fully immersed model is towed through a water basin [16.33]. The speed must only be 1/15 of the speed in a wind tunnel. Meeting of trains, and entering a crosswind gust have been studied [16.34].

**Full-Scale Cars and Trains**

*Aerodynamic drag:* the aerodynamic drag coefficient of a vehicle can also be measured in a coast-down test [16.35] (this recent reference may well serve as an introduction to the subject of fuel economy, and



**Fig. 16.40** Cross-wind test with small-scale model in a wind tunnel, schematic

in specific, to coast-down testing, the related literature, and the official regulations). It must be conducted on a long, straight, level test track. Several methods have been developed for the consideration of the influence of natural wind, although it is better yet to perform the test with no wind at all. The test vehicle is first accelerated to its top speed and then allowed to coast freely by disengaging the engine. The change of vehicle speed is continuously recorded versus time.

The deceleration is caused by the aerodynamic drag  $D_A$  and mechanical resistance  $D_M$  according to

$$m(1+f)\frac{dV(t)}{dt} = D_A + D_M,$$

where  $m$  is the vehicle mass (kg),  $f$  takes into account the rotating masses,  $V(t)$  is the vehicle speed (m/s) as a function of time  $t$ , and  $D_A$  is the aerodynamic drag (N)

$$D_A = c_D \frac{\rho}{2} V^2 A.$$

$D_M$  is the mechanical resistance (N); it is composed of the tire rolling resistance, and the resistances of the driveline and bearings:

$$D_M = \mu_R m g,$$

where  $\mu_R$  is the coefficient of rolling resistance, which is a function of speed  $\mu_R = \mu_R(V)$ ;  $m$  is the vehicle mass (during the test, which means including the driver and gasoline) and  $g$  is acceleration due to gravity.  $f$  is obtained from the equation of motion of the rotating components

$$f = \frac{I_d/r_d^2 + I_0/r_0^2}{m},$$

where  $I_d$  is the moment of inertia of the rotating components of the driveline including the wheels of the driven axle (Nms<sup>2</sup>),  $I_0$  is the same value of the non-driven axle (Nms<sup>2</sup>) and  $r_d$  and  $r_0$  are the dynamic rolling radii of the tires on the driven and non-driven axles (m).

The main difficulty with coast-down tests consists of accurately measuring the rolling resistance of the wheels. Its measurement on a drum leads to erroneous results. Considerable differences are found (either on the outside or inside surface of the drum) compared to on a level road. Furthermore, an additional effect is caused by the vehicle's suspension geometry (i. e., wheel camber, toe-in).

There are three possibilities for taking rolling resistance into consideration:

- rolling resistance is measured on a moving belt;
- it is measured with a trailer designed for investigating single wheels where all the wheel parameters (load, tire pressure, camber, etc.) of influence can be set [16.36];
- it is measured by towing the test car, which is covered by a shrouding trailer [16.37].

Alternatively, the determination of the mechanical drag  $D_M$  can be circumvented:

- when only increments of aerodynamic drag – due to additional parts such as spoilers or panels on the underside – have to be determined;
- when an artificial drag increment (with lift and pitching moment unchanged) can be produced and quantified by wind-tunnel measurements.

*Crosswind sensitivity:* the crosswind sensitivity of a vehicle is not easy to assess because the driver *must* be included. The traditional method is to subject the vehicle to an artificially generated crosswind gust during a straight-ahead drive on a test track [16.38]. Figure 16.41 shows a schematic illustration of such a test. Usually, the vehicle's lateral deviation  $y(t)$  from the initial straight-ahead direction is considered as a characteristic measure.

This kind of crosswind tests can be performed in two ways:

1. The driver does not apply any steering correction. The steering wheel is held either in its original position (fixed control) or it remains untouched (free control).
2. The driver attempts to minimize the lateral deviation  $y$  of the vehicle by counteraction with the steering wheel.

The first method considers the reaction of the vehicle alone. On a first glance it seems to be well suited for

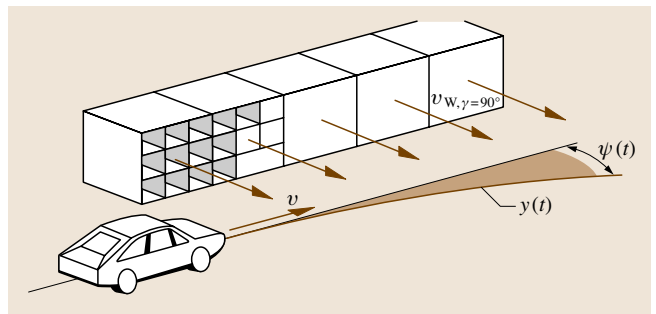


Fig. 16.41 Cross-wind test with real car, schematic

comparative tests. However, it does not have much to do with reality.

The second method includes the driver's reaction; thus the test result also depends on the driver. This procedure has the great advantage that the closed control loop made up by the driver, vehicle, and road is reproduced and is very close to a real-life situation. At the same time, the driver is acting as a sensor – by seeing the deviation and feeling the accelerations (yaw and roll) – and as an actuator – by operating the steering wheel.

Different crosswind facilities are in operation by the automobile manufacturers. Regarding their length, size, position, and number of blowers, and wind speed, they differ significantly from each other. As a result, the test data obtained in different facilities are hard to compare.

An error frequently incurred with crosswind tests, especially when carried out by the press, is that the yawing angle is set too high:  $\beta \approx 45^\circ$ . Such high yawing angles are rather unlikely to occur at the *high* road speeds where such a crosswind can affect the vehicle and be dangerous. Yawing angles on the order of  $\beta = 20^\circ$  (to  $30^\circ$ ) are considered more appropriate for realistic crosswind sensitivity comparisons among vehicles.

A realistic assessment of the effect of wind on the system made up of the vehicle and driver can only be achieved by driving under real conditions (stochastically changing wind) on public roads. Over time, several procedures have been developed that include the driver in the assessment (see [16.39] for the most recent).

Also *cooling tests* and *break tests* are carried out on road. Load is *produced* either in the mountains or with a break trailer on a level road.

### 16.1.9 Measurement Technique

The measurement technique applied in vehicle aerodynamics makes use of the same physical principles as in other areas of fluid dynamics. Differences exist

with regard to technical details and in application, and only those will be considered here. The quantities to be measured are compiled in Table 16.2.

#### Forces and Moments

In vehicle aerodynamics forces and moments are stated in a *vehicle fixed* coordinate system, as sketched in Fig. 16.42. The reference point is the position on ground where the longitudinal centerline crosses the perpendicular line halfway along the wheel base ( $a/2$ ). Instead of quoting the moments of yaw, pitch and roll as such, they are declared as force increments on the front and rear wheels, which makes communication with vehicle dynamicists easier.

To measure the resulting forces and moments produced by the flow and to reduce them to components, specific balances have been developed. In comparison to those used in aviation the following differing specifications exist:

- forces in horizontal and vertical direction are of the same order of magnitude;
- the resulting force and moment are reduced in a vehicle-fixed system;
- the balance swiveling  $\beta = \pm 180^\circ$ .

Time in a vehicle wind tunnel is rare and very expensive. The balance must be designed for quick model change, and the measuring time must be short. Frequently, manipulations on the underside of the vehicle have to be executed. Therefore the balance should be completed by a device to lift the vehicle (1.80 m) and to relocate it exactly. Some balances are designed to be equipped with a moving belt and mini-belts to rotate the wheels.

According to the manner in which the vehicle is connected to the balance three types can be distinguished (Fig. 16.43):

1. *Wire suspension*: this *classical* technique borrowed from aviation is no longer applied in vehicle aerodynamics as assembling the model is too slow. However, it still offers several advantages. The thin wires disturb the flow far less than struts or stings, and their drag can easily be calibrated out. Furthermore, the suspension makes it possible to allow the vehicle's wheel roll on a broad, moving belt with reduced and controlled wheel load.
2. *Sting*: the vehicle is held by a rigid sting, either from above or from the rear. Flow is disturbed to varying degrees, especially separation at the rear. This technique is widely used for racing cars. Wheels

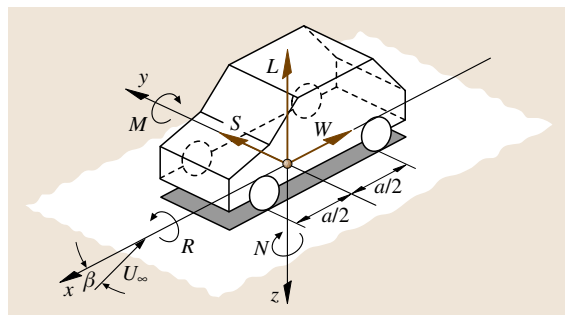
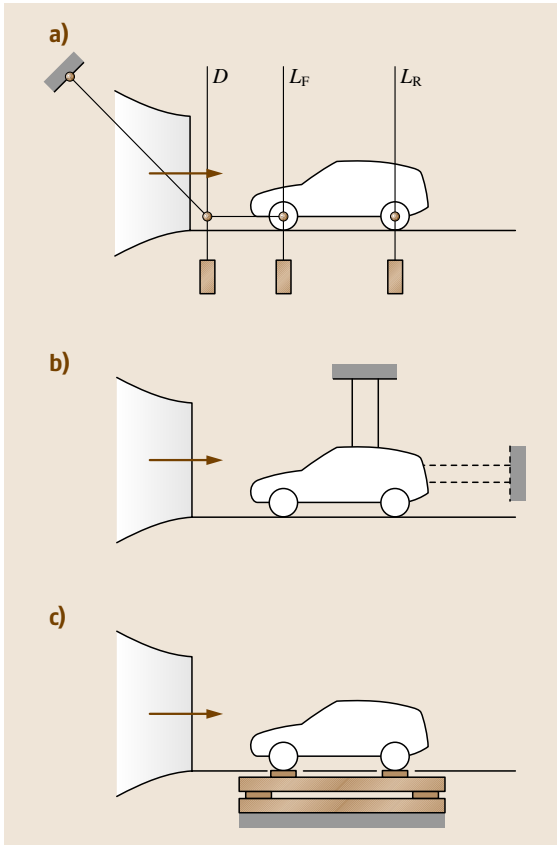


Fig. 16.42 Vehicle coordinate system





**Fig. 16.43a–c** Three possibilities to assemble a model to a wind-tunnel balance, schematic; (a) traditional wire suspension; (b) with sting from top or rear; (c) on platform

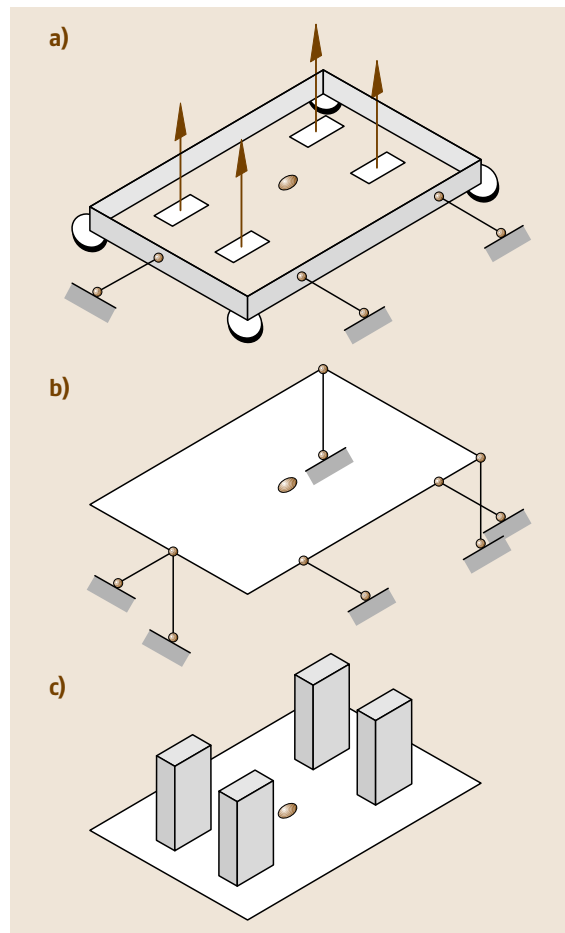
are mechanically disconnected from the vehicle's body, held from outside by covered two-component balances or stings, and can roll on the moving belt.

3. *Floor balance*: the vehicle rests with its four wheels on four small platforms that can be adjusted for the wheel base and track. This type is preferred in vehicle aerodynamics, and allows for the integration of devices to rotate the wheels.

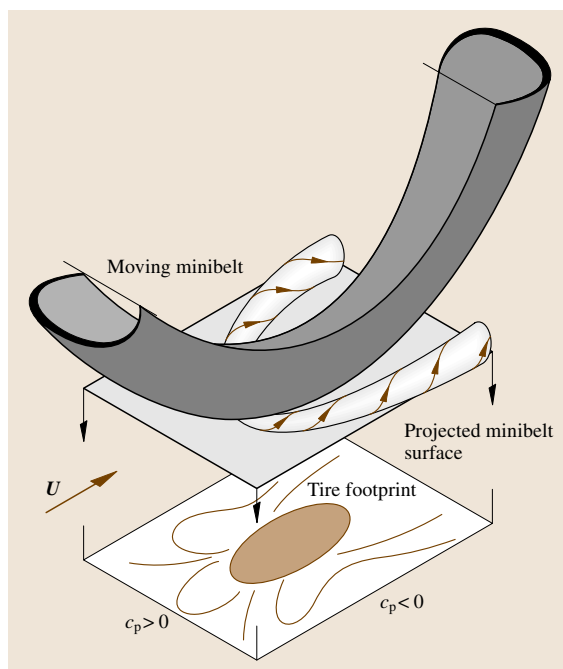
Traditionally, floor balances were designed to separate the forces and moments in the six degrees of freedom mechanically [16.40]. One quality measure of a balance was how well the cross-effects were eliminated. Today this is no longer practiced; the decoupling is performed strictly numerically.

Three different designs of balances are in use (Fig. 16.44):

1. *Floating-frame balance*, seven components: vertical and horizontal components are mechanically decoupled. The frame is floating on hydrostatic bearings; drag and side forces on the front and rear axle are measured via connecting struts. The lift balances are mounted inside the frame, one for each wheel. Horizontal displacement of the test object (elastokinematic elements, tires) has no effect on the measurement.
2. *Platform balance*, six components: the platform is held by six struts that are connected with force-measuring elements. Horizontal forces move the test object and have an effect on the force distribution. The movement is measured optically and corrected for. The six forces are not mechanically decoupled.



**Fig. 16.44a–c** Different designs of platform balance, schematic; (a) floating frame; (b) rigid platform; (c) four/two columns

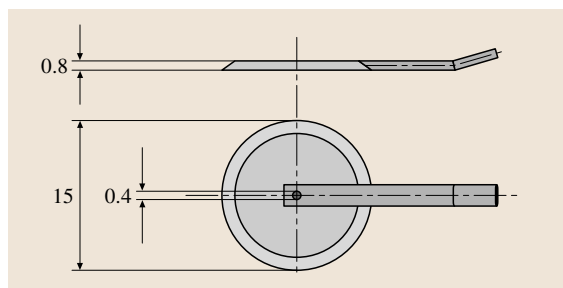


**Fig. 16.45** Pressure distribution around a wheel, needed for wheel-pad correction, schematic

The interaction is registered during calibration and stored in a matrix.

3. **Column balance, 4×6 components:** The test object rests on four columns that are assembled on a rigid, common ground plate and can be adjusted to the wheel base and track. For testing motor cycles only two are needed. Each column is equipped with a complete six-component balance.

In any case, each wheel rests on a small rectangular surface – be it a rigid pad or a minibelt – which is inevitably wider and longer than the footprint of the tire. Thus it is subjected to the pressure field around



**Fig. 16.46** Flat pressure probe, called a *bed bug*

the footprint (Fig. 16.45), and has an effect on lift. By measuring the pressure field on the pads an empirical correction can be applied.

### Pressure

When it is not permissible to drill a hole into the sheet metal of the body of the test object, pressure is measured by thin disc-like probes (so-called *bed bugs*), as shown in Fig. 16.46, which are fixed to the surface of the body by an adhesive. If more than one probe is used attention must be paid not to impair the local flow due to the plastic hoses connecting the probe to the pressure transducer.

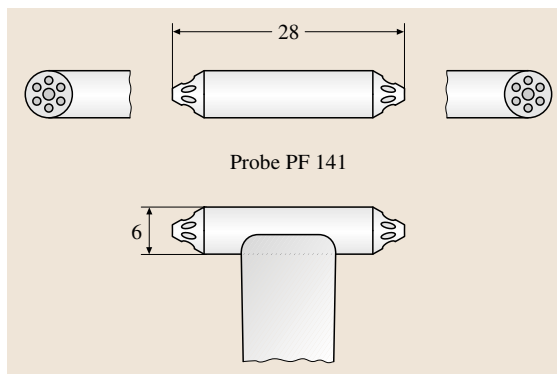
Pressure-sensitive paints (PSP) have not yet gained acceptance in routine vehicle aerodynamics for three main reasons:

- because of the relatively low flow speeds, pressure differences to ambient are low
- the expenditure for preparing the model is high
- calibration needs a lot of time.

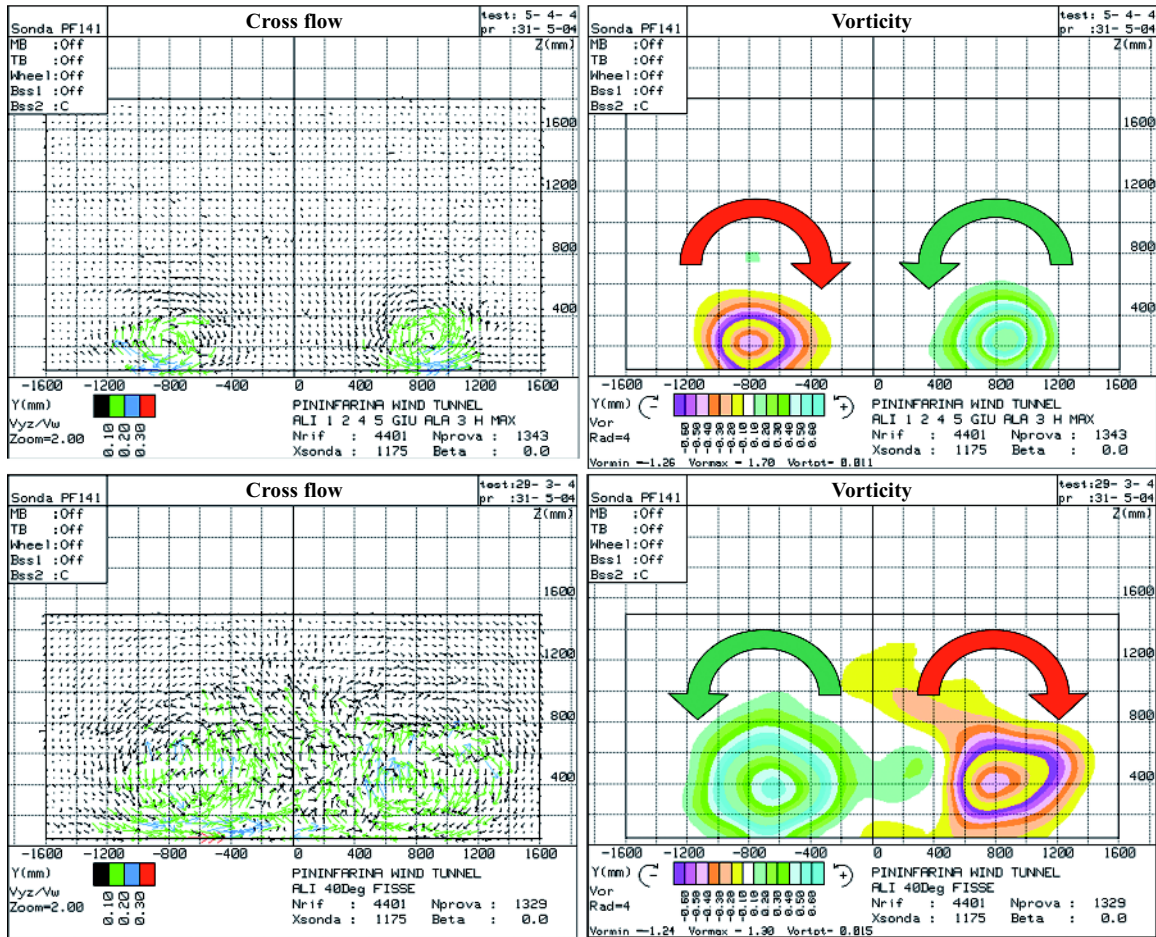
To scan fields of pressure and velocity in the space around the vehicle so-called multi-hole probes are used. The most prominent example is the 14-hole probe developed by A. Cogotti [16.41] (Fig. 16.47). Local values for the velocity  $v(z, y)$  and the loss of total pressure in a plane  $x = \text{const}$  behind the test object give an indication of where on the vehicle drag is generated. In the case of Fig. 16.48 upwind and downwash were produced with the flaps seen in Fig. 16.19 in specific stationary positions, leading to the vorticity shown on the diagrams on the right-hand side of Fig. 16.48.

### Velocity

Vehicle aerodynamicists like to measure the air velocity with a vane anemometer; a collection is depicted



**Fig. 16.47** 14-hole probe after A. Cogotti [16.41]



**Fig. 16.48** Cross flow and vorticity for upwash and downwash produced by the flaps shown in Fig. 16.19 in specific steady-state positions (after A. Cogotti)

in Fig. 16.49. Often they are handheld to detect local flow streaks, for instance in front of breaks. Probes with a diameter of 80–100 mm but very thin are used to measure the flow distribution in front of (or behind) a radiator or condenser.

Measuring the flow velocity in discrete loci but continuous in time is the domain of laser Doppler anemometry (LDA). Using three pairs of laser beams all three components of the velocity vector can be measured. Its application is described in [16.42]. If continuous information of speed in a plane is needed particle image velocimetry (PIV) is well suited [16.43]. It allows recording the complete flow field in a plane within a few microseconds. Thus it makes it possible to get insight into an unsteady flow field, such as the vortex filed in a plane  $x = \text{const}$  behind a car.

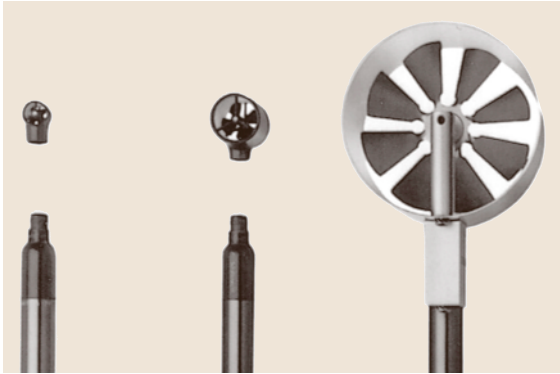
### Air Flow Rate

The air flowing through a vehicle's passenger compartment serves as a transport medium for mass and heat. It is its task to control thermal comfort and hygiene. Apertures designed into a body are:

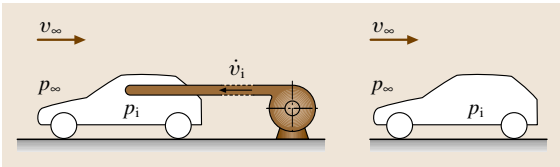
- inlet: for cars generally in front of the windshield
- outlet: for cars at the rear; formerly at the C-pillars, now in a region of moderate (low) pressure, for instance at both sides, hidden behind the rear bumper.

Besides these designed openings there are other unwanted ones, so-called leaks, where air may come in or go out.

Generally, the air flow rates through all these apertures depend on the flow field around the vehicle, i. e., on the driving speed. Measurement of this volume flow is

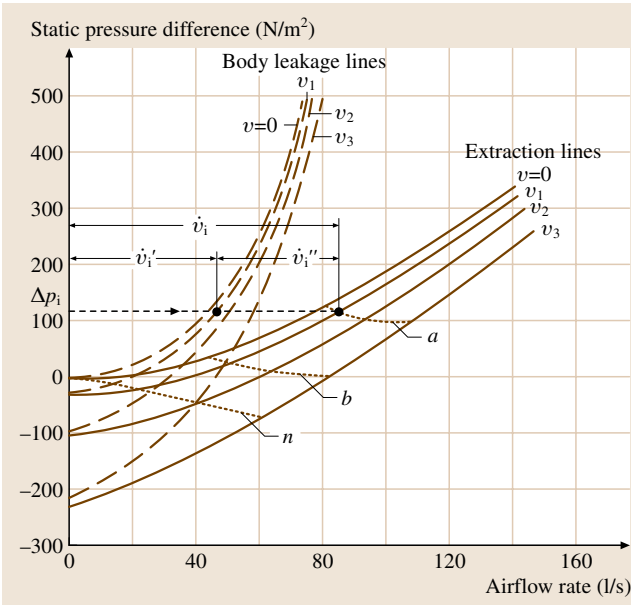


**Fig. 16.49** Vane anemometers, diameter (from left to right): 11, 22, and 88 mm

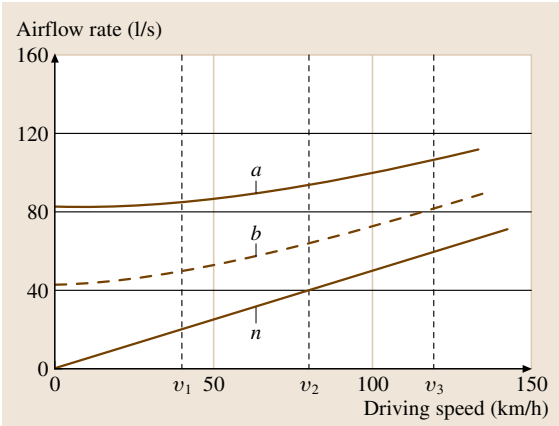


**Fig. 16.50** Test set up to measure the air flow rate through a passenger compartment, schematic; *left*: outside auxiliary blower to measure the extraction line; *right*: air flow test

carried out in a wind tunnel in two steps, as summarized in the schematic in Fig. 16.50:



**Fig. 16.51** Measurement of air-flow rate, extraction lines



**Fig. 16.52** Air flow rate versus driving speed for three different fan stages

1. measuring the *extraction curves* with an external blower
2. determination of the air flow rate using these curves

This technique is attributed to Wallis [16.44], however it was in fact developed independently in several places. The reference in both cases is the interior pressure  $\Delta p_i = p_i - p_\infty$ .

In order to measure the extraction curve all *inlet* openings are sealed; the *exit* openings remain open. While the wind is on, air is fed into the compartment through a hole in one of the windows from an external blower and hose. The static pressure inside the compartment,  $\Delta p_i = p_i - p_\infty$ , is measured as a function of the volume flow  $\Delta p_i = f(\dot{V})$ . The volume flow of the blower  $\dot{V}$  is measured using a flow meter inside the tube. This measurement is repeated for several wind speeds  $U_\infty$  and plotted in a graph (Fig. 16.51).

In a second step the external blower and the supply hose are removed, and the inlet apertures are opened. Now the interior pressure  $\Delta p_i$  is measured again for the same wind speeds  $U_\infty$  as above,  $\Delta p_i = f(U_\infty)$ . All important settings of the control flaps of the HVAC system and speeds of its fan are investigated. For each set of  $(n, \Delta p_i, U_\infty)$  the volume flow can be read as a function of wind speed, and is plotted as shown in Fig. 16.52.

If these two steps are repeated with the outlet apertures sealed the leakage air flow rate can also be measured.

### Flow Visualization

Flow visualization serves as an important aid in experimental vehicle aerodynamics, in wind tunnels and on





**Fig. 16.53** Traditional flow visualization with wool tufts (photo Volkswagen AG)

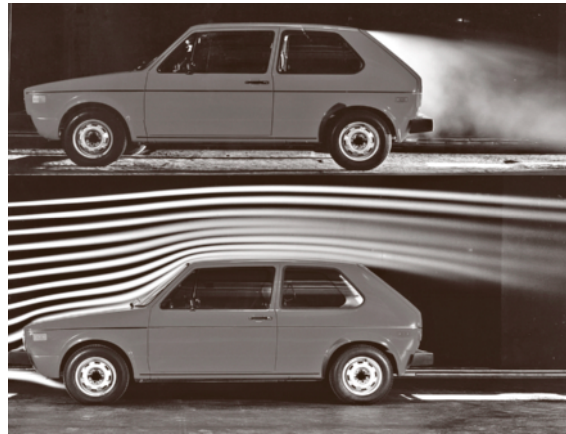
the road or track. Traditionally wool tufts were used, and they are sometimes still used even today, in various versions:

- tufts on the surface of the body, as shown in Fig. 16.53; this technique, although preparation of the model is lavish, was applied to localize separation; it is also suitable for tests on the road and track;
- tufts in an orthogonal screen (positioned behind the vehicle) to visualize longitudinal vortices;
- a tuft on a single probe, to detect the local flow direction, for instance in front of breaks.

A useful technique to visualize the flow on the surface is the application of a liquid film of petroleum and gasoline containing colored or luminescent pigments. Figure 16.54 displays a typical result. The liquid is painted (or sprayed) onto the surface, and the wind is quickly accelerated and kept on until the film dries. However, such painted images must be interpreted carefully,



**Fig. 16.54** Flow visualization with emulsion of Schlemmkreide (photo Daimler Chrysler AG)



**Fig. 16.55** Flow visualization with *smoke*; top: smoke introduced into the near wake; bottom: smoke introduced into the undisturbed oncoming flow (photo Volkswagen AG)

especially in regions of separated flow, for example, at the vertical areas of the vehicle body, where gravity affects the paths of the particles.

A device frequently used is a smoke generator. By feeding thin smoke streaks into an airstream, the path of the air flow becomes visible. Generally, an alcohol/water mixture is evaporated in the generator. An optical dense nontoxic vapor – frequently called *smoke* – develops, and is injected into the airstream with a long thin (heated) stem at two different locations:

- into the *undisturbed* flow ahead of the vehicle; streamlines become visible, as depicted in the lower part of Fig. 16.55;
- into the *separated* flow, where it fills the entire near wake up to the separation point, as seen in the upper part of Fig. 16.55.

Good illumination is a prerequisite for flow visualization. To generate a plane of light, light from a high-performance laser (5–24 W) must be first led through a cylindrical lens and then deflected with a mirror in such a way that the vehicle can be illuminated in each desired section across its full width, length or height. The thickness of the light sheet should be between a few millimeters and several centimeters.

Alternatively, the flow in a region of separation can be investigated with a bubble generator. Helium-filled soap bubbles are introduced into the air flow and photographed. If the exposure time is well chosen, individual flow paths are visible (Fig. 16.56). This method is well suited to small-scale models, but is occasionally also applied to full-size cars.





**Fig. 16.56** Flow inside near wake made visible with He-filled soap bubbles (photo Adam Opel AG)

A simple and very sensitive method to detect lines of separation is offered by the application of talcum. The location where separation is expected to occur is sprayed with a very thin oil film before the test. During the test talcum is blown into the zone of separated flow. It deposits where the flow separates, and a line of separation becomes clearly visible. Because talcum is dirt for a wind tunnel, this technique should only be used for special problems. However, on the road and track it can be used without restriction.

Water tunnels are extremely well suited for flow visualization. Formerly, methods in which flow patterns on the surface became visible were preferred. Later, methods in which the three-dimensional flow was made visible were introduced. One possibility is to add a thin colored streak of liquid (milk) to the flow; the most prominent example is Reynolds' experiment from 1883, with which he made the transition from laminar to turbulent flow in a pipe visible. However, adding a colored liquid to the flow of a tunnel with a closed circuit has the disadvantage that the colors dilute the water and make it quickly unusable.

Instead, the effect of electrolysis can be used. A thin wire is spanned across the flow and a pulsed direct-current (DC) voltage applied. Hydrogen bubbles are generated and carried away with the flow. If the wire is isolated, equidistant bubble streaks become visible, similar to the smoke streaks in a wind tunnel. As an example Fig. 16.57 depicts the shear layer over an open cabriolet. Pictures like this can be used for comparison with CFD results. If the wire is spanned in an area of separation similar pictures as with the He bubbles can be produced.

However, although very attractive pictures can be produced this way, water tunnels are barely used in the course of vehicle development anymore.



**Fig. 16.57** Flow visualized by H-bubbles generated with a wire in a water tunnel (photo Daimler Chrysler AG)

### Flow Noise

The measurement of flow noise has two objectives [16.45, 46]:

- *Exterior noise:* the typical example is a high-speed train. To get authorization to run a train the operator has to prove that the train conforms with noise regulations. Specifically, the sound pressure level must be below 90 dB(A) at a distance of 25 m. To ensure this, during the development of the train the noise sources have to be localized and methods to attenuate them have to be developed.
- *Interior noise:* such as the noise inside the passenger compartment of a car, a bus or a wagon. Interior noise is an important matter of comfort. In this case not only objective data have to be recorded. The noise must be assessed according to subjective criteria and speech recognition.

What makes this task delicate is that interior noise can only be measured when a prototype exists. However, once a project is in the prototype phase only minor modifications can be performed. Therefore it is necessary to know how exterior noise sources and interior noise level correlate. Only then can measures be developed to keep interior noise at a level that is assessed as comfortable.

Four measuring systems are on hand to determine the data:

- a single microphone
- two microphones built into the auditory canals of an artificial head
- an acoustic mirror with one or more microphones
- a microphone array.

The latter two systems have been developed to localize sound sources on *moving* objects such as trains or cars. Of course they can also be used in a wind tunnel, however, only in those with an open test section.

*Single microphone:* a microphone is an extremely sensitive pressure sensor, transforming an alternating pressure into an alternating-current (AC) voltage. According to George [16.47, 48] in the frequency range of interest the measurement signal should vary by not more than  $\pm 2$  dB with frequency. Condenser microphones meet this prerequisite, provided that the diameter of the membrane is matched to the frequency range under consideration. This linearity is lost as the wavelength of the sound signal approaches the diameter of the membrane. Microphones with a small diameter are suitable for high frequencies. Inside a passenger compartment a frequency range of 20 Hz to 12 kHz must be covered. The appropriate microphone diameter is  $1/2''$  (12.7 mm).

Because of pseudo-noise generated by the flow around a microphone, in-flow measurements with a microphone are hardly ever performed. Even a well-streamlined nose cone, which was formerly used for this purpose, cannot overcome this effect. Instead, noise close to a surface is measured with so-called surface microphones with the dimensions of a small coin: outer diameter 20 mm, thickness 2 mm. A typical test set up is shown in Fig. 16.58, where the sound pressure on the surface of a side window close to the wake of the side mirror is measured. The result is shown in Fig. 16.59. The difference in sound pressure level with and without mirror is compared for two different mirrors: the *noisy* mirror, lower diagram, increases the wind noise by approximately 20 dB compared to the case with-



**Fig. 16.58** Test set up with surface microphones according to Brüel and Kjaer (Photo courtesy Forschungsinstitut für Kraftfahrwesen und Fahrzeugmotoren Stuttgart (FKFS))

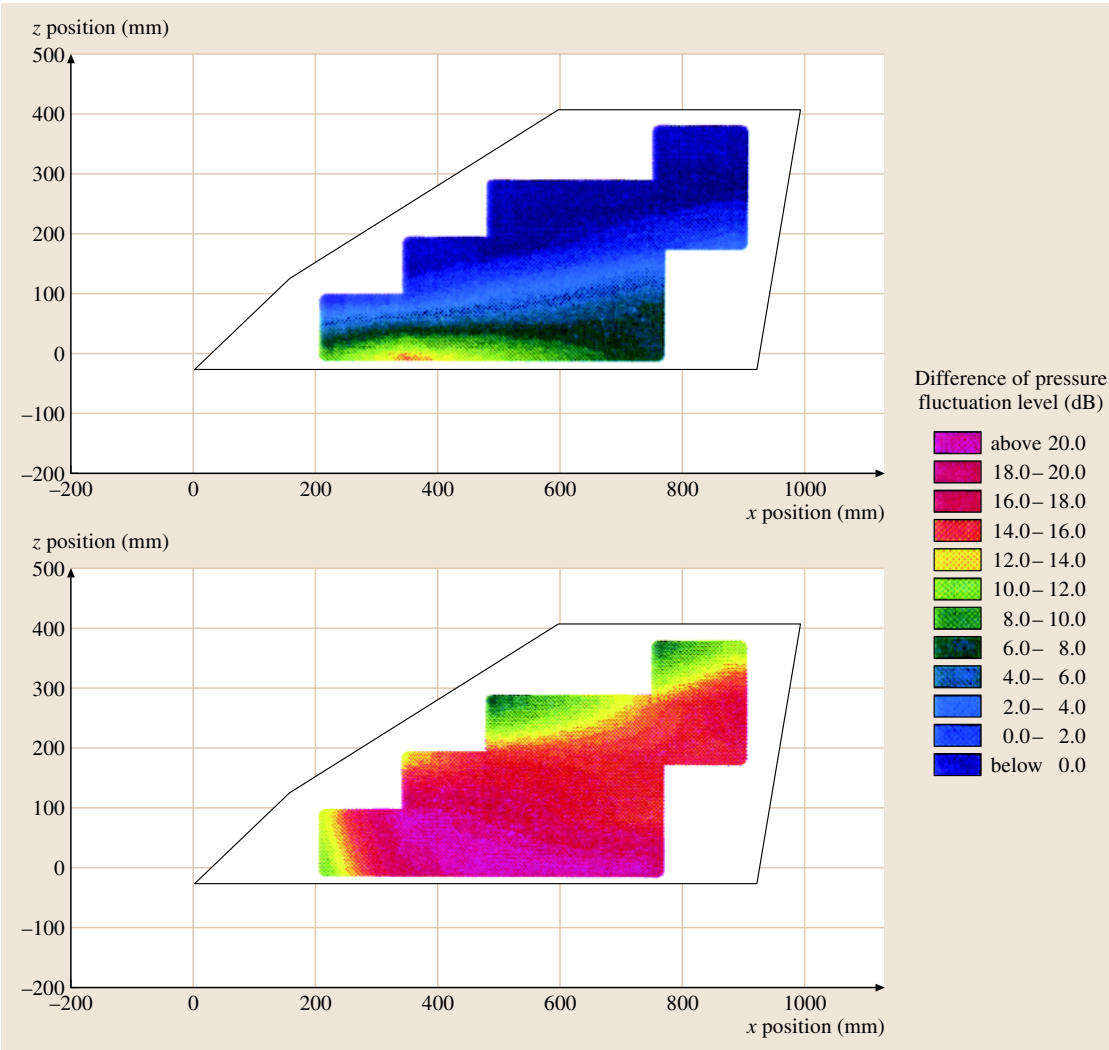
out a mirror, while the *silent* adds only 2–10 dB to the (exterior) noise.

When measurements are carried out in rooms with only very low wind speed, such as inside a passenger compartment, a definite and repeatable position of the microphone must be observed. Admittedly, because of the multiple reflections at the walls the noise field is diffuse, and the level of sound pressure is independent of the microphone's position. However, very close to the walls, which themselves are noise sources, this is no longer true. As shown in Fig. 16.60 the sound pressure level increases when the microphone approaches the side window. The left ear of the driver is within the near field of the side window [16.49]. Therefore, this position was formerly selected as the standard for comparison of interior noise inside a passenger car. A typical result is shown in Fig. 16.61. In this case, the interior noise was measured twice: with the exterior mirror in place and without. The mirror is perceptible in the high-frequency range.

*Artificial head:* to subjectively assess the interior noise more like a driver or passenger the single microphone can be replaced by an artificial head (Fig. 16.62). The noise is recorded by two microphones built into the auditory canals of this head model. Subsequent to the test in the vehicle the noise is analyzed, reproduced binaurally and listened to with a head set. Different noise signals can be compared by quickly switching from one to another, and the effect of specific frequency bands can be assessed. The target is to tailor an agreeable spectrum, and measures are elaborated with which it can be reproduced inside the car, a task known as *sound engineering*.

*Acoustic mirror:* noise sources, either stationary or moving, can be localized with an acoustic mirror. Its working principle evolves from Fig. 16.63 [16.50]. The mirror is made up from an ellipsoid of revolution. One focus is directed at the object, while the microphone is located in the other, where the sound waves emitted from the object arrive. The sound pressure level is between 20–40 dB higher than that measured with a single microphone without a mirror, although the amplification depends on frequency and is lowest at low frequencies.

The surface under investigation must be scanned point by point. More than one point can be measured at a time when several microphones are placed at the focus of the mirror (Fig. 16.64). However, their amplification is not the same, and must be calibrated before the test.



**Fig. 16.59** Sound-pressure field difference behind an exterior mirror as compared with the case of no mirror in place; *bottom: noisy mirror, top: silent mirror* [courtesy Forschungsinstitut für Kraftfahrwesen und Fahrzeugmotoren Stuttgart (FKFS)]

When applied in a wind tunnel the mirror must be placed out of flow, and two effects have to be observed:

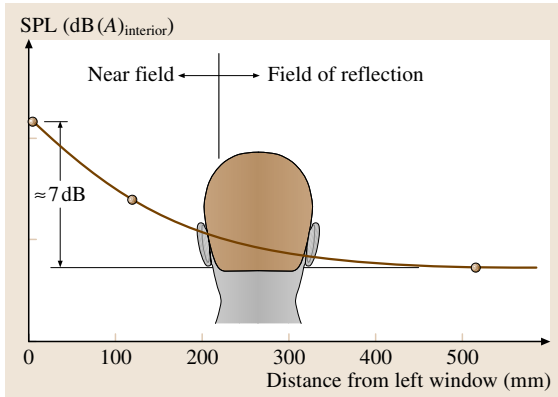
- the sound wave emitted by a source located on the object is transported by the airstream of the wind tunnel. The source of sound appears to be further downstream;
- refraction of the waves at the airstream's boundary make the noise source appear bigger than it is.

*Microphone arrays:* noise sources on moving objects can be localized with a phased array of

microphones, as described in [16.51]. Only with these can the movement of a sound source be considered. Even narrow-band tones are correctly reproduced, because the Doppler effect can be regained. Figure 16.65 shows a schematic of the installation: 15 microphones produce one-dimensional (1-D) sensitivity.

### Geometrical Quantities

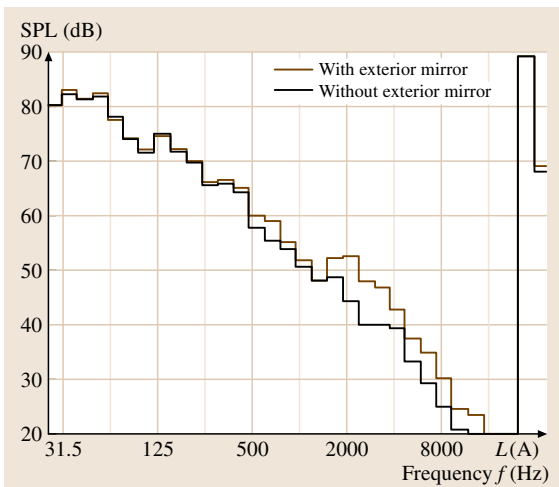
In vehicle aerodynamics several geometrical quantities must be measured:



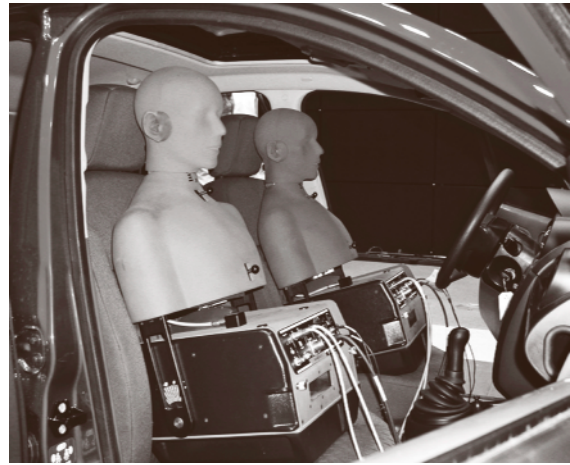
**Fig. 16.60** Increase of SPL at the left ear of the driver when coming close to the side window (after [16.49])

- the frontal area of the vehicle (Fig. 16.7), which is the reference area for nondimensional coefficients
- the exact coordinates of the test object's surface; each shape modification must be documented consistently with the computer-aided design (CAD) dataset for communication with the design team
- stationary and unsteady deformations of body parts (e.g., hoods, doors or ballooning of the roof of a cabriolet).

Optical methods have been developed for these purposes. Of course, these are not fluid-dynamic methods, but they are indispensable tools for the vehicle aerodynamicists.



**Fig. 16.61** Effect of outside mirror on SPL in the high-frequency range (after [16.45])

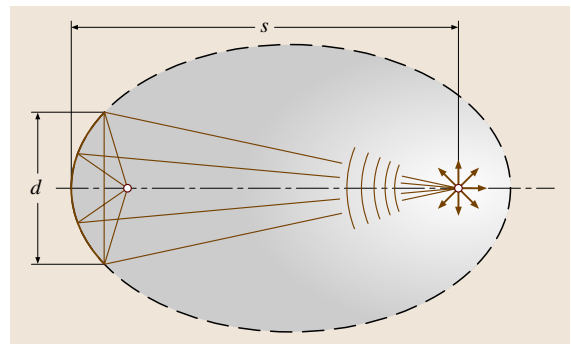


**Fig. 16.62** Artificial head (photo Ford Werke GmbH)

Traditionally the frontal area is determined from the vehicle's shadow image, which is generated with a flash light positioned at a large distance. The contour projected onto a screen is drawn by hand and the area is determined with a planimeter. The divergence of the light beam is corrected for by comparing the shadow image of a rectangular plane of a precisely given magnitude (i. e., 2 m<sup>2</sup>).

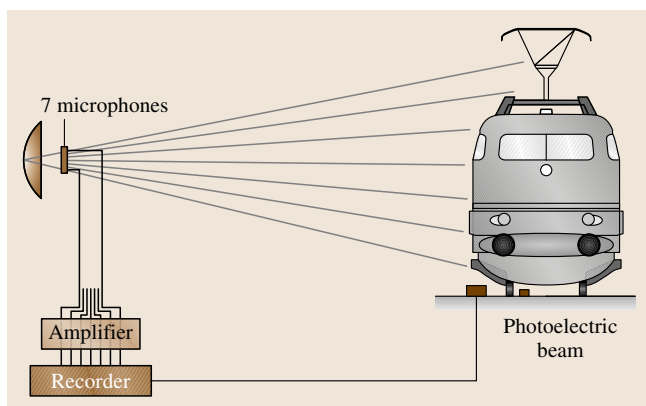
Newer methods make use of *edge tracking*. The disadvantage of these methods is that each measured point has to be (automatically but nevertheless time-consumingly) focused, because not all these points are in the same plane. The accuracy of  $\pm 0.3\%$  is said to be sufficient. The time required to measure one frontal area is about 45 min.

A much faster method has also been developed [16.52]. The outline of the vehicle's shadow image is projected onto a screen with a 50 mm-diameter laser beam that is moved by the wind tunnel's traversing gear.



**Fig. 16.63** Acoustic mirror (after [16.50])





**Fig. 16.64** Array of seven microphones close to the focal point of an acoustic mirror

The contour is tracked with a frequency of 10 Hz, and a photograph of each point is taken by a digital camera. This event is repeated as long as the contour is closed. The photo, which is taken by a digital camera oblique to the laser beam, is inverted and the pixels inside the contour are counted and multiplied by their area. The time needed to measure one frontal area can be reduced to 8 min, with accuracy remained the same.

With trains one goes without measuring the frontal area; it is *set* to  $10 \text{ m}^2$ .

In the course of developing the body's shape in a wind tunnel numerous shape modifications are carried out. Their geometry has to be documented. While this was formerly performed by taking off hand-made patterns or metering on a measuring plate, today use is

made of photogrammetry and triangulation, as described in detail in [16.53, 54].

Three kinds of tasks have to be performed:

1. static measurement of (many) single points
2. dynamic measurement of (many) single points
3. static measurement of free-formed surfaces.

For the first of these a single (digital) camera is needed. The object, which must be prepared with (at least) three marks, is photographed by hand from several directions. For the second, for instance to measure the lift off of a cabriolet's roof (*ballooning*), two cameras, mounted on a common console, are needed. For the third case two cameras are also needed. In addition, a projector, which is located between the cameras on the same console, projects a grid onto the object.

The registration of the surface data of a complete model at a scale of 1 : 4 can be done in 20–30 min, while for a full-scale model 3 h are needed. The accuracy is  $\pm 0.1 \text{ mm}$ .

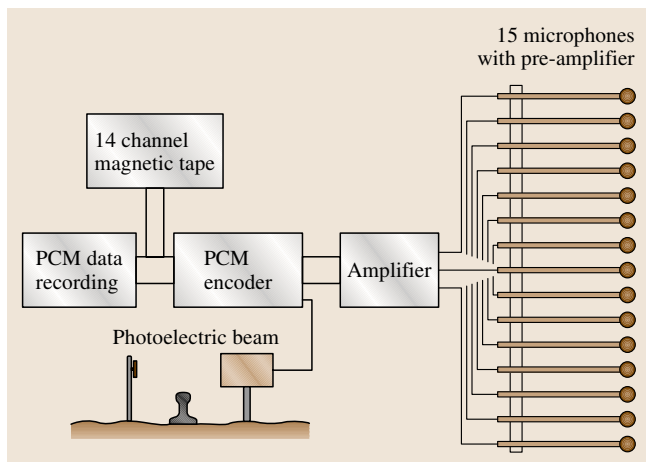
### 16.1.10 Support by Computational Fluid Dynamics

To a large extent aerodynamic development work is based on empiricism. This is all the more relevant for optimizing the shape of a vehicle, a process which is performed by *trial and error*. All the information you get after a shape modification is a set of six coefficients. If, for instance,  $c_D$  was reduced, you will continue to modify the shape in the same direction. If not, you take the previous modification back and try your luck at another location. In neither case do you obtain information about *why* the shape change had a positive or negative effect on the flow.

Deeper insight into the flow physics can be gained by performing detailed measurements in the flow field, for instance a wake traverse, as shown with Fig. 16.48. However, this kind of measurement is a rare exception; time does not allow its performance very often.

In this situation computational fluid dynamics (CFD) is gaining importance. Once the basic equations are solved you can get almost any information you want – velocity vectors, pressure, shear stress, separation of flow and reattachment – throughout the entire space simply by appropriate postprocessing. All this information can be used as a rationale for the next stage of shape modification.

A survey of the related state of the art of CFD in vehicle aerodynamics was recently given in [16.55].



**Fig. 16.65** Microphone array (after [16.51])



## 16.2 Short-Duration Testing of High Enthalpy, High Pressure, Hypersonic Flows

In hypervelocity flows the speed of the considered fluid is much larger than the speed of sound. Commonly the hypersonic flow regime is considered to start above a Mach number of  $M = 5$ . Ground-based testing of such flows is performed in many different types of facilities. The reason for this is the large range of flow conditions and phenomena encountered in hypersonic flight and the fact that no single facility can simulate all relevant flow parameters simultaneously. Therefore, in hypersonic testing, partial simulation of the complete flow situation concentrating on selected flow phenomena are performed in different types of facilities. Examples are Mach–Reynolds number simulation in cold hypersonic ground-based test facilities, verification and qualification of hot structures of space vehicles in arc-heated test facilities, and the investigation of the influence of the chemically reacting flow past an entry or re-entry vehicle on its aerodynamic behavior in shock tunnels or shock expansion tunnels. Comprehensive overviews of ground-based testing of hypersonic flows are given by, e.g., *Lukasiewicz* [16.56], and *Lu and Marren* [16.57].

One possibility to increase the Mach number in ground-based facilities is by reducing the free-stream temperature, i. e., the free-stream speed of sound. In this case, high Mach numbers can be achieved while the free stream velocity is significantly lower than the actual flight velocity. However, characteristic of high-Mach-number hypersonic flight with  $M \approx 10$  and higher is that the kinetic energy of the flow is large enough that high-temperature effects such as vibrational excitation or dissociation of the fluid molecules occur in the flow past hypersonic vehicles. For such hypersonic, high-velocity flows the term hypervelocity flow is used. The high flow velocities and subsequently the high-temperature effects are not duplicated in cold hypersonic ground-based test facilities. During the re-entry flight of a space vehicle in the Earth's atmosphere or the interplanetary atmospheric entry of space vehicles or meteorites, speeds in excess of 6 km/s are achieved. Considering a flow with this speed in a test section with an area of 1 m<sup>2</sup> and a density of 0.003 kg/m<sup>3</sup>, a power requirement of 300 MW already results. Therefore, continuous flow facilities are not a practical way to generate such high-enthalpy, hypersonic flows. Additionally, the correct simulation in ground-based testing of the chemical relaxation length of the dissociation reactions of the fluid molecules occurring, for example, behind the strong bow shock in front of the nose of a re-entry vehicle, requires the duplica-

tion of the flight binary scaling parameter, the product of the free-stream density  $\rho$  and a characteristic flow length  $L$  [16.58]. Consequently, the smaller the scale of the wind tunnel model is chosen, the higher the free-stream density or pressure needs to be. Considering that the flight trajectory range of a re-entry vehicle from low Earth orbit in about 70 km altitude, where the highest heat flux typically occurs, the atmospheric density is approximately 10<sup>-4</sup> kg/m<sup>3</sup>. Using a geometrical scaling factor of 30, a free-stream density in the ground-based facility of 0.003 kg/m<sup>3</sup> is required. If a flow with this free-stream density and a velocity of 6 km/s is generated by expansion in a convergent–divergent hypersonic nozzle from a reservoir at rest without adding energy, a total specific enthalpy of about 23 MJ/kg and a nozzle reservoir pressure on the order of 90 MPa is required. This results in a nozzle reservoir temperature of about 10 000 K. It is clear that such conditions can only be achieved in impulse facilities with short flow duration. The most successful types of facility that are able to generate high-enthalpy and high-pressure hypersonic flows are shock tunnels and shock expansion tunnels with typical test times of approximately 5 ms and less. The principle of these facilities is to store the energy over a long period of time, therefore reducing the necessary power requirement and subsequently releasing the stored energy rapidly. Due to the high flow speeds, test times on the order of a few ms are still sufficient for the development of a steady flow over a model. According to *Hornung* [16.59], a reasonable, conservative correlation of the necessary test time to establish a steady flow is

$$\tau = 20 \frac{L}{U_{\infty}},$$

where  $L$  is the model length and  $U_{\infty}$  is the free-stream velocity. For a test using the aforementioned flow condition and a 0.3 m-long wind tunnel model, the required test time would be 1 ms. The high-pressure, high-velocity flows that can be generated in shock tunnels and shock expansion tunnels make these facilities not only suitable for the investigation of space vehicle aerothermodynamics but also for studying complete air-breathing propulsion systems, particularly supersonic combustion ramjets (scramjets) at flight Mach numbers of  $M_{\infty} = 8$  and above.

In the present chapter, the basic working principle of different types of shock tunnels and shock expansion tunnels, the special aspects of measurement techniques

in such short-duration facilities with test times of approximately 5 ms and less and some selected typical applications in existing facilities will be discussed. In the different types of facilities discussed here, the wind tunnel model is stationary, i. e., it is not moving. So-called hypervelocity range facilities in which the model is free flying at high speeds or combinations of hypervelocity range facilities and, e.g., shock tunnel facilities, so-called counterflow range facilities are not discussed here. Details of these facilities can be found, e.g., in [16.56,57].

16.2.1 Working Principle of Shock Tubes/Tunnels and Shock Expansion Tubes/Tunnels

Basic Principle of Ideal Shock Tubes

The basic layout of a diaphragm-driven shock tube is shown in Fig. 16.66. It consists of two chambers of equal and constant cross section separated by a diaphragm. Both chambers are filled with gases at different conditions  $p_4, T_4, m_4, \gamma_4$  and  $p_1, T_1, m_1, \gamma_1$ , where  $p$  is the pressure,  $T$  the temperature,  $m$  the molecular weight and  $\gamma$  the ratio of specific heats. Initially the gases are at rest in both chambers. As a convention for the present discussion of shock and shock expansion tubes and tunnels, the left section is called the driver or high-pressure section, containing the driver gas, and the right part the driven or low-pressure section, containing the test gas. After instantaneous removal of the diaphragm, a shock wave is moving into the driven section and the head of a centered expansion wave is moving into the high-pressure region.

In 1860, this basic principle of shock tubes was investigated theoretically by the mathematician Bernhard Riemann in Göttingen, Germany [16.60]. The first practical application of a diaphragm-driven shock tube was performed in 1899 by Paul Vieille in Paris, France, studying the establishment and propagation of discontinuous waves in columns of air traveling faster than the speed of sound [16.61]. In Vieille’s shock tube with a length of 6 m and a diameter of 22 mm, shock wave speeds of up to 600 m/s were measured by expanding pressurized air from 2.74 MPa to atmospheric pressure using diaphragms of paper or collodion sheets.



Fig. 16.66 Schematic layout of a diaphragm-driven shock tube

The measured propagation speeds agreed well with ideal shock tube theory.

After this first application of a shock tube this efficient apparatus was more or less forgotten until about 40 years later. Since the 1940s, shock tubes have been extensively used for investigations related to gas dynamical phenomena such as shock wave propagation, shock wave reflection at obstacles or shock wave refraction at contact surfaces, research of detonation waves, studies related to aerodynamics, aerothermodynamics, determination of the physical and chemical kinetics properties of high-temperature gases and applications in laser technique, medicine or calibration of fast acting measurement gauges. Descriptions of their working principle and discussions of shock tube applications are given by, e.g., Lukasiewicz [16.62], Glass and Hall [16.63], Oertel [16.64], Lukasiewicz [16.56], Anfimov [16.65] or Takayama [16.66].

The flow field developing after diaphragm removal in the vicinity of the diaphragm location, i. e., when the waves have not yet reached the left and right boundary, is shown in an  $x-t$  wave diagram (Fig. 16.67), where  $x$  is the streamwise coordinate with its origin at the position of the diaphragm location, and  $t$  is the time with  $t = 0$  at diaphragm rupture. The solution of this Riemann or shock tube problem can be obtained as an exact solution of the one-dimensional, time-dependent Euler equations for thermally and calorically perfect gases. A discussion of this solution is given, e.g., by Sod [16.67] in connection with the investigation of different finite-difference methods for the numerical solution of systems of nonlinear, hyperbolic conservation laws. It is interesting to note in this context that the approximate solution of Riemann problems with generalized initial conditions on either side of the grid cell interfaces (or diaphragm in the context of shock tubes) are a core element of many modern

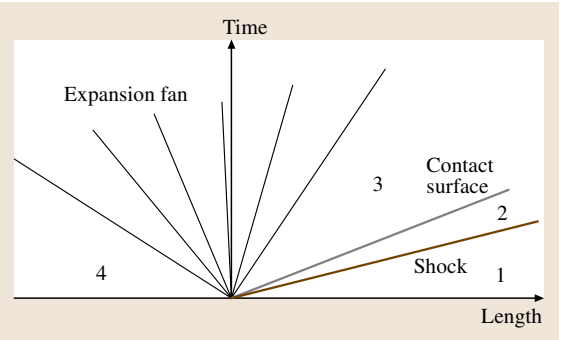


Fig. 16.67 Wave ( $x-t$ ) diagram of the flow developing in a constant-area shock tube

upwind computational fluid dynamics schemes [16.68]. These schemes are based on a numerical method applying the exact solution of the Riemann problem at the cell interface developed by *Godunov* [16.69]. The numbers used in Figs. 16.66 and 16.67 denote distinct regions of the flow. Region 2 contains the shock compressed test gas, while in region 3 the driver gas processed by the unsteady expansion wave is contained. The test and driver gas are separated by a contact surface.

The initial filling conditions of the driver and driven section uniquely define the properties of the developing unsteady expansion and shock wave. The pressure and velocity obtained in region 3 by expansion of the driver gas is given by e.g. [16.70]

$$\frac{u_3}{a_1} = \frac{a_4}{a_1} \left( \frac{2}{\gamma_4 - 1} \right) \left[ 1 - \left( \frac{p_3}{p_1} \frac{p_1}{p_4} \right)^{(\gamma_4 - 1)/2\gamma_4} \right].$$

In order subsequently to generate a graphical solution of the shock tube flow, the pressure and speed of sound in regions 3 and 4 are nondimensionalized with their respective quantities in region 1. The velocity in region 3 is normalized by the speed of sound in region 1,  $a_1$ . A graphical interpretation of this relation is plotted in the left part of Fig. 16.68 for  $p_4/p_1 = 1000$  and different speed of sound ratios  $a_4/a_1$  and  $\gamma_4 = 1.4$ . The pressure and velocity obtained in region 2 by shock compression of the test gas can be obtained by the relation

$$\frac{u_2}{a_1} = \frac{1}{\gamma_1} \left( \frac{p_2}{p_1} - 1 \right) \left( \frac{\frac{2\gamma_1}{\gamma_1 + 1}}{\frac{p_2}{p_1} + \frac{\gamma_1 - 1}{\gamma_1 + 1}} \right)^{1/2}.$$

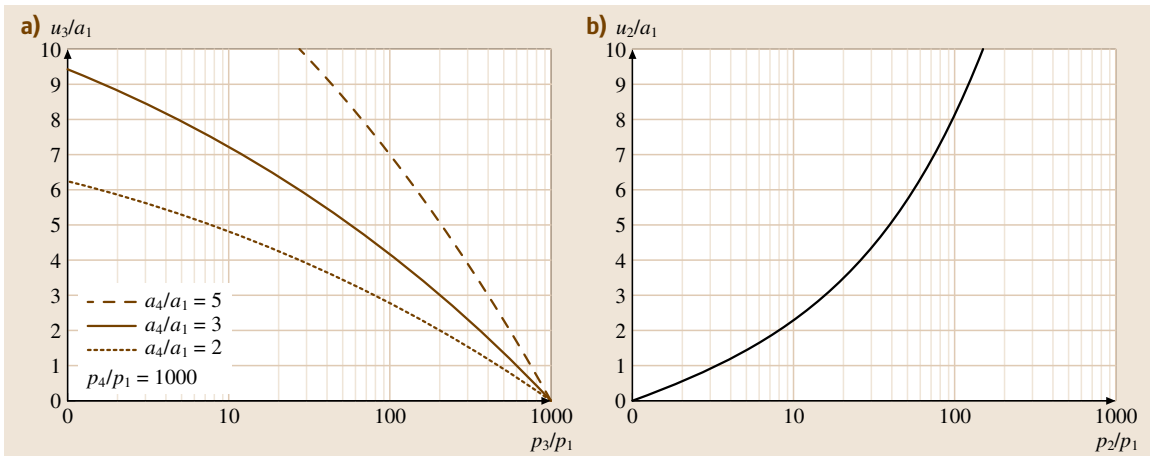
This relation is plotted in the right part of Fig. 16.68. At the contact surface in Fig. 16.67 the conditions  $p_2 = p_3$  and  $u_2 = u_3$  must be fulfilled. Combining these boundary conditions with the above two equations results in the relation

$$\frac{p_4}{p_1} = \frac{p}{p_1} \left( 1 - \frac{(\gamma_4 - 1) \left( \frac{a_1}{a_4} \right) \left( \frac{p}{p_1 - 1} \right)}{\sqrt{2\gamma_1 \left[ 2\gamma_1 + (\gamma_1 + 1) \left( \frac{p}{p_1 - 1} \right) \right]}} \right)^{-2 \frac{\gamma_4}{(\gamma_4 - 1)}}.$$

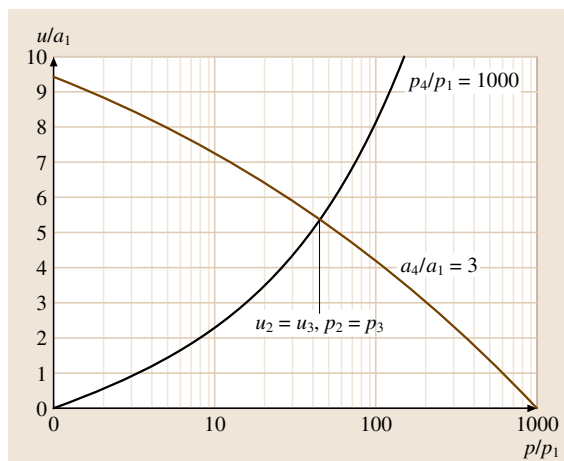
Graphically, the solution of the shock tube problem can be obtained by the point of intersection of the curve in the right part of Fig. 16.68 with one of the curves in the left part of the same figure. This is shown in Fig. 16.69 using  $a_4/a_1 = 3$ .

The velocity, temperature, density, and pressure distribution of the flow in a constant-area shock tube at a point in time after diaphragm rupture is shown in Fig. 16.70. The position of the incident shock, contact surface, and head of the unsteady expansion wave are denoted by  $a$ ,  $b$  and  $c$ , respectively. It can be seen that the pressure and velocity distributions are continuous at the contact surface while the temperature and density show a discontinuity.

After reflection of the incident shock wave at the right end wall of the shock tube, the test gas is brought to rest in region 0 (Fig. 16.71). Subsequently, the reflected shock wave penetrates the contact surface. Depending on the local conditions, three types

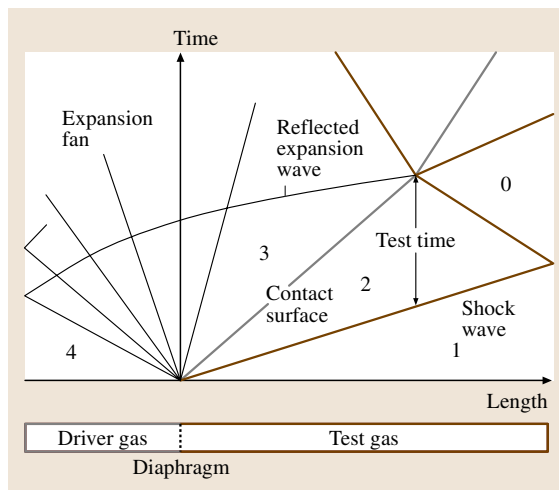


**Fig. 16.68a,b** Determination of the pressure and velocity in region 3 by separate consideration of processing the driver gas in region 4 by the unsteady expansion for different ratios of  $a_4/a_1 = \sqrt{T_4/T_1}$  (a) and compression of the test gas in region 1 by the shock wave (b);  $p_4/p_1 = 1000$  and  $\gamma_4 = \gamma_1 = 1.4$



**Fig. 16.69** Determination of the pressure and velocity in region 3 with  $u_2 = u_3$ ,  $p_2 = p_3$  at the contact surface;  $a_4/a_1 = 3$

of shock wave/contact surface interaction can be differentiated. If  $p_0/p_2 = p_5/p_3$  the reflected shock wave penetrates the contact surface without reflection, and the contact surface is brought to rest. This case is called a tailored interface condition, and the pressure remains constant in region 0 (Fig. 16.72). If  $p_0/p_2 > p_5/p_3$  the undertailored interface condition is obtained, and an expansion wave is generated which lowers the pressure in region 0. For the case of an overtailored

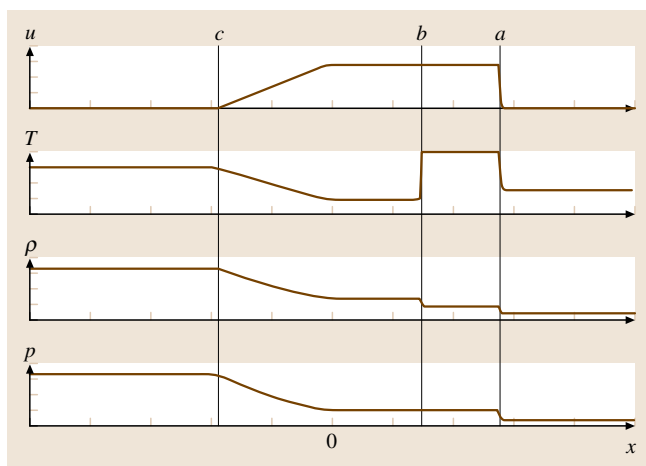


**Fig. 16.71** Wave ( $x-t$ ) diagram of the flow in a constant area shock tube after the expansion wave and the incident shock wave were reflected at the end walls

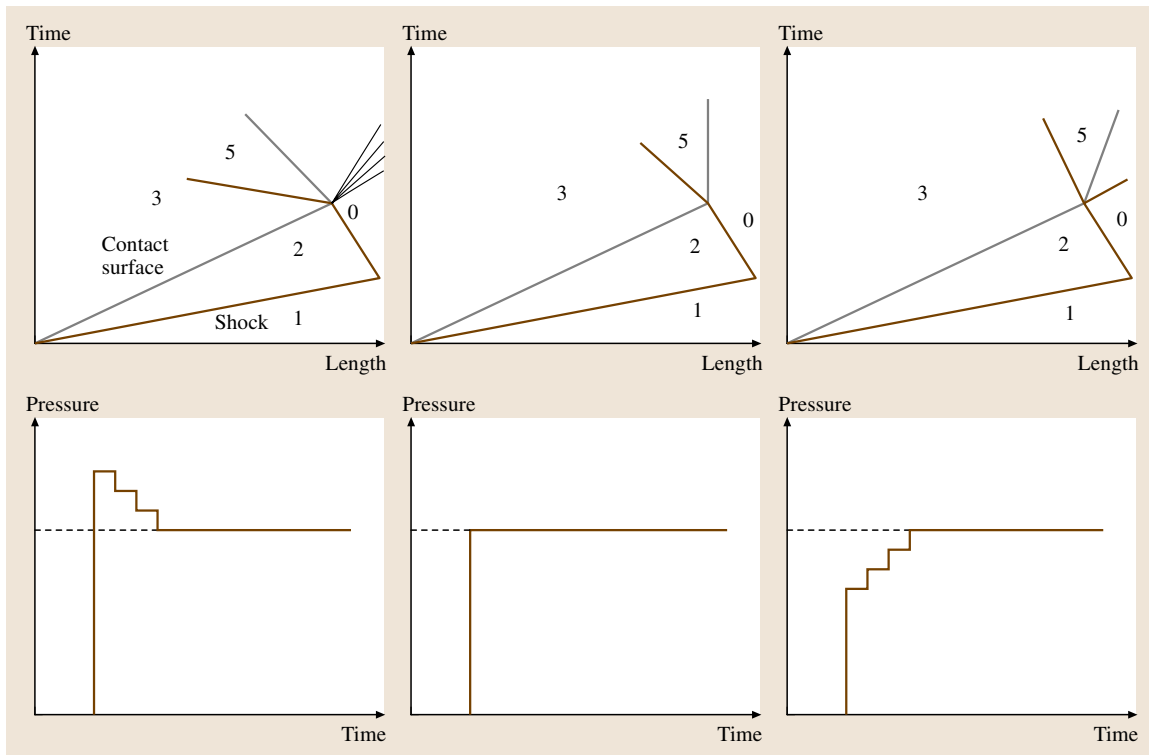
interface condition ( $p_0/p_2 < p_5/p_3$ ), a shock wave propagates into region 0, increasing the pressure in region 0. Due to the fact that the shock compressed and heated slug of gas in region 0 is used in shock tube research for, e.g., the determination of physical or chemical kinetics properties of high-temperature gases or in reflected shock tunnel operation as the reservoir driving the flow in the nozzle and test section, shock tube operation in tailored interface mode is most desirable.

For a given driver section condition, a tailored interface condition can only be obtained for one particular driven section filling condition. For this reason different types of driver gas conditions and driver gas mixtures are used to achieve tailored interface conditions for different stagnation enthalpies [16.56].

The head of the unsteady expansion wave is reflected at the left wall of the driver section and is subsequently accelerated by interaction with the centered expansion wave (Fig. 16.71). Due to the fact that the head of the reflected expansion wave has a higher velocity than the incident shock wave, the lengths of the driver and driven sections must be chosen such that the arrival of the reflected expansion at the end of the shock tube is delayed as much as possible. If for example the shock processed gas contained between the shock and the contact surface is used as test flow, the reflected expansion wave should not intersect with the reflected shock wave before this intersects with the contact surface. In this way, the nominally available



**Fig. 16.70** Velocity, temperature, density, and pressure distribution of the flow in a constant-area shock tube at a constant point in time after diaphragm rupture; position of the incident shock wave (a), contact surface (b), and head of the unsteady expansion wave (c)



**Fig. 16.72** Shock wave/contact surface interactions for undertailored (*left*), tailored (*middle*) and overtailored (*right*) interface condition; wave ( $x$ - $t$ ) diagram (*upper row*) and time history of pressure in region 0 (*lower row*)

time of constant flow conditions in region 2 can be maximized.

### Shock Tunnels – Ideal Operation

If air is used as the test gas, the flow generated in shock tubes in region 2 can be used to duplicate stagnation enthalpies and pressures that occur during the re-entry flight of a space vehicle [16.56]. However, the Mach number is limited to  $M \approx 3$ . To overcome this limitation and to be able to generate hypersonic flows, the shock tunnel was proposed by *Hertzberg* [16.71]. Since then, many types of shock tunnels have been developed and are operated in laboratories around the world. Overviews of the facilities and their application can be found in, e.g. [16.64, 72, 73]. The basic principles of the two different ways of shock tunnel operation, the straight-through shock tunnel and the reflected shock tunnel will be discussed in the subsequent sections.

**Straight-Through Shock Tunnel Operation.** The basic layout and wave diagram of a shock tunnel operating in

straight-through mode are shown in Fig. 16.73. At the end of the shock tube, a divergent nozzle is attached, in which the supersonic flow behind the incident shock is accelerated to hypersonic Mach numbers. The time increment to start the nozzle is reduced by initial evacuation of the nozzle and test section. For this reason, a secondary, thin diaphragm is placed at the end of the shock tube. The steady test flow is established in the test section after the incident shock wave, a contact surface and a system of waves has reached the nozzle exit. The wave traveling with the local velocity  $u + a$  is an upstream facing wave that is initiated by a mismatch of the post incident shock wave condition and the condition generated by the nozzle expansion. Due to the fact that this wave is moving into a supersonic flow, it is swept downstream. The test time is finished after the  $u + a$  wave generated by the arrival of the shock tube contact surface or the reflected expansion wave reaches the nozzle exit. In Fig. 16.73, the length of the facility has been chosen such that both waves reach the nozzle entrance at the same time. In their study and utilization of a straight-through shock tunnel *Stalker* and *Mud-*



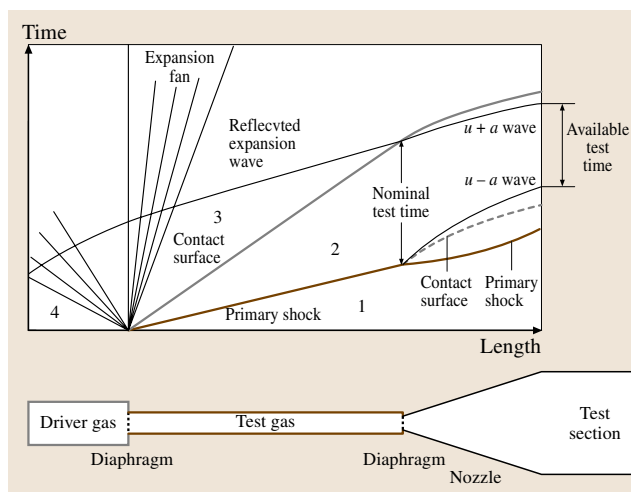


Fig. 16.73 Wave diagram for a straight-through shock tunnel

ford [16.74] obtain test times in the order of  $10 \mu\text{s}$ . More details concerning the straight-through shock tunnel can be found in, e.g. [16.56, 64].

**Reflected Shock Tunnel Operation.** The reflected shock tunnel is characterized by a convergent–divergent nozzle that is attached to the end of the shock tube. Similar to the straight-through shock tunnel, a thin secondary diaphragm is placed at the nozzle entrance in order to allow evacuation of the nozzle, test section and vacuum tank before the run. The nozzle entrance diameter is cho-

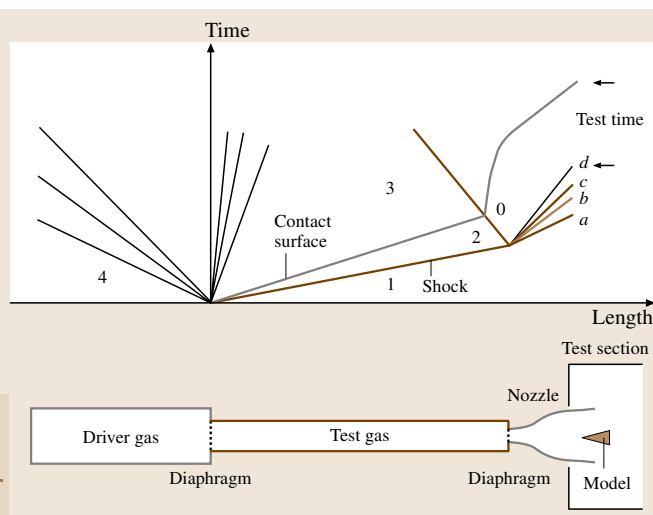


Fig. 16.74 Schematic and wave ( $x$ – $t$ ) diagram for a reflected shock tunnel

sen sufficiently small such that the incident shock wave is almost completely reflected, compressing and heating the test gas again. The stagnant slug of test gas, generated by the shock reflection, is subsequently expanded through the hypersonic nozzle. The principal layout and wave diagram of a reflected shock tunnel are shown in Fig. 16.74. In contrast to the shock tunnel and shock tube configurations discussed above, the facility sketched in Fig. 16.74 has different driver section and driven section diameters. This area change at the driver–driven tube intersection generates a steady expansion until the condition  $M = 1$  is reached at the throat section followed by an unsteady expansion wave. For a given pressure difference between the driver and driven section, a steady expansion provides a higher velocity increase in subsonic flow than an unsteady expansion [16.56, 75]. In supersonic flow the opposite applies. Therefore, the area change is a means of improving the shock tube and shock tunnel performance.

For an ideal shock tube performance, i. e., not considering effects such as viscosity or multidimensional flows, the test flow quality and resulting test time depends on several aspects. The first is the wave pattern that is obtained when the reflected shock intersects with the contact surface. Based on the discussion on basic principles of ideal shock tubes, it is clear that the shock tunnel operation should be tuned in such a way that a tailored interface condition is obtained, resulting in a nozzle reservoir with constant conditions. Further, the shock tunnel geometry should be chosen such that the reflected expansion wave does not reach the nozzle entrance before the contact surface. An additional flow feature that influences the available test time is the nozzle starting process. Similar to the flow establishment in the divergent nozzle of the straight-through shock tunnel, a wave system has to pass through the nozzle before a steady flow is established. This process was studied by a quasi-one-dimensional analysis by Smith [16.76]. The waves resulting from this analysis are shown in Fig. 16.74. The incident shock wave ( $a$ ) is followed by a contact surface ( $b$ ), an upstream-facing secondary shock wave ( $c$ ), and the upstream head of an unsteady expansion ( $d$ ). Compared to the straight-through mode, significantly larger test times of the order of several ms can be achieved with a reflected shock tunnel.

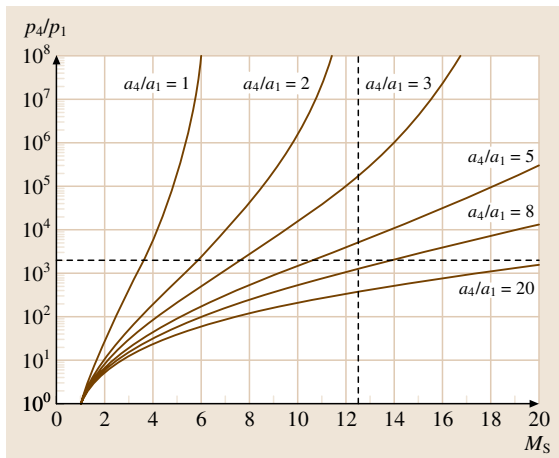
**Techniques for Total Specific Enthalpy Augmentation in Reflected Shock Tunnels.** For reflected shock tunnels, a good approximation to the total specific enthalpy of the nozzle reservoir condition is given by

$h_0 = u_S^2$ , where  $u_S$  denotes the speed of the incident shock wave [16.59]. Introducing the shock Mach number  $M_S$  and still assuming that the gases are thermally and calorically perfect, the relation between the initial pressure and speed of sound ratio between the driver and driven section reads:

$$\frac{p_4}{p_1} = \frac{2 \cdot \gamma_1 \cdot M_S^2 - (\gamma_1 - 1)}{\gamma_1 + 1} \times \left[ 1 - \frac{\gamma_4 - 1}{\gamma_1 + 1} \cdot \frac{a_1}{a_4} \cdot \left( M_S - \frac{1}{M_S} \right) \right]^{-\frac{2\gamma_4}{\gamma_4 - 1}}.$$

This correlation is plotted in Fig. 16.75. Considering high-enthalpy flows, as a first approximation, the total specific enthalpy is approximately equal to the kinetic energy of the flow. Assuming the case that an air flow in the test section with a velocity of  $u_\infty = 6 \text{ km/s}$  should be generated, a total specific enthalpy of  $18 \text{ MJ/kg}$  ( $h_0 \approx 0.5u_\infty^2$ ) would be required. Due to practical reasons, air at room temperature is used in the driven section of reflected shock tunnels and consequently an approximate shock wave speed of  $4.2 \text{ km/s}$  and a shock Mach number of  $M_S = 12.5$  results. According to Fig. 16.75, using a pressure ratio of  $p_4/p_1 = 2000$ , this shock Mach number requires a ratio of speeds of sound of about  $a_4/a_1 = 8$ .

When increasing the shock Mach number in air such that the post-shock temperature exceeds an approximate value of  $800 \text{ K}$ , inner degrees of freedom of the test gas molecules are excited and, at temperatures above



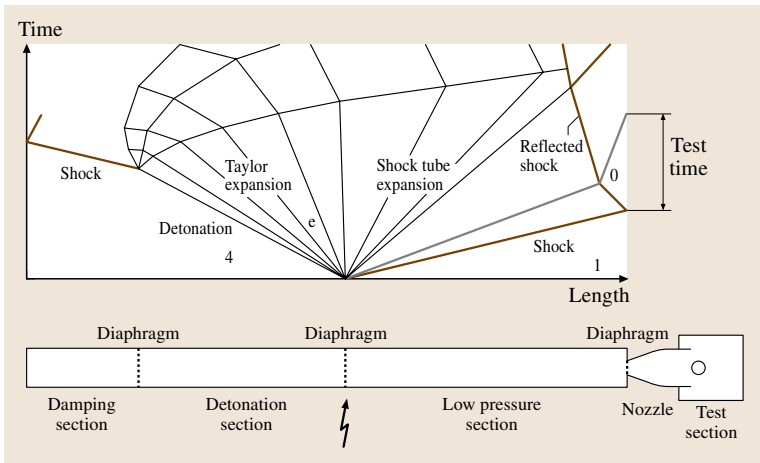
**Fig. 16.75** Shock Mach number  $M_S$  as a function of  $p_4/p_1$  and  $a_4/a_1$  for a perfect monatomic driver ( $\gamma_4 = 5/3$ ) and diatomic test gases ( $\gamma_1 = 1.4$ )

approximately  $2500 \text{ K}$ , oxygen molecules start to dissociate. Therefore, the assumption of a constant specific heat ratio is no longer valid. The influences of these high-temperature effects must be considered for the design and performance prediction of shock tunnels and they will be addressed later. Here the discussion is restricted to reveal basic dependencies.

A high ratio of  $a_4/a_1$ , i.e., a high value of  $a_4$  ( $a_1$  is fixed by the choice of using air at room temperature as test gas) can be obtained by reducing the molecular weight  $m_4$  or by increasing the temperature of the driver gas. The first point is fulfilled by using hydrogen or helium as the driver gas. With this choice of driver gas, in conventional reflected shock tunnels, a ratio of  $a_4/a_1 \approx 3$  can be achieved. The second way to increase the speed of sound ratio requires heating of the driver gas. Several heating techniques to increase the incident shock Mach number and the stagnation enthalpy have been developed and will be presented in the subsequent sections.

**Electrically Heated Shock Tunnels.** The driver gas can be heated by external or internal electrical resistance heaters. External heaters can be used to heat a light driver gas up to a temperature of  $800 \text{ K}$ . Using helium, this results in  $a_4/a_1 \approx 5$ , for hydrogen  $a_4/a_1 \approx 6.2$ . External heating must be applied over a long period of time and is limited by the material strength behavior of the high-pressure driver tube with increasing temperature. For this reason internal heaters with heating duration of about one minute were applied to minimize the tube heating [16.56]. Examples of electrically heated shock tunnels are the **LENS I** facility at the Calspan-UB Research Center Buffalo, New York, USA [16.77] and the Aachen shock tunnel TH2 at the Rheinisch-Westfälische Technische Hochschule (RWTH) Aachen University, Germany [16.78]. For the **LENS I** tunnel, test section velocities of up to  $5 \text{ km/s}$  ( $h_0 \approx 14 \text{ MJ/kg}$ ) using a hydrogen driver and in TH2 velocities of up to  $3.6 \text{ km/s}$  ( $h_0 \approx 7 \text{ MJ/kg}$ ) using helium as driver gas are reported.

**Deflagrative Combustion Driven Shock Tunnels.** In deflagrative combustion-driven shock tunnels, a stoichiometric mixture of hydrogen and oxygen diluted by helium or a helium–nitrogen mixture is utilized to create a hot driver gas [16.79]. The amount of helium dilution of the hydrogen–oxygen mixture is on the order of 70% by volume. An example of this type of facility is the 16-Inch Shock Tunnel of the National Aeronautics and Space Administration (**NASA**) Ames Research Center [16.80]. In this facility the combustion is initiated by wires extending over the length of

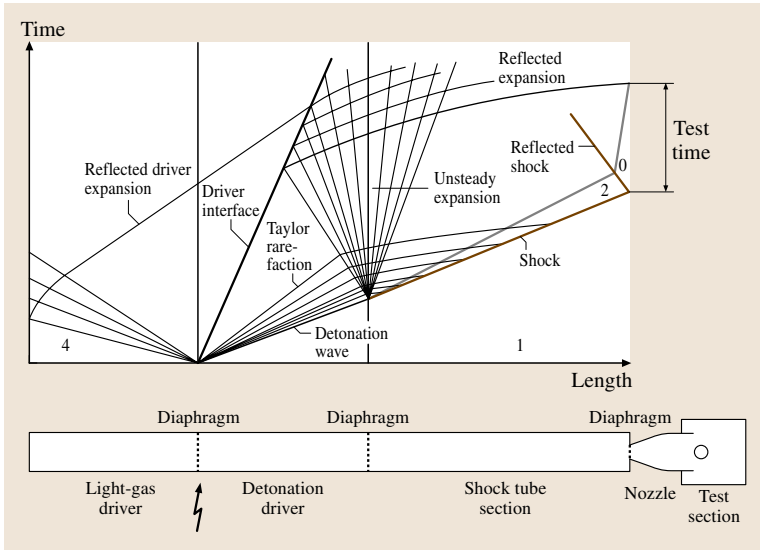


**Fig. 16.76** Schematic and wave ( $x-t$ ) diagram of a detonative combustion-driven shock tunnel operated in backward or upstream propagation mode including damping section

the driver section and heated by the discharge of a capacitor bank. The subsequent deflagrative combustion raises the pressure and temperature in the driver gas. For this facility, which has been applied to hypersonic air-breathing propulsion research, shock Mach numbers of  $M_s \approx 10$  and total specific enthalpies of  $h_0 \approx 12$  MJ/kg at nozzle reservoir pressures of  $p_0 \approx 350$  bar have been reported [16.81]. In principle, the performance capability of deflagrative combustion driven shock tunnel exceeds that of electrically heated shock tunnels and detonative combustion-driven shock tunnels [16.82]. However, in the high-enthalpy regime the true performance of this type of facility is unknown and a limitation concerning the achievable driver pressure exists because

for driver operating conditions with post-combustion pressures higher than about 400 bar, deflagrative combustion is difficult to maintain and local detonations may occur that could result in large driver pressure fluctuations [16.79].

**Detonative Combustion-Driven Shock Tunnels.** In detonative combustion-driven shock tunnels, the conventional driver is replaced by a detonation section that is filled with a gaseous reactive mixture. Typically, stoichiometric mixtures of oxygen and hydrogen are used as the driver gas, with dilution by helium or argon. Two main principles are applied in detonative combustion-driven shock tunnels. These are the back-



**Fig. 16.77** Schematic and wave ( $x-t$ ) diagram of a detonative combustion-driven shock tunnel operated in forward or downstream propagation mode including a shock-induced detonation technique

ward (or upstream) and the forward (or downstream) propagation mode [16.83]. The schematic and wave diagram of a detonative combustion-driven shock tunnel operated in backward or upstream mode is shown in Fig. 16.76. The detonation is initiated at the location of the main diaphragm and it moves backward, i.e., upstream toward the left end wall of the driver section. The flow velocity behind the detonation is directed in the same direction as the detonation wave. Due to the Taylor expansion that follows the detonation, the burnt driver gas is decelerated and brought to rest. This quasi-steady driver condition, obtained behind the characteristic labeled (e) in Fig. 16.76, acts similar to a high-temperature driver of a conventional shock tunnel and the wave processes in the driven section and the nozzle develop as discussed before. At the left end of the driver section, a damping section is added. This section is filled with low-pressure nitrogen. Initially, the detonation section is separated from the damping section by a thin diaphragm. After reaching the damping section, the detonation is converted into a shock wave, which attenuates in the damping section and is subsequently reflected at the end wall. The addition of this section is necessary in order to avoid the high mechanical loads on the tube when the detonation wave would be reflected at the end of the detonation section [16.83]. At the driver–damping section interface a rarefaction wave is generated that moves downstream and finally interacts with the reflected shock wave in the driven section (Fig. 16.76).

In the forward (or downstream) propagation mode, the detonation is initiated at the upstream end of the detonation section as indicated in Fig. 16.77 [16.84]. For the discussion of the basic working principle of the downstream propagation mode, the light gas driver shown in Fig. 16.77 should be ignored. After initiation, the burnt gas and the detonation wave move downstream towards the main diaphragm. As the detonation wave hits the main diaphragm, the hot accelerated combustion products, which yield an effective unsteady driver condition, drive the incident shock wave in the shock tube [16.84]. In the downstream propagation mode, the incident shock wave is attenuated by interaction with the Taylor expansion following the detonation wave, leading to unsteady flow conditions in the nozzle reservoir if a facility operation as sketched in Fig. 16.77 is used.

Due to the fact that with the forward propagation mode the kinetic energy behind the detonation wave can be used to drive the incident shock wave, higher shock Mach numbers can be achieved with this mode compared to the backward mode, where the driver gas is

first accelerated toward the left end of the driver section thereby wasting some of the chemical energy of the detonation. This potential performance gain in the forward mode resulted in the development of different techniques to reduce and control the extent of the rarefaction caused by the Taylor expansion. The shock-induced detonation technique for example utilizes a light driver gas attached at the upstream end of the detonation section as shown in Fig. 16.77 [16.79]. This additional driver is used to generate a shock wave in the combustible driver gas mixture that subsequently initiates the detonation wave. The interface between the light driver gas and the detonation wave processed driver gas acts as a gaseous piston that leads to a higher pressure level behind the detonation wave as would be obtained if the detonation is initiated at a closed end wall. Further means of increasing the performance of tunnels operated in the forward mode are to increase the length of the detonation driver to decrease the flow gradients behind the detonation wave or to generate additional waves in the detonation driver to decrease the effect of the Taylor expansion, e.g., by an area change at the driver–driven section interface or the utilization of a cavity ring or a throat section in the detonation driver [16.83].

Examples of detonative combustion-driven shock tunnels are the TH2-D tunnel of the RWTH Aachen University, Germany, the JF-10 and the BFJ-60 tunnels of the Institute of Mechanics of the Chinese Academy of Sciences, Beijing [16.83] and the HYPULSE facility of the Alliant Techsystems Inc. – General Applied Science Laboratories (ATK–GASL) in Ronkonkoma, USA [16.79]. Using the backward (TH2-D) and forward propagation mode (JF-10), total specific-enthalpy and nozzle reservoir pressure conditions of 14.6 MJ/kg, 220 bar (resulting in a free-stream velocity of 4.9 km/s) and 19.6 MJ/kg, 800 bar respectively, are reported [16.83]. The available test time range is approximately 2–4 ms. According to the relations given in the framework of the discussion of the total specific enthalpy augmentation, these conditions would result in shock Mach numbers of  $M_s \approx 11$  and  $M_s \approx 13$ . Concerning the ratio of the speed of sound in the driver and driven section, an effective value of  $a_4/a_1 \approx 8$  can be achieved with detonative combustion-driven shock tunnels.

**Electric-Arc-Driven Shock Tunnel.** In electric-arc-driven shock tunnels, an electric discharge heats the driver gas hydrogen or helium to temperatures of about 8000 K for hydrogen, and about 20 000 K for helium. As in conventional shock tunnels, the driver gas is separated from the test gas by a diaphragm that bursts due to the rise

in pressure within the driver during the capacitor-bank discharge, initiating the shock tube flow as discussed in previous sections. An example of this type of facility is the Electric Arc Shock Tunnel (EAST) at the NASA Ames Research Center [16.85–87]. The facility can be used in shock tube as well as shock tunnel mode. Due to its ability to generate very strong shock waves in the shock tube – in hydrogen shock wave speeds up to 50 km/s are reported – EAST is used to investigate the effects of radiation and ionization that occur during very high-velocity atmospheric entries such as that performed by the Galileo probe, which entered the atmosphere of the planet Jupiter in 1995.

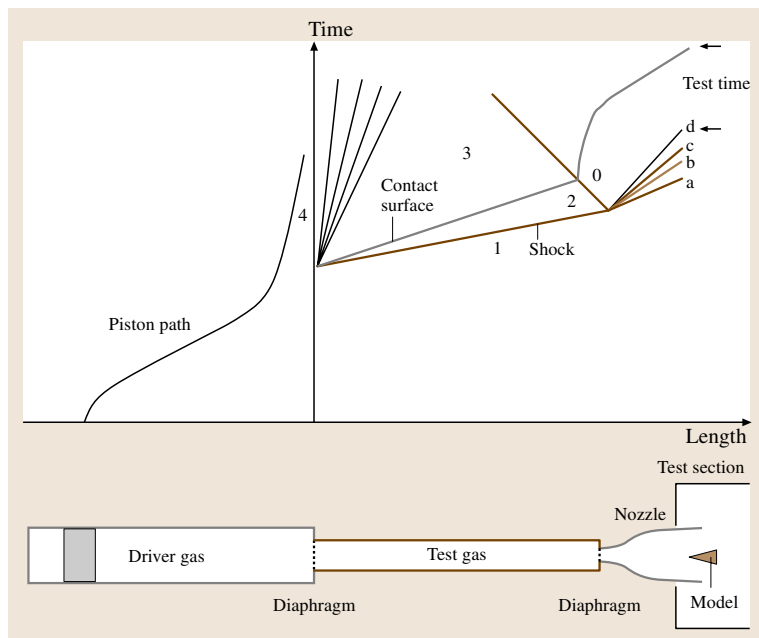
The energy for the electric arc which heats the constant volume driver is supplied by a 1530  $\mu\text{F}$  capacitor bank capable of storing 1.25 MJ when charged to a maximum of 40 kV. The arc, which is generated by the discharge of the capacitor bank through electrodes in the driver section, is contained within an insulated chamber and is initiated by a tungsten wire that extends along the driver. In the first phase of the discharge, the electric current passes mainly through the tungsten wire heating it up. This heat is transferred to the driver gas causing ionization and thereby allowing a portion of the electrical current to pass through the generated plasma. Subsequently, after reaching a temperature of about 4000 K, the tungsten wire explodes and vaporizes and an arc forms in the driver. Approximately 50  $\mu\text{s}$  after the dis-

charge was started, the diaphragm is fully open and the shock tube flow is initiated [16.86]. During the discharge process, a maximum current of approximately 600 kA is reached.

In the shock tunnel mode the EAST shock tube is connected to a 760 mm-diameter test section by a convergent–divergent nozzle. Using nitrogen as the test gas, tailored interface conditions were obtained at  $7 \leq M_s \leq 19$ , resulting in total specific enthalpies of  $7 \text{ MJ/kg} \leq h_0 \leq 40 \text{ MJ/kg}$ . Using helium heated up to 8000 K as the driver gas, this results in  $a_4/a_1 \approx 15$ . The nozzle reservoir pressure varies from 44 bar (40 MJ/kg) to 20 bar (7 MJ/kg). The test time ranges from 0.5 ms at the highest total specific enthalpy to 1.5 ms at the lowest total specific enthalpy [16.85].

Computational investigations of the potential operating conditions of EAST in reflected and straight-through shock tunnel mode using air as test gas show that shock Mach numbers of up to  $M_s \approx 16$  would allow testing at equivalent flight velocities of up to 8700 m/s. For the reflected shock tunnel mode, the nozzle reservoir pressure drops when increasing the total specific enthalpy. In the equivalent flight velocity regime above 5500 m/s it ranges from about 400 bar at 14 MJ/kg to approximately 170 bar at 36 MJ/kg [16.87].

**Free-Piston-Driven Shock Tunnels.** In a free-piston-driven shock tunnel, the conventional driver of a shock



**Fig. 16.78** Schematic and wave ( $x-t$ ) diagram of a free-piston-driven shock tunnel; the waves  $a$ ,  $b$ ,  $c$ , and  $d$  are explained in the section related to reflected shock tunnel operation



tunnel is replaced by a free piston driver. This concept was proposed by *Stalker* [16.88]. A schematic and wave diagram of this type of facility is shown in Fig. 16.78. Free-piston-driven shock tunnels consist of an air buffer, a compression tube, separated from an adjoining shock tube via the primary diaphragm, and a subsequent nozzle, test section and vacuum tank. The high-pressure air stored in the air buffer is utilized to accelerate a heavy piston down the compression tube. During this quasi-adiabatic compression and heating of the light driver gas (typically helium or a helium argon mixture), the piston reaches a maximum velocity in the order of 300 m/s. The driver gas temperature increases with the driver gas volumetric compression ratio. In principle, there is no limit to the compression ratio used and therefore, there is also no limit to the stagnation enthalpy that can be generated [16.73].

When the main diaphragm burst pressure is reached it ruptures and the wave process, as in a conventional reflected shock tunnel, is initiated. The trajectory of the piston is chosen in such a way that, after the main diaphragm rupture, the pressure and temperature of the driver gas is maintained approximately constant. This is achieved by selecting the velocity of the piston at diaphragm rupture, and therefore the subsequent movement of the piston, such that it compensates for the loss of the driver gas flowing into the shock tube. For this reason, in contrast to the constant-volume driver of conventional shock tunnels, the free piston driver is a constant-pressure driver. Due to the large forces occurring during the operation of the free piston driver, the compression tube, shock tube, nozzle assembly is allowed to move freely in the axial direction. An inertial mass placed at the compression tube/shock tube junction can significantly reduce the recoil motion of the facility during operation. The test section and the vacuum tank remain stationary. A sliding seal is used at the nozzle/test section interface. In principle no limit on the achievable stagnation enthalpy exists for free-piston-driven shock tunnels. However, in real facility operation, effects such as contamination of the test gas impose upper limits. Tailored interface operation at shock Mach numbers of  $M_s = 18.5$  in air has been reported [16.73, 88]. This results in a total specific enthalpy of about 40 MJ/kg.

Considering the different types of high-performance shock tunnel drivers, the free-piston technique appears to be the most developed and most distributed. After a series of free-piston-driven shock tunnels, T1–T3 (Australian National University, Canberra), T4 (The University of Queensland, Brisbane) were built in Australia between the early 1960s and the late

1980s [16.73, 89], this type of facility was implemented in a number of different institutions worldwide. The largest ones of these are the T5 at the Graduate Aeronautical Laboratories of the California Institute of Technology, USA [16.90], the High Enthalpy Shock Tunnel Göttingen (HEG) of the German Aerospace Center [16.91] and the High Enthalpy Shock Tunnel (HIEST) of the Japan Aerospace Exploration Agency (JAXA) at Kakuda [16.92]. The latter uses the largest nozzle with an exit diameter of 1200 mm. The maximum stagnation enthalpy used is 25 MJ/kg at a 1500 bar nozzle reservoir pressure, resulting in a test time of 2 ms.

#### Performance Considerations of Real Shock Tunnels.

The deviation from the ideal shock tunnel performance as discussed for the straight-through shock tunnel and for the reflected shock tunnel is caused by various phenomena, e.g. [16.56].

The opening of the main diaphragm has so far been considered as an instantaneous process. However, due to the high pressure ratios  $p_4/p_1$  the diaphragm usually deforms before rupture followed by a gradual opening process of the diaphragm, e.g. [16.64]. Both effects result in an initially two-dimensional flow with a curved shock wave and contact surface. The shock wave propagates across the shock tube, resulting in repeated reflections at the wall and the center line. The interaction of the shock and the reflected waves cause the shock front to become planar within several tube diameters downstream of the diaphragm location. However, the bulging of the diaphragm and the gradual opening causes that the contact surface becomes and stays curved [16.93, 94]. For high initial pressure ratios across the diaphragm, it was found that the measured shock wave speed can exceed the shock speed predicted by one-dimensional model-

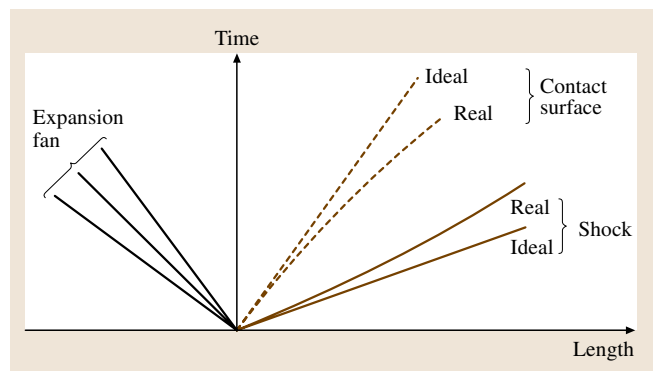
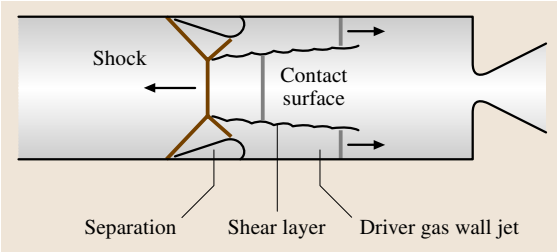


Fig. 16.79 Wave  $x$ - $t$  diagram of shock tube performance for ideal (inviscid) and real (viscous) flow



**Fig. 16.80** Schematic of the reflected shock wave/boundary layer interaction which leads to shock bifurcation and the development of a driver gas wall jet

ing of the ideal shock tube. These higher than ideal shock speeds can be partially explained by the wave processes that occur during the gradual opening of the diaphragm [16.93].

A large impact on the real shock tunnel performance have viscous effects in the shock tube and the hypersonic nozzle. The effects of the growing boundary layer within the shock tube can be explained, for example, by the model developed by Mirels [16.95]. The wall boundary layer developing behind the moving shock acts as a sink that removes mass from the region between the shock wave and the contact surface. This causes deceleration of the shock wave and acceleration of the contact surface (Fig. 16.79). A limiting condition is reached at which the shock wave and the contact surface move at the same speed when the mass flow through the shock wave is equal to the mass flow in the boundary layer past the contact surface. Based on the ideal shock tube performance, the available test time as indicated in Fig. 16.71

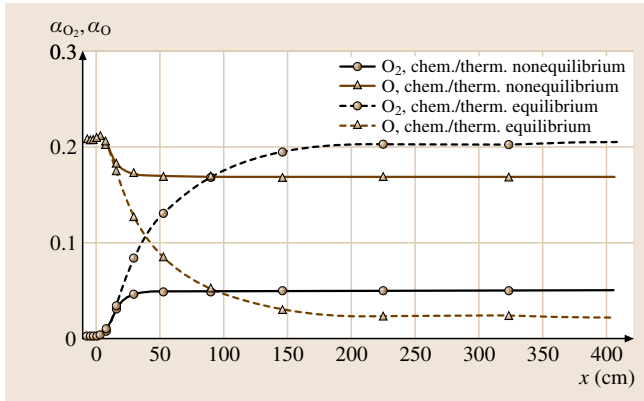
would only depend on the length of the shock tube if the driver would be chosen sufficiently long such that the arrival of the reflected expansion waves is sufficiently delayed. However, the means of gaining test time by extending the shock tube length is limited due to the boundary-layer development.

For reflected shock tunnels, early driver gas contamination is an important issue that is also linked to the viscous flow developing in the shock tube. After reflection of the incident shock wave at the shock tube end wall, it intersects with the shock tube side-wall boundary layer. Due to this shock wave–boundary layer interaction, the reflected shock wave is bifurcated, and when it interacts with the contact surface a wall jet of driver gas is generated (Fig. 16.80), which arrives prematurely at the nozzle entrance where it contaminates the test gas [16.58]. Various devices have been developed to detect the arrival of driver gas in light-gas-driven facilities [16.73]. A discussion of this issue for detonative combustion-driven facilities is given [16.79].

The expansion of the test gas in hypersonic nozzles to high free-stream Mach numbers generates relatively thick boundary layers at the nozzle wall. This needs to be taken into account in the nozzle design process because the effective nozzle area ratio is reduced by viscous effects. Furthermore, the wave pattern dominating the nozzle starting process is influenced by the interaction with the nozzle wall boundary layer and multidimensional flow effects [16.96].

At high shock Mach numbers, the behavior of the test gas air deviates from that of an ideal gas due to the excitation of vibrational degrees of freedom of the molecules and chemical reactions that are generated in the shock heated gas. In the shock tube flow the test gas can be considered as being in thermal and chemical equilibrium. The largest differences between modeling the test gas air in the shock tube as an ideal gas or as a high-temperature equilibrium gas occur at high shock Mach numbers and low shock tube filling pressures. The temperatures in region 2 (behind the incident shock wave) and region 0 (behind the reflected shock wave) are significantly reduced due to the high-temperature effects [16.97].

When operating reflected shock tunnels at high total specific enthalpies, the temperature in the nozzle reservoir can be as high as 10 000 K. If air is used as the test gas the molecular species oxygen and nitrogen are highly dissociated. This high-temperature, high reservoir slug of test gas is subsequently expanded in a convergent–divergent nozzle to hypersonic velocities. In the first



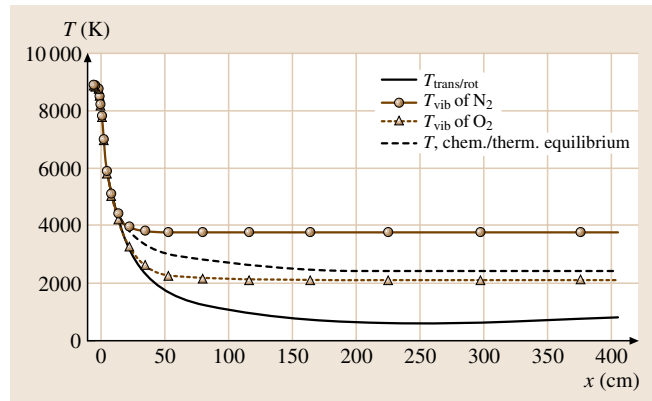
**Fig. 16.81** Computed concentration of molecular and atomic oxygen along the center line of the HEG nozzle; the flow is modeled in chemical and thermal equilibrium as well as nonequilibrium conditions

part of the expansion, the resident time of a particle in a certain flow environment is long enough that the flow remains in thermal and chemical equilibrium. However, with increasing flow velocity a condition is reached that the characteristic time to reach equilibrium is larger than the residence time at the corresponding flow condition. Therefore, the chemical relaxation process, i. e., the recombination of dissociated species freezes. An example of this process is shown in Fig. 16.81 for the High Enthalpy Shock Tunnel Göttingen [16.98]. In this figure, the computed mass fraction of molecular and atomic oxygen is plotted as function of the stream wise direction along the nozzle center line, starting from the nozzle reservoir until the nozzle exit for a high-enthalpy condition. In the nozzle reservoir, the molecular oxygen is fully dissociated. Due to the decreasing temperature in the nozzle expansion, the oxygen atoms recombine. The different flow models assuming the flow in chemical/thermal equilibrium or in chemical/thermal nonequilibrium reveal the freezing point in the nozzle expansion about 25 cm downstream of the nozzle throat. The corresponding translational/rotational temperature and vibrational temperature distributions along the nozzle center line are shown in Fig. 16.82. The applied model to describe the thermal relaxation process shows that similar to the chemical relaxation, the thermal relaxation also freezes approximately 25 cm downstream the nozzle throat. Due to the partly dissociated free-stream flow which is generated in reflected high-enthalpy shock tunnels, the calibration process of these facilities is very complex and the knowledge of the free stream is important for the evaluation of the data obtained in high-enthalpy shock tunnels. An approach that strongly couples detailed diagnostics and computational fluid dynamics tools is required [16.99].

### Shock Expansion Tubes/Tunnels

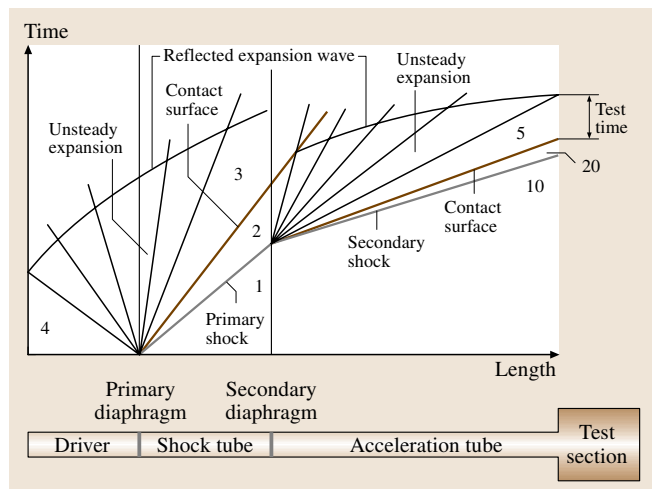
In reflected shock tunnels, the heating of the test gas is performed by the incident and reflected shock wave resulting in very high nozzle reservoir temperatures at high total specific enthalpy operating conditions. In practice this imposes limitations on shock tunnel operation at very high enthalpies. Shock expansion tubes/tunnels [16.100–103] overcome these limitations by avoiding the stagnant flow region in the nozzle reservoir.

The wave  $x-t$  diagram of an ideal shock expansion tube is shown in Fig. 16.83. The set up of this type of facility is similar to a shock tube with the addition of a light secondary diaphragm that separates the driven section into two parts: an intermediate section follow-



**Fig. 16.82** Numerical prediction of the translational/ rotational temperature and vibrational temperatures of molecular nitrogen and oxygen along the nozzle center line of the HEG nozzle resulting from different flow models (chemical and thermal equilibrium and nonequilibrium)

ing the driver section and an acceleration section further downstream. Similar to the shock tube operation, the driver section is initially filled to high pressure with a low-molecular-weight gas such as helium. The shock tube is filled with the desired test gas to a pressure that is generally sub-atmospheric. The acceleration section (region 10 in Fig. 16.83) is filled with the acceleration gas at a lower pressure than the initial filling pressure of the shock tube. Typically, the same gas is used in both the shock tube and acceleration section. The flow is initiated by bursting the primary diaphragm leading to the wave processes as discussed in Sect. 16.2.1. Upon strik-



**Fig. 16.83** Wave  $x-t$  diagram of an ideal shock expansion tube

ing and rupturing the secondary diaphragm, the incident (primary) shock wave acquires a higher Mach number as it enters the acceleration section (secondary shock wave) generating the flow in region 20. In order to equilibrate the pressure and velocity from region 2 to 20 an unsteady expansion is generated that accelerates the test gas of region 2 to the high velocity in region 5. The test section is located at the exit of the acceleration section. The available test time is the period between the arrival of the acceleration gas/test gas interface and the first wave that disrupts the uniform test flow. This can be caused by the arrival of the tail of the unsteady expansion wave generated after bursting of the secondary diaphragm. A second wave that can be responsible for terminating the uniform test flow is the reflected expansion wave which is generated when the leading wave of the unsteady expansion intersects with the driver gas–test gas interface. As indicated in Fig. 16.83, in an optimum shock expansion tube configuration, both limiting waves arrive simultaneously at the test section location. Adjustments to achieve a particular operating condition of the shock expansion tube are made by varying the driver gas speed of sound and pressure, as well as the shock tube and acceleration section filling pressures, and by changing the relative lengths of the shock tube and acceleration tube sections by changing the location of the secondary diaphragm.

The difference between a shock expansion tube and a reflected shock tunnel is the unsteady expansion from region 2 to 5. In a shock tunnel all the energy is added to the flow by heating of the incident and reflected shock wave. Subsequently, the test gas is expanded to high Mach numbers by means of a steady expansion in a convergent–divergent nozzle. The steady expansion is a constant total specific enthalpy process and is described by

$$H = h + \frac{1}{2}u^2 = \text{const},$$

or  $dH = 0$ . In a shock expansion tube, the incident (primary) shock wave adds only a fraction of the final enthalpy of the flow and the test gas is not stagnated. It is processed by the unsteady expansion which is generated after the secondary diaphragm burst. For this process,

$$2\frac{a}{(\gamma - 1)} + u = \text{const}$$

applies. From this follows that

$$dH = -(M - 1)dh.$$

Since the incident shock wave is sufficiently strong to establish supersonic flow ( $M > 1$ ) in the test gas upstream

of the unsteady expansion and since for an expanding flow  $dh < 0$ ,  $dH$  is always positive. Therefore, it follows that the total specific enthalpy and total pressure are amplified by the unsteady expansion. The total pressures achievable in the test section are far in excess of the initial pressure of the driver gas. The shock expansion tube process adds more energy per unit mass of test gas than the reflected shock tunnel process and is therefore better suited for very high-enthalpy ground testing [16.59]. However, the available test time is generally approximately one order of magnitude shorter than that for reflected shock tunnels when comparing facilities of similar size. In a shock expansion tube, the wind tunnel model is placed either inside or at the end of the acceleration tube. Therefore, the core flow and model size is limited by the tube diameter. Similar to straight-through shock tunnels, a divergent nozzle can be added to the end of the shock expansion tube to expand the hypersonic flow to a larger area. This configuration is termed the shock expansion tunnel, e.g. [16.79, 102].

For the former NASA Langley Research Center shock expansion tube/tunnel with a 15.24 cm inner diameter tube, using an unheated helium driver to accelerate test gases such as dry air or carbon dioxide to test section velocities of approximately 5.6 km/s, test times of 100–300  $\mu\text{s}$  are reported [16.102]. The large 0.6 m inner diameter of the LENS X shock expansion tunnel at the Calspan-UB Research Center Buffalo, New York, USA allows test times of approximately 2–3 ms to be achieved at a flow velocity of about 3.5 km/s [16.104].

**Techniques for Total-Specific-Enthalpy Augmentation in Shock Expansion Tubes/Tunnels.** Since the first part of a shock expansion tube or tunnel is identical to a shock tube or tunnel, the same type of different driver techniques as used for shock tunnels can be applied for shock expansion tubes/tunnels to increase the shock Mach number in the shock tube. An overview of possible driver techniques is given in [16.82]. In the subsequent sections, examples of these applications are given.

**Detonative Combustion-Driven Shock Expansion Tube/Tunnel.** The forward running detonation driver of the HYPULSE facility of ATK-GASL in Ronkonkoma, USA [16.79] is used to operate the facility as a reflected shock tunnel as well as a shock expansion tube/tunnel. The set up of the different tube sections of the facility is flexible such that optimum component sizing for its

different operating modes can be achieved. For shock expansion tube/tunnel operation, the ratio of shock to acceleration tube length is chosen in such a way that the reflected expansion waves and the secondary expansion wave all arrive simultaneously at the end of the acceleration tube. The facility with an inner tube diameter of 15.24 cm is used to generate hypersonic flows up to a total specific enthalpy of 12–22 MJ/kg. For these conditions, test times of 0.25–0.55 ms are achieved.

#### Free-Piston-Driven Shock Expansion Tubes/Tunnels.

In order to study the flow past spacecrafts at superorbital velocities (above 8 km/s) in various atmospheres of the solar system, a series of free-piston-driven shock expansion tubes/tunnels was developed at the University of Queensland, Australia [16.73, 105, 106]. These facilities basically utilize the free piston driver as described in the section related to free piston driven shock tunnels. Modifications of this driver concept by using a two-stage piston or the addition of a compound driver to the basic shock expansion tube set up shown in Fig. 16.83 were investigated in order to increase the performance of superorbital shock expansion tubes [16.106]. The X3 facility is the largest of the superorbital shock expansion tubes/tunnels at The University of Queensland [16.107]. The inner diameter of the acceleration tube is 18.3 cm. The operation of X3 relies on a two-stage free-piston compression process, to generate a high-temperature compressed driver gas. Typical test times of the order of 300  $\mu$ s are achievable at test section flow velocities of about 8.4 km/s. For the smaller X2 facility with an inner accelerometer tube diameter of 8.5 cm, total specific enthalpy conditions of 60 MJ/kg (10.3 km/s) using nitrogen as the test gas are reported. The test time for this condition is of the order of 50  $\mu$ s [16.108]. The X1 facility has an accelerometer tube diameter of 3.7 cm. Electron density investigations were performed in an air test flow at a total specific enthalpy of 110 MJ/kg (12 km/s) with a test time of 20  $\mu$ s [16.109].

**Performance Considerations of Real Shock Expansion Tubes/Tunnels.** Similar to shock tubes, there are a number of non-ideal processes during operation of the shock expansion tube that cause the actual operating cycle to deviate from the ideal. In addition to the phenomenon related to the opening of the primary diaphragm and the viscous attenuation of the incident (primary) shock wave as it progresses down the shock tube, the non-ideal rupture of the secondary diaphragm is an important feature of shock expansion tube operation.

In the distance–time ( $x$ – $t$ ) wave diagram of an ideal shock expansion tube as shown in Fig. 16.83 it is assumed that the secondary diaphragm ruptures instantaneously on impact by the incident (primary) shock wave, and that its mass contributes no inertia to the test gas for subsequent acceleration. However, in practice the diaphragm rupture requires a finite period of time, resulting in a reduction of the available test time [16.59]. Furthermore, the incident shock wave is reflected off the diaphragm traveling upstream into the oncoming test gas. For air as the test gas, the entropy generated may be sufficient to cause significant oxygen dissociation that can only be eliminated by recombination in the subsequent unsteady expansion. Investigations of this issue and additional references can be found, e.g., in [16.93, 110].

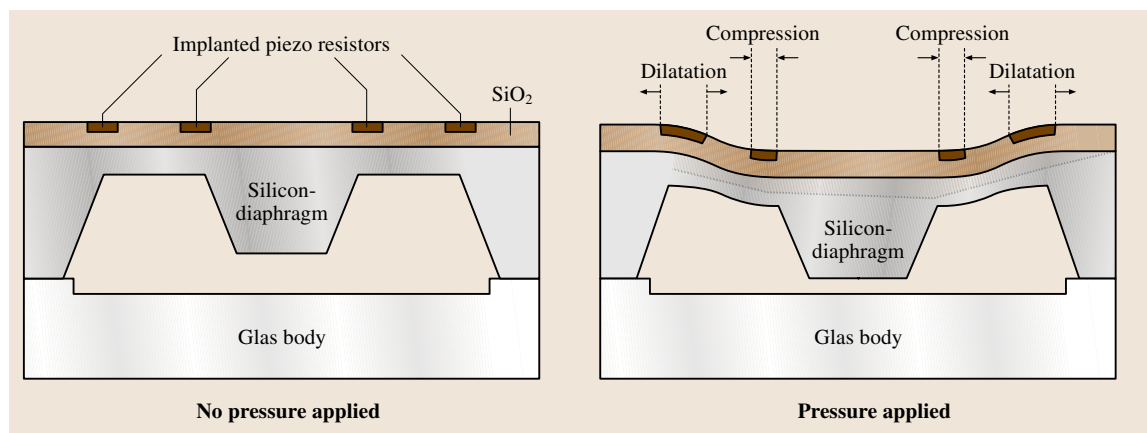
Further, viscous attenuation of the secondary shock wave and growth of the boundary layer along the acceleration tube walls influence the test gas conditions and test section flow. At total specific enthalpy conditions on the order of 22 MJ/kg, the level of test flow dissociation is reduced in shock expansion tubes/tunnels when compared with reflected shock tunnels. However, for extremely high total specific enthalpies ranging from approximately 60–100 MJ/kg, nonequilibrium chemistry effects during the unsteady expansion have to be considered for molecular test gases. Using, e.g., air as test gas at these high total specific enthalpy conditions, results in a highly dissociated free stream.

### 16.2.2 Measurement Techniques

#### Pressure

Surface pressure measurements in short-duration facilities require different approaches than for continuously running facilities. Because the measurement time is short, pressure transducers with fast response times have to be used. Additionally the susceptible area of the transducer has to be installed close to the surface to minimize the filling time of the tubing system in front of the susceptible area. The most commonly used pressure gauges in short-duration hypersonic ground-based test facilities are based on the piezoelectric and on the piezoresistive effect. Piezoelectric pressure transducers are explained in detail in Sect. 8.2. The piezoresistive effect leads to an increase of the resistance of a semiconductor when a pressure load is applied. Optical fibre pressure transducers, which are based on different principles including intensity modulation, interferometry, polarization effects, refractive index changes, reflectometry and fibre Bragg grating are currently under





**Fig. 16.84** Schematic of the Kulite piezoresistive pressure transducer

development. A review of micromachined pressure gauges is given by *Eaton and Smith* [16.111]. A recent development of an optical pressure gauge based on a Fabry–Pérot interferometer [16.112] with a natural frequency above 1 MHz enables data capture over a bandwidth exceeding 100 kHz. This results in response times that are suitable for short-duration hypersonic testing.

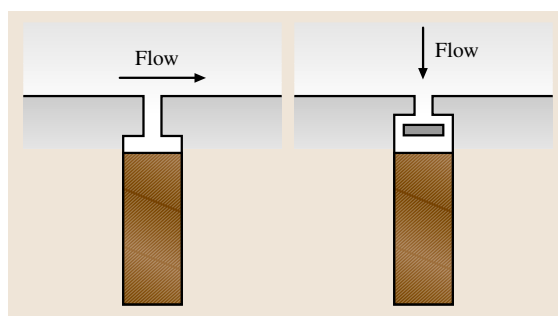
Miniaturized fast piezoresistive pressure transducers are manufactured by Kulite. Depending on the pressure range, the Kulite XCEL-100 pressure gauge with a diameter of 2.4 mm has a natural frequency between 240 kHz and 1 MHz and a bandwidth of 20 kHz. Figure 16.84 shows the schematic of a Kulite pressure transducer. It uses a silicon element for the mechanical diaphragm structure, and the sensing element itself is an integral part of the silicon element. The piezoresistors are formed within the silicon diaphragm by either diffusion or implantation of atoms. Two of these resistors are positioned on the silicon diaphragm such that they experience a compressive strain, and two are positioned where they experience a tensile strain. They are connected such, forming a fully active Wheatstone bridge. These transducers may be manufactured at very small sizes: diameters of the housing can be in the range 1–2 mm.

To achieve fast response times, it is necessary to position the susceptible area of the transducer as close as possible to the model surface. As shown in Fig. 16.85, small holes are drilled in the model which act as pressure tapings. The gauge is placed directly behind these tapings. The influence of the pressure tapping shape and manufacturing quality on the measured signal is discussed in Sect. 4.1. In Fig. 16.85 the schematic of two

different types of pressure gauge installations as used in short-duration facilities is shown.

The pressure transducers are colored dark brown. Typical tapping diameters range from 0.5 to 1.5 mm. The schematic on the left-hand side of Fig. 16.85 shows an installation suited for tapings perpendicular to the flow. This installation is not suited for stagnation regions, where the flow may directly stagnate on the pressure transducer leading to high heat flux on the susceptible area. A stagnation point installation is shown on the right-hand side of Fig. 16.85. Here the susceptible area of the transducer is protected by a stagnation plate. Examples of pressure measurements using both configurations are given in Fig. 16.86.

This test has been conducted in a small shock tube. Two transducers have been installed in the end wall, where they measure the pressure rise caused by the incident shock wave. The presence of the stagnation plate extends the rise time for the used tapping diameter and cavity size by about 0.15 ms.

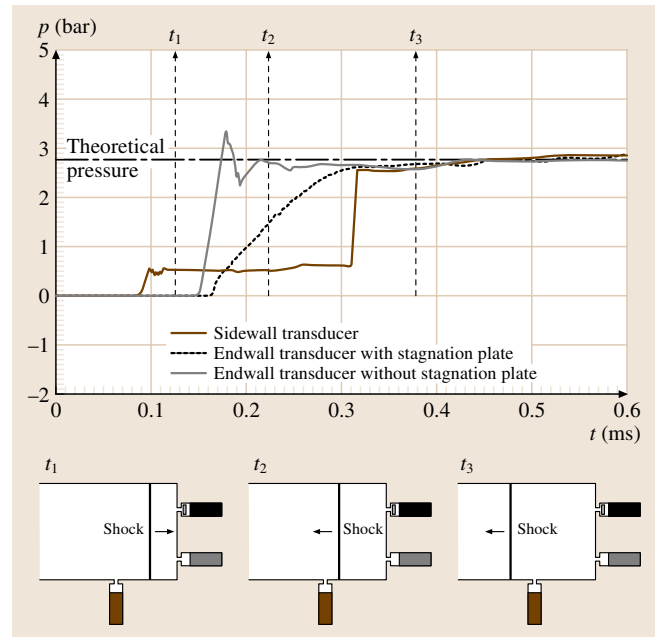


**Fig. 16.85** Installation of pressure transducers into a model wall (transducers shown in dark brown)

### Surface Heat Flux

In short-duration high-enthalpy, hypersonic ground-based test facilities the most common way to measure wall heat flux is by utilizing thin-film gauges or thermocouples. Due to the harsh environment in these facilities with high wall shear stresses during the starting process of the flow, the most robust and reliable technique to measure heat flux is the application of surface-mounted coaxial thermocouples. The principle of operation of thermocouples is the Peltier–Seebeck or thermoelectric effect [16.113].

In order to allow a detailed instrumentation of wind tunnel models, miniaturized thermocouples with diameters as small as 0.4 mm are used. Figure 16.87 shows a schematic view of a miniaturized coaxial ultrafast thermocouple manufactured by Medtherm Corporation [16.114]. Coaxial thermocouples are built with a core consisting of one conductive material separated by insulation from the outer ring made of a different material. Possible material combinations and their official Instrument Society of America (ISA) code are given in Table 16.3 together with their application range. The electrical connection on the top surface is realized either by coating the surface with one of the materials or simply by sanding of the transducer surface. In either case the mass of the electrical connection in comparison to the mass of the transducer body is small leading to response times of thermocouples in the order of a few  $\mu\text{s}$ . Additionally, the heat flux into the transducers is dominated by the thermocouple body and the junction itself is negligible due to its low mass. The sensitivity of thermocouples range from  $1\ \mu\text{V/K}$  to  $70\ \mu\text{V/K}$ . The thermocouple inherits the advantage that the shape of the transducer can be adopted to any wall curvature by



**Fig. 16.86** Rise-time investigation for different pressure gauge installations in shock tube walls

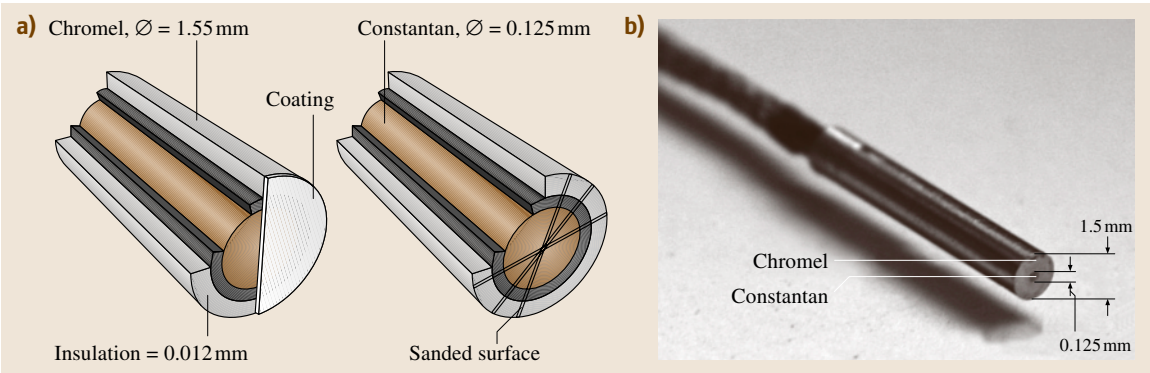
sanding. In case of transducer failure, it can be repaired in situ by sanding the surface again.

Alternatively to thermocouples, in areas with less-harsh flow environments, such as wake flows or surfaces at small angles of attack, thin-film gauges can be used to measure the temperature history in order to evaluate the heat flux (see e.g. [16.115, 116]). Thin-film gauges consist of a nonconductive substrate on which a metallic film with a typical thickness of less than  $1\ \mu\text{m}$  is met-

**Table 16.3** Possible material combinations and application ranges of thermocouples

ISA code	Material A (+)	Material B (–)	Application range
B	Platinum 30% rhodium	Platinum 6% rhodium	1640 K to 1970 K
C	95% W5Re tungsten 5% rhenium	W26Re tungsten 26% rhenium	1920 K to 2585 K
E	Chromel	Constantan	365 K to 1170 K
J	Iron	Constantan	365 K to 1030 K
K	Chromel	Alumel	365 K to 1530 K
N	Nicrosil	Nisil	920 K to 1530 K
R	Platinum 13% rhodium	Platinum	1140 K to 1720 K
S	Platinum 10% rhodium	Platinum	1250 K to 1720 K
T	Copper	Constantan	70 K to 620 K

Chromel\* – 90% nickel, 10% chromium; alumel\* – 95% nickel, 2% manganese, 2% aluminium, 1% silicon; constantan – 55% copper, 45% nickel; nisil<sup>+</sup> – 95.6% nickel, 4.4% silicon; nicrosil<sup>+</sup> – 84.1% nickel, 1.3% silicon, 14.6% chromium  
 \* Trademarks of Hoskins Manufacturing Company  
<sup>+</sup> Trademarks of Harrison Alloys Inc.

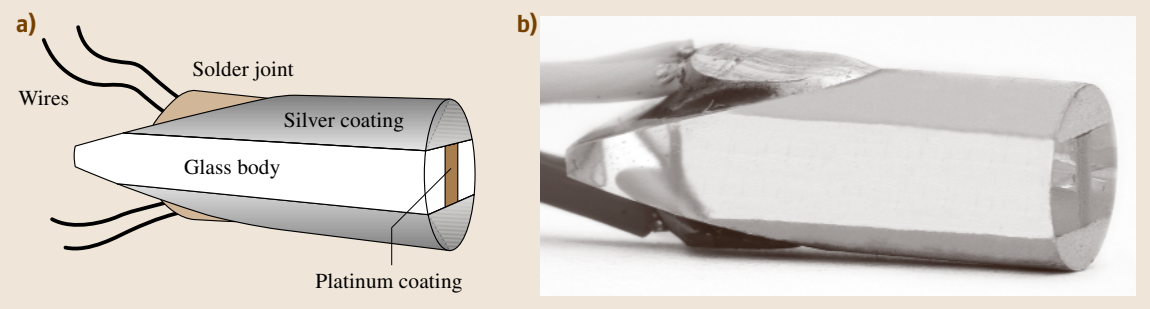


**Fig. 16.87a,b** MedTherm type E thermocouple: (a) schematic, and (b) photograph

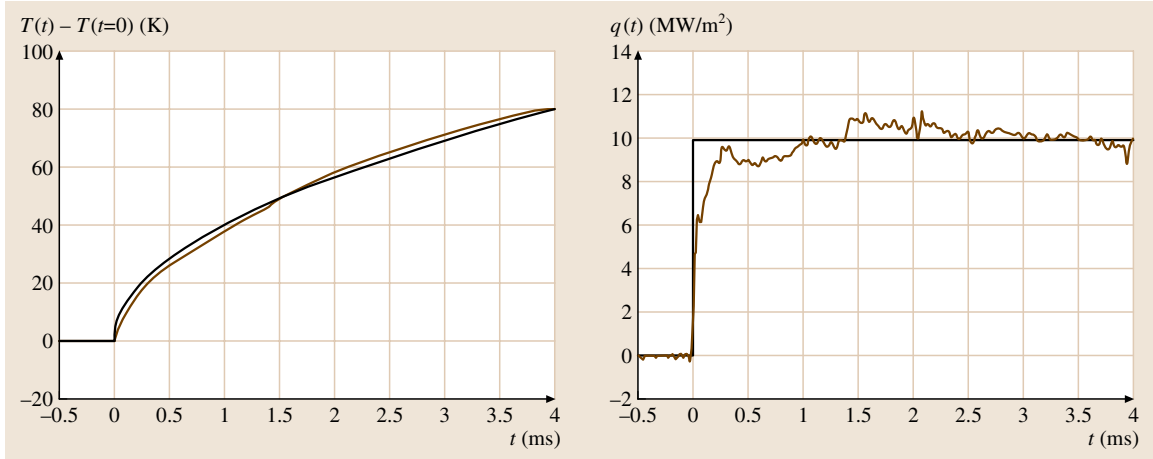
alized. The working principle of these gauges is based on the dependence of the electrical resistance of the metallic film on temperature. For the metallic film noble metals are used because they exhibit the largest sensitivity. Again, the mass of the susceptible area is very small compared to the body in which the heat is conducted. Therefore, similar response times as for thermocouples are obtained.

As an example (Fig. 16.88) a thin-film gauge as manufactured by the French–German Research Institute of Saint Louis (ISL) is shown. The measuring point is a thin platinum film, which is metallized on a glass body. The electrical connection to the measurement wires is realized by a silver coating of the upper and lower third of the glass body. The typical diameter of these gauges is in the order of millimeters. The temperature sensitivity and signal-to-noise ratio of thin-film gauges are superior to thermocouples. However, disadvantages are the missing robustness in harsh flow environments usually found in short-duration facilities, the large effort of adapting the susceptible area to curved surfaces and the missing possibility to repair the gauge in situ.

Two assumptions are used to evaluate the heat flux from the measured temperature traces using coaxial thermocouples or thin-film gauges. The first assumption is that the measurement is dominated by one-dimensional heat conduction in the sensor body, and the second is that the gauge itself acts as a semi-infinite body [16.117]. To ensure that the first assumption is valid, only the transducer face should be exposed to the flow, and the combination of wind-tunnel model wall material and transducer material has to be chosen in an appropriate way. The validity of the semi-infinite body assumption requires  $x \geq \sqrt{\alpha t}$  [16.118], where  $x$  is the length of the transducer,  $\alpha$  the diffusivity and  $t$  the time. The diffusivity  $\alpha$  is defined as the ratio of the heat conductivity  $\kappa$  and the product of density  $\rho$  and specific heat capacity  $c$ ,  $\alpha = \kappa/(\rho c)$ . For thermocouples of ISA code E with a length of 10 mm the time before the heat reaches the end of the transducer is approximately 3 s. This period of time is orders of magnitude higher than the typical test times in short-duration facilities of a few ms. If the two assumptions mentioned can be regarded as valid, the heat conduction problem in the transducer body is described by the following differential equation:



**Fig. 16.88a,b** ISL thin-film gauge: (a) schematic, and (b) photograph (courtesy ISL)



**Fig. 16.89** Heat flux evaluation of a temperature recording in a shock tunnel (brown) compared with the temperature evolution based on a stepwise heat transfer load (black)

$$\frac{\partial^2 T}{\partial x^2} = \frac{1}{\alpha} \frac{\partial T}{\partial t} \quad (16.2)$$

Here,  $T$  is the temperature minus a suitable reference temperature,  $x$  is the coordinate normal to the wind tunnel model wall and  $t$  the time. With the boundary conditions that the heat flux into the model wall,  $\dot{q}_w(x=0) = -\kappa(\partial T/\partial x)$  and  $T(x=\infty)=0$ , the following equation can be derived for the evaluation of the heat flux

$$\dot{q}_w(t) = \sqrt{\frac{\rho c k}{\pi}} \left( \frac{T(t)}{\sqrt{t}} + \frac{1}{2} \int_0^t \frac{T(t) - T(\tau)}{(t - \tau)^{3/2}} d\tau \right), \quad (16.3)$$

as shown by Schultz and Jones [16.117].

For the evaluation of the wall heat flux by numerical integration of digitally stored temperature data, this relationship is replaced by a discretized form such as

$$\dot{q}_w(t_n) = 2\sqrt{\frac{\rho c k}{\pi}} \sum_{j=1}^n \frac{T_j - T_{j-1}}{\sqrt{t_n - t_j} + \sqrt{t_n - t_{j-1}}},$$

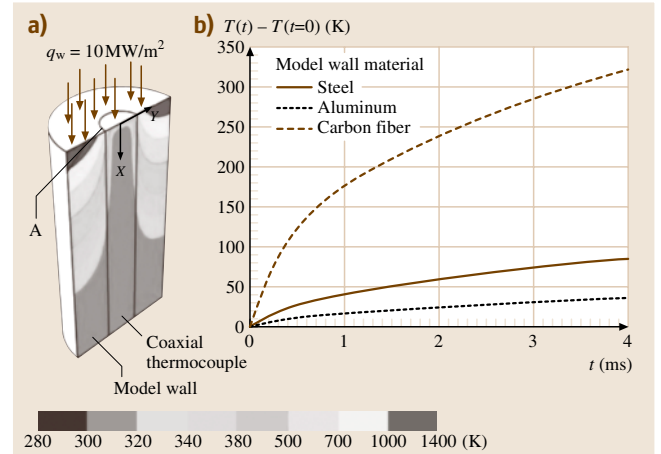
proposed by Cook et al. [16.119] or an alternative scheme described by, e.g., Kendall et al. [16.120].

In Fig. 16.89 an example obtained with the data evaluation method of Cook et al. [16.119] is presented. In the left plot of Fig. 16.89, the temperature development measured by a type E thermocouple installed in the stagnation point of a sphere positioned in a hypersonic flow with total specific enthalpy of  $h_0 = 15 \text{ MJ/kg}$  is indicated by the brown line. In the right plot of Fig. 16.89 the resulting heat flux versus time (brown line) is shown. If the heat flux into the wall is given by an ideal step function, the exact solution for the temperature rise at  $x = 0$

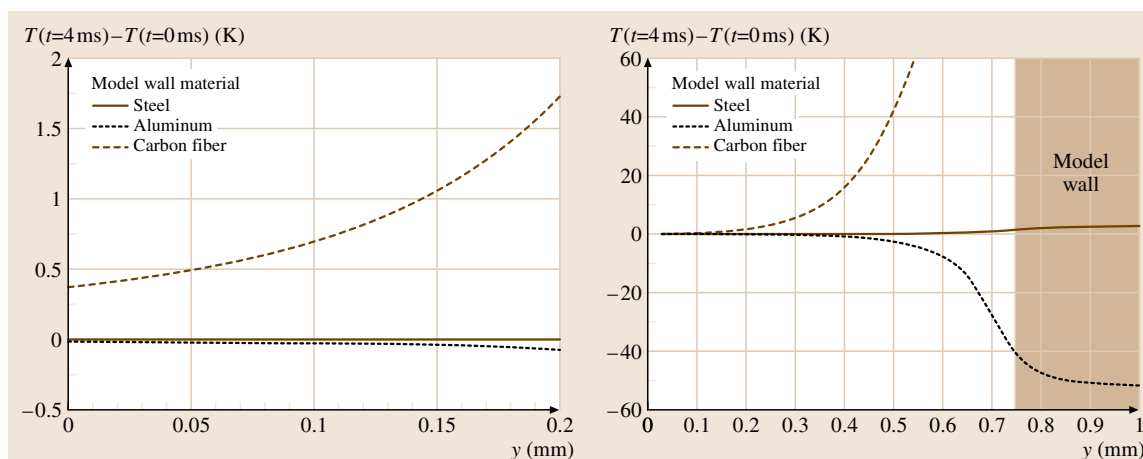
resulting from (16.2) is

$$T_w(x=0, t) = \frac{2\dot{q}_w}{\sqrt{\pi}} \sqrt{\frac{t}{\rho c k}}. \quad (16.4)$$

Using a constant heat flux into the transducer body of  $\dot{q}_w = 10 \text{ MW/m}^2$  as approximation of the measured heat flux evolution (the black line in the right plot of Fig. 16.89), the parabolic temperature history pro-



**Fig. 16.90a,b** Unsteady finite-element analysis of the heat conduction process in a type E thermocouple and the adjacent model wall for a wall heat flux of  $10 \text{ MW/m}^2$ ; axisymmetric temperature distribution at  $t = 4 \text{ ms}$  for a carbon-fibre model wall (a) and time evolution of the temperature at the interface (A) between the thermocouple and the model wall for different wall materials (b)



**Fig. 16.91** Difference of radial computed temperature distribution at the model wall and thermocouple surface obtained for different thermocouple/wall material combinations compared to the combination chromel/chromel for which no temperature difference between the thermocouple and wall exists

file shown as black line in the left plot of Fig. 16.89 is obtained.

To ensure that the measurement is not affected by conduction in the wall tangential direction, the thermocouple type should be chosen in such a way that the material properties of the model wall match those of the thermocouple at the measurement position. The influence of different thermocouple/model wall material combinations on the measured temperature distribution is shown in Fig. 16.90 and Fig. 16.91. These results were obtained by numerical investigation of the unsteady heat conduction process in a type E thermocouple with 1.5 mm diameter and a length of 15 mm, installed in model walls of different materials, using Ansys (CAD-FEM GmbH). The thermocouple is modeled as a solid cylinder consisting of chromel. At the top surface a constant heat flux of  $q_w = 10 \text{ MW/m}^2$  is applied. The temperature evolution at the contact point between the thermocouple and the model wall is given in Fig. 16.90b for three different model wall materials. Depending on the material, large differences of the temperature evolution are obtained.

The difference of the radial temperature distribution at the model wall and thermocouple surface obtained for the thermocouple/wall material combination chromel/chromel, i. e. a combination for which no temperature difference between the thermocouple and the model wall exists, and the material combinations chromel/steel, chromel/aluminium and chromel/carbon fibre are plotted in Fig. 16.91. On the left-hand side of Fig. 16.91, a zoom of the core region of the ther-

mocouple is shown. The right-hand side of Fig. 16.91 shows the distribution up to a radius of 1 mm. In case of a coated thermocouple with dimensions as shown in Fig. 16.87, the temperature measurement takes place at  $y = 0-0.0625 \text{ mm}$ , the location of the chromel/constantan junction. For a thermocouple which is adapted to a three-dimensional surface or repaired in situ by sanding, the chromel/constantan junction is not precisely defined and the complete thermocouple surface may act as the measurement location. As can be seen from Fig. 16.91, depending on the thermocouple/wall material combination the assumption of one-dimensional heat conduction can be violated.

From (16.3) it becomes evident that the error in the estimation of the heat flux is directly proportional to the error of the value of  $\sqrt{\rho c k}$ . To determine this value accurately two procedures may be applied. The contact procedure is used for thermocouples and thin-film gauges and is based on the fact that under the assumption of one dimensional heat conduction, the contact temperature of two media is only dependent on their temperature before contact and on the thermal properties ( $\sqrt{\rho c k}$ ) of both media. Knowing the thermal properties of one media allows to determine the gauge properties. A possible set up is a mechanically driven device that generates an instantaneous contact between the gauge and a liquid surface. Such a method is discussed in [16.121]. The electric discharge calibration can only be applied for thin-film gauges. It utilizes the effect that with an electric discharge, the thin film itself can be heated with a known and constant heat flux. Fol-



lowing (16.4), the measurement of the temperature of the thin-film gauge results in the determination of  $\rho c k$ . This procedure is described in e.g. [16.122].

### Forces and Moments

The ability to perform integrated force and moment measurements in ground-based testing facilities is an important part of the design and development of hypersonic vehicles. For a force balance to operate in short-duration ground-based test facilities with test times of order ms or less, it would become necessary for the balance to have an extremely short response time. However, given the short test times and the response times of force measurement techniques for conventional wind tunnels, e.g. [16.123], static equilibrium between the model and support structure is rarely established, i. e., it may only be obtained using unrealistically small models. Therefore, it becomes necessary to use specialized measurement methods that account for the dynamic response of the system. The basic force measurement techniques that have been applied in short-duration flows are outlined in the subsequent paragraphs. An overview of these techniques is given in [16.124].

**Free-Flight Force Measurement Techniques.** By using a free-flying (or a very weakly constrained) model, it is possible to directly measure the motion of a model in a wind tunnel. This can be achieved by measuring model accelerations (e.g. [16.125, 126]) or by visualization techniques to record the time history of model displacements (e.g. [16.127]). From these measurements, the applied forces and moments can be recovered.

The experiments performed by *Naumann et al.* [16.125] involved a model instrumented with accelerometers that was released by a fast-opening chuck just before the test flow arrives. The model used was 140 mm in length, and small quartz accelerometers with built-in amplifiers from PCB (model 309A) were used. Motion during the first few ms was small. Therefore, thin wires from the accelerometers were required such that the motion of the model was not disturbed. This technique overcomes the assumptions regarding balance stiffness, as there are no connections between the model and the support structure. By using an inertial matrix of the model and the measured accelerations, the applied forces can be determined via Newton's law (e.g. [16.128]). It is necessary to have the model equipped with six or more accelerometers to realize a six-component force balance and the inertial matrix must be determined in each individual case. The advantage of this technique is that it is relatively simple, avoiding expensive devices such as

telemetry and complicated isolating supports. Further, once the inertial matrix is known, the data evaluation procedure is straightforward.

Other investigations by *Kussoy and Horstmann* [16.127] relied on recording photographically the trajectory of a free flying model. Since the model's displacement of its center of mass was much larger than any displacement due to model flexibility, reasonable results were obtained. *Bernstein and Scott* [16.129] attempted to account for model flexibility in free flying models. This was necessary as the facility used had a shorter test time, resulting in smaller displacements and therefore model flexibility was an issue. Laser interferometry was used for the detection of small displacements. The model was 120 mm long and the resulting displacement data was fitted to parabolic curves. Hence, it was assumed that the model had constant acceleration and thus failed to overcome the underlying problem of model flexibility.

The next two methods to measure forces and moments which will be discussed, the strain gauge force balance and the stress wave force balance, are based on utilizing a model/support structure assembly.

The basic features of the response of a structure as function of time after a load has been applied can be discussed by looking at a simple one degree of freedom system. If damping is neglected, such a system of mass  $M$  on a spring of stiffness  $k$  obeys the equation of motion

$$M\ddot{u} + ku = F(t),$$

where  $u$  is the displacement,  $\ddot{u}$  the acceleration (second time derivative of the displacement), and  $F(t)$  the loading. Assuming a sudden application of a constant load  $F_0$ , the solution to the equation of motion is

$$u = \frac{F_0}{k}[1 - \cos(\omega t)],$$

with  $\omega = \sqrt{k/M}$  and the fundamental natural frequency  $f = \omega/(2\pi)$ . These relations show, that the natural frequency of the system can be increased by increasing the stiffness and reducing the mass.

**Strain Gauge Force Balances.** Strain gauge force balances are used in short-duration test facilities for measurements of forces and moments. In combination with a model of sufficiently high stiffness and low moments of inertia, natural frequencies of approximately 1 kHz can be achieved. Although acceleration compensation can be used to account for support flexibility, it generally remains an issue. Thus, in order to avoid flexible models, they are generally small, un-instrumented and lightweight.

Jessen and Grönig [16.130] designed a six-component strain gauge force balance for use in the RWTH Aachen University Shock Tunnel in Germany. This facility has a test time of 2–6 ms. The design resulted in a compromise between high stiffness and sufficient strain sensitivity (i. e., models of high stiffness and low moments of inertia were utilized). The balance was designed to work without acceleration compensation. Because the balance is part of the sting it is virtually independent of the model and may be calibrated statically with a high accuracy. However, strong coupling between the six force components was seen, resulting in extensive calibration being required to obtain accurate results. Since interference between components is significant, a third-order description of the system was used to calibrate the force balance. The relation between the signal and load is given by

$$S_i = R_{oi} + \sum_{j=1}^6 a_{ij} Z_j + \sum_{j=1}^6 \sum_{k=j}^6 b_{ijk} Z_j Z_k + \sum_{j=1}^6 c_{ij} Z_j^3, \\ i = 1, 2, 3, \dots, 6,$$

where  $S_i$  is the signal of the strain gauge bridge for component  $i$ ,  $R_{oi}$  is the signal of bridge  $i$  without load,  $Z_j$  the total load acting on component  $j$ ,  $a_{ij}$  the calibration factors for linear terms,  $b_{ijk}$  the calibration factors for square terms, and  $c_{ij}$  the calibration factors for cubic terms.

This balance was also investigated further by Störk-mann et al. [16.131]. The balance outputs were improved with compensation of low frequency oscillations but no attempt was made to account for model flexibility. Compensation was performed using two methods – sting-based acceleration compensation, which compensated only for frequencies less than the first resonant frequency of the system, and model-based compensation in which six accelerometers were used to measure the acceleration of the model. Experiments were conducted on three different models – a conical model, a model of the Apollo command module and a model of the elliptical aerodynamic configuration (ELAC) I (a delta wing configuration). Good results were obtained with the conical and Apollo models as they were sufficiently stiff, however, the ELAC I model was quite flexible. Consequently the balance outputs for this model contained large oscillations.

As discussed in Sect. 16.2.3, a similar type of strain gauge force balance with acceleration compensation was used in the HIEST shock tunnel of JAXA, Japan by Itoh

et al. [16.132] for the investigation of the aerothermodynamic characteristics of the H-II Orbiting Plane (HOPE) space vehicle.

**Stress Wave Force Measurement Technique.** The stress wave force balance relies on the ability to measure the dynamic response of the model and supporting structure, and consequently any effects such as model flexibility and mass distribution are accounted for (e.g. [16.124]). Instead of using a static calibration as done for the strain gauge force balances, stress wave force balances require a dynamic calibration of the complete model, balance, and support structure assembly.

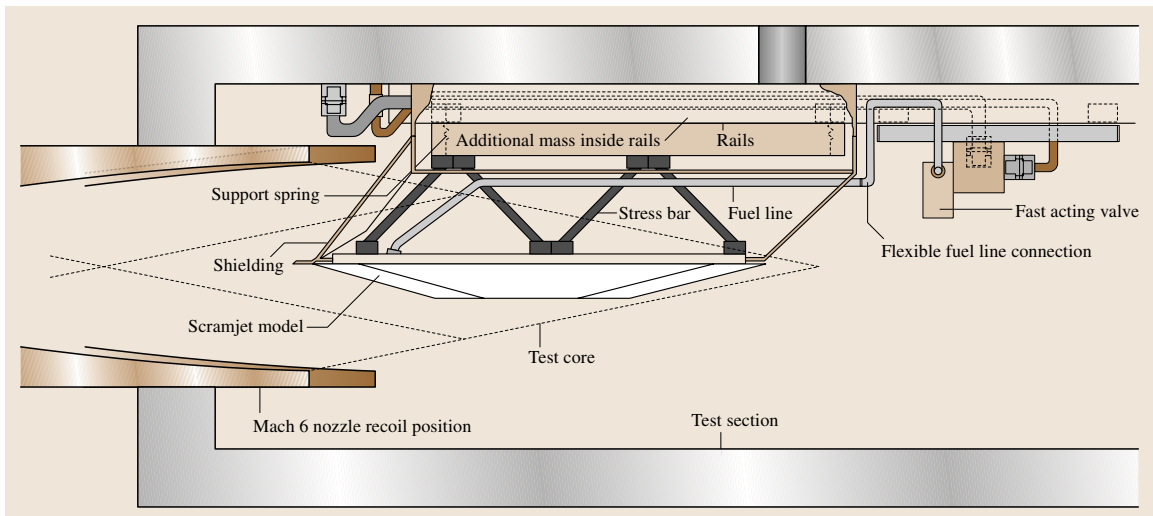
Upon flow arrival, stress waves propagate through the model at the speed of sound of the material and subsequently enter a stress bar that is instrumented with a strain gauge to record the time history of strain. If the system is linear, the resulting strain signal  $y(t)$  can be related to the applied aerodynamic load  $u(t)$  via an impulse response function  $g(t)$  as described by the convolution integral,

$$y(t) = \int_0^t g(t - \tau) u(\tau) d\tau.$$

The aerodynamic force in an experiment can be determined by the deconvolution of the strain signal with the impulse response function. The impulse response function is determined either through experimental calibration or through finite element analysis. However, in order to reduce errors due to modeling approximations it is usually preferable to determine the impulse response function experimentally.

It has been found that deconvolution is best performed in the time domain using the algorithm of Prost and Goutte [16.133]. Additionally, beginning the deconvolution technique using the time history of Pitot pressure scaled in magnitude to the expected force component level improves the accuracy and stability of the process [16.134].

Sanderson and Simmons [16.135] first demonstrated the technique by measuring the drag force on a 15° conical model, 200 mm in length in a reflected shock tunnel. The model was made from aluminum and attached to a 2 m-long hollow brass bar. This stress bar or sting, was instrumented with strain gauges to record the axial strain time history. The test time was approximately 1 ms and the aerodynamic load was subsequently found through a numerical deconvolution process. The measured drag was found to be in good agreement with theoretical calculations.



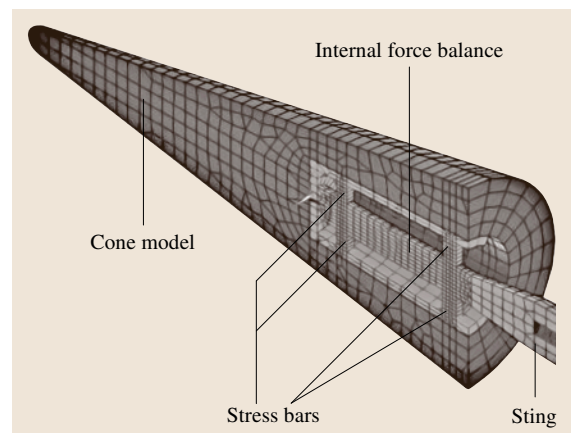
**Fig. 16.92** Schematic of scramjet model and external stress wave force balance in the test section of the T4 shock tunnel (after Robinson et al. [16.136])

The technique was then extended to measure multiple components of force by Mee et al. [16.134]. This was done on a  $15^\circ$  cone with an internal balance arrangement. The lift, drag, and pitching moments were measured by short, stiff stress bars instrumented with strain gauges. The technique has subsequently been applied to a wide variety of models, including models with simultaneous measurements of pressure and heat flux. The major disadvantage with this technique is that aerodynamic shielding and vibration isolation of the support structure is required to separate the stress waves generated in the model from that of the test section environment. Calibration of the model is usually performed using an instrumented impact hammer or via a cut-weight technique. In order to maximize the performance of stress wave force balances, an individual design for each configuration to be tested is recommended.

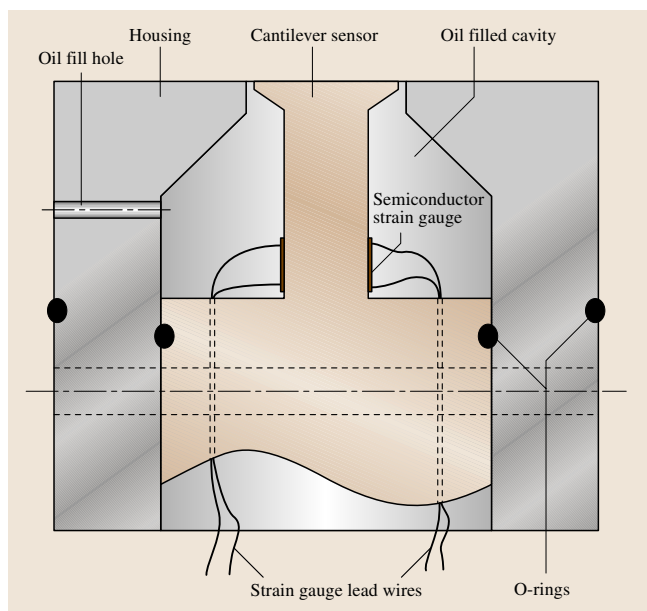
Stress wave force balances have been developed with external as well as internal stress bar arrangements. A three-component stress wave force balance used by Robinson et al. [16.136] to measure the thrust, lift, and pitching moment of a supersonic combustion ramjet (scramjet) model in the T4 shock tunnel of The University of Queensland, Australia is shown in Fig. 16.92. Four stress bars are located above the model. They connect the scramjet model to a base plate. The bars are instrumented to measure axial strain using piezo-resistive strain gauges. The heavy base plate is suspended from the test section by light support springs to provide vibration isolation of the balance from the

test section when the tunnel is operated. An aerodynamic shield, shown in the upper section of Fig. 16.92, isolates the elements of the force balance from aerodynamic forces so that only forces on the scramjet model are detected.

The internal three-component force balance applied by Robinson and Hannemann [16.137] in the High Enthalpy Shock Tunnel Göttingen (HEG) is shown in Fig. 16.93. Four short, stiff stress bars are mounted on a sting and each bar is instrumented with semiconductor strain gauges to measure the time history of strain.



**Fig. 16.93** Finite-element discretization of the internal stress wave force balance – cone model set up used in the HEG shock tunnel



**Fig. 16.94** VPI skin friction gauge design (after Novean et al. [16.138])

In summary, force measurements in test times of the order of ms in duration are a challenging and difficult area. Of the methods outlined, each has its own advantages and disadvantages, and the selection of the technique to use is somewhat dependent on the test time capability of the facility, the model to be tested, and

the aims of the test campaign. For a very stiff or very large model for which the application of the strain gauge or stress wave technique is not feasible, the free-flight measurement technique is preferable.

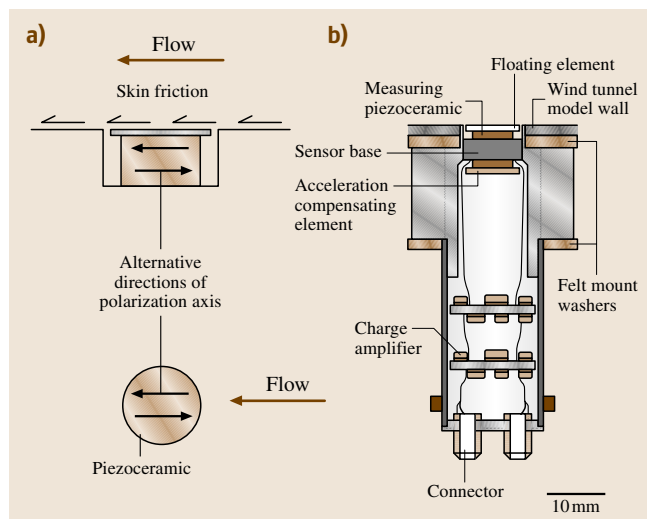
A high natural frequency is particularly important for strain gauge force balances because a static calibration is performed for this type of balance, and a model with high natural frequency allows that within the available test time the mean values of the measured forces and moments approach the static value as close as possible. To obtain mean level information, approximately five cycles of the lowest natural frequency are required.

If the goal of a test campaign is to use many different models with slight geometry changes and for cost-efficiency reasons the models are manufactured from plastic, which is lightweight, then a strain gauge force balance with acceleration compensation might be chosen. In facilities with test times of 1 ms and below, and if, for example, a heavy model is required with simultaneous pressure and heat flux measurements, then a stress wave force balance may be most suitable.

### Skin Friction

Indirect measurement of skin friction or the use of the Reynolds analogy have several disadvantages, including lack of direction sensitivity, a dependency on assumptions regarding the nature of the flow field, and lower precision with respect to direct measurements. Due to the importance of accurate skin friction measurement for supersonic flows and the prevalence of short-duration facilities for supersonic testing, skin friction gauges with high-frequency response have been developed. An overview of the application of skin friction gauges in short-duration facilities is given, e.g., in [16.140]. Typically, the gauge is mounted with the sensing face flush with the instrumented body's surface such that the skin friction force acts on this sensing face. A piezoelectric skin friction gauge was used in the shock tunnels of the Cornell Aeronautical Laboratory (now Calspan) by Holden [16.141]. The gauge consisted of two piezoceramic beams in bending mode supporting a measurement diaphragm flush with the model surface. The natural frequency of the gauge was approximately 5 kHz [16.140].

In the case of the miniature cantilever gauge design of the Virginia Polytechnic Institute (VPI) [16.138], the sensor face lies at the end of a cantilever beam, which is instrumented at the base with two strain gauges mounted at 180° to one another. A schematic of the VPI gauge is shown in Fig. 16.94. The wall shear force from the passing flow minutely deflects the sensor head leading to a change in the resistances of the semiconductor



**Fig. 16.95a,b** UQ skin friction gauge design: (a) principle of operation; (b) design layout (after Goyne et al. [16.139])



gauges, which are incorporated in a Wheatstone bridge configuration. The cavity between the sensing element and the housing is filled with either a silicon oil or a silicon rubber compound. The rubber-filled variant was designed to reduce maintenance, although it leads to increased manufacturing and modeling complexity. These gauges had a natural frequency of 20 kHz and the uncertainty in skin friction measurement was estimated at 10% for the complex supersonic flows considered.

The piezoceramic skin friction gauge design developed at The University of Queensland (UQ), Australia is shown in Fig. 16.95 [16.139]. In this case, the sensing face is a floating element that is directly attached to a piezoceramic ring. The polarization direction of the piezoceramic is mounted parallel to the skin friction force direction. Acceleration compensation is achieved through an acceleration compensating element that is mounted inside the gauge. The element and associated piezoceramic for both the floating element and the acceleration compensating element are of the same dimensions and mounted similarly. The gauge is calibrated for transient shear and acceleration in separate bench tests and pressure calibration is achieved during experiments using adjacent pressure transducers. The UQ gauges had a lowest natural frequency of approximately 40 kHz and the uncertainty in skin friction measurement was estimated at  $\pm 47\%$ ,  $\pm 16\%$ , and  $\pm 7\%$  for laminar, transitional and turbulent boundary layers, respectively [16.142].

### Optical Techniques

**General Application of Optical Techniques.** As in conventional ground-based facilities, in hypersonic short-duration test facilities optical techniques can provide a large range of data with the advantage of being able to obtain information without physically disturbing the flow. Without going into a detailed description, an overview of the major optical measurement techniques used in impulse facilities are summarized in this section (see also Chap. 20).

Laser-induced fluorescence (LIF) was applied to measure temperatures in the free stream of a high-enthalpy shock tunnel [16.143, 144].

Planar laser-induced fluorescence (PLIF) is a frequently used optical imaging method in short-duration ground-based facilities. A laser is tuned to a certain frequency such that it excites a chosen energy level in a probed molecule in the test flow. The tuned laser light is formed into a sheet and passed through the flow. An image of the fluorescence can be recorded which is directly related to the concentration of the

probed molecule within the laser sheet. Commonly probed molecules in hypersonic flows include nitric oxide (NO), which is often naturally occurring in shock tunnels, and hydroxide (OH), which is present in oxygen–hydrogen combustion flows. This method can also be extended to measure temperature and velocity in hypersonic flows. The measurement of species concentrations, vibrational temperatures, and velocities has been performed in short-duration test facilities by, e.g., Wollenhaupt [16.145], O’Byrne et al. [16.146], Palma et al. [16.147], Ben-Yakar et al. [16.148], and Kovachevich et al. [16.149].

Tunable diode laser absorption (TDLAS) is used to measure translational/rotational temperatures, gas velocities, and concentrations of various molecules and atoms (e.g. [16.150–154]).

The application of temperature and pressure-sensitive paint in hypersonic short-duration test facilities is still under development. A discussion of the application of these techniques is given by Nakakita and Asai [16.155], and Ohmi et al. [16.156].

A method to obtain planar velocity visualization, called Doppler picture velocimetry (DPV), has been developed and used for short-duration measurements at the French–German Research Institute of Saint Louis (ISL) [16.157]. A specially designed Michelson interferometer transforms the Doppler shift of the scattered light of the flow particles into a shift in light intensity which is subsequently converted into a flow velocity.

The coherent anti-Stokes Raman spectroscopy (CARS) uses two pulsed laser beams with known pulse and Stokes frequencies. These beams are focused to a point generating an output with an anti-Stokes frequency. The analysis of this output allows information such as temperature and relative species densities to be obtained. This point measurement method has been applied in short-duration test facilities by, e.g., O’Byrne et al. [16.158], and Danehy et al. [16.159].

Flow tagging is a non-intrusive laser-based method for direct velocity measurements. The method is based upon laser-enhanced ionization velocimetry in which a tagged region is created by two-step excitation of sodium and subsequent collisional ionization. The achieved depletion of neutral atoms is then interrogated by planar laser-induced fluorescence, providing a measurement of the velocity. Velocities in the range of 9 km/s have been measured [16.160].

Electron-beam fluorescence is based on the fact that the inelastic collisions between electrons and gas molecules produce a radiative emission that is characteristic for the gas state properties. By creating



a high-energy electron beam and passing it through a gas, the emission can be initiated and analyzed. While the intensity of this emission is related to the number density and to features of the electron beam, the spectral characteristics are related to the composition, density and temperature of the gas. General introductions into the technique are given by, e.g., Muntz [16.161], and Bütefisch and Vennemann [16.162]. Applications in shock tunnel environment are reported by Shelton and Casady [16.163], and Muntz et al. [16.164].

**Phase-Step Holographic Interferometry.** Interferometry may be used as a technique to measure the variation of the refractive index of a gaseous flow in the test section of a short-duration facility. This information can be used to evaluate the density distribution of the investigated flow field. Holographic interferometry does not require special machining or manufacturing of test section windows, mirrors or lenses with high precision, because any imperfections in these components are automatically balanced out by the holographic two step procedure. Therefore, related to the application in short-duration ground-based test facilities, this technique has replaced the classical and labor-intensive Mach–Zehnder interferometry.

**Determination of the Refractive Index by Interference Phenomena.** The absolute speed  $c_0$  at which light travels in absolute vacuum is constant. In any kind of gaseous media the speed of light  $c$  will be lower. The ratio of the two speeds defines the refractive index

$$n(\rho) = \frac{c_0}{c} = 1 + K^\lambda \rho.$$

The Gladstone–Dale relation describes that in a gaseous media consisting of one species the refractive index depends on the density  $\rho$  and the Gladstone–Dale constant  $K^\lambda$  [16.165].  $K^\lambda$  is weakly dependent on the wavelength and is specific for each gas. For gas mixtures the refractive index is given by a linearly composed Gladstone–Dale constant

$$n(\rho) = 1 + \rho \sum_{i=1}^S K_i^\lambda \xi_i,$$

where  $K_i^\lambda$  are the Gladstone–Dale coefficients for the individual gas species,  $\xi_i$  are the species mass fractions,  $S$  is the number of species, and  $\lambda$  is the wavelength of the laser light used. The definition of a linearly composed Gladstone–Dale constant applies to general gas mixtures including chemically reacting, excited and ionized species.

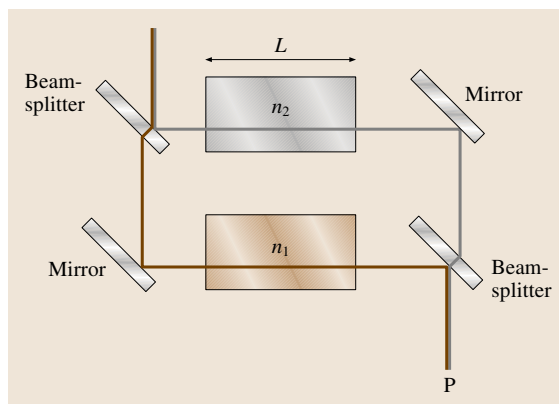


Fig. 16.96 Schematic of interference experiment

The basic principle of interferometry is shown in Fig. 16.96. Two rays of coherent light interfere in point P. Each ray passes through zones with different refractive index, which leads to a time shift  $\Delta t$  due to the different speeds of light in the two zones:

$$\Delta t = \frac{L}{c_2} - \frac{L}{c_1} = \frac{L}{c_0}(n_2 - n_1).$$

With the time shift the difference in the optical path length evaluates to

$$\Delta l = c_0 \Delta t = L(n_2 - n_1).$$

If the difference in the optical path length equals the wavelength, then the phase shift between both rays equals  $2\pi$ . Therefore, it follows that:

$$\frac{\Delta l}{\lambda} = \frac{\phi}{2\pi} = \frac{L}{\lambda}(n_2 - n_1) = \frac{K^\lambda L}{\lambda}(\rho_2 - \rho_1).$$

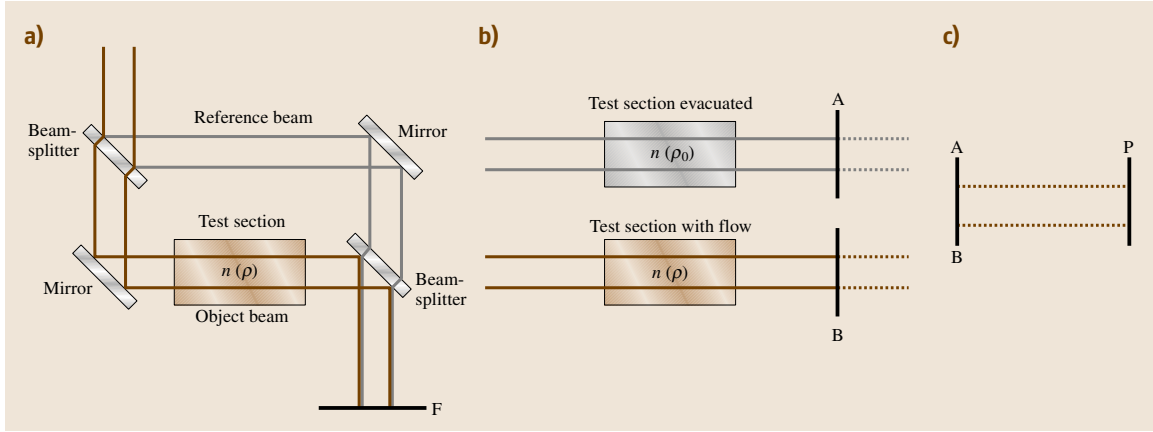
As will be derived later, the intensity, which is measured at the point P, is dependent on the phase shift between the two rays:

$$I \propto \cos \phi.$$

In summary it is clear that the measurement of the intensity or phase shift  $\phi$  at point P is connected directly to the density difference in the two regions.

Using a Mach–Zehnder interferometer, which is shown schematically in Fig. 16.97a, the density in the test section can be evaluated if the density distribution is known at a reference point.

The schematic emphasizes that any imperfection that influences the beams, disturbs the interference in the measurement plane F. To avoid this, the measurement can be performed in two steps (Fig. 16.97b,c). In the first step, the light beam (grey) passing through the evacuated test section is recorded and the subsequently light



**Fig. 16.97a–c** Principle of Mach-Zehnder (a) and holographic interferometry (b,c)

beam (brown) passing through the test section with the flow is recorded in the second step. Both beams are then reconstructed starting from the recording planes A and B are brought to interference in the measurement plane F. Any imperfection within the optical set up is present in both beams, because they pass through the same optical components. As will be shown later, these imperfections cancel out.

To store and reconstruct both beams, a holographic storage technique has to be used. Therefore, this two-step measurement technique is called holographic interferometry.

**Holographic Recording.** Photoactive media is sensitive to the amount of light energy it receives during the exposure time. An electromagnetic wave such as light can be described by specifying the temporal and spatial dependence of its electric intensity vector  $\mathbf{E}$ . A more complete description requires specification of the magnetic intensity  $\mathbf{H}$ , the electric displacement  $\mathbf{D}$ , and the magnetic induction  $\mathbf{B}$ . The present consideration is restricted to  $\mathbf{E}$  because photoactive media respond primarily to the electric field. Let  $E_O(x, y, t)$  be the electrical field strength of an object light wave

$$E_O(x, y, t) = A_O(x, y)e^{i[\varphi_O(x, y) + \omega t]},$$

with amplitude  $A_O$ , phase  $\varphi_O$ , and circular frequency  $\omega$  within an area  $F(x, y)$  at the time  $t$  on the photoactive medium. Then the energy density is

$$W_{\text{phot}} = \frac{E_O E_O^*}{Z} t_B = \frac{A_O^2(x, y)}{Z} t_B,$$

where  $t_B$  is the exposure time, and  $Z$  is the characteristic impedance of the volume in which the light wave

propagates.  $E_O^*(x, y, t)$  is the complex conjugate value of  $E_O(x, y, t)$ . The energy density in this equation no longer contains any information about the phase distribution  $\varphi_O(x, y)$  of the object wave.

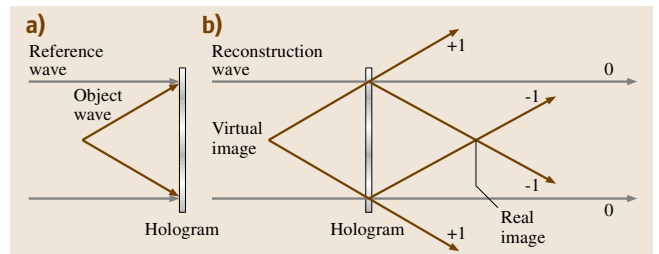
If an interference of the object wave  $E_O(x, y, t)$  with a coherent background in the form of a second light wave,

$$E_R(x, y, t) = A_R(x, y)e^{i[\varphi_R(x, y) + \omega t]}$$

with the same wavelength is generated (Fig. 16.98a), the energy in any point of the photoactive medium is given by

$$\begin{aligned} W_{\text{holo}} &= \frac{t_B}{Z} (E_O + E_R)(E_O^* + E_R^*) \\ &= \frac{t_B}{Z} [A_O^2 + A_R^2 + 2A_O A_R \cos(\varphi_O - \varphi_R)]. \end{aligned}$$

Using this holographic recording technique, it is possible to store the phase-shift between the object and the reference wave. Depending on the phase-shift  $\varphi_O - \varphi_R$ , a distribution of high and low energy density on the area  $F$  (photoactive material) is obtained, leading to a strong



**Fig. 16.98a,b** Holographic recording (a) and holographic reconstruction (b) for a point light source

or weak exposure of the photoactive material. The resulting recorded interference pattern is called a hologram.

**Holographic Reconstruction.** The recorded object wave can be reconstructed by illuminating the developed hologram with a reconstruction wave

$$E_{RC}(x, y, t) = A_{RC}(x, y)e^{i[\varphi_{RC}(x, y) + \omega t]},$$

as shown in Fig. 16.98b.

The reconstruction wave is identical to the reference wave. During the passage of the reconstruction wave through the holographic plate, it is damped depending on the exposure of the holographic plate. Behind the holographic plate a wave is formed that is an identical copy of the original object wave with respect to the distribution of amplitude and phase. The following energy distribution is formed behind the hologram (the exposure time and impedance are neglected)

$$\begin{aligned} E_{RC} W_{\text{holo}} \sim & A_{RC} e^{i(\varphi_R + \omega t)} (A_O^2 + A_R^2) \\ & + A_O A_R A_{RC} e^{i(\varphi_O + \omega t)} \\ & + A_O A_R A_{RC} e^{i(2\varphi_R - \varphi_O + \omega t)}. \end{aligned}$$

The result is a system of three waves. The first term is the reconstruction wave with a modification in the amplitude. The second term is the reconstructed object wave, and the third wave also contains information on the object wave. Discussing the function of the hologram in terms of a diffraction grating, the three waves are identical with the zeroth and first diffraction order of the reconstruction wave. The unchanged reconstruction wave is of zeroth diffraction order. The reconstructed

object wave (*direct wave*) is of the order  $+1$ , while the third wave (*conjugate wave*) is of the order  $-1$ .

**Application of Holographic Interferometry.** An example of the set up of a holographic interferometer, as used at the High Enthalpy Shock Tunnel Göttingen (HEG) of the German Aerospace Center (DLR), is discussed here. In Fig. 16.99, a schematic of this set up is shown. The grey line shows the light path of the reference beam and the brown line shows the light path of the object beam. The object beam passes through the test section and is brought to interference with the reference beam on the holographic plate; here the interference pattern is recorded as discussed in the previous sections. To achieve interference between the object and the reference beams, a light source with sufficient coherence length is needed. In this set up, a seeded Nd:YAG laser from Innolas (model Spitlight 300), emitting light at 532 nm is used. It has a coherence length larger than 1 m. The optical path length of one of the beams is about 15 m. The alignment of the optical path length difference between the two beams in the range of this coherence length allows to set up a functioning optical system.

As discussed above, the first exposure of the holographic plate with one reference beam is done prior to the run in the HEG and a second exposure with the other reference beam is done during the test time. After the chemical treatment of the holographic plate, two reconstruction waves are created in a separate reconstruction unit. The reference waves used in the reconstruction unit are identical to the reference waves used for both exposures. Each of the reconstruction wave forms a system of waves as shown in the previous section. Both reconstructed object waves (described by second term in previous equation) are aligned in such a way that they interfere on a charge-coupled device (CCD) camera behind the holographic plate. Let  $R_1(x, y)$  and  $R_2(x, y)$  be the reconstructed object waves:

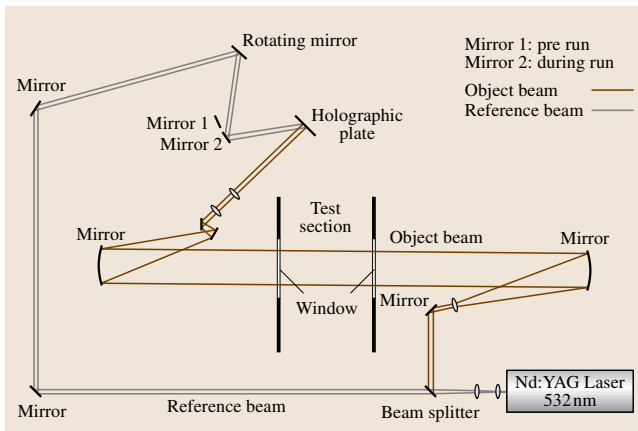
$$R_1(x, y) = A_{O1} A_{R1} A_{W1} e^{i(\varphi_{O1} + \omega t)},$$

$$R_2(x, y) = A_{O2} A_{R2} A_{W2} e^{i(\varphi_{O2} + \omega t)}.$$

Then the resulting energy distribution of the interference pattern on the CCD camera is:

$$\begin{aligned} W_{HI} &= (R_1 + R_2)(R_1^* + R_2^*) \\ &= (A_{O1} A_{R1} A_{RC1})^2 + (A_{O2} A_{R2} A_{RC2})^2 \\ &\quad + 2A_{O1} A_{R1} A_{RC1} A_{O2} A_{R2} A_{RC2} \cos(\varphi_{O1} - \varphi_{O2}). \end{aligned}$$

It is obvious from the last term that the camera sees the phase distribution of the light during the experiment  $\varphi_{O2}$



**Fig. 16.99** Schematic set up of the HEG holographic interferometry system

relative to the phase distribution of the original object wave  $\varphi_{O1}$  before the experiment in the form of an intensity distribution. This intensity  $I(x, y)$  on each pixel of the **CCD** camera is defined by

$$I(x, y) = I_0 \{1 + m(x, y) \cos [\phi(x, y)]\},$$

where  $m$  is a contrast function and  $I_0$  is the background intensity. These terms contain all the amplitude modulations within the interference pattern.  $\phi(x, y) = (\varphi_{O1} - \varphi_{O2})$  is the phase-shift distribution. For the evaluation of the fringe distribution, the phase-shift technique is used. Here the optical path of one of the reconstruction waves is lengthened or shortened by a piezoelectric mirror, thus adding up a known phase shift with respect to the reconstruction wave. Three individual phase distributions are generated:

$$I_1(x, y) = I_0 \{1 + m(x, y) \cos [\phi(x, y) + \Theta_1]\},$$

$$I_2(x, y) = I_0 \{1 + m(x, y) \cos [\phi(x, y) + \Theta_2]\},$$

$$I_3(x, y) = I_0 \{1 + m(x, y) \cos [\phi(x, y) + \Theta_3]\}.$$

This system of equations defined  $\phi(x, y)$ . The background intensity and the contrast function can be determined and thus eliminated from the interference pattern.

As already shown, the phase shift  $\phi(x, y)$  is coupled to the density difference  $\Delta\rho$  by

$$\frac{\phi(x, y)}{2\pi} = \int \left( \frac{\Delta\rho(x, y, z) - \rho_\infty}{\lambda} \sum_{i=1}^S K_i^\lambda \xi_i(x, y, z) \right) dz,$$

where  $K_i^\lambda$  are the Gladstone–Dale coefficients of the gas species,  $\xi_i$  are the species mass fractions,  $S$  is the number of species, and  $\lambda$  is the wavelength of the laser light. The two-dimensional projection of  $\phi(x, y)$  contains line of sight integrated information of the three dimensional flow field. The density difference distribution may be reconstructed from the measurements only if the measured flow field is two dimensional or axisymmetric. In the case of a general three-dimensional flow field, the measurement of the two-dimensional phase shift distribution may be compared to computed line-of-sight integrated phase-shifts, resulting from three-dimensional **CFD**.

### Holographic Interferometry Using Two Wavelengths.

When a gas is heated to a sufficiently high temperature, some electrons are excited to the point where they separate from the nucleus and create a plasma. The refractive index of the plasma is the sum of the refractive indices of the atoms, ions, and electrons weighted by their number densities. The refractive index of the heavy particles

is described by the Gladstone–Dale relation and it is of similar order of magnitude for the different species of a gas. The refractive index of electrons is given by

$$n_e = \sqrt{\left(1 - \frac{N_e e^2 \lambda^2}{2\pi m_e c^2}\right)}.$$

Here  $N_e$  is the number density,  $n_e$  the refractive index,  $e$  the charge, and  $m_e$  the mass of the electron. Evaluation of the constants leads to

$$n_e = \sqrt{(1 - 8.92 \times 10^{-16} \lambda^2 N_e)}.$$

With  $\sqrt{1-x} \approx 1 - (1/2)x$  for  $x \ll 1$ , the equation above can be approximated by

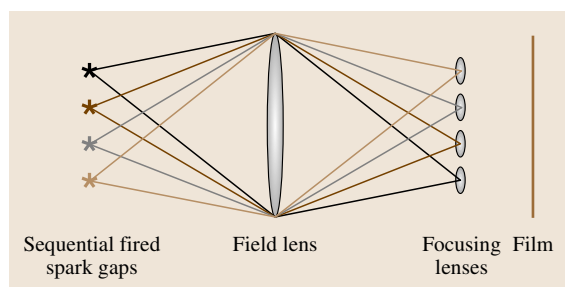
$$n_e - 1 = -4.46 \times 10^{-16} \lambda^2 N_e.$$

It is important to note that the refractive index of electrons is strongly dependent on  $\lambda$ . Further, the contribution of electrons to the refractive index of a considered gas is an order of magnitude higher than the contributions of atomic and molecular species, and is of opposite sign. The electrons therefore dominate the refractive index of moderately and highly ionized plasmas. Because of this strong dispersion, a measurement of the refractive index of the electrons at two different wavelengths at the same time allows to determine the electron density directly from

$$\begin{aligned} n(\lambda_1) - n(\lambda_2) &\cong n_e(\lambda_1) - n_e(\lambda_2) \\ &= -4.46 \times 10^{-16} (\lambda_1^2 - \lambda_2^2) N_e. \end{aligned}$$

Reviews of the initial efforts using this technique are reported by *Zaidel'* et al. [16.166], and *Jahoda* et al. [16.167]. Application of two-wavelength holographic interferometry in a flow created by a superorbital shock expansion tube has been performed by *McIntyre* et al. [16.109].

**High-Speed Flow Visualization.** The principal of flow visualization methods may be subdivided into methods that observe changes in the refractive index, methods that observe particles or tracing elements which have been added to the flow, and methods that introduce energy into the flow converting selected portions of the flow into luminous or visible areas. Most of the high-speed flow visualization (HSFV) systems rely on the first method and are based on the shadowgraph and Schlieren technique, for which the fundamentals are given, e.g., by *Schardin* [16.168], and *Merzkirch* [16.165]. A comprehensive review of shadowgraph or Schlieren techniques is given by *Settles* [16.169]. Further details may also be found in Chaps. 6,11. A comprehensive review



**Fig. 16.100** Schematic of the Cranz–Schardin camera principle

about the current state of high-speed photography and photonics is given by Ray [16.170].

**Light Sources.** To visualize intermittent flow phenomena, it is important to use adequate light sources. If the required exposure times can be achieved by the use of either mechanical shutters for film cameras or by controlling the exposure time of the light-sensitive element in digital cameras itself, continuous light sources may be used.

Continuous light sources that may be used are tungsten–halogen lamps, compact arc lamps, xenon flash tubes and light-emitting diodes (LEDs). Details and more information about continuous light sources are given by Ray [16.170], and Settles [16.169].

The oldest intermittent light sources are spark gaps, which have already been used by Toepler [16.171] and Mach and Salcher [16.172]. In these early days of flow visualization, flash light durations from 0.1–1  $\mu\text{s}$  were achieved. Modern Nanolite spark flash lamps, which are based on the design by Fischer [16.173], achieve flash durations of 5 ns with 20 kHz repetition rates [16.174]. Lasers and laser diodes offer pulse duration times in the

ns range with high repetition rates up to 250 kHz and usually an order of magnitude higher energy than spark gaps. Semiconductor light sources such as LEDs can be pulsed in the sub- $\mu\text{s}$  range.

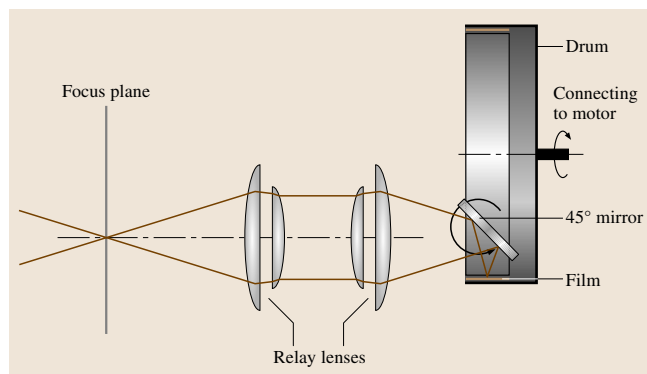
The choice of the light source depends strongly on the application. Lasers and laser diodes offer high energies. However, optical artefacts are introduced, due to the monochromatic and coherent nature of their light. The laser illumination exhibits a binary Schlieren cut-off, and fringes appear due to diffraction which diminish the optical quality of the pictures. Generally, the use of coherent light sources transforms the classical Schlieren set up into a Schlieren interferometer. Broad-band or incoherent white-light sources provide better Schlieren and shadowgraph images, but may not be used in certain applications. Especially in hypervelocity flow environments incorporating large energies, the resulting high level of self-illumination (usually broad-band) overlays the recorded flow pictures. Therefore, using a narrow-band light source like a laser in combination with a filtering system may be the only solution to achieve satisfactory flow visualization.

**High-Speed Cameras.** To record the light representing the flow picture, numerous systems and techniques using photographic film or modern electronic cameras have been used and the development especially in the electronic domain is a quickly developing process. Digital cameras are based on either charge-coupled devices (CCDs) or recently on the complementary metal oxide semiconductor (CMOS) technology. A review of analogue and digital camera systems is given, e.g., by Holzfuß [16.175].

The main question is to achieve sufficiently short exposure times. This can be achieved by either using an adequate intermittent light source with sufficient energy or by using a continuous light source that is interrupted by either a shutter in the optical path, or by the camera system itself. Modern cameras allow short exposure times using electronic shutters.

One of the key developments for high-speed photography was the Cranz–Schardin camera. In Fig. 16.100, a schematic of the principle is shown. The framing rate is controlled by electronically firing the spark gaps one after another. The optical set up allows to record the individual frames at different locations on the film and no moving parts are required.

Other camera types used for high-speed flow visualization are the rotating drum (Fig. 16.101) and rotating-mirror/prism (Fig. 16.102) cameras. In the first case, the film is transported at high speed to record the



**Fig. 16.101** Schematic of a rotating-drum camera



sequential images on different locations of the film. In the latter case a fast rotating prism or mirror is deflecting the light to different locations on the stationary film. Rotating drum cameras reach film speeds up to 300 m/s allowing to record up to 200 images with 50 kHz. To achieve these high speeds the drum housing is evacuated to reduce friction effects. One of the fastest rotating-mirror cameras is manufactured by Cordin. The framing rate is 25 million frames per second. A small turbine rotates the center mirror at 20 000 rotations per second.

The availability of fast and sensitive digital elements led to the development of rotating-mirror systems, where the film is replaced by a number of CCD or CMOS elements.

**Example of a High-Speed Flow Visualization Schlieren Set Up.** The set up shown in Fig. 16.103 is used at the HEG of the German Aerospace Center. It uses a Z-path layout for the object light path with spherical mirrors (Halle SDH4300) with a diameter of 300 mm and a focal length of 1500 mm.

The light source for this set up is a diode pulsed Nd:YAG laser from Lightwave Electronics (Model 612) emitting at 532 nm. It has the capability to operate at pulse rates up to 50 kHz. The laser light is widened by a telescope system (L1 and L2) and then expanded by a lens (L3) onto the spherical main mirror (H1), which aligns the beam to a parallel light-bundle of diameter 300 mm through the test section. On the other side of the test section the beam is collimated by the second spherical main mirror (H2). With the lens L4, the test section is focused onto the film plane (A) and a razor blade (R) is used at the focal point formed by the lens L4. The images are recorded with a Cordin rotating-drum camera (Model 318) on black-and-white film (Kodak TMAX 100). The camera consists of a rotating drum, which is equipped with 35 mm film stripes of 1 m length. The shutter of the camera remains open during the experiment. The narrow pulse width of the laser has a pseudo-framing function during the process of image recording on the moving film. More information about the HEG HSFV system is given by Martinez et al. [16.176].

One application of high-speed flow visualization is to investigate if the flow phenomena that are studied in short-duration ground-based facilities reach a steady state during the available test time. In Fig. 16.104 one such example – the establishment of the hypersonic, high-enthalpy flow past a cylinder – is shown.

The experiment was conducted in HEG at a total specific enthalpy of 15 MJ/kg using air as test gas.

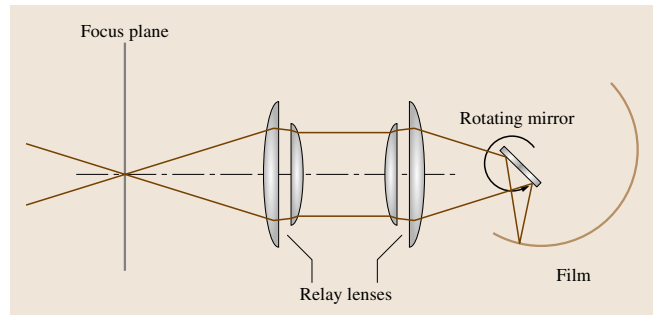


Fig. 16.102 Schematic of a rotating-mirror camera

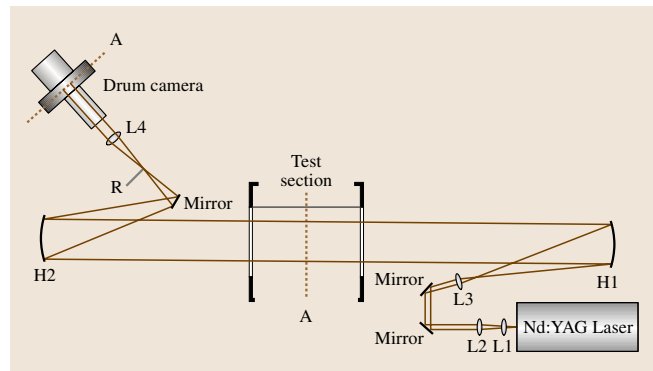


Fig. 16.103 Schematic of a high-speed flow visualization Schlieren set up using a drum camera

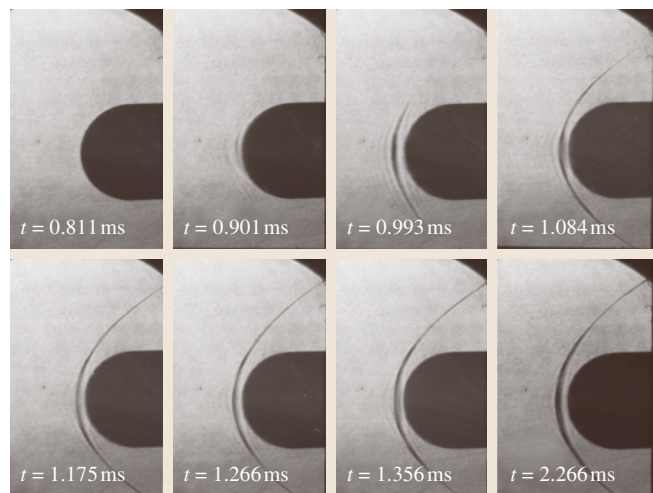


Fig. 16.104 High-speed flow visualization of the establishment of the hypersonic, high-enthalpy flow past a cylinder in the HEG

### 16.2.3 Typical Applications of Shock Tunnel and Shock Expansion Tunnel Facilities

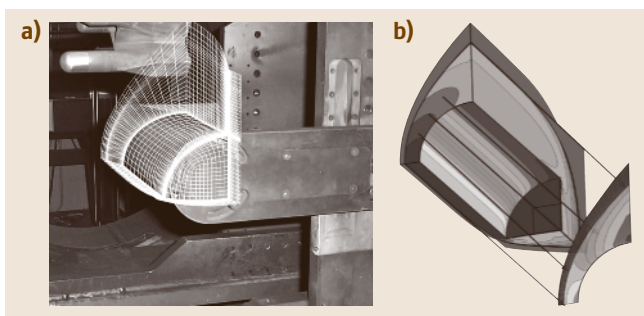
In the subsequent sections, typical applications of shock tunnel and shock expansion tunnel facilities are summarized. The main objective of this overview is to highlight selected work and to refer the interested reader to references which cover the corresponding research in more detail.

#### Hypersonic, High-Enthalpy Flows Past Generic Flow Configurations

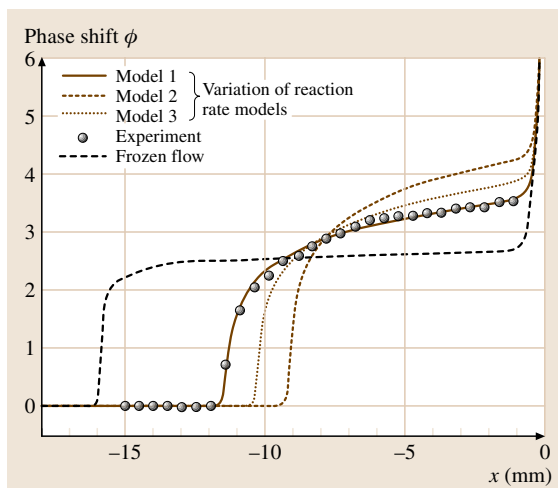
When considering the re-entry trajectory of a space vehicle returning from low Earth orbit into the atmosphere, the most critical point concerning the heating loads on the vehicle is found in the continuum flow region in approximately 70 km altitude. In this region of the re-entry path, the velocity of the vehicle is approximately 6 km/s and the flow past the vehicle is accompanied by strong shock waves, leading to high temperatures that cause dissociation reactions. The fundamental influence of the thermal and chemical relaxation processes caused by these high-temperature effects on the external aerodynamics, i.e., the pressure distribution, flap efficiency, shock–shock and shock–boundary layer interactions and on the heating loads can be investigated by looking at the flow past basic generic flow configurations which are especially designed in order to focus on one of these effects. Additionally, these studies are well suited to validate the ground-based facility performance, measurement techniques and computational fluid dynamics (CFD) codes. A summary of the effects occurring in hypervelocity aerodynamics with chemical nonequilibrium is given by *Stalker* [16.58].

Pioneering work related to the investigation of relaxation processes in the shock layer of generic bodies was performed in the T3 free-piston-driven shock tunnel of the Australian National University in the 1970s. Many of the tests were performed using nitrogen as test gas at total specific enthalpies of 22 MJ/kg and above. One aspect of chemical nonequilibrium generated behind the shock wave of a wedge is that the attached shock wave is no longer straight, as obtained in a perfect gas, but curved towards the wedge surface. The measurement of the shock curvature was used by *Kewley* and *Hornung* [16.177] in order to determine the dissociation rate of nitrogen at high temperatures. The investigation of the relaxation processes on shock detachment on a wedge showed that the detachment distance of the bow shock wave increases gradually with the wedge angle in the case of a relaxing flow and more rapidly in a perfect gas flow [16.178].

In the HEG of DLR, holographic interferometry to measure the density distribution in the shock layer as well as surface pressure and heat flux measurements were applied in conjunction with detailed CFD investigations to study the flow in the shock layer of a cylinder placed with its axis transverse to the flow [16.179]. The experimental data which was obtained at total specific enthalpies of approximately 12–22 MJ/kg for air as the test gas served as a basis for the validation of physico-chemical models used in CFD codes. The cylinder model was mounted on the nozzle centerline (Fig. 16.105a). The large shock stand-off distance generated by this



**Fig. 16.105a,b** Cylinder model in the HEG test section including the grid used for the three-dimensional flow-field computations (a) and line of sight reconstruction of the phase-shift distribution from flow-field computations (b)



**Fig. 16.106** Experimentally and numerically determined phase shift in the shock layer of a cylinder – the influence of using different chemical models is shown

model is advantageous for the investigation of the gas properties in the shock layer using optical measurement techniques. The phase shift distribution in the shock layer of the cylinder which can be correlated to the density difference between the free stream density and the density in the shock layer, was measured and simultaneously reconstructed utilizing three-dimensional flow field computations (Fig. 16.105b). The computations were performed using different chemical reaction rate models. Based on the comparison of the different computed phase-shift distributions and the measurements, the most suitable chemical reaction rate model for the present flow conditions can be selected (Fig. 16.106). The plot in Fig. 16.106 also includes the phase shift distribution resulting from the assumption of frozen chemistry in the shock layer, i.e., infinitely slow reaction rates. It is obvious that the various flow models cause large differences in the shock stand-off distance.

The interaction between a shock wave and a separated region in a hypersonic flow is a very important flow feature which appears for example at aerodynamic control surfaces of re-entry vehicles. In addition to the correct prediction of the pressure distribution on the control surface, the heat transfer and the length of the separation needs to be predicted correctly in the design process of a re-entry vehicle. Generic configurations such as different types of double-cone configurations or hollow cylinder flare configurations were used in the large-energy national shock (LENS) facility at the Calspan–University at Buffalo Research Center (CUBRC) to provide a benchmark dataset at well-calibrated test conditions with fully laminar hypersonic flow [16.180, 181]. These tests were performed using nitrogen as test gas at total specific enthalpies of approximately 4 MJ/kg. Numerical computations of these flow fields using continuum mechanical flow solvers as well as particle methods such as the direct simulation Monte Carlo method were performed by, e.g., Candler et al. [16.182]. In these numerical investigations, issues such as the influence of vibrational freezing in the free stream of the ground-based facility or slip flow boundary conditions on the model were examined.

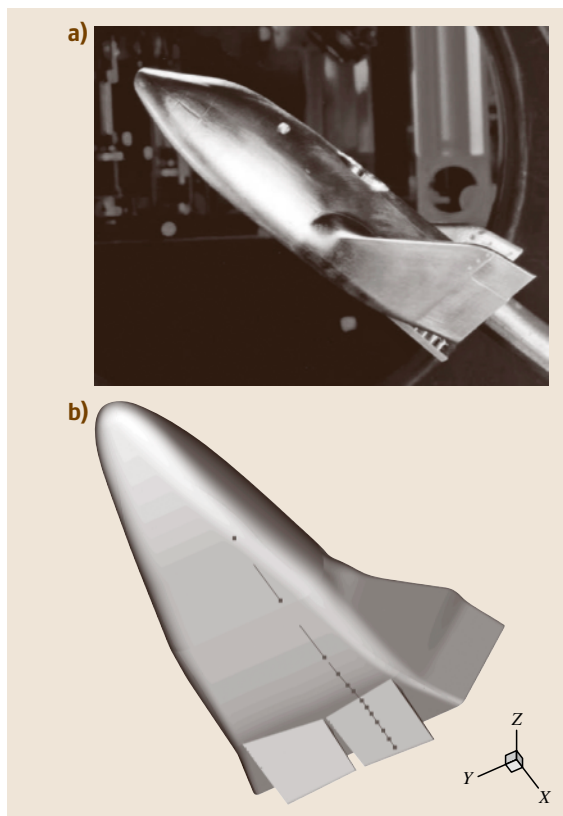
When a weak oblique shock wave impinges on the strong bow shock wave ahead of a blunt body, it is known that the shock–shock interaction pattern can cause extremely high local surface pressure and heat flux on the blunt body. Therefore, the understanding of the phenomena associated with this type of flow is of particular interest for the design of hypervelocity vehicles. The influence of high-temperature effects on the shock–shock interaction generated when an oblique

shock wave interacts with the bow shock of a circular cylinder was investigated by Sanderson [16.183] in the T5 free-piston-driven shock tunnel of Graduate Aeronautical Laboratories, California Institute of Technology (GALCIT), USA and by Schnieder [16.184] in the HEG of the German Aerospace Center.

The shock–boundary layer interaction in hypersonic, high-enthalpy flow including high-temperature effects on wedge-type compression ramps were investigated in the T3 free-piston-driven shock tunnel of the Australian National University in Canberra by Mallinson et al. [16.185], in the T5 free-piston-driven shock tunnel by Davis [16.186] and Davis and Sturtevant [16.187], and in the HEG by Martinez Schramm and Eitelberg [16.188]. These tests covered a total specific enthalpy range of 3–22 MJ/kg.

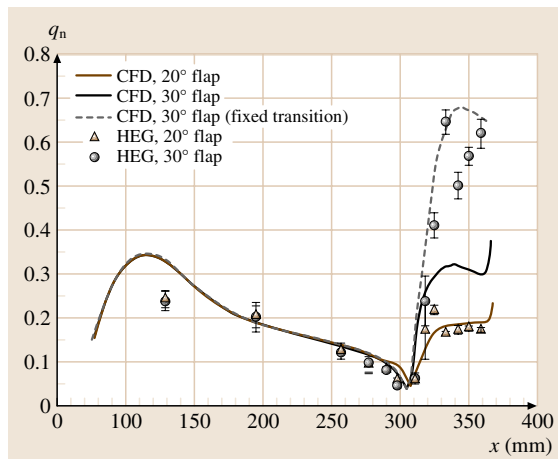
### High-Enthalpy Flows Past Re-entry Configurations

The X-38 program was a joint effort of the US National Aeronautics and Space Administration (NASA) and the European Space Agency (ESA). The objective of this program was to demonstrate the technologies required for the development of the future crew return vehicle (CRV) for the International Space Station (ISS), providing the crew members with the capability to return to Earth in the event of an emergency. Within the X-38 program, the intention was that key design and operational aspects should be validated by flying a full-scale technology demonstrator. The determination of the aerodynamics and aerothermodynamics of the X-38/CRV was based on a close cooperation between ground-based testing and CFD [16.189]. Investigations in the HEG were performed which represented the first experiments using the X-38 configuration in the high total specific enthalpy flow regime up to 22 MJ/kg ( $u_\infty = 6000$  m/s) for pressure and heat flux measurements [16.190]. The stainless-steel 1 : 24-scale wind tunnel model of the X-38, with a length of  $l = 360$  mm, mounted in the HEG test section, is shown in Fig. 16.107a. The positions of the thermocouples used to present the normalized heat flux distribution along a streamwise cut including the body flap in Fig. 16.108 are indicated in Fig. 16.107b. The set of heat flux gauges consists of six transducers on the fore body and seven transducers on the flap. The heat flux measurements and the computed heat fluxes have been normalized using the stagnation point heat flux on X-38. Additionally to the normalized heat flux, the standard deviation of the measured data during the test time window is shown in the Fig. 16.108. The normalized measured and computed heat flux on the 20°



**Fig. 16.107a,b** X-38 model in the HEG test section (a) and locations of the heat flux gauges used in Fig. 16.108 (b)

and 30° deflected body flap using HEG operating condition I (22 MJ/kg) is shown in Fig. 16.108. Except at the first gauge position, where the measured heat flux is significantly lower than the computed one, the comparison between CFD and experiment along the fore body is good. In the reattachment region the measured heat flux distribution shows a clear peak that is not reproduced by the laminar flow computation. At the peak, the heat flux is about 25% higher than that measured further downstream on the flap. It is obvious that in the separated flow region the standard deviation is higher than at neighboring gauge positions located further upstream and downstream. This behavior was consistently reproducible during the test campaign and is regarded as being related to oscillations of the flow in this region. In the reattachment region and further downstream the measured heat flux on the 30° flap is approximately two times higher than the one predicted by the laminar flow computation. Therefore, a computation was performed assuming transitional flow past X-38 with fixed transi-



**Fig. 16.108** Normalized heat flux distributions on the X-38 model; test gas: air at a total specific enthalpy of 22 MJ/kg



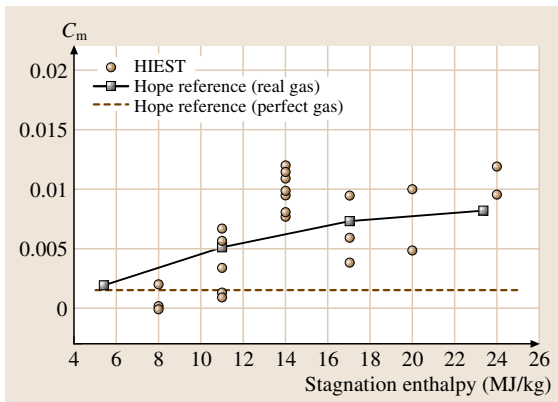
**Fig. 16.109** HOPE 2.5% model equipped with force balance in the Hiest test section (from Itoh et al. [16.132])

tion in front of the body flap hinge line. This result approximately matches the heat flux level at reattachment. However it does not correctly reproduce the measured drop and subsequent increase of heat flux on the flap.

From an engineering point of view the significant increase of the heat flux for the 30° deflected body flap is a very important result indicating that in spite of the fact that the unit free stream Reynolds number of the HEG operating condition would suggest that the flow past the model should be laminar, the flow in the separated flow may be governed by flow instabilities or transitional/turbulent flow. This behavior was also identified on other vehicle configurations and is still in the focus of current research programs.



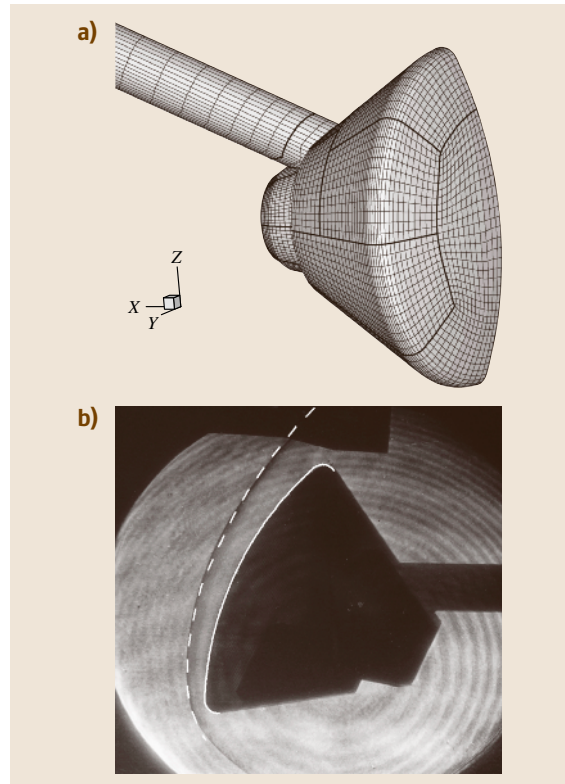
The aerothermodynamics of the Japanese space vehicle HOPE was investigated in the High Enthalpy Shock Tunnel (HIEST) of the Japan Aerospace Exploration Agency (JAXA) at Kakuda [16.132, 191]. The aim of these tests was to prove chemical nonequilibrium effects on the aerodynamics of the HOPE vehicle. In particular, the research was focused on the investigation of the nonequilibrium effect of oxygen dissociation by force measurements in HIEST. The tests were conducted at stagnation enthalpies of 8–24 MJ/kg in which oxygen dissociation probably dominates the nonequilibrium aerodynamic characteristics, and the binary scaling parameter was chosen such that the nonequilibrium dissociating flow around HOPE could be duplicated. The wind tunnel model had a length of  $l = 400$  mm. The forces and pitching moment were measured by a strain gauge force balance with aid of acceleration compensation for the low frequency vibrations of the bending motion of the sting and the pitching motion of the model. The influence of nonequilibrium effects is most pronounced for the pitching moment. The pitching moment coefficient  $C_m$  of HOPE is plotted in Fig. 16.110 as function of the stagnation enthalpy. The measured data is compared with the respective values of the HOPE reference data base which was determined by cold hypersonic testing and nonequilibrium CFD results. The dissociation rate of nitrogen is much smaller than that of oxygen and it was found that except at the nose region almost no dissociation of nitrogen occurs. Except for the subsonic region at the nose where the pressure increases due to dissociation, on the main part of the body and wing, the pressure decreases with oxygen dissociation. Regarding the pitching moment, both the increase in nose pressure



**Fig. 16.110** Pitching moment coefficient as function of stagnation enthalpy for the HOPE space vehicle (after Itoh et al. [16.132])

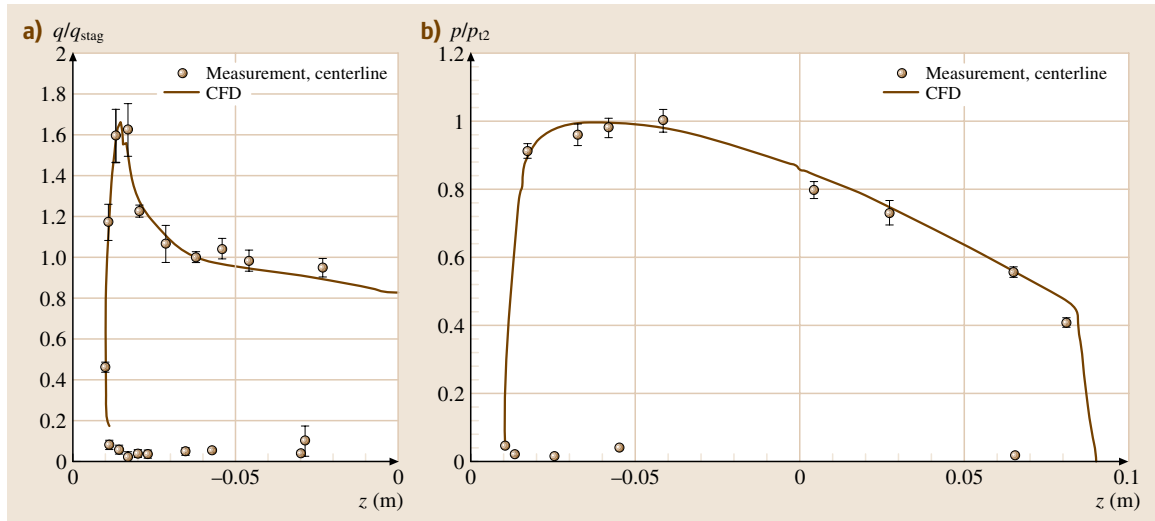
and the decrease in fuselage pressure can increase  $C_m$ . This effect is revealed in Fig. 16.110. Compared to a perfect gas flow which results in a pitching moment coefficient which is independent of the stagnation enthalpy, the measurements in HIEST and the numerical predictions, modeling the nonequilibrium flow past HOPE, result in an increasing  $C_m$  with increasing stagnation enthalpy. In addition, at a total specific enthalpy of 14 MJ/kg, the measurements in HIEST show a peak in the  $C_m$  distribution. Analysis of the ratio of the flow characteristic time and the relaxation time of oxygen dissociation led to the suggestions that this peak may be caused by the chemical nonequilibrium effect of oxygen dissociation, which for the considered flow becomes most critical at this moderate stagnation enthalpy condition.

The successful flight of the atmospheric re-entry demonstrator (ARD) in late 1998 marked the first civil atmospheric re-entry and recovery achieved by European nations. Launched on an Ariane 5 from the Guiana space port in Kourou, the capsule reached a maxi-



**Fig. 16.111a,b** Surface grid for the ARD wind-tunnel model (a), and Schlieren image showing the measured and computed (dashed line) bow shock shape in HEG (b)

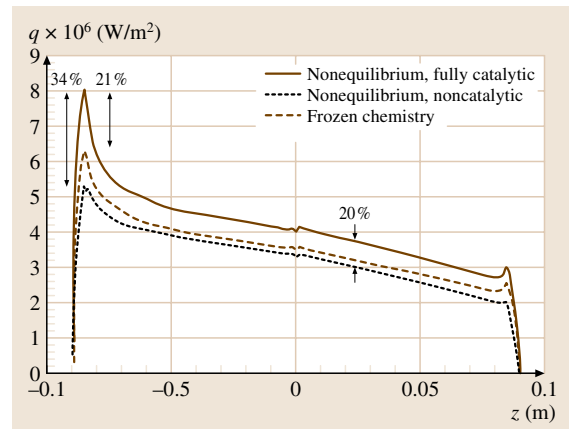




**Fig. 16.112a,b** Normalized heat flux distributions around the windward shoulder (a) and normalized pressure distribution along the centerline (b) of the ARD model;  $h_0 = 12$  MJ/kg

altitude of 830 km before descent to re-entry and splashdown within 5 km of its target point. The project was conducted primarily to validate existing and future ground-based experimental and numerical aerothermodynamic models, to qualify the design of thermal protection materials, and to help assess navigation, guidance and control system performance [16.192]. A post-flight simulation campaign for the ARD capsule has been conducted and coordinated by the prime contractor EADS Launch Vehicles. As part of the campaign, a range of numerical and experimental research work was performed at DLR to reproduce aero heating and aerodynamic data for the capsule in hypersonic flight [16.193]. The scale-model experiments were performed in the HEG using air as test gas at total specific enthalpy conditions of 12–22 MJ/kg. One objective of the work was to help refine and cross-check the available numerical and experimental ground-based simulation facilities through use of a single geometry. In HEG, Schlieren visualization and both surface pressure and heat flux results were recorded. Parallel to these experiments, three dimensional flow field computations were conducted. This combined effort provided results and insight in the advantages and deficiencies of the numerical and experimental techniques that would not be achievable otherwise. The CFD simulations, for example, allowed the effects of flow nonuniformity and the presence of experimental artefacts in the test facility to be assessed. Likewise, comparison with experimental results allowed identification of possible defects in

the numerical solutions. Resembling the geometry of the Apollo capsules, the ARD capsule has a spherical nose and an axisymmetric shape. In Fig. 16.111a the grid around the ARD scale model is shown. It is designed to capture the full flow field around the model mounted on a sting in the shock tunnel. The grid allows assessment of the impact of sting and leeward flow on the forebody flow field. The substantial bluntness of the forebody supports a large subsonic region encompassing most of the windward shock layer, even at high Mach numbers. The size of the subsonic region presented challenges for obtaining good measurements in the short-duration test flows,



**Fig. 16.113** Effect of chemistry models on the centerline heat flux profile on the ARD configuration;  $h_0 = 22$  MJ/kg

and for maintaining accuracy and stability of CFD simulations. All experiments were performed with the ARD scale model mounted at a  $20^\circ$  angle of attack and no yaw. In Fig. 16.112a, the normalized heat flux measurements made along the model centreline around the windward shoulder are plotted together with the computed data. On the windward shoulder the maximum heat flux occurs, and it can be seen from Fig. 16.112a that this peak is well reproduced by CFD. In Fig. 16.112b, the measured and computed normalized surface pressure is shown along the centreline of the ARD configuration. Several CFD computations were performed to estimate the influence and importance of thermochemical processes in the flow field past the ARD capsule in HEG. For an inflow corresponding to a 22 MJ/kg total specific enthalpy HEG operating condition, Fig. 16.113 shows the computed heat flux results along the centreline produced under different chemistry assumptions. The simulations presented were all performed assuming that the gas species remained in thermal equilibrium, since numerical tests showed that thermal nonequilibrium effects were negligible. The figure shows that the default chemistry model – nonequilibrium (finite-rate) chemical reactions with a fully catalytic model surface – results in significantly more heat flux than the frozen-flow assumption. A maximum difference of 21% was observed at the windward shoulder, while a difference of about 14% occurs over most of the remainder of the model forebody. The assumption of a noncatalytic ARD surface also results in a lower heat flux compared to the default chemistry model, differing by a maximum of 34%. The difference in heat flux results can be explained by considering the chemical processes occurring throughout the flow. Under finite-rate reaction chemistry, the molecular dissociation occurring in the shock layer means that some of the gas thermal energy is absorbed as species formation energy. This process is manifested in a much cooler shock layer and smaller shock stand-off, compared to non-reacting (frozen) flow. When the incident flow subsequently impinges on a fully catalytic model surface, species recombination causes the heat of formation to be released and results in an increased heat transfer to the body. In contrast, if the surface is noncatalytic or partially catalytic, then only some of the heat of formation will be recovered immediately with the remainder being swept downstream in the atoms or molecules which have not recombined fully. This process results in the lower heat flux observed for the nonequilibrium–noncatalytic simulation. In the case of frozen flow, where no dissociation or recombination occurs, flow energy acquired from shock heating is stored purely in thermal form and then transferred to

the surface by conduction. The simulated heat flux for frozen flow is lower than for the nonequilibrium–fully catalytic case, because the sudden release of energy due to species recombination does not occur.

As discussed e.g. by McIntyre et al. [16.194] aerocapture is the process in which an interplanetary vehicle acquires sufficient drag for orbit insertion in a single pass through a planet's atmosphere. This process requires that the vehicle enters the lower altitudes, where the atmospheric density, and therefore the drag generated, is sufficiently large. Significant heat flux can result, and this necessitates the development of suitable heat shields, the design being dependent on the entry speed and type of atmosphere. Current aerocapture studies focus on two approaches, the use of the aeroshell and the ballute. In the former, the drag is generated by a forward-facing ablative heat shield on the vehicle. The



**Fig. 16.114** Interferometric flow visualization of the flow past a toroidal ballute in the X2 shock expansion tube; flow from left,  $\text{H}_2$ –Ne test gas representing the atmosphere of Neptune, equivalent velocity 12 km/s (from McIntyre et al. [16.194])

latter approach involves the deployment of a large towed balloon/parachute (ballute) assembly behind the space vehicle that generates equivalent drag at lower densities, and thus indirectly reduces the heat flux on the vehicle.

A configuration consisting of a spherical spacecraft followed by a toroidal ballute similar to the one shown in Fig. 16.114 was investigated in the GALCIT T5 free-piston-driven shock tunnel by *Rasheed et al.* [16.195]. The test gases studied were carbon dioxide, nitrogen and hydrogen to simulate actual future missions to Mars, Titan and Neptune, respectively. The carbon dioxide runs were performed with reservoir pressures ranging from 5 MPa to 30 MPa and total specific enthalpies ranging from 12 MJ/kg to 23 MJ/kg. The nitrogen runs were performed with nominal reservoir pressures from 4 MPa to 10 MPa and nominal total specific enthalpies from 23 MJ/kg to 26 MJ/kg. The hydrogen runs were performed with reservoir pressures from 3 MPa to 25 MPa and total specific enthalpies ranging from 27 MJ/kg to 80 MJ/kg. The data collected for each run consisted of a resonantly enhanced shadowgraph and heat flux data on the ballute ring and the spacecraft. The results in T5 showed that the flow past the space vehicle/ballute configuration is steady. The experimental simulation of the flows in the Mars and Titan atmospheres could be used to permit extrapolation to the flight Reynolds numbers of planned missions with reasonable confidence.

An experimental investigation of hypersonic, high-enthalpy flow over the configuration shown in Fig. 16.114 was conducted in the X2 shock expansion tube facility of The University of Queensland, Australia [16.194]. Imaging using near-resonant holographic interferometry (Fig. 16.114) showed that the flows were steady and not subject of choking except when the opening of the toroid was blocked. Measurements at moderate total specific enthalpy conditions (15–20 MJ/kg) in nitrogen and carbon dioxide showed peak heat fluxes of around 20 MW/m<sup>2</sup> on the toroid. At higher enthalpies (> 50 MJ/kg) in nitrogen, carbon dioxide, and a hydrogen–neon mixture, heat fluxes above 100 MW/m<sup>2</sup> were observed.

### Laminar Turbulent Transition in High-Enthalpy Flows

The knowledge of the transition from laminar to turbulent boundary layer flow on a entry or re-entry vehicle is an important point in the aerothermodynamic design of such vehicles, because, e.g., the prediction of heat flux depends critically on this process. Concerning laminar to turbulent boundary layer transition, one of the important differences between low-speed and hypersonic

flows is that the dominant instability mode in the latter is the second or *Mack* [16.196] mode, in which the boundary layer acts as a waveguide for acoustic noise, where selected frequencies are trapped and amplified, eventually leading to transition. The second important difference is that in high-enthalpy hypersonic flows the relaxation processes associated with vibrational excitation and dissociation provide mechanisms for damping acoustic waves and may therefore be expected to affect the second mode [16.197].

It was pointed out by *Hornung* [16.197], that a large part of the experimental work on the problem of stability and transition at high Mach number has been done in cold, hypersonic ground-based test facilities. These investigations, together with the linear stability analysis by *Mack* [16.196] provide a substantial basis for understanding the path to transition in cold hypersonic flow, however, they are not able to capture the high-temperature effects that occur in hypervelocity flows.

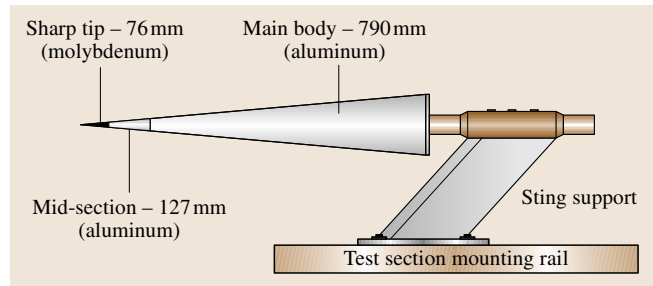
An extensive experimental program on transition in hypervelocity flows was conducted at GALCIT in the T5 free-piston-driven shock tunnel in which the focus was specifically on the regime where relaxation processes associated with vibrational excitation and dissociation are important. A summary of this work is given by *Hornung* [16.197].

As pointed out earlier, the typical test time of free-piston-driven shock tunnels at high-enthalpy conditions is approximately 1–2 ms. Due to the fact that the frequencies of the most strongly amplified modes are typically 1–3 MHz, the short test time is not a serious limitation. The configuration used for the transition experiments in T5 was a slender cone (Fig. 16.115). The flow over this configuration has the advantages that the pressure gradient is zero, and that it is free of side-effects. A 5° half-angle cone was selected in order to be able to compare the new high-enthalpy results with those from cold hypersonic testing. The velocity in the T5 test section ranged up to 6 km/s, and the transition location on the cone as a function of the total specific enthalpy was determined from the distinct rise in heat flux that coincides with the transition process. The Reynolds number at transition, evaluated at the reference temperature [16.197] and based on the distance from the cone tip to the transition location, versus the total specific enthalpy of the flow is shown for different test gases in Fig. 16.116. It is obvious that a significant increase in transition Reynolds number with increasing total specific enthalpy is obtained. This increase is slightly larger in air than in nitrogen. Tests with helium, which behaves like a perfect gas in the T5 total specific enthalpy condi-

tions, revealed that even at 15 MJ/kg, the same transition Reynolds number as at low total specific enthalpy was obtained. Carbon dioxide, which exhibits strong vibrational and dissociational effects in the used enthalpy range lead to a significantly larger transition Reynolds number. These results show that a dramatic transition delay, which is completely absent at low speeds, is evident at high enthalpy, and that the magnitude of the phenomenon and the enthalpy at which it sets in are different for different gases. Linear stability computations performed by Johnson et al. [16.198] agree with the trends observed in T5 and illustrate how strongly thermochemical nonequilibrium effects can influence the growth rate of disturbances (Fig. 16.117). The mechanism responsible for this transition delay is shown to be the damping of the acoustic second-mode instability by relaxation processes. In additional tests in T5 it was demonstrated that transition could be further delayed by up to a factor of two by suitable blind porosity of the surface [16.197].

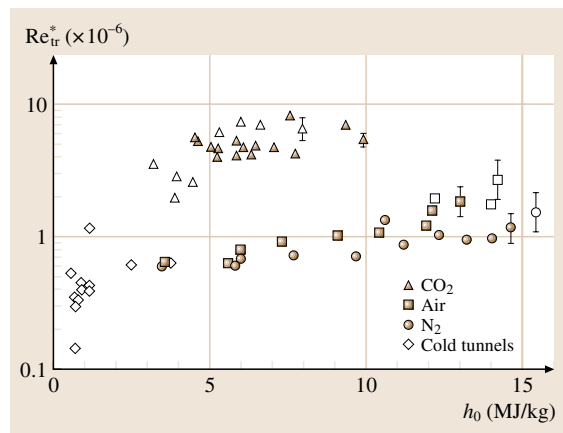
Experiments to investigate the process of boundary layer transition in hypervelocity boundary layers were performed in the T4 free-piston-driven shock tunnel at The University of Queensland, Australia by Mee and Goynne [16.200], Mee [16.201]. An array of flush-mounted thin-film heat flux gauges was used to measure surface heat flux and to detect the location and extent of the transitional region on a 1500 mm-long 120 mm-wide flat plate that formed one of the inner walls of a duct that captured the core flow of the test section. The thin-film gauges, manufactured at The University of Queensland, consisted of a nickel film, 1 mm long  $\times$  0.3 mm wide  $\times$  1  $\mu$ m thick, deposited onto a fused-quartz cylinder of 2.1 mm diameter. The gauges and associated instrumentation were estimated to have response times of 2  $\mu$ s. The experiments were performed in a test gas of air at nozzle supply enthalpies of 6 and 12 MJ/kg. At the lower total specific enthalpy condition the unit Reynolds number (based on free-stream conditions) was varied from  $1.7 \times 10^6 \text{ m}^{-1}$  to  $4.9 \times 10^6 \text{ m}^{-1}$ . At the high-enthalpy condition, the unit Reynolds number was  $1.6 \times 10^6 \text{ m}^{-1}$ . A typical heat flux distribution along the test surface with a smooth surface is shown in Fig. 16.118. The measurements indicate the transition of the boundary layer from a laminar region to a turbulent region along the test surface.

The detailed analysis of the measurements obtained in T4 by the individual thin-film gauges showed that transition takes place through initiation, growth and merger of turbulent spots in the considered flat plate hypervelocity boundary layer. The rates of initiation and growth of turbulent spots appear to be the factors which



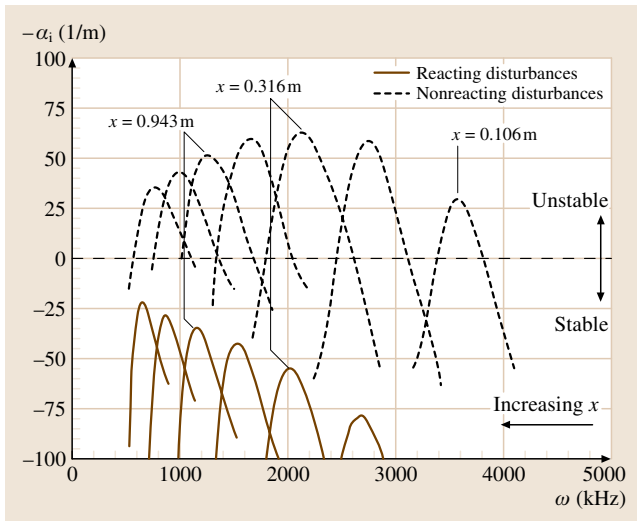
**Fig. 16.115** Slender cone model used for the transition experiments in T5; the main body is hollow and instrumented with thermocouple surface heat flux gauges (after Hornung et al. [16.199])

will determine the length of the transition region. It was found that the spanwise extent of spots can be identified and spreading rates can be determined. Further experiments in T4 showed that earlier transition can be promoted by using both isolated and distributed roughness elements. Using distributed roughness elements located 100 mm downstream of the plate leading edge with a ratio of roughness element height to boundary layer thickness of 1.1 leads to the result in Fig. 16.119. The distributed roughness elements caused earlier transition at the low- and high-enthalpy condition used for the testing. An isolated rounded roughness element with a height 50% of the boundary-layer thickness was found



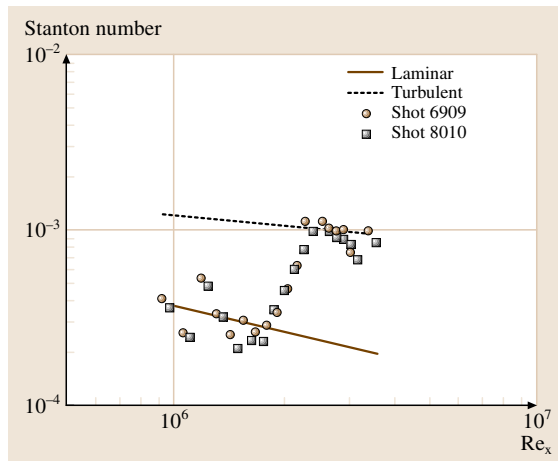
**Fig. 16.116** Transition Reynolds number evaluated at reference conditions as function of total specific enthalpy for different test gases. Open symbols correspond to cases where the flow was laminar to the end of the cone. The references for the cold tunnel data are given by Hornung [16.197]; the carbon dioxide results show a large transition delay relative to the nitrogen and air results (after Hornung (2006) [16.197])



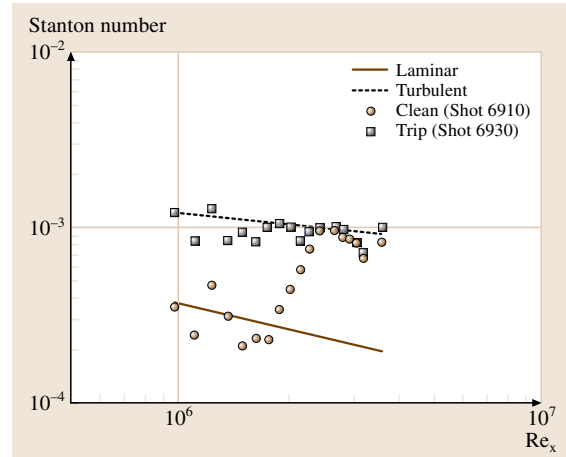


**Fig. 16.117** Results of linear stability calculations with thermochemical nonequilibrium at the conditions of T5 (4.0 MJ/kg in carbon dioxide); the diagram shows growth rate of disturbances as function of disturbance frequency at several distances along the cone; the dotted curves show the results at the same conditions as for the continuous curves but with the rate processes turned off [16.198] (after Hornung [16.197])

to be capable of producing a turbulent patch immediately behind the element.



**Fig. 16.118** Dimensionless mean heat flux along the test surface resulting from two different T4 runs [ $h_s = 6.2 \text{ MJ/kg}$ ,  $Re = 2.6 \times 10^6 \text{ m}^{-1}$  (based on free-stream conditions)]; the continuous and dashed lines indicate laminar and turbulent heat flux levels obtained from empirical correlations (after Mee [16.201])



**Fig. 16.119** Dimensionless mean heat flux along the test surface [ $h_s = 6.2 \text{ MJ/kg}$ ,  $Re = 2.6 \times 10^6 \text{ m}^{-1}$  (based on freestream conditions)] for the smooth surface (circles) and distributed roughness elements located 100 mm downstream of the plate leading edge (squares); the continuous and dashed lines indicate laminar and turbulent heat flux levels obtained from empirical correlations (after Mee [16.201])

The same test geometry as used by Mee [16.201], was used by Goyne [16.140], and Goyne et al. [16.142] to conduct skin friction measurements in laminar, transitional and turbulent boundary layers in addition to pressure and heat flux measurements. The tests were performed in a total specific enthalpy range of 4–13 MJ/Kg and a Reynolds number (based on the distance from the leading edge) range of  $0.16\text{--}21 \times 10^6$ . For the transitional boundary layer, the characteristics of turbulent spots were investigated and similar results were obtained using heat flux and skin friction measurements.

### Supersonic Combustion Ramjet Research

The goals to reduce the specific transport costs and to increase the reliability and flexibility of new transportation systems require that future space programs develop partly or fully reusable vehicles with improved propulsion systems. The supersonic combustion ramjet (scramjet), an air-breathing propulsion concept, is one option for a new and advanced type of engine to be operated at flight Mach numbers above  $M = 8$ . The efficiency gains of such engines potentially allow improvements in size of payload, cost/kg and reliability of future launch vehicles.

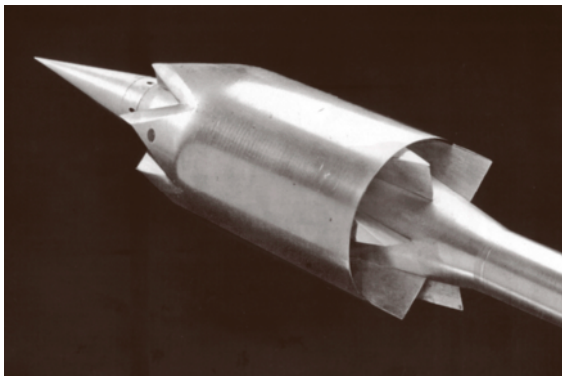
Recently significant advances have been made in developing scramjet engines, including The University



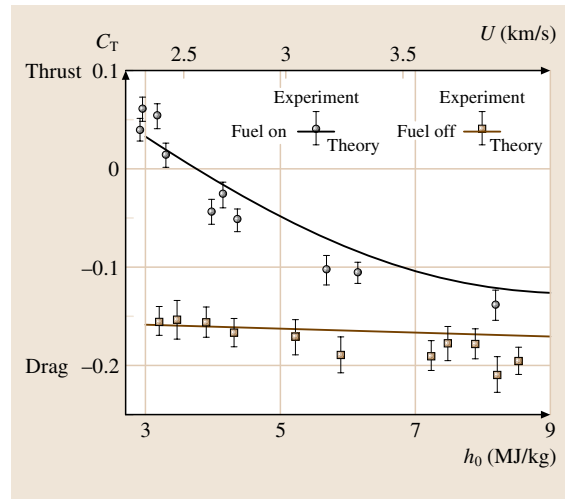
of Queensland's supersonic combustion flight experiment HyShot [16.202] with its first successful flight performed in July 2002 and the flights of NASA's X-43A in March and November 2004 as part of the Hyper-X programme [16.203,204]. Supersonic combustion had not occurred in flight until the performance of HyShot and it had not been used in an engine which propelled a flight vehicle until the X-43A flight of March 2004 [16.205]. Ground-based testing in reflected shock tunnels and a shock expansion tunnel represent significant contributions to these flight experiments.

Test techniques and strategies for large scale scramjet testing in large reflected shock tunnels are discussed by *Deiwert et al.* [16.207]. For the Ames 16-Inch deflagrative combustion-driven shock tunnel, large- to full-scale scramjet combustor test capabilities over the flight Mach number range 12 to 16 are reported.

The extensive scramjet research conducted in Australia in the T3 and T4 free-piston-driven shock tunnels was summarized by *Paull and Stalker* [16.208] and *Stalker et al.* [16.205]. The research programmes conducted in these facilities include the investigation of the thrust/drag performance of an integrated axisymmetric scramjet configuration consisting of intake, combustor and thrust nozzle, shown in Fig. 16.120 with a stress wave force balance by *Paull et al.* [16.206]. The model consists of an axisymmetric center body, with six combustion chambers and associated intakes arranged about its periphery. These intakes consist of compression ramps formed by the splitters which separate the combustion chambers. The thrust coefficient determined for this configuration as function of the total specific



**Fig. 16.120** Integrated axisymmetric scramjet model used in the T4 free-piston-driven shock tunnel of The University of Queensland, Australia for net thrust measurements [16.206] (picture courtesy A. Paull, The University of Queensland)



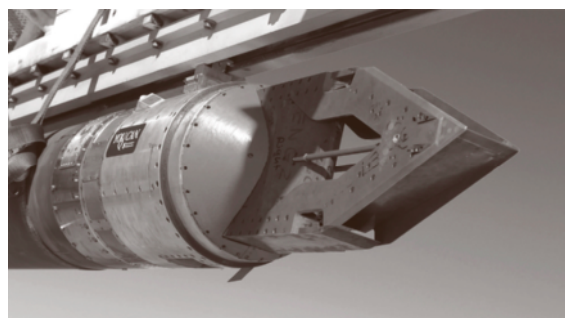
**Fig. 16.121** Performance of the axisymmetric integrated scramjet model of Fig. 16.120; measured thrust coefficient for fuel off (*squares*) and fuel on (*circles*) versus total specific enthalpy and test section free-stream velocity; the lines indicate the calculated thrust coefficients [16.205,206]

enthalpy of the flow and the test section free-stream velocity is shown in Fig. 16.121. The measured data points for fuel-on and fuel-off experiments are plotted together with two continuous lines indicating calculated axial forces. The important result of this investigation is that the difference between the fuel off and the fuel on data clearly shows the generation of thrust and for stagnation enthalpies below approximately 3.5 MJ/kg, positive net thrust could be demonstrated in a ground-based test facility.

The HyShot supersonic combustion flight experiment was led by The University of Queensland in Australia with contributions from a number of international partners [16.202]. The scramjet payload was launched by an unguided sounding rocket from the Woomera launch range in Australia on a highly parabolic trajectory to an altitude in excess of 328 km. The scramjet experiment was conducted during re-entry, and consisted of a double-wedge intake with two back-to-back constant-area combustion chambers, one fueled with hydrogen at an equivalence ratio of about 0.33, and the second unfueled (Fig. 16.122). In the fueled combustor, gaseous hydrogen was injected perpendicularly to the flow through a series of four portholes (Fig. 16.123a). Supersonic combustion data was successfully collected at flight Mach numbers of approximately  $M = 7.8$ – $7.95$  in an altitude range from 35 km down to 29 km [16.209].

As part of the HyShot flight programme, extensive ground-based testing of the supersonic combustion experiment was performed in the T4 free-piston-driven shock tunnel. These experiments included pre- as well as post-flight test campaigns. An experimental and numerical post-flight analysis was also conducted at the German Aerospace Center, and the European Space Research and Technology Center (ESTEC) of the European Space Agency (ESA) [16.210, 211]. The experiments were performed in the HEG. The flow path geometry of the wind tunnel model used in the HEG HyShot post-flight analysis was identical to the flight configuration. A comparison between the measured and calculated surface pressure distribution in the combustion chamber for a HEG operating condition which duplicates the HyShot flight condition at an altitude of 32.5 km is shown together with the surface pressure of the fueled combustor measured in flight in Fig. 16.123b. The scatter bars of the HEG measurements indicate the root-mean-square (RMS) values of the pressure during the test time. The fuel-off static surface pressure obtained from CFD analysis compares well with the wind-tunnel experiment. Further, the pressure gain due to fuel injection in the HEG measurements is obvious. While some issues concerning the quantitative comparison of the ground-based, flight and CFD data are not yet fully resolved, the post flight analysis in HEG confirmed the interpretation of the flight data that supersonic combustion was successfully established.

A modification of the HyShot configuration used in the first and second flight of the programme was developed at the Japan Aerospace Exploration Agency (JAXA) using the High Enthalpy Shock Tunnel (HIEST) [16.212]. In this configuration, the porthole injection is

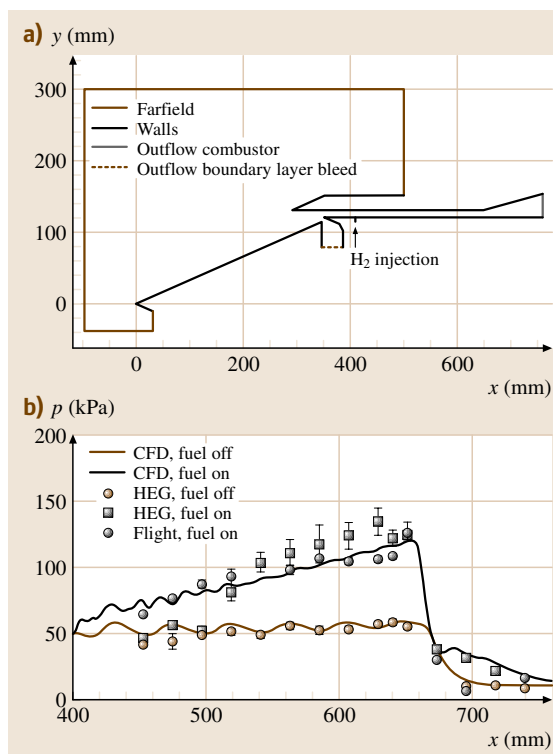


**Fig. 16.122** HyShot supersonic combustion flight experiment configuration, used during the first two flights of the programme, mounted on top of a two-stage sounding rocket at the Woomera launch range in Australia (Photo courtesy The University of Queensland)

replaced by a *HyperMixer* injection which utilizes generators of longitudinal vortices to enhance the supersonic air flow fuel mixing and the combustion process.

Further scramjet research performed in HIEST is presented by Itoh et al. [16.132]. An integrated scramjet configuration of 2 m length was investigated in the total specific enthalpy range of 3.3–7.5 MJ/kg which corresponds to the flight Mach number range of 7–13. The model was suspended by very thin wires and could move freely in the test section. Therefore, using the 13 accelerometers integrated on the model, the thrust/drag characteristic of the engine as a function of the fuel equivalence ratio and the stagnation enthalpy was investigated.

As part of the NASA Hyper-X programme, the X-43A (Fig. 16.124), a small-scale research vehicle to provide flight data for a hydrogen-fueled, airframe-integrated scramjet engine at flight Mach numbers



**Fig. 16.123a,b** HyShot supersonic combustion flight experiment configuration, used during the first two flights of the programme, geometry of the fueled combustor including the boundary conditions for the CFD analysis (a) and computed and measured pressure distributions in the fueled and unfueled combustor; flight altitude: 32.5 km (b)

of 7 and 10 was developed [16.204]. In addition, aerodynamic, thermal, structural, guidance, flush-air-data-system, and other data were to be obtained. The 3.66 m-long research vehicles were dropped from the NASA Dryden B-52, rocket-boosted to the test point by a modified Pegasus first stage, separated from the booster, and then operated in autonomous flight. The flight tests were conducted at an altitude of approximately 30 km.

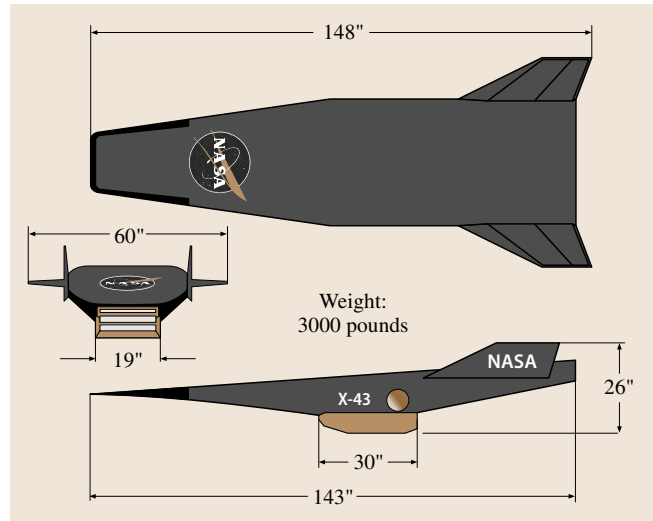
Tests of the Hyper-X scramjet engine flow path have been conducted in the HYPULSE shock tunnel facility of ATK-GASL in Ronkonkoma, USA at conditions duplicating the stagnation enthalpy at flight Mach numbers of 7, 10, and 15 [16.213, 214]. For the tests at Mach number 7 and 10, HYPULSE was operated as a reflected shock tunnel; at Mach number 15, HYPULSE was operated as a shock expansion tunnel. A data base for the operation of the scramjet was obtained by variation of a number of flow parameters including the fuel equivalence ratio from lean to rich and the fuel composition from pure hydrogen to mixtures of 2% and 5% silane in hydrogen by volume to aid ignition.

Comparisons of the ground test data with selected data from the successful  $M = 10$  flight showed good agreement for HYPULSE test runs in which the hydrogen fuel was augmented with silane to prompt ignition and combustion. Comparisons of tare data acquired without fueling the flow in both ground test and flight operation also exhibited very good agreement, confirming that scramjet testing in the ms time scale available in shock tunnels does provide meaningful data [16.214], thereby expanding the ground test regime for hypersonic air-breathing propulsion concepts.

### Hot Model Technique

The requirement of ground-based testing at high total enthalpies and high pressures to properly duplicate high temperature effects leads to facilities with typical test times in the order of ms. Therefore, in these facilities the ratio of total temperature to wall temperature of a wind tunnel model can be approximately simulated, however, the absolute temperature of the model surfaces stays at room temperature. In order to overcome this partially, heated models were used in the shock tunnel facilities.

The influence of wall temperature on the shock wave/boundary layer interaction on a ramp configuration in hypersonic flow was investigated in the shock tunnel TH2 at the RWTH Aachen University, Germany [16.215]. For these investigations, TH2 was operated with the conventional and the heated helium



**Fig. 16.124** X-43A vehicle geometry; measures in inches (after Voland et al. [16.204])

driver. The model surface was heated by electric heater elements. Actively cooled gauges to measure pressure and temperature (coaxial thermocouples) were integrated in a model and color Schlieren and infrared thermography were additionally applied. The ramp model consisted of a sharp leading edge flat plate at a  $0^\circ$  angle of attack and a second plate at  $15^\circ$  angle of attack. The total specific enthalpy was varied between 1.68 MJ/kg (total temperature 1520 K) and 4.12 MJ/kg (total temperature 3630 K) and the wall temperature could be varied between 293 K and 840 K. Using pressure measurements, the influence of the wall temperature and the stagnation conditions on the size of the separation bubble generated in the hinge line region was demonstrated for a flow that was laminar before the separation and possibly transitional at reattachment. At constant total temperature and increasing wall temperature, the size of the separation bubble increased. Increasing the total temperature at constant wall temperature led to a reduction of the size of the separation bubble. Furthermore, the pressure level in particular at reattachment increased with increasing wall temperature.

In atmospheric re-entry flight with a high level of aerodynamic heating, the utilization of low-catalytic surface materials, such as  $\text{SiO}_2$ -based materials, is desired in order to minimize the increase in vehicle surface temperature by reducing the recombination of atomic species at the wall. From experiences of ground and flight tests, it has been suspected that surface catalysis

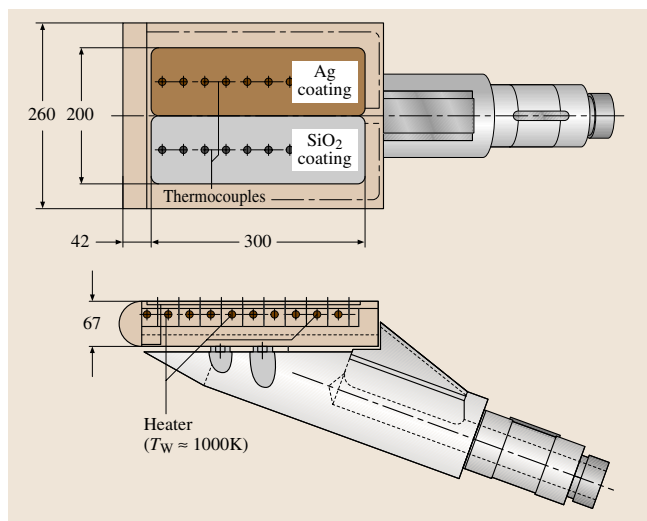
may strongly depend on changes in surface temperature and density. However, the detailed characterization of surface catalycity is still an actual research topic, mainly due to the lack of experimental data at sufficiently high density equivalent to flight conditions, since ground tests have been conducted mainly in low-density facilities such as arc-heated wind tunnels and plasma wind tunnels. High-density flows can be generated in high-enthalpy shock tunnels, however, the short available test duration is a severe drawback. Starting with room temperature, the wall temperature of test models in shock tunnels increases by only a few degrees. Therefore, an experimental research program to study the influence of the wall temperature on wall catalysis was conducted in the **HIEST** of **JAXA** utilizing a preheated wind tunnel model [16.132].

The test model was a 373 mm-long 260 mm-wide flat plate with blunt leading edge (Fig. 16.125). Silicon dioxide, as a material with low catalycity, was used to coat one half of the flat plate and silver (Ag) was used to coat the second half, providing the reference for a highly catalytic material. Heat flux measurements were performed using 10 thermocouples mounted in line on both sides. The surface catalycity effect was investigated by comparing the heat fluxes measured on the  $\text{SiO}_2$  surface with those obtained with the Ag coating or with **CFD** results. Heaters were installed in the model which allowed wall temperature adjustment from 300 K to 1000 K. The tests in **HIEST** were carried out at 14 MJ/kg total specific enthalpy and 20 MPa nozzle reservoir pressure. From **CFD**

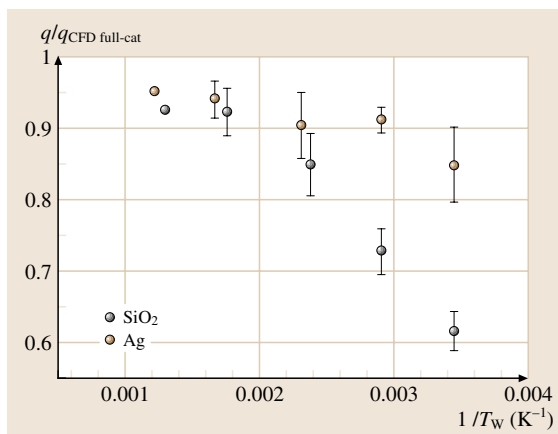
analysis, it was found that most of the oxygen molecules should be dissociated in the high recovery temperature region in the hypersonic boundary layer near the wall, and the increment in heat flux due to recombination by wall catalysis was estimated to be 40% of the total heat flux. The experiments were conducted at wall temperatures of up to 800 K and the results are summarized in Fig. 16.126. The measured heat flux is normalized by the fully catalytic **CFD** results and subsequently averaged over the flat plate and plotted as function of the inverse of the wall temperature. A strong temperature dependence of the surface catalysis of the  $\text{SiO}_2$ -coated surface was observed from room temperature up to 570 K, as the normalized heat flux increased with wall temperature. It is pointed out by *Itoh et al.* [16.132], that the temperature dependence of surface catalysis appears at a relatively low temperature in the tests performed in **HIEST** compared to data obtained in lower-density wind tunnel tests where this dependence is found in the 400–800 K range. It is concluded that this early appearance of the temperature dependence of surface catalysis may be associated with the higher-density operation in the shock tunnel.

The same model as shown in Fig. 16.125 was also tested in **HEG** of **DLR** by *Ueda et al.* [16.216]. As part of this comparative study performed in two large free-piston-driven shock tunnels, the same trend concerning the temperature dependence of the surface catalycity of  $\text{SiO}_2$  as first observed in **HIEST** was also found in **HEG**.

One concept for improving the efficiency of scram-jet engines is that of injecting the fuel on the intake.



**Fig. 16.125** Heated flat plate model used in **HIEST** (after *Itoh et al.* [16.132])



**Fig. 16.126** Temperature dependence of the catalytic behavior of the  $\text{SiO}_2$  surface obtained in **HIEST**; the data points show averaged values over the plate (after *Itoh et al.* [16.132])

The fuel injection before the combustion chamber allows the fuel to mix with the air prior to entering the combustion chamber and the length of the combustion chamber required for complete combustion is therefore reduced. Extensive testing of this concept has been conducted in the T4 shock tunnel facility at The University of Queensland, Australia. In contrast to real flight conditions, the wall temperature will only marginally increase during the available test time in T4. Therefore, realistic wall temperatures similar to those achieved in flight and the influence of the wall temperature on premature ignition on the intake can only be investigated by using a preheated model. For this reason, cold wall intake experiments were compared with experiments using a heated intake model with wall temperatures up to 700 K for total specific enthalpy conditions of 3.6 MJ/kg [16.149]. In the considered boundary layers

on the intake, temperatures exist close to the wall that are, for both the unheated and heated model, significantly higher than the wall temperatures. These peak temperatures are above the ignition temperature of hydrogen. Therefore, the intake fuel injection must be performed in such a way that the fuel does not penetrate this region close to the wall downstream of the injection location. Planar laser-induced fluorescence using hydroxide (OH) radicals as the target species to identify regions where combustion occurs and pressure measurements on the intake were performed. No hydroxide was observed on the intake when the wall temperature was varied from 300 K to 700 K. Furthermore, no static pressure increase was observed along the intake model. These factors indicate that no premature combustion of hydrogen was occurring for the investigated flow fields.

## 16.3 Bluff Body Aerodynamics

### 16.3.1 Flow Physics, Facilities, and Approach

Bluff body wakes are complex; they involve the interactions of three shear layers in the same problem, namely a boundary layer, a separating free shear layer, and a wake. As has been remarked by *Roshko* [16.217], “the problem of bluff body flow remains almost entirely in the empirical, descriptive realm of knowledge”, although our knowledge of this flow is extensive. In fact the recent surge of activity on wakes, over the last two decades, from experiment, direct numerical simulation and analysis has yielded a wealth of new understandings.

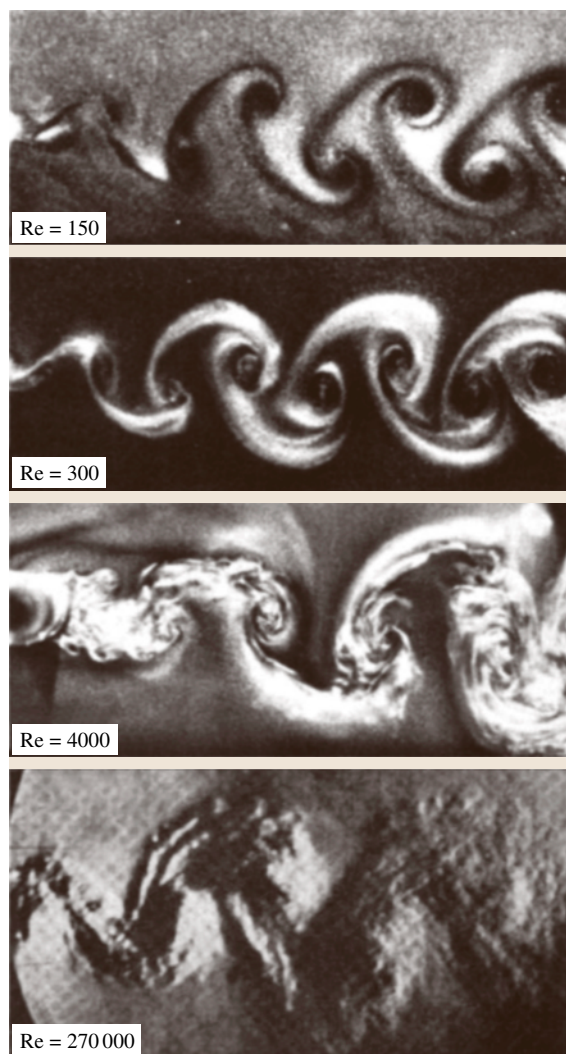
In this section, we shall briefly present the *experimental* approaches to studying bluff-body flows. However, rather than simply list the approaches and techniques used to study such flows, we shall present the different quantitative and qualitative approaches that have been employed, while at the same time presenting some of the fascinating, rich, and sometimes beautiful, physical phenomena that have been found in bluff body flows, as one progressively increases the Reynolds number (Reynolds number =  $Re = UD/\nu$ , where  $U$  is the free-stream velocity,  $D$  is the width of the body and  $\nu$  is the kinematic viscosity). We shall also present some of the key nondimensional parameters as a function of  $Re$ , and functional relationships to represent these variations in practice.

The nominally *two-dimensional* vortex-shedding process from bluff bodies has been described in

a number of review papers over the last 50 years (*Rosenhead* [16.218]; *Morkovin* [16.219]; *Berger and Wille* [16.220]; *Oertel* [16.221]; *Coutanceau and Defaye* [16.222]; *Roshko* [16.217]; and *Williamson* [16.223]). In experiments, significant steps forward in our understanding of wake vortex dynamics have come from the many recent studies of three-dimensional (3-D) phenomena, which have led to some new explanations of longstanding controversies which were hitherto assumed to have two-dimensional origins (see the recent review of *Williamson* [16.223]).

Bluff-body wake flows have direct engineering significance. The alternate shedding of vortices in the near wake, in the classical *vortex street* configuration, leads to large fluctuating pressure forces in a direction transverse to the flow, and may cause structural vibrations, acoustic noise, or resonance, which in some cases can trigger failure. A recent review of vortex-induced vibrations arising from such effects can be found in *Williamson and Govardhan* [16.224]. The classical view of a *vortex street* in cross section is shown in Fig. 16.127, where regions of concentrated vorticity are *shed* into the downstream flow from alternate sides of the body (and with alternate senses of rotation), giving the appearance of an upper row of negative vortices and lower row of positive vortices. Interestingly, it will be shown later that these particular cross-sectional photographs actually contain useful information regarding the distribution of the *three-dimensional* vortex structure (see the figure caption).





**Fig. 16.127** Visualization of laminar and turbulent vortex streets. These photographs show the development of Karman vortex streets over a wide range of  $Re$ . Streamwise vorticity, in the *braid* between Karman vortices, is indicated by the white regions, and is visible for  $Re = 300$  up to the highest  $Re = 270\,000$ . The aluminium flake visualizations are from Williamson [16.223, 227]. The Schlieren photograph at  $Re = 270\,000$  is from Thomann [16.228]

These visualizations in Fig. 16.127 come from a thin light sheet shining on aluminium flakes suspended in water in the wake of a towed vertical circular cylinder. Visualizations of the cross sections of such vortices are often made in water, using ordinary dye, as well as using fluorescent dye employing the laser-induced fluo-

rescence (LIF) technique, examples of which are shown later in Figs. 16.137, 138. Surface particle techniques, using aluminium flakes on the water surface were originally used to excellent effect by Prandtl in the 1920s, and have also been employed more recently by Williamson and Roshko [16.225], for example. Subsurface particle visualization will be seen here from a study by Mills et al. [16.226] in Fig. 16.129. Hydrogen bubble wires in water, employed by Rockwell and his group at Lehigh University have also been extremely effective, and an example may be observed in Fig. 16.139. Rockwell at Lehigh University, and Gharib at Caltech, have also been pioneers in the development of the particle image velocimetry technique (PIV) in the field of research concerning bluff bodies. An excellent example of this approach can be found from Rockwell's group, showing near-wake vortex dynamics in Fig. 16.140.

In air, visualization has been conducted using smoke from arrays of tubes, but also from the very effective smoke wire technique introduced in the 1950s, and optimized by Hassan Nagib and Tom Corke at IIT (Cimbala et al. [16.229]; Corke et al. [16.230]; and Goldstein [16.231], which is also an excellent reference for several of these techniques). In Fig. 16.127, we also see an example of a Schlieren photograph of a vortex street at  $Re = 270\,000$ , where the variation of density in the flow is exploited in this case. In essence, there are a number of flow visualization techniques, which can lead to new discoveries in these flows, as well as to beautiful images of significant fluid flow phenomena.

Facilities in use for studies of bluff-body aerodynamics include not only wind tunnels, but also water facilities. For example, in our vortex dynamics and wake studies at Cornell, we utilize very low-turbulence wind tunnels, along with a recirculating water channel, which is indispensable for providing continuous flow. However, the use of a computer-controlled XY towing tank is extremely powerful, in that quite unsteady motions to bodies (periodic or transient) can be imparted in two degrees of freedom to bodies in the large ( $8\text{ m} \times 1.25\text{ m} \times 1.25\text{ m}$ ) facility. One of the other key aspects of such a facility is the fact that one can study flow structures far downstream of a body, by waiting long times after the body has passed the region of interest. A further facility often used over the last few decades is the closed-circuit water tunnel, whose test section is enclosed, unlike the water channel. Other facilities for high-speed flows include shock tubes, which are described elsewhere in this book. A good resource for discussion of all the above facilities for use in bluff body aerodynamics, and the

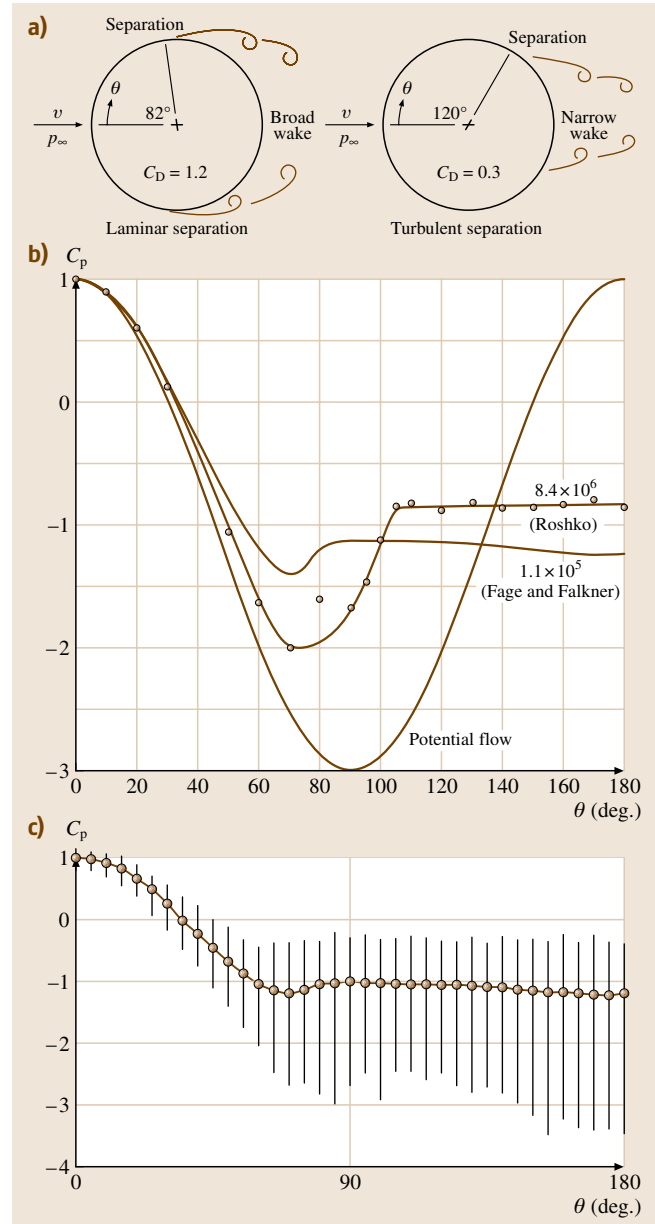
**Fig. 16.128a–c** Pressure measurements for a cylinder with laminar or turbulent boundary layer separation. A laminar boundary layer separates at an angle of around  $82^\circ$  (see (a)) leading to the pressure distribution from Fage and Falkner [16.232] in (b). At a higher Re, as plotted by Roshko [16.233] in (b), the separation point shifts to higher angles (typically  $110$ – $120^\circ$ ), leading to a thinner wake, with weaker vortices, and a much lower drag  $C_D$ . In (c) we observe the mean and fluctuating surface pressures at  $Re = 140\,000$  (after Cantwell and Coles [16.234]); the vertical lines show the maximum and minimum instantaneous pressures found over several thousand cycles, and it is therefore quite surprising that the mean pressure remains so uniform over the rear (or *base*) of the cylinder

various relevant techniques, is the book by Goldstein [16.231].

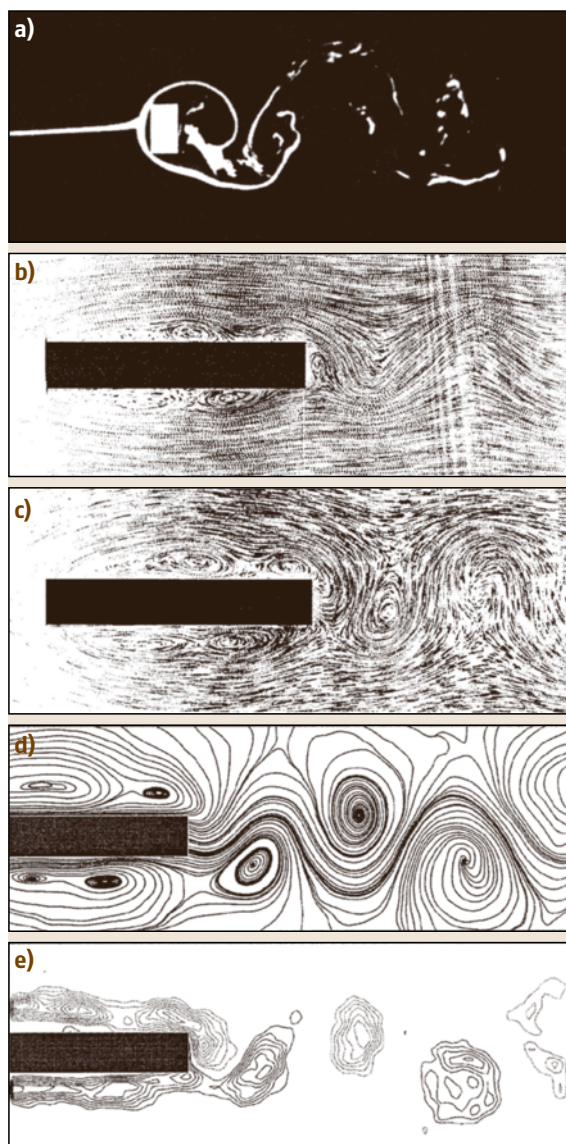
To return to the flow structure from bluff bodies, the alternating formation of vortices mentioned earlier, were the origin of Strouhal's [16.235] classical measurements of the sound frequency produced by translating cylindrical rods through air, and for the Aeolian tones, which are produced by the wind blowing over a wire or a string in an *Aeolian harp*. In a historical review by Rott [16.236], he discusses the later contributions of Lord Rayleigh [16.237] in normalizing Strouhal's frequency data using the *Strouhal* number

$$S = \frac{fD}{U}, \quad (16.5)$$

where  $f$  is the frequency of vortex shedding,  $D$  is diameter, and  $U$  is flow velocity. A great deal of impetus in this flow was triggered by the classical work of von Karman in 1911 [16.238], who not only analyzed the stability of vortex street configurations, but established a theoretical link between the vortex street structure and the drag on the body. This work came about from experiments conducted by Hiemenz (within Prandtl's laboratory in Göttingen), who had initially interpreted wake oscillations from a cylinder as an artifact of the experimental arrangement. However, von Karman viewed the wake oscillations and alternate generation of vortices as an *intrinsic* phenomenon, and went on to investigate their linear stability. Some descriptive understanding of the near-wake vortex formation process can be found from Gerrard [16.239] and from Perry et al. [16.240]. Gerrard suggested that a forming vortex draws the shear layer (of opposite sign) from the other side of the wake across the wake centreline, eventually cutting off the supply of vorticity to the growing vortex.



A great many experimental measurements have been carried out for the bluff-body wake including Strouhal numbers, coefficients of lift and drag, base pressure (i. e., the pressure at a point right at the downstream end of a body), separation points, surface shear stress, wake velocity measurements such as mean and fluctuation velocity profiles and Reynolds stresses, and estimates of the length and width of the *vortex formation* region.



**Fig. 16.129a–e** Flow around rectangular cross-sections, indicated by various visualization techniques. In (a) the ratio of streamwise length to width of the body ( $l/h$ ) is near a critical value which maximizes the drag [16.241], and we see a classic dye technique. In (b) and (c), the flow around a long rectangular cylinder is made clear using particle streaklines, and shows the usefulness of employing different reference frames (fixed with respect to the body and the wake vortices, respectively). In (d) and (e), we observe streamlines and vorticity from measurements using PIV. The images (b) to (e) are from Mills et al. [16.226]

like a streamlined body, such as an airfoil, where the width of the body decreases gradually towards the trailing edge, a bluff body has a more dramatic reduction of body width in the after-portions, and a larger adverse pressure gradient, leading to boundary layer separation. The subsequent rolling up of the separated vorticity in the free shear layers, causes the formation of concentrated local regions of vorticity, known as wake vortices. It is these vortices, and their associated low-pressure centers, in proximity to the rear of the body, which yield very large fluctuating pressures behind a bluff body, but also a surprisingly uniform region of low pressure behind the body (Fig. 16.128b). By integrating such a pressure distribution around the body, we can understand the large drag of a bluff body to be due to the difference between the high-pressure region in the vicinity of the front stagnation point, and the low uniform pressure in the rear (or *base*) region of the body. The drag coefficient is given by

$$C_D = \frac{\text{Drag}}{1/2 \rho U^2 DL}, \quad (16.6)$$

where  $\rho$  is the fluid density,  $D$  is the width of the body and  $L$  is the span length. Obviously, the *real* pressure distribution differs markedly from the potential flow distribution, where the front and rear velocity field (or pressures) are symmetric fore and aft, yielding zero drag.

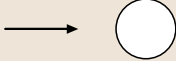
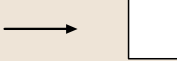
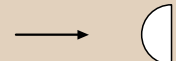
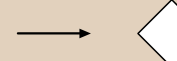
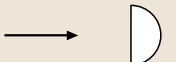
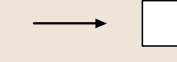

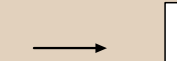
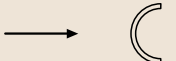
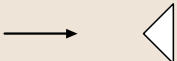
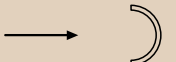

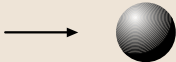
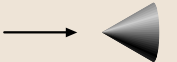

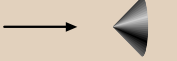
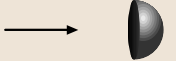
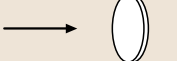
In the case of the circular cylinder, we see in the pressure distribution of Fig. 16.128, that if the boundary layer remains laminar around the frontal portions of the body (for roughly  $Re < 200\,000$ ), then the separation point for the layer occurs at an angle  $\theta \approx 80^\circ$  from the front stagnation point (see the point of inflection in the early classic measurements of *Fage* and *Falkner* [16.232], at  $Re = 110\,000$ ). If the Reynolds number is increased to  $8.4 \times 10^6$ , in Fig. 16.128, then the boundary layer on the body becomes turbulent prior to separation, and remains attached for longer against the adverse pressure gradient. The layer only separates at around  $\theta \approx 110^\circ$ , and the relatively weaker and smaller wake vortices exert

Such measurements may be found in a number of well-known reviews in the literature that were mentioned earlier. We shall mention several of these measurements in Sect. 16.3.2, as a function of increasing Reynolds number.

### 16.3.2 How Bluff is a Bluff Body?

A bluff body is one for which the boundary layer separates from the sides of the body at some point, typically from a point near the maximum width of the body. Un-

**Table 16.4** Drag coefficients and Strouhal numbers for common two- and three-dimensional shapes. One interesting point may be made using the example of a semicircular cylinder. When the flat face is upstream, the drag is high, and the Strouhal number is low, and it is roughly equivalent to a flat plate. When the curved face is upstream, the drag is lower, and the Strouhal number is higher, and now the body is roughly equivalent to the circular cylinder. We note that, as the drag  $C_D$  increases, the frequency  $S$  decreases, which is a trend first clearly pointed out by *Roshko* [16.242]

2-D BODY	$C_D$	$S$	2-D BODY	$C_D$	$S$
Circular cylinder 	1.2	0.21	Square cylinder 	2.1	0.13
Semi-circular cylinder 	1.2	0.21	Square cylinder at 45° 	1.6	0.15
	1.7	0.16	Rectangular cylinder (2:1) 	1.8	0.08
Flat plate 	2.0	0.16	Rectangular cylinder (1:2) 	2.4	0.14
Half tube 	1.2	0.21	90° wedge 	1.6	0.18
	2.3	0.13		2.0	0.13
3-D BODY	$C_D$	$S$	3-D BODY	$C_D$	$S$
Sphere 	0.47	0.19	60° cone 	0.80	0.19
Hemisphere 	0.4	–	90° cone 	1.2	0.16
Hemisphere 	1.2	–	Disk 	1.1	0.13

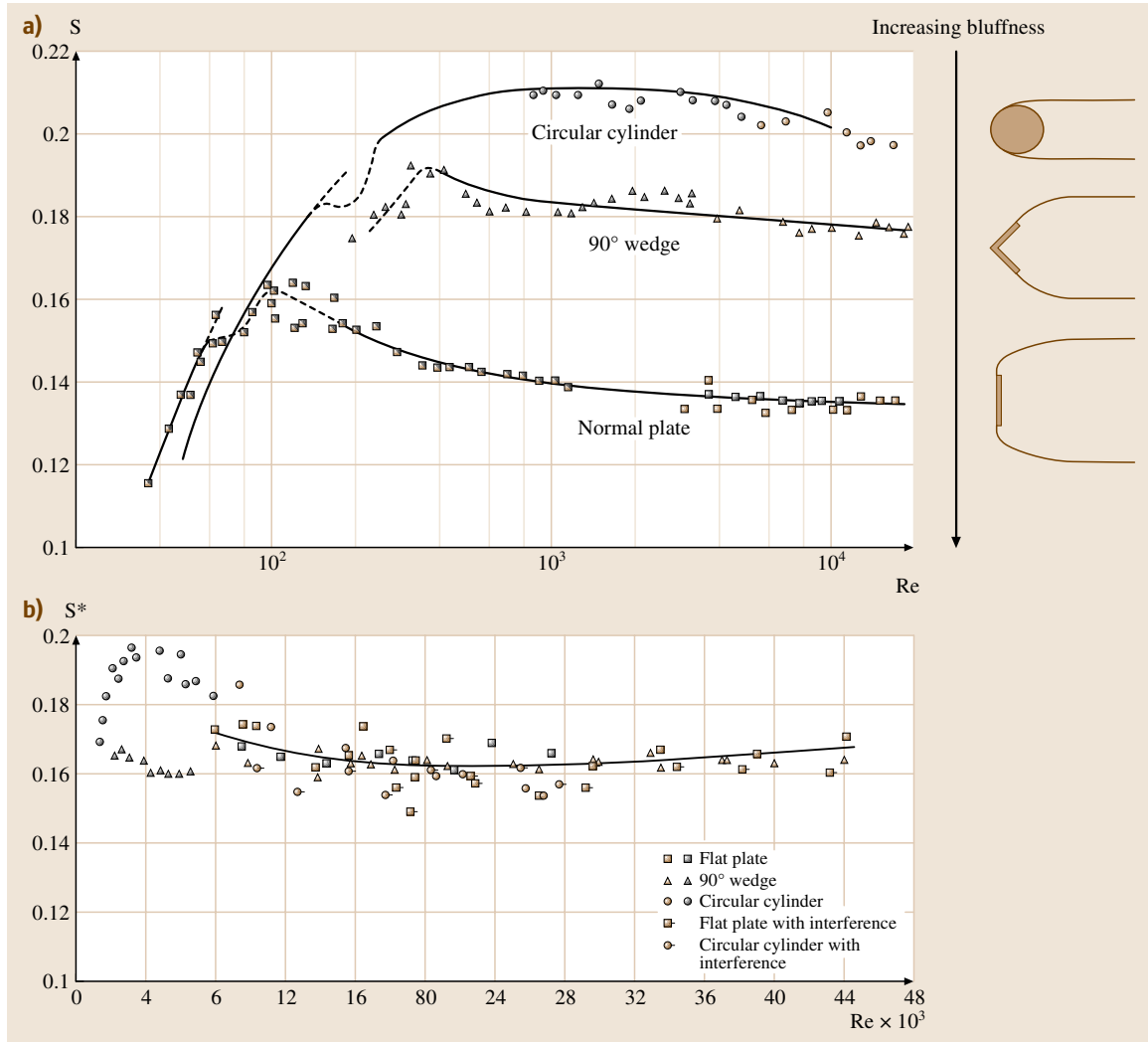
far less *base suction* on the rear of the body, pulling it downstream. The ensuing dramatic reduction of drag is

known as the *drag crisis*, and will be discussed in the next section.



The degree of *bluffness* was addressed by Roshko in a classic paper on bluff-body wakes (*Roshko* [16.242]), and he made it clear that, even if different bodies had the same width, they could generate different base pressures (the roughly uniform low pressure behind the body), as a result of divergence of the separating shear layers to quite different degrees, depending on their shape. We have compiled a set of drag coefficients and Strouhal numbers for a number of two-dimensional shapes, and three-dimensional objects in Table 16.4, for Reynolds

numbers around 10 000. The large variation of  $C_D$  values is evident. An illustrative example (Table 16.4) is given by the two half-cylinder shapes. When the flat face is downstream, one can imagine that the shape is more streamlined, and the separating shear layers will emerge from the body roughly as they do for the full circular cylinder, giving  $C_D = 1.2$ , and a vortex frequency or Strouhal number of  $S = 0.21$ . If, on the other hand, the flat face is upstream, the shear layers emerge from the body sides at a large angle normal to the free stream,



**Fig. 16.130a,b** Strouhal numbers ( $S$ ) for different shapes, versus  $Re$ , and the introduction of a wake Strouhal number ( $S^*$ ) by *Roshko* [16.242]. His idea was to normalize the Strouhal number by the wake width and the wake velocity close to separation, as shown in (b), rather than scaling the Strouhal number simply on the body width and free-stream velocity as in (a)



the wake vortices will be larger and stronger, forming in a wider formation region behind the body. The drag is now significantly higher,  $C_D = 1.7$ , and the larger width of vortex formation corresponds with a lower normalized vortex shedding frequency,  $S = 0.16$ . As pointed out by Roshko, the shedding frequency scales with the width of the wake, rather than the physical width of the body itself.

We present a further example, which illustrates how the streamwise length of a body has an effect on the drag, even if the front face is kept a constant shape. If one studies the drag of a family of rectangular cross sections, as in Fig. 16.129a, then one finds the existence of a critical value of  $L/h$  (streamwise length/width). Bearman and Truesdell [16.241] showed that  $C_D$  increases from 2.0 to 3.0, as the length increases from a normal flat plate ( $L/h \approx 0$ ) to the critical ratio  $L/h = 0.6$ . As the length of the body is stretched further, the drag diminishes, ultimately reaching a lower value than for the flat plate. Again, the proximity of the separating shear layers, and their roll up into strong wake vortices, close to the rear surface of the body is key to dictating the pressure distribution and drag of the body.

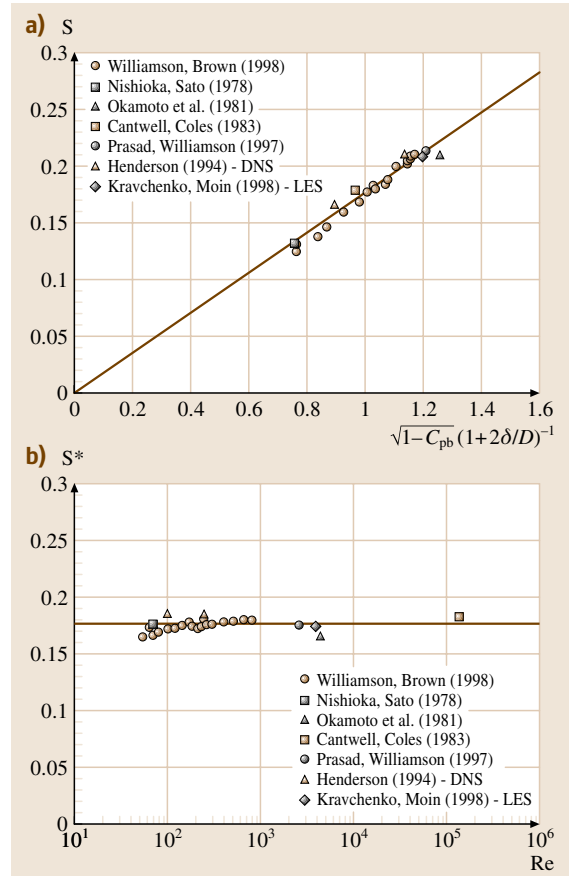
In Fig. 16.129b,c, we also present visualizations of long rectangular (nominally two-dimensional) shapes [16.226], which use particle streak photography. Clear differences can be found if one uses the reference frame fixed with respect with the body or fixed with the vortices, as illustrated also in Williamson and Roshko [16.225] and Perry et al. [16.240]. Examples from particle image velocimetry (PIV) are also shown in Fig. 16.129, showing the streamlines and vorticity contours using this powerful quantitative technique, described comprehensively elsewhere in this handbook. The technique shows clearly the shedding of vortices from the front face (leading-edge separation), which then travel along the sides of the cylinder, and largely influence the phase and formation of trailing-edge vortex formation.

As mentioned earlier, these ideas concerning the degree of bluntness of a body were first formulated by Roshko in [16.242]. He measured the Strouhal numbers for a number of bodies, as a function of  $Re$ , as seen in Fig. 16.130. He was essentially the first to note that bluffer bodies diverged the flow more, yielding a lower base pressure (more base suction), and lower vortex shedding frequencies. For example, in order of increasing bluntness, we have: circular cylinder  $\rightarrow$  wedge  $\rightarrow$  normal flat plate. From dimensional analysis, he proposed a Strouhal number based on the physical scales of the near-wake formation to collapse frequency data

from different body shapes. He suggested that the shedding frequency would scale with the wake width ( $L^*$ ) rather than simply the body dimensions ( $D$ ), and on a relevant velocity scale ( $U^*$ ) for the vortex formation in the near wake, rather than simply on the free-stream velocity ( $U$ ). He put forward a wake Strouhal number:

$$S^* = \frac{fL^*}{U^*} \approx \text{const.} \quad (16.7)$$

The wake width  $L^*$  for different bodies was found using free-streamline theory, while the velocity scale was taken to be that velocity just outside the sepa-



**Fig. 16.131a,b** Collapse of frequency data for a circular cylinder. This approach uses a wake length scale involving the body diameter plus the shear layer thickness (evaluated near separation). This scaling collapses the wake Strouhal number ( $S^*$ ) well for a particular body, in this case a circular cylinder, over a wide regime of  $Re$  (as shown in Williamson and Brown [16.243]). (References are found in therein)

ration point ( $U_s$ ) which, to a good approximation, is calculated from the base pressure coefficient. (Following a boundary layer approximation,  $1/2U_s^2$  is the flux of vorticity shed into the wake.) This *wake* Strouhal

number, shown in Fig. 16.130b, and other such *universal* Strouhal numbers that have been put forward, for example by *Bearman* [16.244] and by *Griffin* [16.245], resulted in a very reasonable collapse of the shedding-frequency data for many different bluff bodies. These results confirm the merit of considering the characteristic scales of wake formation, rather than simply body dimensions (and free-stream velocity), to generate an effective Strouhal number representing vortex shedding frequency.

Such ideas also provide a basis for a functional relationship for  $S$ – $Re$  measurements for a given bluff body. It is possible to consider different length and velocity scales upon which the shedding frequency might depend. *Bauer* [16.247] measured the vortex shedding frequencies behind flat plates parallel to the flow (whose cross sections were bullet-shaped). He normalized the Strouhal numbers by a characteristic lengthscale equal to twice the boundary layer displacement thickness ( $\delta^*$ ) plus the plate (or *bullet*) thickness (i. e.,  $D + 2\delta^*$ ). A subsequent study by *Eisenlohr* and *Eckelmann* [16.248] for many different plates showed a good collapse of their frequency data when it was plotted using such a Strouhal number.

Concerning the circular-cylinder wake, consistent with the above discussion, *Williamson* and *Brown* [16.243] use the concept that the frequency will scale with  $(D + 2\delta)^{-1}$ , where  $\delta$  is a characteristic shear layer *vorticity* thickness, so that in (16.7), they have  $L^* = (D + 2\delta)$ , and  $U^* = (U_s) =$  velocity measured at separation, giving:

$$S^* = \left(\frac{fD}{U}\right) \left(\frac{U}{U_s}\right) \left(1 + \frac{2\delta}{D}\right). \quad (16.8)$$

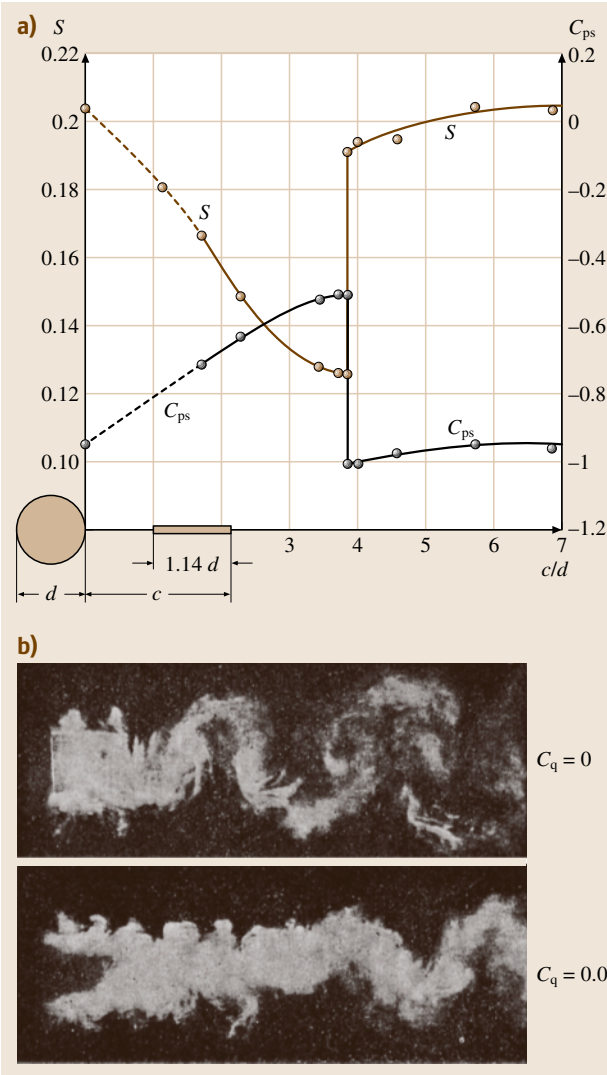
It can be shown [16.242] that  $U_s$  is related to the base pressure coefficient (to a good approximation) by

$$\frac{U_s}{U} = \sqrt{1 - C_{pb}}, \quad (16.9)$$

giving an expression for the Strouhal number as

$$S = S^* \sqrt{1 - C_{pb}} \left(1 + \frac{2\delta}{D}\right)^{-1}. \quad (16.10)$$

Experimental support for the use of the Strouhal number  $S^*$  in (16.10) comes from Fig. 16.131a, showing  $S$  plotted against  $\sqrt{1 - C_{pb}}(1 + 2\delta/D)^{-1}$ . We note that the data lies closely along a straight line, whose gradient yields the best-fit value for  $S^* = 0.176$ . One should note that the available data from the literature for this plot includes the wide range of  $Re$  from 55 up to 140 000. A plot of calculated  $S^*$  values versus  $Re$  in Fig. 16.131b



**Fig. 16.132a,b** Effect of a wake *splitter plate* on the base pressure coefficient ( $C_{ps}$ ) and Strouhal number ( $S$ ). Effect of *base bleed* on the wake structure. Both of these classic techniques, introduced respectively by *Roshko* [16.242] and by *Bearman* [16.246], can dramatically influence the wake flow structure as well as the base pressure, vortex shedding frequency, and also the drag of a bluff body. The principal effect is to stretch the vortex formation region, and to shift the low-pressure vortices further downstream from the base region of the body

gives another indication of the constancy of  $S^*$  over this large range of  $Re$ , and thus suggests that it is a reasonable means to collapse frequency data for this body.

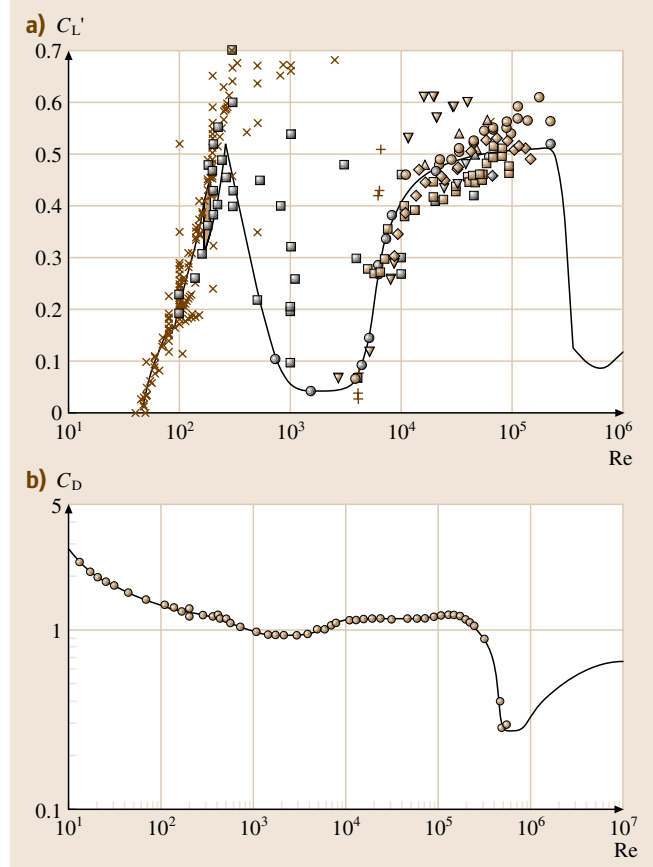
Regarding the primary wake instability, a revealing experiment was conducted by *Roshko* [16.242], who studied the effect of a splitter plate (parallel to the free stream) located downstream of a bluff body at high  $Re$ . He found that, by bringing such a plate closer to the cylinder, he could interfere with the vortex shedding instability within a critical distance from the body, which caused a jump decrease in both the shedding frequency and base suction ( $-C_{pb}$ ), as shown in Fig. 16.132a. A downstream shift of the low-pressure vortices reduced the suction near the base of the cylinder. The ensuing wider and longer vortex formation region exhibits a lower shedding frequency.

One may define a vortex formation length [16.246, 251] as that point downstream of the body where the velocity fluctuation level has grown to a maximum (Fig. 16.142b) and thereafter decays downstream. *Bearman* [16.246], also using splitter-plate wake interference, made the discovery that the base suction was very closely inversely proportional to the formation length, which has often been assumed since that time. It has generally been found in these studies that an increase in formation length ( $L_F/D$ ) is associated with a decrease in the level of velocity fluctuation maximum  $u'_{rms}/U_\infty$  (or Reynolds stress maximum) and a decrease in the base suction. *Bearman* [16.244], on the other hand, used *base bleed* to bleed a rate of fluid flow out of the base region of a body, to alter the wake formation process. This is readily evident from his smoke visualizations for zero or finite bleed rates in Fig. 16.132b, where even small bleed rates show remarkable control of the downstream vortex formation.

It is also relevant in the discussion of the vortex-shedding regimes to consider that, if one averages over large time (compared to the shedding period), one can define a *mean recirculation region* in the wake, which is symmetric and closed. This was discussed in *Roshko* and *Fiszdon* [16.252], and in *Roshko* [16.217], where he linked the recirculation *bubble* length with the base pressure  $C_{pb}$ , and the Reynolds stresses ( $\rho u'v'$ ), in an effective model of bluff-body flow.

### 16.3.3 Base Pressure, Drag, Lift, and Strouhal Number

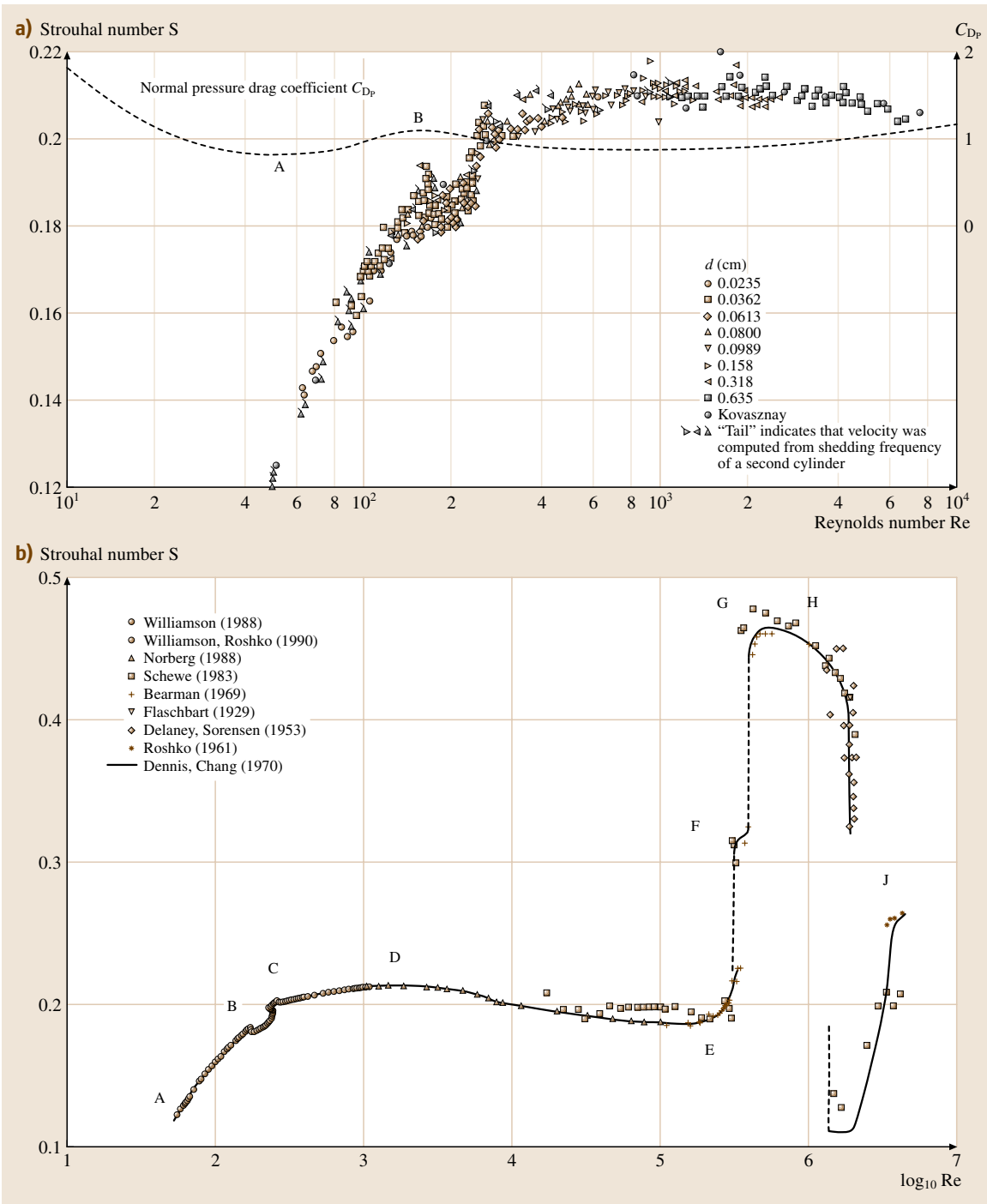
In this section, we present the important variations of lift and drag, Strouhal number, and base pressure as a function of Reynolds numbers. At this point, we restrict



**Fig. 16.133a,b** Fluctuating lift coefficient ( $C'_L$ ) and mean drag coefficient ( $C_D$ ) as a function of  $Re$ . One can observe that the *drag crisis*, seen as the sharp reduction of drag at  $Re \approx 200\,000$ , is coincident with a sharp reduction in fluctuating lift. The lift variation and its measurement is discussed comprehensively in *Norberg* [16.249], where the symbols are defined in his Fig. 2. The drag variation includes classic data from *Wieselsberger* [16.250], which has been remarkably *robust* in the face of modern techniques. Data at the highest  $Re \approx 10^6 - 10^7$  come from *Roshko* [16.233]

ourselves to discussion of the circular cylinder alone, since many of the variations exhibit similar features for the different bluff-body shapes.

Drag and lift forces are measured using many different techniques, which are discussed at length in the review of lift force measurements by *Norberg* [16.249], and in the book of *Goldstein* [16.231]. These techniques include, for example, pressure distribution measurements (described well in the early 1928 paper by *Fage* [16.253]), use of strain gauges, linear variable displacement transducers (LVDTs), and piezo-



**Fig. 16.134a,b** Classic measurements by *Roshko* [16.254] of the Strouhal number versus Reynolds number for a circular cylinder in (a), and an updated plot showing the key regimes in (b) compiled for this handbook (References are found in [16.223])

electric transducers. Vortex shedding frequencies are generally measured using LDV (laser Doppler velocimetry), and hot-wire anemometers, or possibly by noting the lift force spectrum. The base pressure coefficient:  $C_{pb} = (2p_b - p_s)/\rho U^2$  (where  $p_b$  is the base pressure,  $p_s$  is the static pressure of the free stream), is generally measured using a small pressure hole (tap) at the base of the bluff body.

It is immediately clear from Fig. 16.133 that the lift and drag variations are significantly different as a function of  $Re$ . The unsteady lift coefficient, which shows large variations, is influenced by the types of instability in the near wake, as Reynolds numbers are varied. These instabilities will be discussed in the following section. In brief, the rise of  $C_L$  to the first major peak at around  $Re \approx 190$  is associated with increasingly energetic laminar vortex shedding in the near wake. The second broader peak at much higher  $Re \approx 10\,000$ – $200\,000$ , corresponds with the energetic separated shear layer instability, which results in high shear stresses and stronger unsteady wake vortices in the near wake.

The drag force, on the other hand, shows remarkably little of the large fluctuations that characterize the lift. The presented data points in Fig. 16.133b are from some classic measurements by Wieselsberger [16.250], and indicate the reduction of  $C_D$  until around  $Re \approx 1000$ . In fact, the drag varies roughly as  $C_D \approx 1/Re$  at the lowest  $Re \ll 1$ . Because it is extremely difficult to measure drag force on thin wires at very low  $Re$ , any fine variations in  $C_D$  around  $Re \approx 100$ – $200$ , due to the onset of the energetic laminar vortex shedding, are not evident. An effective approach to determine the subtle variations in  $C_D$ , is to use direct numerical simulations, as completed to very high resolution by Henderson [16.255].

It is remarkable that the drag, and the Strouhal number in Fig. 16.134, remains almost constant at around  $C_D \approx 1.2$ , and  $S \approx 0.20$ , over a very wide regime of  $Re$ , from 1000 to 200 000, and it is usefully assumed by practising engineers that the flow field is reasonably independent of Reynolds numbers over this wide regime. On the other hand, the base pressure and lift force exhibit changes indicative of the shear layer instability becoming more energetic as  $Re$  increases. We go on to discuss the vortex instabilities in these flows in the next section.

An important effect, mentioned earlier, is the sharp drop in drag at  $Re \approx 200\,000$ , which is caused by the transition of the attached boundary layer into a turbulent state. The turbulent layer is more able to withstand the adverse pressure gradient around the cylinder, and separates later, causing weaker smaller vortices and less base suction contributing to the reduced drag. This sig-

nificant effect is called the *drag crisis*, and in some cases the purposeful roughening of a bluff body will actually induce early transition and an advantageous reduction in drag.

The variation of Strouhal number was first defined by Roshko over a wide range of Reynolds numbers [16.242], and indicated a change in regime at around  $Re \approx 300$ , as seen in Fig. 16.134a, leading to the well-known  $S$ – $Re$  relationships:

$$S = 0.212 - \frac{4.494}{Re}, \quad Re \approx 50\text{--}150; \quad (16.11)$$

$$S = 0.212 - \frac{2.692}{Re}, \quad Re \approx 300\text{--}2000. \quad (16.12)$$

A more-complete  $S$ – $Re$  variation is shown in Fig. 16.134b, showing the existence of a number of regimes, and along with the base pressure measurements, will form the basis of the flow regime discussions in the next section.

A highly accurate representation of the variation of Strouhal numbers with  $Re$  was put forward by Williamson and Brown [16.243], based on the form of (16.10), noting that the shear layer thickness will scale on  $1/\sqrt{Re}$ , as for the attached boundary layer. In fact they have put forward the expression:

$$S = \left( A + \frac{B}{\sqrt{Re}} + \frac{C}{Re} + \dots \right). \quad (16.13)$$

An excellent fit for the laminar (parallel) shedding regime, based on a truncation of the series (9), using data from Williamson [16.256], gives

$$S = \left( 0.285 - \frac{1.390}{\sqrt{Re}} + \frac{1.806}{Re} \right), \quad Re < 190. \quad (16.14)$$

If we apply the  $\sqrt{Re}$  formulation to the frequency data from Williamson [16.227] for higher  $Re$ , we find:

$$S = 0.2234 - \frac{0.3490}{\sqrt{Re}}, \quad Re \approx 260\text{--}1300. \quad (16.15)$$

For higher regimes of  $Re$ , the curve fits of Fey et al. [16.257] may be effectively used, as follows:

$$S = 0.204 - \frac{0.3364}{\sqrt{Re}}, \quad Re \approx 1300\text{--}5000; \quad (16.16)$$

$$S = 0.1776 - \frac{2.2023}{\sqrt{Re}}, \quad Re \approx 5000\text{--}200\,000. \quad (16.17)$$

For the complexity of the  $S$  variation for  $Re > 200\,000$ , it is probably worth using the plot in



Fig. 16.134b directly. Accurate data for vortex shedding frequencies ( $S$ ) as well as base pressures ( $C_{pb}$ ), for a variation of aspect ratios (cylinder length/diameter), are given by *Norberg* [16.258].

### 16.3.4 Overview of Vortex Shedding Regimes

It is particularly revealing as a key for this section to consider the plot of base pressure coefficient ( $C_{pb}$ ) as a function of Reynolds number in Fig. 16.135. In contrast to some of the other parameters of the flow, the base pressure responds sensitively to the changes in flow instabilities and phenomena throughout the Reynolds number range. An incisive overview of the flow regimes was first given in *Roshko* and *Fiszdon* [16.252]. This was updated by *Roshko* [16.217] and *Williamson* [16.223], stimulated by the completion of the previously elusive data at low laminar-shedding Reynolds numbers by *Williamson* and *Roshko* [16.259]. In some of these studies, it was found convenient to refer to a *base suction* coefficient ( $-C_{pb}$ ), rather than the base pressure itself.

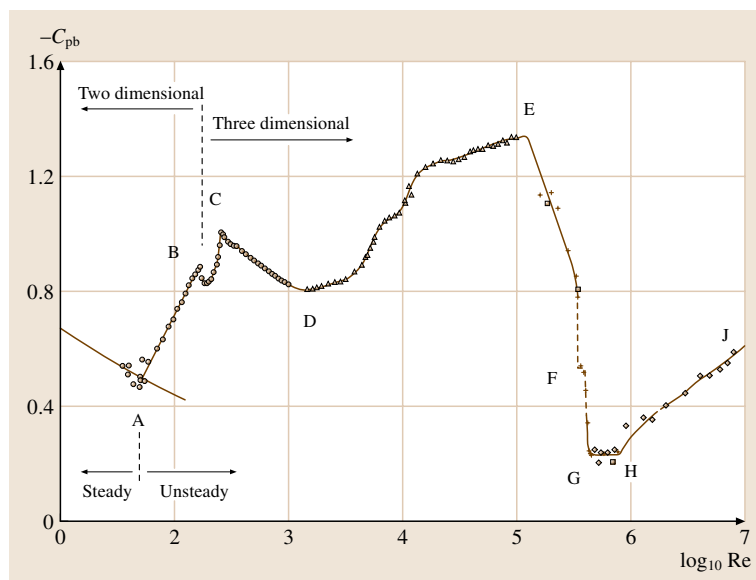
Regarding the plot of base pressure in Fig. 16.135, it should be mentioned that this comes from experiments using a smooth cylinder in good flow quality (turbulence levels typically around 0.1%), and also from the simulations of *Henderson* [16.255]. It is known that roughness, turbulence levels (as well as the character of turbulence spectra), cylinder aspect ratio, end con-

ditions, and blockage affect the transitions, although the trends remain the same. The first definition of flow regimes based on measurements of velocity fluctuation, spectra and frequency was given by *Roshko* [16.254]. He found a *stable* (periodic) laminar vortex shedding regime for  $Re = 40\text{--}150$ , a transition regime in the range  $Re = 150\text{--}300$ , with an *irregular* regime for  $Re = 300\text{--}10\,000$ , where velocity fluctuations showed distinct irregularities. Similar regimes were confirmed by *Bloor* [16.263].

Referring now to the plot of base suction coefficient versus  $Re$  in Fig. 16.135, and following the lead of *Roshko* [16.217] and *Williamson* [16.223], we shall define the various shedding regimes with respect to the letters marked on this plot, and exhibit some of the principal results and experimental approaches that have been taken.

#### Regime up to A: Laminar Steady Regime ( $Re < 49$ )

At  $Re$  below around 49, the wake consists of a steady recirculation region of two symmetrically placed *vortices* on each side of the wake, whose length grows as the Reynolds number increases. This trend has been shown experimentally by *Taneda* [16.264], *Gerrard* [16.265], and *Coutanceau* and *Bouard* [16.266], and is supported by the computations of *Dennis* and *Chang* [16.267]. However, from analysis and computation in (constrained to be) steady two-dimensional (2-D) flow, it has proven surprisingly difficult to define the variation



**Fig. 16.135** Plot of base suction coefficients ( $-C_{pb}$ ) over a large range of Reynolds numbers. A plot of base suction coefficient is particularly useful as a basis for discussion of the various flow regimes. The base suction coefficient (negative of base pressure coefficient, or  $-C_{pb}$ ) is surprisingly sensitive to the process of vortex formation in the near wake, which itself is affected strongly by the evolution of various two- and three-dimensional wake instabilities, as Reynolds numbers are varied. The sources of the data, in order of increasing  $Re$ , data are from computations of *Henderson* [16.255]; and experiments of *Williamson* and *Roshko* [16.259], *Norberg* [16.258], *Bearman* [16.260], *Flaschbart* [16.261], *Shih* et al. [16.262]

of bubble shape with Reynolds number as  $Re$  becomes large [16.268], as discussed in *Roshko* [16.217]. It appears that the asymptotic formula for  $C_D(Re)$  for this steady wake is not yet available. It should be noted that, as the length of the steady wake bubble increases, due to the viscous stresses, so the recent DNS (direct numerical simulation) computations of *Henderson* [16.255] and the measurements of *Thom* [16.269] clearly show a decrease in the base suction.

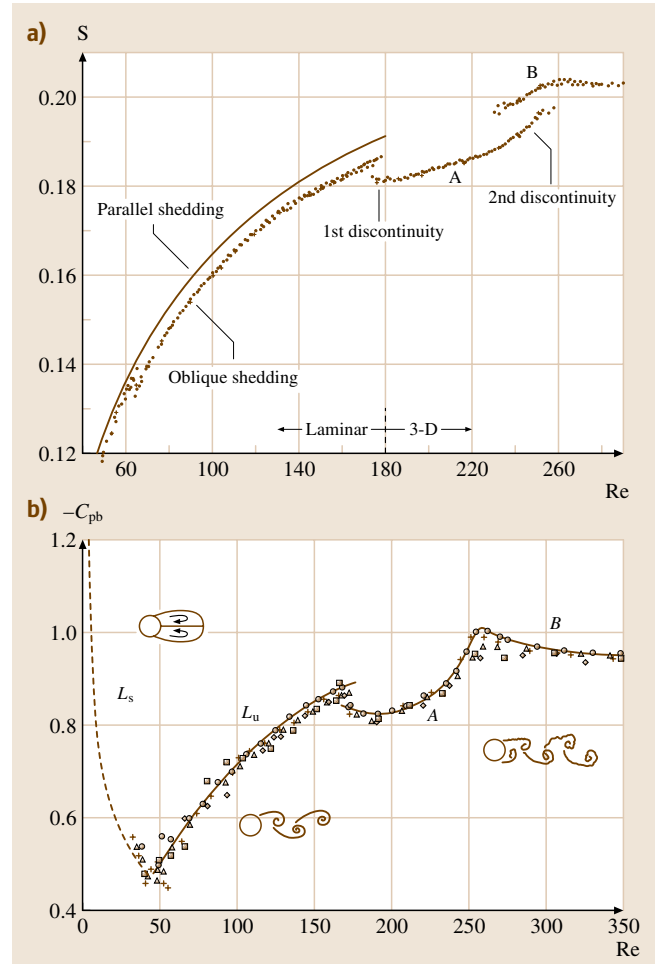
### Regime A–B: Laminar Vortex Shedding Regime ( $Re = 49$ to $190$ )

In this regime, the variation of base suction with  $Re$  shows a sharp deviation in trend from the steady wake regime discussed above (Fig. 16.135). The recirculation region develops instabilities, initially from the downstream end of the bubble, whose strength and amplification grows with  $Re$ . This effect may be measured by a monotonic increase in the amplitude of maximum wake velocity fluctuations with  $Re$ , and a gradual movement of the instability maximum (or formation length) upstream towards the cylinder.

The onset of the wake instability near to  $Re = 47$ – $49$  has been found to be a manifestation of a Hopf bifurcation, and the flow represents a dynamical system described by a Stuart–Landau equation [16.270]. As the wake instability becomes amplified, the Reynolds stresses in the *near*-wake region increase, the formation length decreases, and there is a consistent increase in the base suction. There is also an increase in the unsteady forces, as shown from computations [16.255], but not yet detected in experiment at these low  $Re$ .

Some early observations and measurements were made which showed or suggested that vortices can shed at some oblique angle to the axis of the cylinder in what we now term *oblique* shedding [16.220, 271], although towing-tank experiments by *Hama* [16.272] demonstrated only parallel shedding. A further phenomenon, which we shall see is directly related to this, is the phenomenon of discontinuities in the relationship between the Strouhal and Reynolds numbers (see Fig. 16.136a in the laminar (oblique) shedding regime), as first detected very clearly by *Tritton* [16.273] near to  $Re = 75$  [16.274], and subsequently the source of a great deal of debate over a period of 30 years.

Experimental measurements of the Strouhal frequency over the period 1878–1978 showed a scatter of the order of 20% even among the modern experiments [16.223]. This scatter was present despite the fact, as pointed out by *Roshko* [16.275], that “the quantities



**Fig. 16.136a,b** Strouhal number ( $S$ ) and base suction coefficient ( $-C_{pb}$ ) over the laminar and wake transition regimes of Reynolds number. We can see quite sharp changes of mode, caused by: the inception of vortex shedding; the first jump to a mode A three-dimensional instability; and a second jump to mode B instability (after *Williamson* [16.227], *Williamson and Roshko* [16.259])

involved ( $U$ ,  $D$ ,  $\nu$  and  $f$ ) could be rather easily measured to better than 1% accuracy”.  $\nu$  is the kinematic viscosity. Many explanations were put forward over the years, although it was finally shown that, in the absence of certain effects, such as free-stream shear and cylinder vibration, a discontinuity in the  $S$ – $Re$  relation can be caused by the unexplained phenomenon described earlier, namely *oblique shedding*. The  $S$ – $Re$  discontinuity, originally observed by *Tritton* [16.273], is caused by a changeover from one mode of oblique shedding to another oblique

mode, as  $Re$  is increased [16.256, 276–280]. It is shown that the particular boundary conditions at the spanwise ends of the cylinder dictate the angle of shedding over the whole span, even for a cylinder that is hundreds of diameters in length. Gerich and Eckelmann [16.281] had earlier shown that a region close to the ends of a cylinder (about 10 diameters in length) can be influenced in a *direct* manner, causing a cell of lower-frequency shedding to appear near to the ends.

In the towing tank and wind tunnel experiments of Williamson [16.256, 276], it was found that the oblique vortices formed a periodic *chevron* pattern, as shown in Fig. 16.137a. The technique used to observe the vortices clearly involves washing off fluorescent dye from the horizontal cylinders in a towing tank, and employing

laser-induced fluorescence (LIF). Over each half span, the oblique angle is dictated by the end conditions in that half. It was then found that there are several means to achieve parallel shedding by manipulating the end conditions, as in Fig. 16.137b. With parallel shedding, the Strouhal–Reynolds number curve is completely continuous, as shown in Fig. 16.136. (An ingenious approach by Leweke and Provansal [16.282] has involved the study of vortex shedding past a torus, where there are no ends to the curved cylinder.) It was also shown [16.276] that one may define a *universal* Strouhal curve, in the sense that the experimental oblique-shedding data ( $S_\theta$ ) can be closely collapsed onto the parallel-shedding curve ( $S_0$ ) by the transformation

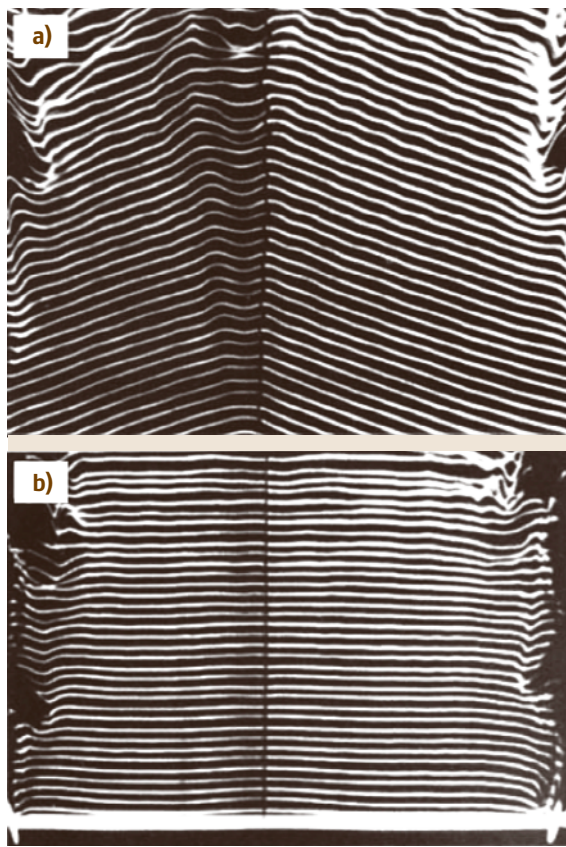
$$S_0 = \frac{S_\theta}{\cos \theta} . \quad (16.18)$$

Some control of vortex shedding angles has been made at higher  $Re$  by Prasad and Williamson [16.283], although the techniques are not as effective as in the laminar shedding regime.

#### Regime B–C: 3-D Wake-Transition Regime ( $Re \approx 190$ to 260)

The significant visualizations of Hama [16.272] showed that the instability in the wake-transition regime takes the form of a three-dimensional waviness on the primary Karman vortices, and the formation of what Gerrard [16.265] later calls “fingers of dye”. It is now known that these dye *fingers* are associated with vortex loops and streamwise vorticity, in similarity with other free shear flows.

The transition to three-dimensionality in the wake can conveniently be described with reference to the measurements of the Strouhal–Reynolds number in Fig. 16.136a, and to the changes in base pressure in Fig. 16.136b, where it may be observed that the transition, originally described by Roshko in 1954 [16.254], actually involves two discontinuous changes (see Williamson [16.284]). At the first discontinuity the Strouhal frequency drops from the laminar curve to one corresponding to a *mode A* 3-D shedding, at close to  $Re = 180$ –190. This discontinuity is hysteretic, and the exact critical  $Re$  depends on whether the flow speed is increased or decreased. We see the inception of vortex loops (in a *mode A* instability), and the formation of streamwise vortex pairs due to the deformation of primary vortices as they are shed, at a wavelength of around 3–4 diameters, as shown in Fig. 16.138a. (The modes of 3-D instability in this figure are visualized using the LIF technique, in the same manner as found in Fig. 16.137.)



**Fig. 16.137a,b** Oblique and parallel shedding are controlled by the end boundary conditions for cylinders of even several hundreds of diameters in length. In (a), we have the *chevron* pattern of shedding, showing the existence of a phase *shock* in the center span, while in (b), we can induce parallel shedding [16.276]

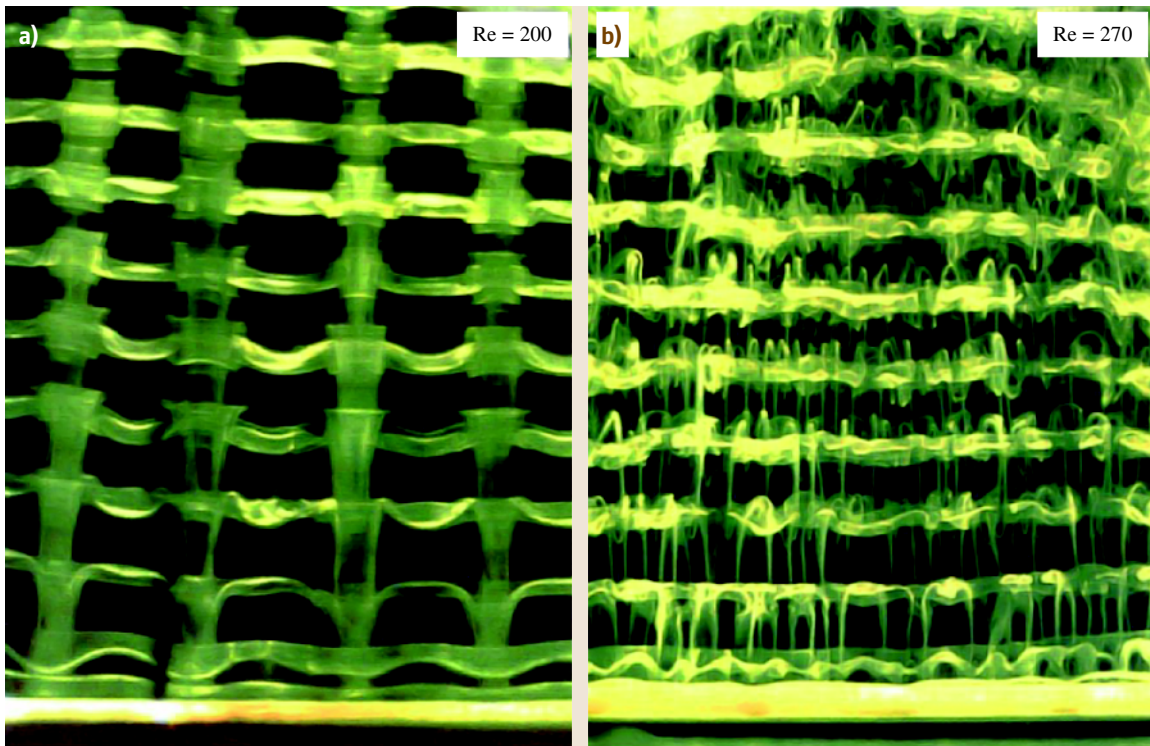


Although there is a large range of reported critical  $Re$  for wake transition,  $Re = 140\text{--}194$ , it should be noted that it is influenced by the end boundary conditions. Floquet stability analysis of *Barkley and Henderson* [16.285] yields a critical Reynolds number of 188.5. *Miller and Williamson* [16.286] found that non-mechanical end conditions (using suction tubes downstream of the body) can yield rather *clean* end conditions, and they find that the laminar regime for parallel shedding could be extended experimentally up to  $Re_{crit} = 194$ .

At the second discontinuous change in the  $S$ – $Re$  relation in Fig. 16.136a, there is a gradual transfer of energy from *mode A* shedding to a *mode B* shedding over a range of  $Re$  from 230–250. The latter mode comprises finer-scale streamwise vortices (Fig. 16.138b), with a spanwise length scale of around one diameter. There is evidence to show that the origin of the *mode A* instability is based on a core elliptic insta-

bility of the primary vortex cores, whereas the *mode B* structures evolve from an instability of the *braid* region of vorticity between the primary vortices. The origin of these instabilities are discussed from experiment in *Williamson* [16.227], and in *Lewke and Williamson* [16.288], and from numerical simulation in *Thompson et al.* [16.289], *Barkley and Henderson* [16.285], and *Thompson et al.* [16.290] and *Zhang et al.* [16.291].

The large intermittent low-frequency wake velocity fluctuations, originally monitored by *Roshko* [16.254] and then by *Bloor* [16.263], have been shown to be due to the presence of large-scale spot-like *vortex dislocations* in this transition regime [16.287]. These are caused by local shedding-phase dislocations along the span. The base suction and Strouhal frequency continue to increase in this regime, but follow curves at a lower level than may be extrapolated from the laminar shedding regime.



**Fig. 16.138a,b** Modes A and B three-dimensional instabilities. (a) Mode A instability. This is associated with the inception of streamwise vortex loops. This example for  $Re = 200$ , corresponds with a spanwise wavelength:  $\lambda/D = 4.01$ , which is remarkably close to the maximum growth rate from Floquet analysis (after *Barkley and Henderson* [16.285]) (b) Mode B instability. This is associated with the formation of finer-scale streamwise vortex pairs.  $\lambda/D$  is roughly 1.0.  $Re = 270$ . Note that both photographs are to the same scale (after *Williamson* [16.227, 287])

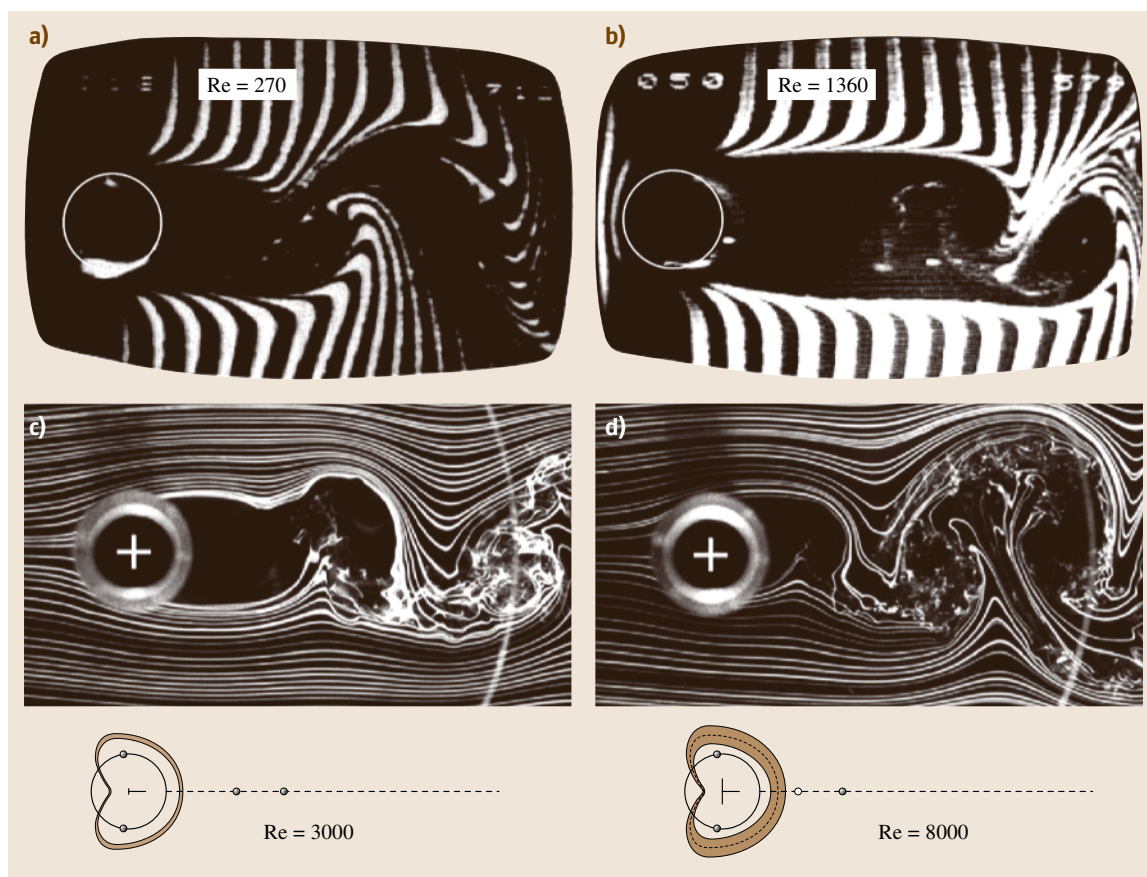
### Regime C–D: Increasing Disorder in the Fine-Scale Three-Dimensionalities

The peak in the base suction close to C, at  $Re = 260$ , is associated with a peak in the Reynolds stresses in the near wake, and a particularly ordered three-dimensional streamwise vortex structure in the near wake [16.227]. At this point, the primary wake instability behaves remarkably like the laminar shedding mode, with the exception of the presence of the fine-scale streamwise vortex structure. As  $Re$  is then increased towards point D in the plot of base pressure in Fig. 16.137, the fine-scale three-dimensionality becomes increasingly disordered, and this appears to cause a reduction in the two-dimensional Reynolds stresses, a consistent reduction in base suction, and an increasing length of the for-

mation region [16.227, 293]. The increased length of the formation region (the downstream distance over which the vortices form), as one increases  $Re$  from 270 to 1360, can be seen clearly in Fig. 16.139, using the hydrogen bubble visualization technique of *Unal* and *Rockwell* [16.293].

### Regime D–E: Shear-Layer Transition Regime ( $Re = 1000$ to $200\,000$ )

In this regime, the base suction increases again, the 2-D Reynolds stress level increases, the Strouhal number gradually decreases (Fig. 16.134), and the formation length of the mean recirculation region decreases [16.294], all of which are again consistent variations. These trends are caused by the develop-



**Fig. 16.139a–d** Visualizations of the wake structure as the Reynolds number is varied. Hydrogen bubble images show the lengthening of the vortex formation region as  $Re$  increases from 270 to 1360, as shown by *Lin* et al. [16.292]. Smoke wire images from *Norberg* [16.249] show the diminishing vortex formation region as  $Re$  increases further from 3000 to 8000, as the stresses from the shear layer instability cause the region to shrink. Diagrams show mean pressure distributions by *Norberg* [16.249]

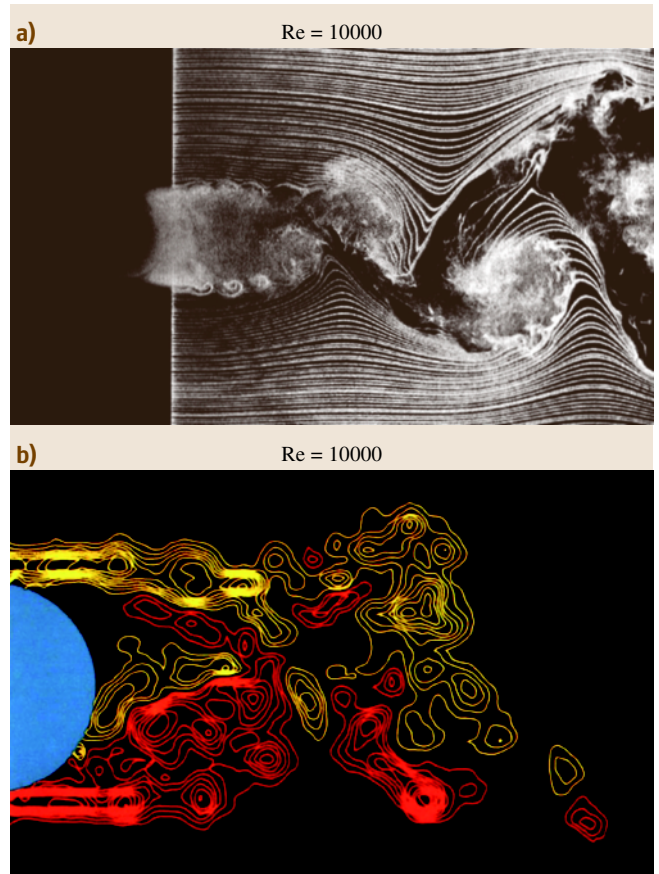


ing instability of the separating shear layers from the sides of the body. As noted by *Roshko* [16.217], this might be called the Schiller–Linke regime, after those who discovered it and who associated this regime with an increase in base suction and drag, while the turbulent transition point in the separating shear layers moves upstream, as  $Re$  increases. The decrease in formation length in the present regime (for  $Re$  increasing from 3000 to 8000), is well demonstrated by the smoke wire visualizations of *Norberg* [16.249], in Fig. 16.139c,d.

Physically, the shear layer vortices take on the appearance of the vortices so often observed in mixing layers, as shown from smoke wire visualization in Fig. 16.140, but in this case the length of the layer is obviously limited by the streamwise extent of the formation region. Evidence of shear layer vortices are seen in the earlier Fig. 16.127 at  $Re = 4000$ , and are found to amalgamate in the near wake into the Karman vortices, as seen in the PIV visualization of *Lin et al.* [16.292] in Fig. 16.140 for  $Re = 10\,000$ . *Unal* and *Rockwell* [16.295] have also shown that the vortex formation can arise from the exponential amplification of the disturbance kinetic energy in accord with linear stability theory applied to the separating shear layer. Shear layer vortices generally appear for  $Re > 1200$ , but have been observed below this  $Re$ , possibly induced by vibration of the test body in some cases.

Although the shear layer transition was considered by *Roshko* [16.254], it was not until *Bloor* [16.263] that the frequency of the shear layer instability waves were studied. She demonstrated that the shear layer instability frequency scaled approximately with  $\sqrt{Re}$ , by considering the thickness and velocity of the separating laminar boundary layer. There is no question that this is of the right order, although even a cursory glance at the actual data points from these investigations does not precisely support the  $Re^{0.5}$  variation (look carefully at the frequency data in Fig. 16.141). For clarity, the frequencies are defined by  $f_{sl}$ , which is the shear layer frequency, and  $f_k$ , which is the Karman vortex frequency. The frequency of shear layer vortices has sometimes been referred to as the Bloor–Gerrard frequency, in honor of the work of Bloor and Gerrard, who first investigated the separating shear layer instabilities, in the particular context of the bluff-body wake.

In the case of the shear layer frequency, a careful reevaluation of all data that could be found from a number of investigators, shows that the exponent  $p$  in the expression  $(f_{sl}/f_k) = A Re^p$  is significantly greater than 0.5 in every case. All the compiled data are plotted in



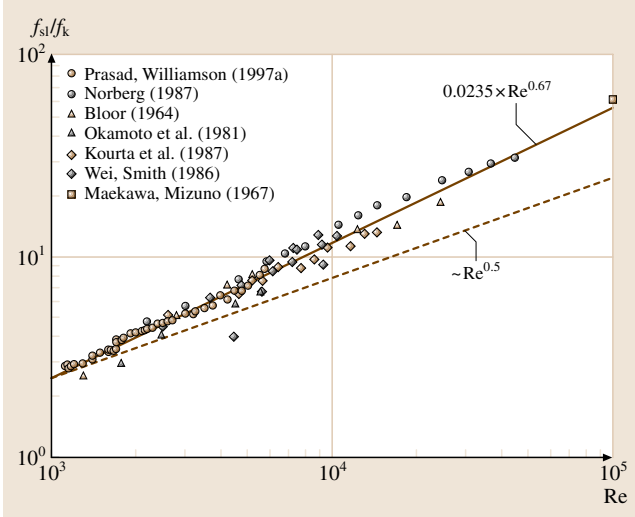
**Fig. 16.140a,b** Clear images of the shear layer instability in the near wake at  $Re = 10\,000$ . In (a) we see the smoke wire technique, and a clear observation of the shear layer vortices, contrasting with the larger wake vortices [16.283]. In a similar flow in (b) the shear layer vorticity, amalgamating into Karman wake vortices, is shown using the PIV technique [16.292]

Fig. 16.141. The least-squares best fit to the data is

$$\left(\frac{f_{sl}}{f_k}\right) = 0.0235 Re^{0.67}$$

and the line for  $Re^{0.5}$ , although clearly of the right order, would not closely fit the measured data. One might note that the data extends over a large range from  $Re = 1200$  up to  $Re = 100\,000$ . On a dimensional basis, one expects that the shear layer frequency will scale with a characteristic velocity and length scale in the form:

$$\left(\frac{f_{sl}}{f_k}\right) \sim \frac{U_{sep}}{\theta_{sl}},$$



where  $U_{\text{sep}}$  is the velocity outside the boundary layer at the separation point, and  $\theta_{\text{sl}}$  is the momentum thickness of the separated shear layer. Bloor suggested, very rea-

**Fig. 16.141** Variation of normalized shear layer frequency with Reynolds number. The plot includes data from all the investigators up to 1997 who measured the shear layer frequency. By looking along the lines from the *left*, with one's nose right down on the page, the fact that the trend is higher than  $\text{Re}^{0.5}$  is rather more obvious, and yields the best fit as:  $(f_{\text{sl}}/f_k) = 0.0235 \text{Re}^{0.67}$  (References are found in Prasad and Williamson [16.283])

sonably, that the momentum thickness scales with the boundary layer thickness just before separation, which itself scales as  $\text{Re}^{-0.5}$ . If one notes that Strouhal number  $S = f_k D/U$ , one finds

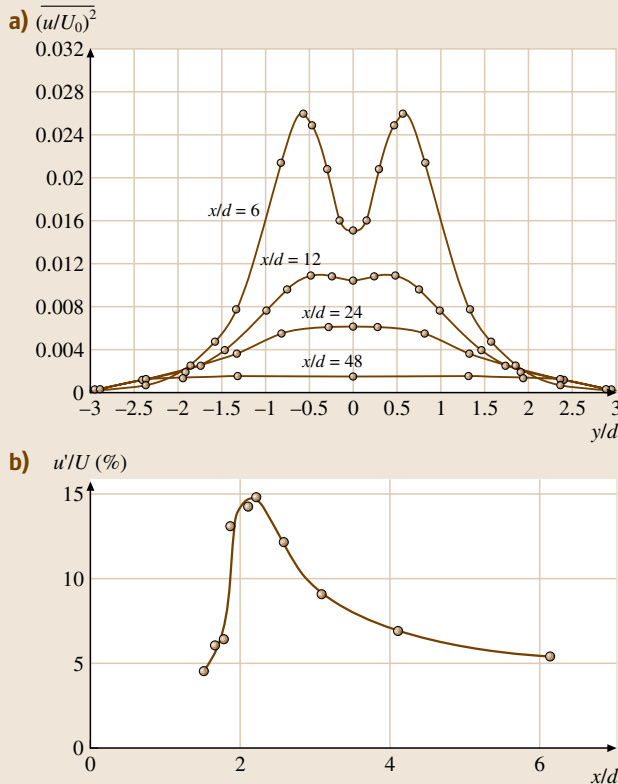
$$\left(\frac{f_{\text{sl}}}{f_k}\right) \sim \text{Re}^{0.5} \frac{(1 - C_{\text{pb}})^{0.5}}{S},$$

where we have used the relationship  $U_{\text{sep}}/U = (1 - C_{\text{pb}})^{0.5}$ . If one assumes, over a large range of  $\text{Re}$ , that  $C_{\text{pb}}$  is approximately constant then one finds the expression used by Bloor

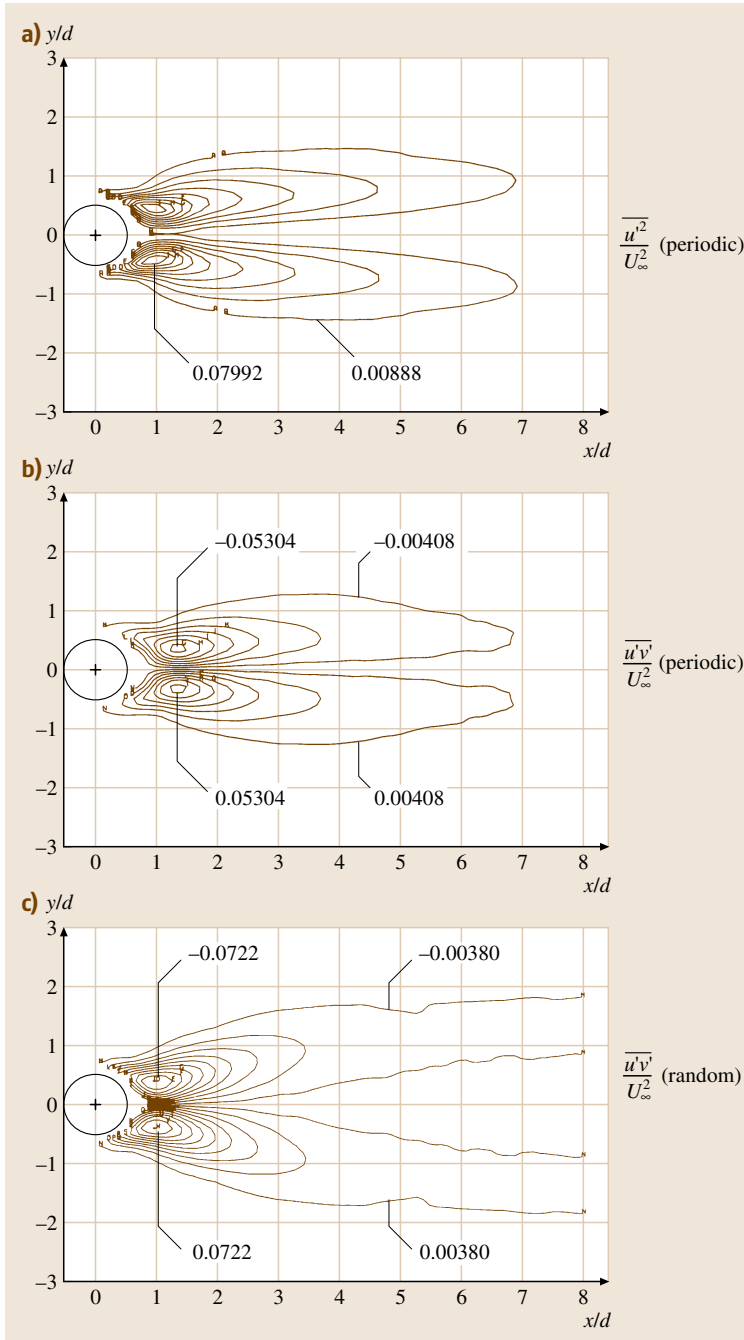
$$\left(\frac{f_{\text{sl}}}{f_k}\right) \sim \text{Re}^{0.5}.$$

Clearly this is of the same order as the measurements. However, the fact that the experimental power law for a comprehensive plot of all the previous studies follows  $\text{Re}^{0.67}$  was shown by Prasad and Williamson [16.297] to be due to the fact that the characteristic lengths and velocities are somewhat different to the values assumed above. In particular it was found that there is indeed a variation of base pressure  $C_{\text{pb}}$  over a range of  $\text{Re}$  (see the range between D–E in Fig. 16.135), and also that the movement of the transition point upstream as  $\text{Re}$  increases affects the shear layer frequency. Both of these influences yield an increase in the exponent, above 0.5. One finds from the analysis that approximately  $(f_{\text{sl}}/f_k) \sim \text{Re}^{0.70}$ , which would explain the experimentally observed shear layer frequency.

It is important to introduce briefly the types of turbulence intensities that have been measured in the near



**Fig. 16.142a,b** Typical velocity fluctuation measurements made in the near wake using hot wire anemometry. In (a), Roshko [16.254] measured the streamwise turbulence intensity profiles at specific downstream stations, showing the characteristic twin peaks associated with the two rows of vortices moving downstream. In (b), Bloor and Gerard [16.296] show the typical streamwise intensity profile along the wake centreline, indicating one of the measures of formation length as given by the location of the peak intensity ( $x/d \approx 2$  in this case)



**Fig. 16.143a–c** Contours of Reynolds stress extracted by an ingenious method involving a flying hot wire. The previous classical profiles in Fig. 16.142 may be related to the streamwise Reynolds stress contours of (a) here. Measurements of Reynolds shearing stresses by *Cantwell and Coles* [16.234] in (b), and (c) show the periodic and random stress components (these combine to give the total shearing stress), so one has some idea of how much stress is due to the periodic vortex shedding.  $Re = 140\,000$

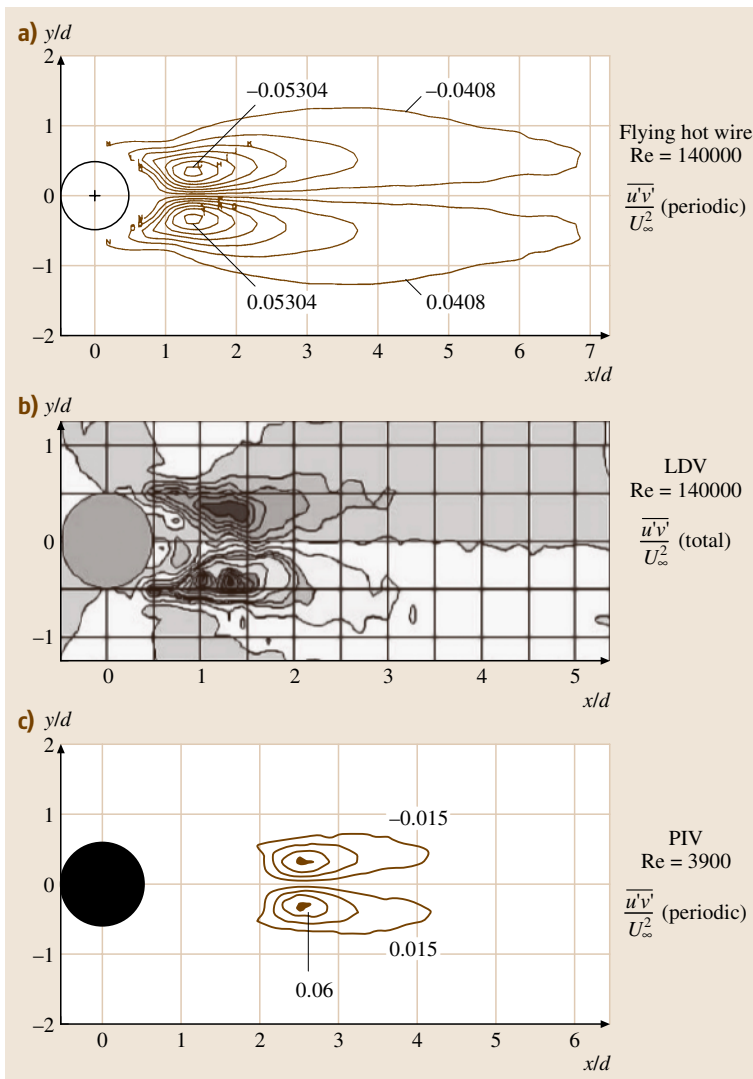
wake of the cylinder. *Roshko* [16.254] and *Kovaszny* [16.298] were the first to measure the streamwise turbulence intensity using the hot wire anemometer.

In Fig. 16.142, Roshko plotted various transverse profiles across the wake, exhibiting the characteristic twin peaks. The intensity reaches a peak and decays down-

stream, as shown from the centreline measurements of Bloor and Gerrard [16.296] in Fig. 16.142b. More-detailed measurements of turbulence quantities have been made extensively since that time, and we shall focus here briefly on some of the data of Cantwell and Coles [16.234] in Fig. 16.143. Their contours of streamwise normal Reynolds stress and Reynolds shear stress show the typical peaks on either side of the near wake. These measurements, made possible with an ingenious flying hot wire, have been subdivided usefully into a periodic and random component.

It is particularly interesting to note from Fig. 16.144 that the periodic component of the Reynolds shear stress

remains remarkably similar between  $Re = 3900$  (from PIV of Govardhan and Williamson [16.300]), and the much higher  $Re = 140\,000$  of Cantwell and Coles. On the other hand, the *random* component of the shear stresses are more than double at the high Reynolds numbers. Govardhan and Williamson observed that a significant portion of the remnant of the stresses, over and above the periodic component, is caused by fluctuations due to the shear layer instability, rather than only representing random fluctuations. Finally, we include here a plot of Reynolds stresses coming from LDV measurements of Djeridi et al. [16.299], completing a figure showing all three techniques, namely



**Fig. 16.144a–c** Comparison of stress measurements using flying hot wire, LDV, and PIV methods. The data in (a) and (b) are at the same  $Re = 140\,000$ , although they measure the periodic and total stresses [16.234, 299]. It is interesting that the PIV data for much lower  $Re = 3900$  in (c) show quite comparable peak values of the *periodic* shearing stresses at  $Re = 140\,000$ , although Govardhan and Williamson [16.300] find that the *random* stresses are far smaller at the lower  $Re$ . It appears that much of the energy of the *random* stresses at high  $Re$  are those caused by the shear layer instability, and so might not be considered all random

hot wire, LDV and PIV, producing a similar set of data.

The level of roughness and the level of free-stream turbulence, amongst other influences, can modify the Reynolds number for the inception of the drag crisis, as indicated by Fig. 16.145. A more turbulent free stream, or a rougher cylinder, will induce an earlier transition to boundary-layer turbulence on the body, and to a dramatic reduction in drag.

#### Regime E–F–G: Asymmetric Reattachment Regime (or Critical Transition)

In this regime, the base suction and the drag decrease drastically, associated with a separation–reattachment bubble, causing the revitalized boundary layer to separate much further downstream on the body sides (at the  $140^\circ$  line) and with a much reduced width of downstream wake than for the laminar case. There is a most interesting phenomenon which occurs at point F in Fig. 16.135, and this corresponds with a separation–reattachment bubble on *only one side* of the body, as discovered by Bearman [16.260], and shown by Schewe [16.303] to be bistable, causing rather large mean lift forces ( $C_L \approx 1$ ). The effect on the base pressure and Strouhal number of this single bubble on one side, or the presence of both bubbles, is shown in Figs. 16.134b and 16.135, where the single-bubble configuration is associated with point F in these plots.

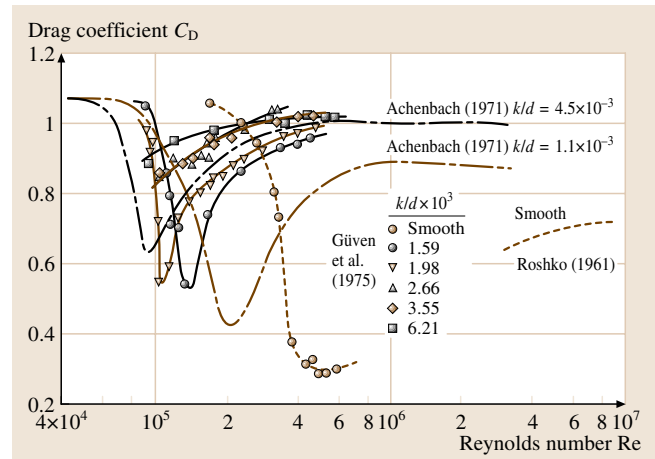
#### Regime G–H: Symmetric–Reattachment Regime (or Supercritical Regime)

In this regime, the flow is symmetric with two separation–reattachment bubbles, one on each side of the body. Some fluctuations are detected in the wake at large Strouhal numbers of around 0.4 [16.260], which is consistent with the relatively thin wake in this regime (one expects that the frequency will scale roughly inversely with the wake width). According to Roshko [16.217], the considerably higher Reynolds stresses of the boundary layer following the separation bubble allow the boundary layer to survive a greater adverse pressure gradient than in the post-critical regime (see below), where transition finally occurs before separation.

#### Regime H–J: Boundary–Layer Transition Regime (or Post-Critical Regime)

The increase in Reynolds numbers through the various regimes to this point is associated with a sequence of fundamental shear flow instabilities, following the order

- wake transition
- shear layer transition
- boundary layer transition.



**Fig. 16.145** The effect of surface roughness in stimulating an earlier drag crisis. Increasing roughness induces a lower critical  $Re$  at which one finds the drop in drag associated with laminar–turbulent transition in the attached boundary layer. However, it is apparent that high roughness then leads to a higher drag, after the crisis, than for smooth cylinders (see also Shih et al. [16.262]). (References are found in [16.301, 302])

The effect of an increase in  $Re$  up to this particular regime (H–J) is to move the turbulent transition point further upstream, until at high enough  $Re$ , the boundary layer on the surface of the cylinder itself becomes turbulent. It was generally assumed that, after this point, the downstream wake would be fully turbulent, and it was not expected that coherent vortices would be observed. However, in 1961, Roshko [16.233] was able to demonstrate the surprising result that periodic vortex shedding is strongly in evidence even in this flow regime, in what one might call a *Roshko street*, in honor of this important discovery. Separation occurs further upstream, yielding higher drag and base suction, and a wider downstream wake than in the previous regime. The drag in Fig. 16.133b and the base pressure of Fig. 16.135 both start to increase again when the vortex shedding resumes after the drag crisis in this regime discovered by Roshko. More-recent data up to very high  $Re \approx 10^7$  may be found in Shih et al. [16.262].

### 16.3.5 Concluding Remarks

Despite the fact that the wake of a bluff body does not easily admit analytical approaches, it is exceedingly rich in flow phenomena. Over the last few years, there has been a surge of experimental discoveries concerning several aspects of bluff-body wakes, but particularly



three-dimensional aspects. These activities have been matched by new understandings of wake flows coming from analysis and experiments and computations. Cellular shedding, vortex dislocations, oblique shedding, phase shocks and expansions, vortex loops, are all three-dimensional vortex dynamics phenomena that are becoming understood and that influence the varia-

tion of important parameters such as base pressure, drag, lift and vortex frequency.

Facilities to study bluff-body aerodynamics utilize both air and water as the fluid medium, and employ a large set of techniques to measure the velocity, vorticity, pressure, and the forces on bluff bodies, and to visualize such flows with a battery of methods.

## References

- 16.1 W.-H. Hucho (Ed.): *Aerodynamik des Automobils*, 5th edn. (Vieweg, Wiesbaden 2005), in German
- 16.2 J.B. Barlow, W.H. Rae, A. Pope: *Low Speed Wind Tunnel Testing* (Wiley, New York 1999)
- 16.3 A. Morelli: *General layout characteristics and performance of a new wind tunnel for aerodynamic and functional tests on full-scale vehicles*, SAE-paper 710 214 (SAE, Warrendale 1971)
- 16.4 E. Mercker, J. Wiedemann: *On the correction of interference effects in open jet wind tunnels*, SAE SP-1145 (SAE, Warrendale 1996) pp.1–15
- 16.5 SAE: *Aerodynamic testing of road vehicles, testing methods and procedures*, SAE J2084 (SAE, Warrendale 1993)
- 16.6 B.C. Nijhof, G. Wickern: *Reference static and dynamic pressures in automotive wind tunnels*, SAE-SP-1786 (SAE, Warrendale 2003) pp.15–31
- 16.7 F. Evert, H. Miehling: *Active suppression of buffeting at the Audi AAWT: Operational experiences and enhancements of the control scheme*, SAE-SP-1874 (SAE, Warrendale 2004) pp. 227–238
- 16.8 G. Wickern, W. von Heesen, S. Wallmann: *Wind tunnel pulsations and their active suppression*, SAE SP-1524 (SAE, Warrendale 2000) pp. 223–236
- 16.9 K.-R. Deutenbach: *Influence of plenum dimensions on drag measurement in 3/3-open-jet automotive wind tunnels*, SAE SP-1078 (SAE, Warrendale 1985) pp.198–198
- 16.10 W.-H. Hucho, L.J. Janssen, G. Schwarz: *The wind tunnel's ground plane boundary layer – its interference with the flow underneath cars*, SAE-Paper 750 066 (SAE, Warrendale 1975)
- 16.11 E. Mercker, H.W. Knappe: *Ground simulation with moving belt and tangentail blowing for full-scale automotive testing in a wind tunnel*, SAE-Paper 890 367 (SAE, Warrendale 1989)
- 16.12 A. Cogotti: *The T-Belt – The New Moving Ground System of the Pininfarina Wind Tunnel*, SAE-Paper 2007-01-1044 (SAE, Warrendale 2007)
- 16.13 J. Wiedemann: *Road simulation requirements and techniques*. In: *Progress in Vehicle Aerodynamics – Advanced Experimental Techniques*, ed. by J. Wiedemann, W.-H. Hucho (Expert, Renningen 2000) pp.48–63
- 16.14 A. Cogotti: *Generation of a controlled turbulent flow in an automotive wind tunnel and its effect on car aerodynamics and aeroacoustics*. In: *Prograss in Vehicle Aerodynamics III – Unsteady Flow Effects*, ed. by J. Wiedemann, W.-H. Hucho (Expert, Renningen 2004) pp.150–176
- 16.15 G. Carlino, A. Cogotti: *Simulation of transient phenomena with the turbulence generation system in the pininfarina wind tunnel*, SAE-Paper 2006-01-1031 (SAE, Warrendale 2006)
- 16.16 W.-H. Hucho: *Aerodynamik der stumpfen Körper* (Vieweg, Wiesbaden 2002)
- 16.17 J. Katz: *Integration of computational methods into automotive wind tunnel testing*, SAE-Paper 890 601 (SAE, Warrendale 1989)
- 16.18 E.Y. Ng, P.W. Johnson, S. Watkins, L. Grant: *Wind-tunnel tests of vehicle cooling performance at high blockage*, SAE SP-1524 (SAE, Warrendale 2000) pp. 25–34
- 16.19 J.W. Yen, W.R. Martindale, E.G. Duell, S.A. Arnette: *Determining blockage correction in climatic wind tunnels using CFD*, SAE SP-1786 (SAE, Warrendale 2003) pp.143–153
- 16.20 R. Künstner, J. Potthoff, U. Essers: *The aero-acoustic wind tunnel of the Stuttgart university*, SAE SP-1078 (SAE, Warrendale 1995) pp.31–47
- 16.21 J. Potthoff: *Future road simulation techniques*. In: *Progress in Vehicle Aerodynamics – Advanced Experimental Techniques*, ed. by J. Wiedemann, W.-H. Hucho (Expert, Renningen 2000) pp. 64–82
- 16.22 J. Wiedemann, G. Wickern, B. Ewald, C. Mattern: *Audi aero-acoustic wind tunnel*, SAE-Paper 930300 (SAE, Warrendale 1993)
- 16.23 J. Wiedemann: *The design of wind-tunnel fans for aeroacoustic testing*. In: *Topics in Wind Noise – Automobile Wind Noise and its Measurement, Part II*, SAE SP-1457, ed. by J.R. Callister, A.R. George (SAE, Warrendale 1999) pp.1–12
- 16.24 G. Antonucci, G. Ceronetti, A. Costelli: *Aerodynamic and climatic wind tunnels in FIAT research center*, SAE-Paper 770 392 (SAE, Warrendale 1977)
- 16.25 R. Buchheim, D. Schwabe, H. Röhe: *Der neue 6 m<sup>2</sup>-Klimawindkanal von Volkswagen, Teil 1*, ATZ **88**, 211–218 (1986), in German

- 16.26 R. Buchheim, D. Schwabe, H. Röhe: Der neue 6 m<sup>2</sup>-Klimawindkanal von Volkswagen, Teil 2, ATZ **88**, 389–392 (1986), in German
- 16.27 A. Cogotti: *Upgrade of the pininfarina wind tunnel – the new “13-fan” drive system*, Draft 06B-406 (SAE, Warrendale 2006)
- 16.28 G.W. Carr: The MIRA quarter-scale wind tunnel, MIRA Rep. **11** (1961)
- 16.29 G.W. Carr: An improved moving-ground system in the MIRA model wind tunnel, MIRA Rep. **2** (1987)
- 16.30 M. Bernard: : La soufflerie à veine longue de l’Institut Aérotechnique de Saint-Cyr-L’Ecole, Rev. Gén. Chemins de Fer **January**, 704–711 (1973)
- 16.31 R.G. Gawthorpe: Wind effects on ground transportation, J. Wind Eng. Indust. Aerodyn. **52**, 73–92 (1994)
- 16.32 N. Kobayashi, M. Yamada: *Stability of a one box type vehicle in a cross-wind – an analysis of transient aerodynamic forces and moments*, SAE-Paper 881 878 (SAE, Warrendale 1988)
- 16.33 L. Larsson, L.U. Nilsson, A. Berndtsson, L. Hammar, K. Knutson, H. Danielson: *Study of ground simulation-correlation between wind-tunnel and water-basin tests of a full-scale car*, SAE-Paper 890 368 (SAE, Warrendale 1989)
- 16.34 H. Neppert, R. Sanderson: *Untersuchungen zur Zugbegegnung. Bauwerk- und Personenpassage im Wasserkanal. Seminar Schnellbahnaerodynamik* (DFVLR-AVA, Göttingen 1978), in German
- 16.35 G. Sovran, D. Blaser: *Quantifying the potential impacts of regenerative braking on a vehicle’s tractive-fuel consumption for the U.S., European, and Japanese driving schedule*, SAE-paper 2006-01-0664 (SAE, Warrendale 2006)
- 16.36 K.-L. Haken: Messung des Rollwiderstands unter realen Bedingungen. In: *Kraftfahrwesen und Verbrennungsmotoren*, ed. by M. Bargende, J. Wiedemann (Expert, Renningen 1999) pp. 488–504, in German
- 16.37 J.C. Kessler, S.B. Wallis: *Aerodynamic test techniques*, SAE-Paper 660 464 (SAE, Warrendale 1966)
- 16.38 E. Széchenyi: Crosswind and its Simulation. In: *Progress in Vehicle Aerodynamics – Advanced Experimental Techniques*, ed. by J. Wiedemann, W.-H. Hucho (Expert, Renningen 2000) pp. 83–96
- 16.39 A. Wagner: *Ein Verfahren zur Vorhersage und Bewertung der Fahrerreaktion bei Seitenwind*, Dissertation (Universität Stuttgart, Stuttgart 2003), in German
- 16.40 L. Polanski, W. Matich, J.T. Kutney Sr.: *A new multi-component wind-tunnel balance for automotive wind tunnels*, SAE SP-1078 (SAE, Warrendale 1995) pp. 137–145
- 16.41 A. Cogotti: Flow field measurements and their interpretation. In: *Progress in Vehicle Aerodynamics – Advanced Experimental Techniques*, ed. by J. Wiedemann, W.-H. Hucho (Expert, Renningen 2000) pp. 97–120
- 16.42 J. Schmitt, K. Wilharm: Measurement of flow fields with LDA. In: *Progress in Vehicle Aerodynamics – Advanced Experimental Techniques*, ed. by J. Wiedemann, W.-H. Hucho (Expert, Renningen 2000) pp. 121–130
- 16.43 J. Kompenhans, M. Raffel, L. Dieterle, H. Richard, T. Dewhirst, H. Vollmers, K. Ehrenfeld, C. Willert, K. Pengel, C. Kähler, O. Ronneberger: Measurement of flow fields with particle image velocimetry (PIV). In: *Progress in Vehicle Aerodynamics – Advanced Experimental Techniques*, ed. by J. Wiedemann, W.-H. Hucho (Expert, Renningen 2000) pp. 131–157
- 16.44 S.B. Wallis: *Ventilation systems aerodynamics – a new design method*, SAE-Paper 710 036 (SAE, Warrendale 1971)
- 16.45 M. Helfer: Localization of sond sources. In: *Progress in Vehicle Aerodynamics – Advanced Experimental Techniques*, ed. by J. Wiedemann, W.-H. Hucho (Expert, Renningen 2000) pp. 170–182
- 16.46 U. Widmann, C. Zörner, N. Lindener: Aeroacoustic measurements and their correct physiological assessment. In: *Progress in Vehicle Aerodynamics – Advanced Experimental Techniques*, ed. by J. Wiedemann, W.-H. Hucho (Expert, Renningen 2000) pp. 183–200
- 16.47 A.R. George (Ed.): *Automobile wind noise and its measurement, Part I*, SAE SP-1184 (SAE, Warrendale 1996)
- 16.48 A.R. George (Ed.): *Automobile wind noise and its measurement, Part II*, SAE SP 1457 (SAE, Warrendale 1999)
- 16.49 W. Dobrzynski: Windgeräuschquellen am Kraftfahrzeug. In: *Akustik und Aerodynamik des Kraftfahrzeuges*, ed. by S.R. Ahmed (Expert, Renningen 1995) pp. 48–73, in German
- 16.50 M. Helfer: Beurteilung von Hohlspiegelmikrofonen zur Schallortung. In: *Akustik und Aerodynamik des Kraftfahrzeuges*, ed. by S.R. Ahmed (Expert, Renningen 1995) pp. 142–151, in German
- 16.51 B. Barsikow, W.F. King., E. Pfizenmaier: Wheel/rail noise generated by a high-speed train with a line array of microphones, Sound Vibration **118**, 337–342 (1987)
- 16.52 W. Weiher, B. Schwab: Modernisierung einer Windkanal-Traversieranlage – Schnelle Vermessung einer Fahrzeugstirnfläche. In: *Virtuelle Instrumente in der Praxis*, ed. by R. Jamal, H. Jaschinski (Hüthig, Heidelberg 2005) pp. 94–97, in German
- 16.53 K. Wilharm: Schnelle optische Formfassung bei der aerodynamischen Formoptimierung, VDI Berichte **1470**, 283–295 (1999), in German

- 16.54 P. Dannhäuser: Einsatz optischer 3D-Messtechnik in der Aerodynamikentwicklung. In: *Kraftfahrwesen und Verbrennungsmotoren, Internationales Stuttgarter Symposium*, ed. by M. Bargende, H.-C. Russ, J. Wiedemann (Expert, Renningen 2005) pp. 490–504, in German
- 16.55 J. Wiedemann, W.-H. Hucho (Eds.): *Progress in Vehicle Aerodynamics – Numerical Methods* (Expert, Renningen 2006)
- 16.56 J. Lukasiwicz: *Experimental Methods of Hypersonics* (Marcel Dekker, New York 1973)
- 16.57 F.K. Lu, D.E. Marren (Eds.): *Advanced Hypersonic Test Facilities*, Progress in Astronautics and Aeronautics, Vol. 198 (AIAA, Reston 2002)
- 16.58 R.J. Stalker: Hypervelocity aerodynamics with chemical nonequilibrium, *Ann. Rev. Fluid Mech.* **21**, 37–50 (1989)
- 16.59 H.G. Hornung: Experimental hypervelocity flow simulation, needs, achievements and limitations. In: *First Pacific International Conference on Aerospace Science and Technology* (Cheng-Kung Univ., Taiwan 1993)
- 16.60 B. Riemann: *Über die Fortpflanzung ebener Luftwellen von endlicher Schwingungsweite*, Vol. 8 (Königliche Gesellschaft der Wissenschaften, Göttingen 1860), in German
- 16.61 P. Vieille: Sur les discontinuités produites par la détente brusque des gas comprimés, *C. R. Acad. Sci.* **129**, 1228–1230 (1899)
- 16.62 J. Lukasiwicz: *Shock Tube Theory and Applications* (National Research Council, Ottawa 1950), Report MT-10
- 16.63 I.I. Glass, J.G. Hall: Shock Tubes. In: *Handbook of Supersonic Aerodynamics NAVORD Rep. 1488*, Vol. 6 (Springer, Berlin, Heidelberg 1959), Sect. 18
- 16.64 H. Oertel: *Stoßrohre* (Springer, Berlin, Heidelberg 1966), in German
- 16.65 N. Anfimov: TSNIMASH Capabilities for aerogasdynamical and thermal testing of hypersonic vehicles. In: *AIAA 17th Aerospace Ground Testing Conference*, AIAA paper 92-3962 (AIAA, Reston 1992)
- 16.66 K. Takayama: Summary of forty years continuous shock wave research at interdisciplinary shock wave research center, Tohoku University. In: *Proc. 24th International Symposium on Shock Waves*, ed. by Z. Jiang (Springer, Berlin, Heidelberg 2004)
- 16.67 G.A. Sod: A survey of several finite difference methods for systems of nonlinear hyperbolic conservation laws, *J. Comput. Phys.* **27**, 1–31 (1978)
- 16.68 E.F. Toro: *Riemann Solvers and Numerical Methods for Fluid Dynamics. A Practical Introduction*, 3rd edn. (Springer, Berlin, Heidelberg 2006)
- 16.69 S.K. Godunov: A difference scheme for numerical computation of discontinuous solutions of the equations of fluid dynamics, *Matem. Sbornik* **47**, 271–306 (1959)
- 16.70 J.D. Anderson Jr.: *Modern Compressible Flow with Historical Perspective*, 2nd edn. (McGraw-Hill, New York 1990)
- 16.71 A. Hertzberg: A shock tube method of generating hypersonic flows, *J. Aerosp. Sci.* **18**(12), 803–805 (1951)
- 16.72 I.I. Glass: Over forty years of continuous research at UTIAS on nonstationary flows and shock waves, *Shock Waves* **1**, 75–86 (1991)
- 16.73 R.J. Stalker: Modern development in hypersonic wind tunnels, *Aeronaut. J.* **January**, 21–39 (2006)
- 16.74 R.J. Stalker, N.R. Mudford: Unsteady shock propagation in a steady flow nozzle expansion, *J. Fluid Mech.* **241**, 525–548 (1992)
- 16.75 E.L. Resler, S.-C. Lin, A. Kantrowitz: The production of high temperature gases in shock tubes, *J. Appl. Phys.* **23**(12), 1390–1399 (1952)
- 16.76 C.E. Smith: The starting process in a hypersonic nozzle, *J. Fluid Mech.* **24**(4), 625–640 (1966)
- 16.77 M.S. Holden, R.A. Parker: LENS hypervelocity tunnels and application to vehicle testing at duplicated flight conditions. In: *Advanced Hypersonic Test Facilities*, Progress in Astronautics and Aeronautics, Vol. 198, ed. by F.K. Lu, D.E. Marren (AIAA, Reston 2002)
- 16.78 H. Olivier, M. Habermann, M. Bleilebens: Use of shock tunnels for hypersonic propulsion testing. In: *35th AIAA/ASME/ASEE Joint Propulsion Conference and Exhibit*, AIAA paper 99-2447 (AIAA, Reston 1999)
- 16.79 R.S.M. Chue, C.-Y. Tsai, R.J. Bakos, J.I. Erdos, R.C. Rogers: NASA's HYPULSE facility at GASL – a dual mode, dual driver reflected-shock/expansion tunnel. In: *Advanced Hypersonic Test Facilities, Progress in Astronautics and Aeronautics*, Vol. 198, ed. by F.K. Lu, D.E. Marren (NASA, Washington 2002)
- 16.80 D.W. Bogdanoff, H.A. Zambrana, J.A. Cavolowsky, M.E. Newfield, C.J. Cornelison, R.J. Miller: Reactivation and upgrade of the NASA Ames 16 inch shock tunnel; Status Report. In: *AIAA 30th Aerospace Sciences Meeting and Exhibit*, AIAA paper 92-0327 (AIAA, Reston 1992)
- 16.81 J.A. Cavolowsky, M.P. Loomis, M.E. Newfield, T.C. Tam: Flow characterization in the NASA Ames 16-inch shock tunnel. In: *28th AIAA/SAE/ASME/ASEE Joint Propulsion Conference*, AIAA paper 92-3810 (AIAA, Reston 1992)
- 16.82 R.J. Bakos, J.I. Erdos: Options for enhancement of the performance of shock-expansion tubes and tunnels. In: *AIAA 33rd Aerospace Sciences Meeting and Exhibit*, AIAA paper 95-0799 (AIAA, Reston 1995)
- 16.83 H. Olivier, J. Zonglin, H.R. Yu, F.K. Lu: Detonation-driven shock tubes and tunnels. In: *Advanced Hypersonic Test Facilities*, Prog. Astronaut. Aeronaut., Vol. 198, ed. by F.K. Lu, D.E. Marren (AIAA, Reston 2002)

- 16.84 F.K. Lu, D.R. Wilson, R.J. Bakos, J.I. Erdos: Recent advances in detonation techniques for high-enthalpy facilities, *AIAA J.* **38**(9), 1676–1684 (2000)
- 16.85 J.O. Reller, N.M. Reddy: Analysis of the flow in a 1-MJ electric-arc shock tunnel, *NASA TN D-6865*, 2160–2165 (1972)
- 16.86 S.P. Sharma, C. Park: Operating of a 60- and 10-cm electric arc-driven shock tube – Part I: The driver, *J. Thermophys. Heat Transfer* **4**(3), 259–265 (1990)
- 16.87 S.P. Sharma, C. Park: Operating of a 60- and 10-cm electric arc-driven shock tube – Part II: The driven section, *J. Thermophys. Heat Transfer* **4**(3), 266–272 (1990)
- 16.88 R.J. Stalker: A study of the free-piston shock tunnel, *AIAA J.* **5**(12), (4–1)–(4–10) (1967)
- 16.89 R.J. Stalker: Shock tunnel for real-gas hypersonics, *AGARD CP 428* (1987)
- 16.90 H.G. Hornung: Performance data of the new free-piston shock tunnel at GALCIT. In: *AIAA 17th Aerospace Ground Testing Conference*, AIAA paper 92-3943 (AIAA, Reston 1992)
- 16.91 G. Eitelberg, T.J. McIntyre, W.H. Beck, J. Lacey: High enthalpy shock tunnel in Göttingen, AIAA paper **92-3955** (1992)
- 16.92 K. Itoh, S. Ueda, T. Komuro, K. Saito, M. Takahashi, H. Miyajima, K. Koga: Design and Construction of HIEST (High enthalpy shock tunnel). In: *Proc. Int. Conference on Fluid Engineering*, Vol. 1 (JSME, Tokyo 1997) pp. 353–358
- 16.93 P. Petrie-Repar: *Numerical Simulation of Diaphragm Rupture*, Dissertation (University of Queensland, Queensland 1997)
- 16.94 H.G. Hornung, J.J. Quirk: Two effects of diaphragm bulge in shock tubes. In: *Advances in Fluid Mechanics and Turbomachinery*, ed. by H.J. Rath, C. Egbers (Springer, Berlin, Heidelberg 1998)
- 16.95 H. Mirels: Test time in low pressure shock tubes, *Phys. Fluids* **6**(9), 1201–1214 (1963)
- 16.96 H.O. Amann: Experimental study of the starting process in a reflection nozzle, *Phys. Fluids* **12**, 150–153 (1969), Suppl. I
- 16.97 B. Esser, H. Grönig, H. Olivier: High enthalpy testing in hypersonic shock tunnels. In: *Advances in Hypersonic, Defining the Hypersonic Environment*, Vol. 1, ed. by J.J. Berlin, J. Périaux, J. Ballmann (Birkhäuser, Boston 1989) pp. 182–258
- 16.98 K. Hannemann, V. Hannemann, S. Brück, R. Radespiel, G.S.R. Sarma: Computational modeling for high enthalpy flows, *Syst. Anal. Model. Simul.* **34**, 253–277 (1999)
- 16.99 K. Hannemann, M. Schnieder, B. Reimann, J. Martinez Schramm: The influence and the delay of driver gas contamination in HEG. In: *21th AIAA Aerodynamic Measurement Technology and Ground Testing Conference*, AIAA paper 2000-2593 (AIAA, Reston 2000)
- 16.100 E.L. Resler, D.E. Bloxson: *Very High Mach Number Flows by Unsteady Flow Principles* (Cornell Univ. Graduate School of Aeronautical Engineering Monograph, Ithaca 1952)
- 16.101 R.L. Trimpi: A preliminary theoretical study of the expansion tube, a new device for producing high-enthalpy short-duration hypersonic gas flows, *NASA Tech. Rep. TR R-133* (1962)
- 16.102 C.G. Miller: A critical examination of expansion tunnel performance, AIAA paper **78-768** (1978)
- 16.103 A. Paull, R.J. Stalker: Test flow disturbances in an expansion tube, *J. Fluid Mech.* **245**, 493–521 (1992)
- 16.104 I. Nompelis, G.V. Candler, T.P. Wadhams, M.S. Holden: Numerical simulation of high-enthalpy experiments in the LENS-X expansion tube facility. In: *42nd AIAA Aerospace Sciences Meeting and Exhibit*, AIAA paper 2004-1000 (AIAA, Reston 2004)
- 16.105 A. Paull, R.J. Stalker, I. Stringer: Experiments on an expansion tube with a free piston driver, 15th Aerodynamic Testing Conf. (American Institute of Aeronautics and Astronautics, Washington 1988) 173–178, Tech. Paper A88-37907 15-09
- 16.106 R.G. Morgan: A review of the use of expansion tubes for creating superorbital flows. In: *35th AIAA Aerospace Sciences Meeting and Exhibit*, AIAA paper 1997-279 (AIAA, Reston 1997)
- 16.107 R.G. Morgan: Development of X3, a superorbital expansion tube. In: *38th AIAA Aerospace Sciences Meeting and Exhibit*, AIAA paper 2000-0558 (AIAA, Reston 2000)
- 16.108 T.I. McIntyre, A.I. Bishop, T.N. Eichmann, H. Rubinsztein-Dunlop: Enhanced flow visualization with near-resonant holographic interferometry, *Appl. Opt.* **42**(22), 4445–4451 (2003)
- 16.109 T.I. McIntyre, M.J. Wegener, A.I. Bishop, H. Rubinsztein-Dunlop: Simultaneous two-wavelength holographic interferometry in a superorbital expansion tube facility, *Appl. Opt.* **36**, 8128–8134 (1997)
- 16.110 G. Wilson: Time-dependent quasi-one-dimensional simulations of high enthalpy pulse facilities. In: *AIAA 4th International Aerospace Planes Conference*, AIAA paper 92-5096 (AIAA, Reston 1992)
- 16.111 W.P. Eaton, J.H. Smith: Micromachined pressure sensors: Review and recent development, *Smart Mater. Struct.* **6**, 530–539 (1997)
- 16.112 S. Watson, W.N. MacPherson, J.S. Barton, J.D.C. Jones, A. Tyas, A.V. Pichugin, A. Hindle, W. Parkes, C. Dunare, T. Stevenson: Investigation of shock waves in explosive blasts using fibre optic pressure sensors, *Meas. Sci. Technol.* **17**, 1337–1342 (2006)
- 16.113 F. Lieneweg: *Handbuch Technische Temperaturmessung* (Vieweg, Braunschweig 1976), in German



- 16.114 Medtherm Corporation: *Coaxial Thermocouple Probes*, Bulletin 500 (Medtherm, Huntsville 2000)
- 16.115 H. Oertel: *Kurzzeitphysik, Wärmeübergangsmessungen* (Springer, Berlin, Heidelberg 1967), in German
- 16.116 C.G. Miller: Comparison of thin-film resistance heat-transfer gages with thin-skin calorimeter gages in conventional hypersonic wind tunnels, NASA TM **83197** (1981)
- 16.117 D.L. Schultz, T.V. Jones: Heat transfer measurements in short duration facilities, AGARD Rep. **165** (1973)
- 16.118 R.H. Eaves, C.T. Kidd: Miniature co-axial surface thermocouples for heat transfer rate measurements in hypersonic wind tunnels. In: *41st Supersonic Tunnel Association Meeting* (1974)
- 16.119 W.J. Cook, E.J. Felderman: Reduction of data from thin-film heat transfer gauges: A concise numerical technique, AIAA J. **4**(3), 561–562 (1966)
- 16.120 D.N. Kendall, W.P. Dixon, E.H. Schulte: Semiconductor surface thermocouples for determining heat transfer rates, IEEE Trans. Aerosp. Electron. Syst. **AES-3**(4), 596–603 (1967)
- 16.121 C. Jessen: *Messung von Druck, Temperatur und Kraft an Modellen im Stosswellenkanal. Dissertation* (RWTH Aachen, Aachen 1993)
- 16.122 G.T. Skinner: *A New Method of Calibrating Thin Film Gauge Backing Materials*, Rep. CAL-105 (Cornell University, Buffalo 1962)
- 16.123 B.FR. Ewald: Review article multi-component force balances for conventional and cryogenic wind tunnels, Meas. Sci. Technol. **11**, R81–R94 (2000)
- 16.124 M. Robinson: *Simultaneous Lift, Moment and Thrust Measurements on a Scramjet in Hypervelocity Flow*, Dissertation (University of Queensland, Queensland 2003)
- 16.125 K.W. Naumann, H. Ende, G. Mathieu, A. George: Millisecond aerodynamic force measurement with side jet model in the ISL shock tunnel, AIAA J. **31**(6), 1068–1074 (1993)
- 16.126 M. Takahashi, S. Ueda, T. Komuro, K. Sato, H. Tanno, K. Itoh: Development of a new force measurement method for scramjet testing in a high enthalpy shock tunnel. In: *9th AIAA International Space Planes and Hypersonic Systems and Technologies Conference*, AIAA paper 1999–4961 (AIAA, Reston 1999)
- 16.127 M.I. Kussoy, C.C. Horstmann: Cone drag in rarefied hypersonic flow, AIAA J. **8**(2), 315–320 (1970)
- 16.128 F.P. Beer Jr, E.R. Johnston, E.R. Eisenberg, W.E. Clausen, D.F. Mazurek, P.J. Cornwell: *Vector Mechanics for Engineers: Statics and Dynamics*, 8th edn. (McGraw-Hill, New York 2007)
- 16.129 L. Bernstein, G.T. Scott: A laser-interferometric trajectory-following system for determining forces on free flying models in a shock tunnel. In: *Proc. 13th Int. Symp. Shock Waves*, ed. by C.E. Treanor, J.G. Hall (State Univ. of New York Press, Albany 1981) pp. 150–158
- 16.130 C. Jessen, H. Grönig: A six-component balance for short duration hypersonic facilities. In: *New Trends in Instrumentation for Hypersonic Research*, ed. by A. Boutier (Kluwer Academic, Dordrecht 1993) pp. 295–305
- 16.131 V. Störkmann, H. Olivier, H. Grönig: Force measurements in hypersonic impulse facilities, AIAA J. **36**(3), 342–348 (1998)
- 16.132 K. Itoh, S. Ueda, H. Tanno, T. Komuro, K. Sato: Hypersonic aerothermodynamic and scramjet research using high enthalpy shock tunnel, Shock Waves **12**, 93–98 (2002)
- 16.133 R. Prost, R. Goutte: Discrete constrained iterative deconvolution algorithms with optimized rate convergence, Signal Process. **7**(3), 209–230 (1984)
- 16.134 D.J. Mee, W.J.T. Daniel, J.M. Simmons: Three-component force balance for flows of millisecond duration, AIAA J. **34**(3), 590–595 (1996)
- 16.135 S.R. Sanderson, J.M. Simmons: Drag balance for hypervelocity impulse facilities, AIAA J. **29**(12), 2185–2191 (1991)
- 16.136 M. Robinson, D.J. Mee, A. Paull: Lift, pitching moment and thrust measurement on a fuelled scramjet. In: *Proc. 23rd International Symposium on Shock Waves*, ed. by F. Lu (2001), on CD-ROM
- 16.137 M. Robinson, K. Hannemann: Short duration force measurements in impulse facilities. In: *25th AIAA Aerodynamic Measurement Technology and Ground Testing Conference*, AIAA paper 2006–3439 (AIAA, Reston 2006)
- 16.138 M.G. Novean, J.A. Schetz, R.D.W. Bowersox: Direct measurements of skin friction in complex supersonic flows, AIAA paper **97-0394** (1997)
- 16.139 C.P. Goyne, R.J. Stalker, A. Paull: Shock-tunnel skin-friction measurement in a supersonic combustor, J. Propuls. Power **15**(3), 699–705 (1999)
- 16.140 C.P. Goyne: *Skin Friction Measurements in High Enthalpy Flows at High Mach Number. Dissertation* (University of Queensland, Queensland 1998)
- 16.141 M.S. Holden: An experimental investigation of turbulent boundary layers at high Mach number and Reynolds numbers, Cornell Aero. Lab. Rep. **AB-5072-A-1**, NASA CR-112147 (1972)
- 16.142 C.P. Goyne, R.J. Stalker, A. Paull: Skin-friction measurements in high-enthalpy hypersonic boundary layers, J. Fluid Mech. **485**, 1–32 (2003)
- 16.143 M. Wollenhaupt, M. Rosenhauer, T. Müller, J. Jourdan, J. Scholz, S. Hartung, W.H. Beck: NO laser-induced fluorescence studies for the application of single-shot two-line thermometry to HEG. In: *Proc. 21st International Symposium on Shock Waves*, ed. by A.F.P. Houwing (Panther, Fyshwick 1997)
- 16.144 J. Scholz, S. Hartung, J. Jourdan, M. Wollenhaupt, W.H. Beck: Temporally resolved NO laser-induced fluorescence investigations for the application of



- two-line thermometry to high enthalpy flows. In: *Proc. 22nd Int. Symp. Shock Waves*, ed. by G.J. Ball, R. Hillier, G.T. Roberts (Southampton Univ. Media, Southampton 1999)
- 16.145 M. Wollenhaupt: Einzelpuls Zwei-Linien-Thermometrie mit planarer laserinduzierter Fluoreszenz an NO-Molekülen in Hochenthalpieströmungen, DLR-FB **97-23** (1997), in German
- 16.146 S.O. O'Byrne, P.M. Danehy, A.F.P. Houwing: Non-intrusive temperature and velocity measurements in a hypersonic nozzle flow, 22nd AIAA Aerodynamic Measurement Technology and Ground Testing Conference (AIAA, Reston 2002)
- 16.147 P.C. Palma, P.M. Danehy, A.F.P. Houwing: Fluorescence imaging of rotational and vibrational temperature in a shock tunnel nozzle flow, *AIAA J.* **41**(9), 1722–1732 (2003)
- 16.148 A. Ben-Yakar, M.G. Mungal, R.K. Hanson: Time evolution and mixing characteristics of hydrogen and ethylene transverse jets in supersonic cross-flows, *Phys. Fluids* **18**(2), 026101–026117 (2004)
- 16.149 A.L. Kovachevich, K.M. Hajek, T.J. McIntyre, A. Paull, M. Abdel-jawad: Imaging of hydrogen fuel injection on the intake of a heated wall scramjet. In: *42nd AIAA/ASME/SAE/ASEE Joint Propulsion Conference and Exhibit*, AIAA paper 2006-5039 (AIAA, Reston 2006)
- 16.150 A.K. Mohamed, D. Henry, D. Bize, M. Ory, W.H. Beck, M. Carl, U. Frenzel: MSTP phase 2 synthesis report: Infrared diode laser absorption spectroscopy in the HEG shock tube facility, *ONERA RTS* **14/7301 PY** (1997)
- 16.151 O. Trinks, W.H. Beck: Application of a diode-laser absorption technique with the D2 transition of atomic Rb for hypersonic flow-field measurements, *Appl. Opt.* **37**(30), 7070–7075 (1998)
- 16.152 W.H. Beck, O. Trinks, A.K. Mohamed: Diode laser absorption measurements in high enthalpy flows: HEG free stream conditions and driver gas arrival. In: *Proc. 22nd Int. Symp. Shock Waves*, ed. by G.J. Ball, R. Hillier, G.T. Roberts (Southampton Univ. Media, Southampton 1999)
- 16.153 M.A. Oehlschlaeger, D.F. Davidson, R.K. Hanson: Temperature measurement using ultraviolet absorption of carbon dioxide behind shock waves, *Appl. Opt.* **44**, 6599–6605 (2005)
- 16.154 T.C. Hanson, D.F. Davidson, R.K. Hanson: Shock tube measurements of water and n-dodecane droplet evaporation behind shock waves. In: *43rd Aerospace Sciences Meeting*, AIAA paper 2005-0350 (AIAA, Reston 2005)
- 16.155 K. Nakakita, K. Asai: Pressure-sensitive paint application to a wing-body model in a hypersonic shock tunnel, 22nd AIAA Aerodynamic Measurement Technology and Ground Testing Conference (2002)
- 16.156 S. Ohmi, H. Nagai, K. Asai, K. Nakakita: Effect of TSP layer thickness on global heat transfer measurement in hypersonic flow, 44th AIAA Aerospace Sciences Meeting and Exhibit (2006)
- 16.157 F. Seiler, M. Havermann, A. George, F. Leopold, J. Srujijes: Planar velocity visualization in high-speed wedge flow using Doppler picture velocimetry (DPV) compared with particle image velocimetry (PIV), *J. Visual.* **6**(3), 253–262 (2003)
- 16.158 S. O'Byrne, P.M. Danehy, A.D. Cutler:  $N_2/O_2/H_2$  dual-pump CARS: Validation experiments, *Proc. 20th Int. Congress on Instrumentation in Aerospace Simulation Facilities* (2003)
- 16.159 P.M. Danehy, S. O'Byrne, A.D. Cutler, C. Rodriguez: CARS as a probe for hydrogen-fuel/air mixing, *JAN-NAF APS/CS/PSHS/MSS Joint Meeting* (2003)
- 16.160 B.N. Littleton, A.I. Bishop, T.J. McIntyre, P.F. Barker, H. Rubinsztajn-Dunlop: Flow tagging velocimetry in a superorbital expansion tube, *Shock Waves* **10**, 225–228 (2000)
- 16.161 E.P. Muntz: The electron beam fluorescence technique, *AGARDograph* **132**, 111 (1968)
- 16.162 K.A. Bütefisch, D. Vennemann: The electron beam technique in hypersonic rarefied gas dynamics, *Prog. Aerosp. Sci.* **15**, 217–260 (1974)
- 16.163 D.P. Shelton, P.E. Cassidy: Electron beam density measurement in a hypersonic shock tunnel flow-field, 17th Aerospace Ground Testing Conference (AIAA, Reston 1992)
- 16.164 E.P. Muntz, F.M. Lufly, I.D. Boyd: The study of reacting, high energy flows using pulsed electron-beam fluorescence, 27th Fluid Dynamics Conference (AIAA, Reston 1996)
- 16.165 W. Merzkirch: *Flow Visualization* (Academic, New York 1974)
- 16.166 A.N. Zaidel', G.V. Ostrovskaya, Y.I. Ostrovskii: Plasma diagnostics by holography (a review), *Sov. Phys. Tech. Phys.* **13**, 1153–1164 (1969)
- 16.167 F.C. Jahoda, R.A. Jeffries, G.A. Sawyer: Fractional-fringe holographic plasma interferometry, *Appl. Opt.* **6**, 1407–1410 (1967)
- 16.168 H. Schardin: Das Toeplersche Schlierenverfahren: Grundlagen für seine Anwendung und quantitative Auswertung, *VDI (Verein Deutscher Ingenieure) Forschungsheft* **367**, 1–32 (1934), in German
- 16.169 G.S. Settles: Schlieren and shadowgraph techniques. In: *Visualizing Phenomena in Transparent Media*, ed. by R.J. Adrian, M. Gharib, W. Merzkirch, D. Rockwell, J.H. Whitelaw (Springer, Berlin, Heidelberg 2001)
- 16.170 S.F. Ray (Ed.): High speed photography and photonics, *SPIE Monograph* **PM120** (2002)
- 16.171 A. Toepler: Optische Studien nach der Methode der Schlierenbeobachtung, *Poggendorfs Annal Phys. Chem.* **210**(6), 194–217 (1867), in German
- 16.172 E. Mach, P. Salcher: *Optische Untersuchung der Luftstrahlen* (Akad. Wiss., Wien 1889), in German
- 16.173 H. Fischer: Simple submicrosecond light source with extreme brightness, *J. Opt. Soc. Am.* **47**(11), 981–984 (1957)

- 16.174 HSPS: *Website* (High-Speed Photo.-Systeme, Wedel 2006), [www.hsp.com](http://www.hsp.com)
- 16.175 J. Holzfuß: Analoge und digitale Hochgeschwindigkeitskinematographie – eine Übersicht (Analogue and digital high speed cinematography – a review), *TM – Technisches Messen* **68**(11), 499–506 (2001), in German
- 16.176 J. Martinez Schramm, S. Karl, K. Hannemann: High speed flow visualization at HEG. In: *New Results in Numerical and Experimental Fluid Mechanics IV*, Notes on Numerical Fluid Mechanics and Multidisciplinary Design, Vol. 87, ed. by C. Breitsamter, B. Laschka, H. Heinemann (Springer, Berlin Heidelberg 2004) pp. 229–235
- 16.177 D.J. Kewley, H.G. Hornung: Non-equilibrium dissociating nitrogen flow over a wedge, *J. Fluid Mech.* **64**(4), 725–736 (1974)
- 16.178 H.G. Hornung, G.H. Smith: The influence of relaxation on shock detachment, *J. Fluid Mech.* **93**(2), 225–239 (1979)
- 16.179 S. Karl, J. Martinez Schramm, K. Hannemann: High enthalpy cylinder flow in HEG: A basis for CFD validation, 33rd AIAA Fluid Dynamics Conference (2003)
- 16.180 M.S. Holden: Experimental studies of laminar separated flows induced by shock wave/boundary layer and shock/shock interaction in hypersonic flows for CFD validation, AIAA paper **2000-0930** (2000)
- 16.181 M.S. Holden, J.K. Harvey: Comparisons between DSMC and Navier–Stokes solutions on measurements in regions of laminar shock wave boundary layer interaction in hypersonic flows, AIAA paper **2002-0435** (2002)
- 16.182 G.V. Candler, I. Nompelis, M.-C. Druguet, M.S. Holden, T.P. Wadhams, I.D. Boyd, W.-L. Wang: CFD validation for hypersonic flight: Hypersonic double-cone flow simulations, *AIAA J.* **2002-0581** (2002)
- 16.183 S.R. Sanderson: *Shock Wave Interaction in Hypervelocity Flow*, Dissertation (California Institute of Technology, Pasadena 1995)
- 16.184 M. Schnieder: *Wechselwirkung einer starken und einer schwachen Stoßwelle in reagierender Hochenthalpieströmung*, Dissertation, DLR-FB 98-31 (RWTH Aachen, Aachen 1999), in German
- 16.185 S.G. Mallinson, S.L. Gai, N.R. Mudford: The interaction of a shock wave with a laminar boundary layer at a compression corner in high-enthalpy flows including real gas effects, *J. Fluid Mech.* **342**, 1–35 (1997)
- 16.186 J.P. Davis: *High-Enthalpy Shock/Boundary-Layer Interaction on a Double Wedge*, Dissertation (California Institute of Technology, Pasadena 1999)
- 16.187 J.P. Davis, B. Sturtevant: Separation length in high-enthalpy shock/boundary-layer interaction, *Phys. Fluids* **12**, 2661–2687 (2000)
- 16.188 J. Martinez Schramm, G. Eitelberg: Shock boundary layer interaction in hypersonic high enthalpy flow on a double wedge. In: *Proc. 22nd Int. Symp. Shock Waves*, ed. by G.J. Ball, R. Hillier, G.T. Roberts (Southampton Univ. Media, Southampton 1999)
- 16.189 T.J. Horvath, S.A. Berry, N.R. Merski, S.M. Fitzgerald: X-38 experimental aerothermodynamics, 34th AIAA Thermophysics Conference (AIAA, Reston 2000)
- 16.190 K. Hannemann, J. Martinez Schramm, S. Brück, J.M.A. Longo: High enthalpy testing and CFD rebuilding of X-38 in HEG, *Proc. 23rd International Symposium on Shock Waves*, ed. by F. Lu (2001), on CD-ROM
- 16.191 K. Itoh, T. Komuro, K. Sato, H. Tanno, S. Ueda: Hypersonic aerodynamic research of HOPE using high enthalpy shock tunnel, AIAA/NAL-NASDA-ISAS 10th International Space Planes and Hypersonic Systems and Technologies Conference (AIAA, Reston 2001)
- 16.192 D. Isakeit, P. Watillon, A. Wilson, C. Cazaux, G. Bréard, T. Leveugl: *The Atmospheric Reentry Demonstrator*, European Space Agency Rep. BR-138 (1998)
- 16.193 I.A. Johnston, M. Weiland, J. Martinez Schramm, K. Hannemann, J. Longo: Aerothermodynamics of the ARD: Postflight numerics and shock-tunnel experiments, 40th AIAA Aerospace Sciences Meeting and Exhibit (AIAA, Reston 2002)
- 16.194 T.J. McIntyre, I. Lourel, T.N. Eichmann, R.G. Morgan, P.A. Jacobs, A.I. Bishop: Experimental expansion tube study of the flow over a toroidal ballute, *J. Spacecr. Rockets* **41**(5), 716–725 (2004)
- 16.195 A. Rasheed, K. Fujii, H.G. Hornung, J.L. Hall: Experimental investigation of the flow over a toroidal aerocapture ballute, 19th Applied Aerodynamics Conference (AIAA, Reston 2001)
- 16.196 L.M. Mack: *Boundary-Layer Stability Theory, Special Course on Stability and Transition of Laminar Flow*, AGARD Rep. 709 (1984)
- 16.197 H.G. Hornung: Hypersonic real-gas effects on transition. In: *IUTAM Symposium on One Hundred Years of Boundary Layer Research*, *Proc. IUTAM Symposium*, ed. by G.E.A. Meier, K.R. Sreenivasan (Springer, Berlin, Heidelberg 2006)
- 16.198 H.B. Johnson, T. Seipp, G.V. Candler: Numerical study of hypersonic reacting boundary layer transition on cones, *Phys. Fluids* **10**, 2676–2685 (1998)
- 16.199 H.G. Hornung, P.H. Adam, P. Germain, K. Fujii, A. Rasheed: On transition and transition control in hypervelocity flow, *Proc. Ninth Asian Congress of Fluid Mechanics* (2002)
- 16.200 D.J. Mee, C.P. Goyne: Turbulent spots in boundary layers in a free-piston shock tunnel flow, *Shock Waves* **6**, 337–343 (1996)
- 16.201 D.J. Mee: Boundary layer transition measurements in hypervelocity flows in a shock tunnel, 39th AIAA Aerospace Sciences Meeting (AIAA, Reston 2001)

- 16.202 A. Paull, H. Alesi, S. Anderson: The HyShot flight program and how it was developed, AIAA/AAAF 11th International Space Planes and Hypersonic Systems and Technologies Conference (AIAA, Reston 2002)
- 16.203 V. Rausch, C. McClinton, J. Sitz: Hyper-X program overview, Proc. Int. Symp. Airbreathing Engines (1999), ISABE 99-7213
- 16.204 R.T. Volland, L.D. Huebner, C.R. McClinton: X-43A hypersonic vehicle technology development, Acta Astronaut. **59**, 181–191 (2006)
- 16.205 R.J. Stalker, A. Paull, D.J. Mee, R.G. Morgan, P.A. Jacobs: Scramjets and shock tunnels – the Queensland experience, Prog. Aerosp. Sci. **41**, 471–513 (2005)
- 16.206 A. Paull, R.J. Stalker, D.J. Mee: Experiments on supersonic ramjet propulsion in a shock tunnel, J. Fluid Mech. **296**, 150–183 (1995)
- 16.207 G.S. Deiwert, J.A. Cavolowsky, M.P. Loomis: Large scale scramjet testing in the Ames 16-inch shock tunnel, 18th AIAA Aerospace Ground Testing Conference (AIAA, Reston 1994)
- 16.208 A. Paull, R.J. Stalker: Scramjet testing in the T3 and T4 hypersonic impulse facilities, Scramjet Propulsion, Vol. 189, ed. by E.T. Curran, S.N.B. Murthy (2000) 1–46
- 16.209 N.E. Hass, M.K. Smart, A. Paull: Flight data analysis of HyShot 2, 13th AIAA/CIRA International Space Planes and Hypersonic Systems and Technologies Conference (AIAA, Reston 2006)
- 16.210 A.D. Gardner, K. Hannemann, J. Steelant, A. Paull: Ground testing of the HyShot supersonic combustion flight experiment in HEG and comparison with flight data. In: 40th AIAA Joint Propulsion Conference, AIAA paper 2004–3345 (AIAA, Reston 2004)
- 16.211 S. Karl, K. Hannemann, J. Steelant, A. Mack: CFD analysis of the HyShot supersonic combustion flight experiment configuration, 14th AIAA/AHI Space Planes and Hypersonic Systems and Technologies Conference (AIAA, Reston 2006)
- 16.212 T. Sunami, K. Itoh, H. Tanno, T. Komuro, K. Sato, M. Kodera, K. Fujimura, T. Maehara, T. Narita: Mach 8 firing tests of a hypermixer scramjet at HIEST, Proc. of the 35th Fluid Dynamics Conference Japan (2003) 123–126
- 16.213 R.C. Rogers, A.T. Shih, C.-Y. Tsai, R.O. Foelsche: Scramjet tests in a shock tunnel at flight Mach 7, 10, and 15 conditions, 37th AIAA/ASME/SAE/ASEE Joint Propulsion Conference and Exhibit AIAA–2001–3241 (2001)
- 16.214 R.C. Rogers, A.T. Shih, N.E. Hass: Scramjet development tests supporting the Mach 10 flight of the X-43, AIAA/CIRA 13th International Space Planes and Hypersonics Systems and Technologies Conference (AIAA, Reston 2005)
- 16.215 M. Bleilebens: *Einfluß der Wandtemperatur auf die Stoß/Grenzschicht-Wechselwirkung an einer Rampe im Hyperschall*, Dissertation (RWTH Aachen, Aachen 2004), in German
- 16.216 S. Ueda, M. Weiland, K. Itoh, K. Hannemann: Comparative experiment on the surface catalyticity in two high enthalpy shock tunnels, 24th AIAA Aerodynamic Measurement Technology and Ground Testing Conference (AIAA, Reston 2004)
- 16.217 A. Roshko: Perspectives on bluff body aerodynamics, J. Wind Eng. Indust. Aerodyn. **49**, 79 (1993)
- 16.218 L. Rosenhead: Vortex systems in wakes, Adv. Appl. Mech. **3**, 185 (1953)
- 16.219 M.V. Morkovin: Flow around a circular cylinder – kaleidoscope of challenging fluid phenomena, Proc. ASME Symp. on Fully Separated Flows (Philadelphia 1964) 102–118
- 16.220 E. Berger, R. Wille: Periodic flow phenomena, Annu. Rev. Fluid Mech. **4**, 313 (1972)
- 16.221 H. Oertel: Wakes behind blunt bodies, Annu. Rev. Fluid Mech. **22**, 539 (1990)
- 16.222 M. Coutanceau, J.-R. Defaye: Circular cylinder wake configurations: A flow visualisation survey, Appl. Mech. Rev. **44**, 255 (1991)
- 16.223 C.H.K. Williamson: Vortex dynamics in the cylinder wake, Annu. Rev. Fluid Mech. **28**, 477 (1996)
- 16.224 C.H.K. Williamson, R. Govardhan: Vortex-induced vibration, Annu. Rev. Fluid Mech. **36**, 413 (2004)
- 16.225 C.H.K. Williamson, A. Roshko: Vortex formation in the wake of an oscillating cylinder, J. Fluid Struct. **2**, 355 (1988)
- 16.226 R. Mills, J. Sheridan, K. Hourigan: Particle image velocimetry and visualization of natural and forced flow around rectangular cylinders, J. Fluid Mech. **478**, 299 (2003)
- 16.227 C.H.K. Williamson: Three-dimensional wake transition behind a cylinder, J. Fluid Mech. **328**, 345 (1996)
- 16.228 H. Thomann: Measurements of the recovery temperature in the wake of a cylinder and of a wedge at Mach numbers between 0.5 and 3, Aero Res. Inst. Sweden (FFA) Rep. No. **84**, 1–30 (1959)
- 16.229 J.M. Cimbala, H.M. Nagib, A. Roshko: Large structure in the far wakes of two-dimensional bluff bodies, J. Fluid Mech. **190**, 265 (1988)
- 16.230 T. Corke, D. Koga, R. Drubka, H. Nagib: A new technique for introducing controlled sheets of smoke streaklines in wind tunnels, IEEE Pub. **77**, 74 (1974), CH 1251–8 AES
- 16.231 R.J. Goldstein: *Fluid Mechanics Measurements* (Taylor Francis, Washington 1996)
- 16.232 A. Fage, V.M. Falkner: An experimental determination of the intensity of friction on the surface of an airfoil, Proc. R. Soc. **129**, 378 (1930)
- 16.233 A. Roshko: Experiments on the flow past a circular cylinder at very high Reynolds number, J. Fluid Mech. **10**, 345 (1961)
- 16.234 B. Cantwell, D. Coles: An experimental study of entrainment and transport in the turbulent near-wake of a circular cylinder, J. Fluid Mech. **136**, 321 (1983)

- 16.235 V. Strouhal: Über eine besondere Art der Tonerregung, *Annal. Phys. Chem. (Leipzig), Neue Folge* **5**, 216 (1878), in German
- 16.236 N. Rott: Lord Rayleigh and hydrodynamic similarity, *Phys. Fluids* **4**, 2595 (1993)
- 16.237 Lord Rayleigh: Aeolian tones, *Phil. Mag.* **XXIX**, 433 (1915)
- 16.238 T. von Karman: Über den Mechanismus des Widerstands, den ein bewegter Körper in einer Flüssigkeit erfährt, *Göttinger Nachr. Math. Phys. Kl.* **509**, 324–330 (1911), in German
- 16.239 J.H. Gerrard: The mechanics of the vortex formation region of vortices behind bluff bodies, *J. Fluid Mech.* **25**, 401 (1966)
- 16.240 A.E. Perry, M.S. Chong, T.T. Lim: The vortex shedding process behind two-dimensional bluff bodies, *J. Fluid Mech.* **116**, 77 (1982)
- 16.241 P.W. Bearman, D.M. Trueman: An investigation of the flow around rectangular cylinders, *Aero. Q.* **23**, 229 (1972)
- 16.242 A. Roshko: On the wake and drag of bluff bodies, *J. Aeronaut. Sci.* **22**, 124 (1955)
- 16.243 C.H.K. Williamson, G.L. Brown: A series in  $1/\sqrt{Re}$  to represent the Strouhal–Reynolds number relationship for the cylinder wake, *J. Fluid Struct.* **12**, 1073 (1998)
- 16.244 P.W. Bearman: On vortex street wakes, *J. Fluid Mech.* **28**, 625 (1967)
- 16.245 O.M. Griffin: Universal similarity in the wakes of stationary and vibrating bluff structures, *J. Fluids Eng.* **103**, 52 (1981)
- 16.246 P.W. Bearman: Investigation of the flow behind a two-dimensional model with a blunt trailing edge and fitted with splitter plates, *J. Fluid Mech.* **21**, 241 (1965)
- 16.247 A.B. Bauer: Vortex shedding from thin flat plates parallel to the free stream, *J. Aeronaut. Sci.* **28**, 340 (1961)
- 16.248 H. Eisenlohr, H. Eckelmann: . In: *Exp. Heat Transfer, Fluid Mech. and Thermod.*, ed. by R.K. Shah, E.N. Ganic, K.T. Yang (Elsevier, Amsterdam 1988) pp. 264–268
- 16.249 C. Norberg: Fluctuating lift on a circular cylinder: Review and new measurements, *J. Fluid Struct.* **17**, 57 (2003)
- 16.250 C. Wieselsberger: Recent statements on the laws of liquid and air resistancy, *Phys. Z.* **22**, 321 (1921)
- 16.251 O.M. Griffin, S.E. Ramberg: The vortex street wakes of vibrating cylinders, *J. Fluid Mech.* **66**, 553 (1974)
- 16.252 A. Roshko, W. Fiszdon: On the persistence of transition in the near wake, *Problems of Hydrodynamics and Continuum Mech.*, SIAM, 606–616 (1967)
- 16.253 A. Fage: The air flow around a circular cylinder in the region where the boundary layer separates from the surface, *Aero. Res. Council R&M* **1179** (1928)
- 16.254 A. Roshko: On the development of turbulent wakes from vortex sheets, *NACA Rep.* **1191** (1954)
- 16.255 R.D. Henderson: Details of the drag curve near the onset of vortex shedding, *Phys. Fluids* **7**, 2102 (1995)
- 16.256 C.H.K. Williamson: Oblique and parallel modes of vortex shedding in the wake of a circular cylinder at low Reynolds numbers, *J. Fluid Mech.* **206**, 579 (1989)
- 16.257 U. Fey, M. Koenig, H. Eckelmann: A new Strouhal–Reynolds number relationship for the circular cylinder in the range  $47 < Re < 2 \times 10^5$ , *Phys. Fluids* **10**, 1547 (1998)
- 16.258 C. Norberg: An experimental investigation of the flow around a circular cylinder: Influence of aspect ratio, *J. Fluid Mech.* **258**, 287 (1994)
- 16.259 C.H.K. Williamson, A. Roshko: Measurements of base pressure in the wake of a cylinder at low Reynolds numbers, *Z. Flugwiss. Weltraum.* **14**, 38 (1990)
- 16.260 P.W. Bearman: On vortex shedding from a circular cylinder in the critical Reynolds number regime, *J. Fluid Mech.* **37**, 577 (1969)
- 16.261 O. Flaschbart: Messungen an ebenen und gewölbten Platten, *Erg. Aerodyn. Versuch. Göttingen* **4**, 96–100 (1932)
- 16.262 W.C.L. Shih, C. Wang, D. Coles, A. Roshko: Experiments on flow past rough circular cylinders at large Reynolds numbers, *J. Wind Eng. Indust. Aerodyn.* **49**, 351 (1993)
- 16.263 M.S. Bloor: The transition to turbulence in the wake of a circular cylinder, *Fluid Mech.* **19**, 290 (1964)
- 16.264 S. Taneda: Downstream development of wakes behind cylinders, *J. Phys. Soc. Jpn.* **14**, 843 (1959)
- 16.265 J.H. Gerrard: The wakes of cylindrical bluff bodies at low Reynolds number, *Philos. Trans. R. Soc. A* **288**, 351 (1978)
- 16.266 M. Coutanceau, R. Bouard: Experimental determination of the main features of the viscous flow in the wake of a circular cylinder in uniform translation: steady flow, *J. Fluid Mech.* **79**, 231 (1977)
- 16.267 S.C.R. Dennis, G.Z. Chang: Numerical solutions for steady flow past a circular cylinder at Reynolds numbers up to 100, *J. Fluid Mech.* **42**, 471 (1970)
- 16.268 B. Fornberg: Steady viscous flow past a circular cylinder up to Reynolds number 600, *J. Comp. Phys.* **61**, 297 (1985)
- 16.269 A. Thom: The flow past circular cylinders at low speeds, *Proc. R. Soc. A* **141**, 651 (1933)
- 16.270 M. Provansal, C. Mathis, L. Boyer: Benard–von Karman instability: Transient and forced regimes, *J. Fluid Mech.* **182**, 1 (1987)
- 16.271 E. Berger: Transition of the laminar vortex flow to the turbulent state of the Karman vortex street behind an oscillating cylinder at low Reynolds number, *Jahrbuch Wiss. Ges. L. R.*, 164–172 (1964), in German
- 16.272 F.R. Hama: Three-dimensional vortex pattern behind a circular cylinder, *J. Aeronaut. Sci.* **24**, 156 (1957)

- 16.273 D.J. Tritton: Experiments on the flow past a circular cylinder at low Reynolds numbers, *J. Fluid Mech.* **6**, 547 (1959)
- 16.274 M. Gaster: Vortex shedding from circular cylinders at low Reynolds numbers, *J. Fluid Mech.* **46**, 749 (1971)
- 16.275 A. Roshko: *Modelling, Past and Future*, Comment paper for Whither Turbulence Workshop, Cornell University, ed. by J.L. Lumley (Cornell Univ., Ithaca 1989) pp. 486–489
- 16.276 C.H.K. Williamson: Defining a universal and continuous Strouhal–Reynolds number relationship for the laminar vortex shedding of a circular cylinder, *Phys. Fluids* **31**, 2742 (1988)
- 16.277 H. Eisenlohr, H. Eckelmann: Vortex splitting and its consequences in the vortex street wake of cylinders at low Reynolds number, *Phys. Fluids A* **1**, 189 (1989)
- 16.278 M. Koenig, H. Eisenlohr, H. Eckelmann: The fine structure in the S–Re relationship of the laminar wake of a circular cylinder, *Phys. Fluids A* **2**, 1607 (1990)
- 16.279 M. Hammache, M. Gharib: A novel method to promote parallel shedding in the wake of circular cylinders, *Phys. Fluids A* **1**, 1611 (1989)
- 16.280 M. Hammache, M. Gharib: An experimental study of the parallel and oblique vortex shedding from circular cylinders, *J. Fluid Mech.* **232**, 567 (1991)
- 16.281 D. Gerich, H. Eckelmann: Influence of end plates and free ends on the shedding frequency of circular cylinders, *J. Fluid Mech.* **122**, 109 (1982)
- 16.282 T. Leweke, M. Provansal: The flow behind rings: bluff body wakes without end effects, *J. Fluid Mech.* **288**, 265 (1995)
- 16.283 A. Prasad, C.H.K. Williamson: The instability of the shear layer separating from a bluff body, *J. Fluid Mech.* **333**, 375 (1997)
- 16.284 C.H.K. Williamson: The existence of two stages in the transition to three-dimensionality of a cylinder wake, *Phys. Fluids* **31**, 3165 (1988)
- 16.285 D. Barkley, R.D. Henderson: Three-dimensional Floquet stability analysis of the wake of a circular cylinder, *J. Fluid Mech.* **322**, 215 (1996)
- 16.286 G.D. Miller, C.H.K. Williamson: Control of three-dimensional phase dynamics in a cylinder wake, *Exp. Fluids* **18**, 26 (1994)
- 16.287 C.H.K. Williamson: The natural and forced formation of spot-like “vortex dislocations” in the transition of a wake, *J. Fluid Mech.* **243**, 393 (1992)
- 16.288 T. Leweke, C.H.K. Williamson: Three-dimensional instabilities in wake transition, *Eur. J. Mech. B Fluids* **17**, 571 (1998)
- 16.289 M. Thompson, K. Hourigan, J. Sheridan: Three-dimensional instabilities in the cylinder wake. In: *Int. Colloq. Jets, Wakes and Shear Layers*, ed. by K. Hourigan (CSIRO, Melbourne 1994)
- 16.290 M.C. Thompson, T. Leweke, C.H.K. Williamson: The physical mechanism of transition in bluff body wakes, *J. Fluid Struct.* **15**, 607–616 (2001)
- 16.291 H. Zhang, U. Fey, B.R. Noack, M. Koenig, H. Eckelmann: On the transition of the cylinder wake, *Phys. Fluids* **7**, 1 (1995)
- 16.292 J.-C. Lin, J. Towfighi, D. Rockwell: Instantaneous structure of near-wake of a cylinder: On the effect of Reynolds number, *J. Fluid Struct.* **9**, 409 (1995)
- 16.293 M.F. Unal, D. Rockwell: On vortex shedding from a cylinder, Part 1. The initial instability, *J. Fluid Mech.* **190**, 491 (1988)
- 16.294 L. Schiller, W. Linke: Druck und Reibungswiderstand des Zylinders bei Reynolds’schen Zahlen 5000 bis 40000, *Z. Flugtech. Motorluft.* **24**, 193 (1933), in German
- 16.295 M.F. Unal, D. Rockwell: On the role of shear layer stability in vortex shedding from cylinders, *Phys. Fluids* **27**, 2598 (1984)
- 16.296 M.S. Bloor, J.H. Gerrard: Measurements on turbulent vortices in a cylinder wake, *Proc. R. Soc.* **294**, 319 (1966)
- 16.297 A. Prasad, C.H.K. Williamson: Three-dimensional effects in turbulent bluff body wakes, *J. Fluid Mech.* **343**, 235 (1997)
- 16.298 L.S.G. Kovaszny: Hot wire investigation of the wake behind cylinders at low Reynolds numbers, *Proc. Roy. Soc.* **4**(198), 174 (1949)
- 16.299 H. Djeridi, M. Braza, R. Perrin, G. Harran, E. Cid, S. Cazin: Near-wake turbulence properties around a circular cylinder at high Reynolds number, *Flow Turb. Combust.* **71**, 19 (2003)
- 16.300 R. Govardhan, C.H.K. Williamson: Mean and fluctuating velocity fields in the wake of a freely-vibrating cylinder, *J. Fluids Struct.* **15**, 489 (2001)
- 16.301 E. Achenbach: Influence of surface roughness on cross-flow around a circular cylinder, *J. Fluid Mech.* **46**, 321 (1971)
- 16.302 O. Güven, V.C. Patel, C. Farrell: Surface roughness effects on the mean flow past circular cylinders, *Iowa Inst. Hydraulic Res. Rep.* **175** (1975)
- 16.303 G. Schewe: On the force fluctuations acting on a circular cylinder in crossflow from subcritical up to transcritical Reynolds numbers, *J. Fluid Mech.* **133**, 265 (1983)